Microfluidic-assisted self-assembly of biocompatible polymersomes : size control, drug-loading and self-assembly mechanism

Anouk Martin

THESE PRESENTEE

POUR OBTENIR LE GRADE DE

DOCTEURE DE L'UNIVERSITE DE BORDEAUX

ECOLE DOCTORALE DES SCIENCES CHIMIQUES

SPÉCIALITÉ : POLYMÈRES

Par **Anouk Martin**

Microfluidic-assisted self-assembly of biocompatible polymersomes: size control, drug-loading and self-assembly mechanism

Auto-assemblage assisté par microfluidique de polymersomes biocompatibles : contrôle de la taille, encapsulation de principe actif et mécanisme d'auto-assemblage

Sous la direction de : Prof. Sébastien LECOMMANDOUX

Soutenue le 30 Juin 2023

Devant la commission d'examen formée de :

Mr LENG Jacques	Directeur de recherche, Solvay	Président du jury
Mr BATTAGLIA Giuseppe	Professeur, Institute for Bioengineering of Catalonia	Rapporteur
Mme LI Min-Hui	Directrice de recherche CNRS, Chimie ParisTech	Rapporteur
Mme LEBLOND-CHAIN Jeanne	Chargée de recherche, INSERM Bordeaux	Examinateur
Mr CALVIGNAC Brice	Professeur, Université d'Angers	Examinateur
Mr BROTONS Guillaume	Professeur, Université du Mans	Examinateur
Mme MUTSCHLER Angela	Maître de conférences, Université de Bordeaux	Examinateur
Mr LECOMMANDOUX Sébastien	Professeur, Bordeaux INP	Directeur de thèse

Remerciements

Je tiens tout d'abord à remercier Sébastien Lecommandoux et Angela Mutschler pour m'avoir accompagnée tout au long de ce projet de thèse. Vous m'avez rapidement accordé votre confiance, en m'accordant responsabilités et autonomie tout en me fournissant un encadrement certain. Je remercie Angela pour son soutien au plus proche des manips, pour sa pédagogie et sa bonne humeur. Un grand merci d'avoir été là jusqu'à bout, et d'avoir accordé autant de soin à la correction de ce manuscrit. Je remercie Sébastien d'avoir su m'accorder le temps nécessaire, dans un emploi du temps pourtant déjà chargé, de m'avoir permis de collaborer avec de nombreux laboratoires, de m'avoir permis de présenter mon projet lors de nombreuses conférences et d'avoir toujours été d'un optimisme à toutes épreuves.

J'adresse également mes remerciements aux membres de mon jury de thèse pour m'avoir fait l'honneur de juger mes travaux et également pour être venus assister à ma soutenance à Bordeaux. Je tiens à remercier mes rapporteurs Min-Hui Li et Giuseppe Battaglia, mes examinateurs Jeanne Leblond-Chain, Brice Calvignac, Guillaume Brotons, ainsi que le président de mon jury Jacques Leng.

Je souhaite remercier le CNRS, qui au travers du financement 80 Prime, a rendu ces travaux de thèse possibles, ainsi que l'université de Bordeaux pour m'avoir permis de poursuivre cette thèse tout en me donnant accès à de nombreuses formations complémentaires.

Je souhaite remercier toutes les personnes avec qui j'ai pu collaborer tout au long de cette thèse, m'accordant leur temps, leur bienveillance, et leur savoir.
Dans un premier temps, je souhaite remercier Jacques Leng, Jean-Baptiste Salmon et Gérald Clisson du Laboratoire du futur (Solvay, Pessac). Vous m'avez apporté un soutien infaillible pour tout ce qui touchait à la microfluidique, soutien aussi bien pratique que théorique, avec notamment la conception de puce et la compréhension des écoulements. Je vous remercie de m'avoir accueilli au LOF, de m'avoir accordé votre temps, tout cela avec gentillesse et pédagogie.

Je souhaite remercier également toutes les parties ayant rendu possible le projet Synchrotron. Je commencerai par remercier Ahmed Bentaleb (Centre de Recherche Peul Pascal, Pessac) pour les expériences préliminaires en Rayon-X, qui a eu la patience de passer mes échantillons et d'optimiser les mesures dans le but de présenter un proposal robuste.

Je tiens ensuite à remercier le laboratoire de Micro et Nanomédecines Translationnelle (Angers) pour m'avoir accueilli au sein du laboratoire pour une semaine de partage scientifique autour de la microfluidique. Je remercie plus particulièrement Brice Calvignac pour son implication dans le projet Synchrotron. Merci d'avoir apporté ton expertise en impression 3D, d'avoir pensé et confectionné les pièces nécessaires à la mesure en ligne et d'avoir apporté des solutions aux problèmes de dernière minute ! Merci à Brice et Jean-Christophe Gimel pour être venus veiller de longues heures à SOLEIL, un grand merci pour votre gentillesse et votre implication.

Je souhaite ensuite remercier Guillaume Brotons (Institut des Molécules et Matériaux du Mans), notre expert Rayon-X, qui nous a ouvert les portes de la presque autonomie au synchrotron,

et qui a eu la patience de m'enseigner les méandres du traitement des datas RX synchrotron avec bienveillance.

Au sein du LCPO, je souhaite remercier tous les permanents qui nous facilitent le quotidien et/ou les tâches administratives : Dominique, Emilie, Séverine, Corinne, Claude et Olivier.

Je remercie aussi les permanents ayant apporté leur pierre à l'édifice, soit par leur soutien scientifique ou leur soutien moral. Je remercie Christophe Schatz et Paul Marque pour leur aide et implication dans les différentes analyses de diffusion de lumière qui ont été omniprésentes durant cette thèse. Je remercie Sylvain Bourasseau pour sa gentillesse, sa disponibilité et sa tentative presque fructueuse de me convertir à la course à pied.

Je souhaite remercier également les permanents de l'équipe 3 qui, au détour d'une salle de manip, ou lors des group meeting, ont apporté leur expertise : Colin Bonduelle, Elisabeth Garanger, Bertrand Garbay, Jean-François Le Meins et Olivier Sandre.

Je souhaite formuler un remerciement spécial à Emmanuel Ibarboure pour son expertise et son écoute. Manu, tu as été une présence inestimable tout au long de cette thèse. J'ai apprécié chaque instant de notre collaboration, mais aussi ton amour des belles images au microscope. De la croissance de magnifiques cristaux de Ganciclovir observés en birefringence, à la formation des « fleurs de douche » au confocal, tu apportes à cette thèse ces plus belles images. Mais au-delà de ces aspects, tu as été un soutien moral à toutes épreuves, apportant de nouvelles idées à mes blocages, et prêtant une oreille attentive à mes déboires quand mes jours se transformaient en Telenovelas. Pour les longues discussions, les gâteaux et les plantes vertes, mille mercis.

Il m'est important de remercier les doctorants et post-doctorants qui ont partagé mon quotidien durant cette thèse.

Je souhaite remercier Coralie Lebleu pour avoir mené les travaux antérieurs à ce sujet, et pour avoir montré l'intérêt de poursuivre cette étude.

Je souhaite remercier Pierre Lalanne, pour avoir traversé ce début de thèse à mes côtés. Pierre, j'ai adoré partager ce projet avec toi, aussi longtemps que cela aura durée. Tu es cette personne rayonnante, investie et tu possèdes ce rire si caractéristique qui me manquera. Tu m'as accompagné dans mes débuts au LCPO, et bien que parti vers d'autres horizons professionnels, pour lesquels je te souhaite le meilleur, tu es resté avec moi jusqu'à la fin, implicitement camouflé dans le nom du polymère que j'aurai utilisé pendant toute cette thèse. Pour Bruno, et pour tout ce que tu as fait pour moi, mille mercis.

Je souhaite remercier tous « les anciens », qui ont su accueillir et épauler la jeune scientifique que j'étais : Martin, Tim, Manon, Pedro, Nadia, Megi, Florian et Boris. Merci d'avoir pris le temps de m'accompagner, malgré vos emplois du temps que je savais très chargés.

Je remercie aussi tous les nouveaux venus après moi, pour avoir apporté leur vision nouvelle et leur énergie au laboratoire : Rosanna, Johanna, Eloïse, Hannah, Leslie, Mostafa, Sarah, Selma, Matthieu, Camille, Julien, Alban, Justine, Barbara, Sifan, Yupei, Valentin, Clémence, Antoine, Yue, Dongxu.

Je souhaite remercier particulièrement Elise, pour avoir pris mon relais, pour m'avoir soutenue dans les batailles du quotidien, pour les discussions potins et pour sa bonne humeur. Je remercie aussi Diana, pour m'avoir supporté aussi bien au « bureau rédaction », à New-York et en conférence, mais aussi pour sa bonne humeur malgré l'adversité. Je souhaite enfin remercier Marie, pour avoir apporté un peu de Belgique au laboratoire, pour sa jovialité, sa spontanéité, mais surtout pour son humanité et son soutien. Merci d'avoir traversé avec moi cette dernière étape de rédaction, et de m'avoir permis de me sentir moins seule dans cette épreuve.

Je souhaite enfin remercier ma famille pour leur soutien tout au long de ce parcours scientifique. Votre amour et vos encouragements ont pavé le chemin aboutissant à ce doctorat.

Je remercie mes parents qui ont veillé à mon éducation et à mon épanouissement. Merci de m'avoir inculqué des valeurs de persévérance, et d'avoir toujours cru en moi.

Mes sœurs, pour les moments de joie et de distraction, les encouragements, les colis surprises et les weekends à trois. Je sais votre soutien et votre confiance en moi infaillible.

Baptiste, pour avoir supporté les extravagances qu'exige une thèse, pour avoir partagé les bons moments, et m'avoir soutenue dans les mauvais. Merci d'avoir apporté ce point de vue extérieur qu'il me manquait parfois, d'avoir patiemment écouté mon charabia scientifique, et d'avoir adouci mon quotidien.

Merci encore à tous ceux qui ont fait partie de ce voyage. Une thèse n'a finalement rien d'une quête laborieuse que l'on fait en ermite. J'ai eu la chance de faire de belles rencontres et d'être entourée tout au long du chemin, et ce sont toutes ces personnes qui ont rendu mon travail possible. A vous toutes et tous ; Merci.

General table of contents

List of abbreviations **11**

List of symbols **13**

General introduction **15**

Chapter I. Literature Review **19**

1. Nanomedicine and the breakthrough of polymer nanoparticles **23**

1.1. Presentation of the general concept of nanomedicine 23

1.2. Exploring nanomaterials based on lipids and polymers 25

1.3. The role of poly(ethylene glycol) for improving stealth properties 28

1.4. Controlled biodistribution of nanoparticles via passive and active targeting mechanism 30

1.5. Controlled drug release of nanoparticles via external stimuli 33

2. Vesicle formulation: the importance of process choice on size control **34**

2.1. Film hydration processes 36

2.2. Solvent-displacement processes 39

3. Adjustment of the size of nanoparticles by post-processing recalibration **45**

3.1. Extrusion 45

3.2. Sonication 46

3.3. Freeze-Thawing 47

4. State of the art of physico-chemical parameters allowing the control of the size and the morphology of polymer nanoparticles **48**

4.1. The effect of solvent 48

4.2. The effect of copolymer concentration 48

4.3. Incorporation of chemical additives 49

4.4. The role of temperature 50

5. Polymersomes as drug delivery systems **51**

5.1. General definitions of drug delivery systems 51

5.2. Drug encapsulation by passive loading 52

5.3. Drug encapsulation by active loading 54

5.4. Evaluation and control of the drug release from nanoparticles 58

Conclusion **62**

References **63**

Chapter II. Microfluidic-assisted self-assembly of polymersomes: *in vitro/in vivo* "ready to use" method with size control **75**

Introduction **79**

1. Experimental section **80**

1.1. Materials 80

1.2. Methods 80

2. Study of parameters for PEG-*b*-PTMC microfluidic-assisted self-assembly **85**

2.1. Effect of osmotic pressure on vesicles 85
2.2. Organic solvents choice towards *in vitro / in vivo* experiments 87
2.3. Nucleation of self-assembly system: critical water content assays 88

3. Microfluidic assisted self-assembly processes 92
3.1. Microfluidic chip design 92
3.2. Optimization of the organic / aqueous solvent ratio in micromixer chip 95
3.3. Optimization of the organic / aqueous solvent ratio in Herringbone chip 98

4. Fine tuning vesicle size with microfluidic parameters 100
4.1. Variation of initial copolymer concentration 100
4.2. Variation of total flow rate as a way to influence solvents mixing speed 103
4.3. Impact on solvent removal conditions on vesicle formation 105
4.4. Measuring mixing time in microfluidic chips 106

5. Conclusion 111

6. Appendix 113
6.1. Viscosity and refractive index of DMSO/PBS and Acetone/Glucose mixtures 113
6.2. Solubility Parameters 114
6.3. Scattered intensity of 100 nm latex under several stirring rate 117
6.4. Multi-Angle Light Scattering, calculations and methods 118
6.5. Dynamic light scattering 124
6.6. Multi Angle Light scattering 126

7. References 131

Chapter III. Drug loading in PEG-*b*-PTMC polymersomes 137

Introduction 141

1. Experimental Section 143
1.1. Materials 143
1.2. Methods 143

2. Critical water content measurement for copolymer and drug compatibility 157
2.1. Evaluation of the critical water content of Ganciclovir 157
2.2. Evaluation of the critical water content of Coumarin 6 159
2.3. Evaluation of the critical water content of Doxorubicin 161

3. Microfluidic assisted passive loading of drugs 162
3.1. Towards PEG_{22}-*b*-$PTMC_{51}$ loaded vesicles 162
3.2. Improving Ganciclovir passive loading by tuning the CWC of PEG_{22}-b-$PTMC_{51}$ 164
3.3. Towards PEG_{46}-*b*-$PTMC_{119}$ loaded vesicles 168

4. Active loading using PEG_{22}-*b*-$PTMC_{51}$ 175
4.1. Active loading through the use of pH gradient 175
4.2. Active loading through the use of ionic gradient 178

5. Conclusion 181

6. Appendix 183
6.1. Temperature measurement during solvent exchange processes 183
6.2. DLS measurement of PEG_{44}-b-$PTMC_m$ self-assemble nanoparticles 183

7. References 185

Chapter IV. Elucidation of self-assembly mechanism 189

Introduction 193

1. Experimental Section 195

1.1. Materials 195

1.2. Methods 195

2. PEG-*b*-PTMC self-assembly study mechanism: step by step observation at the microscale 198

3. *In-operando* monitoring of PEG_{22}-*b*-$PTMC_{51}$ self-assembly by X-Ray measurement (SAXS) 203

3.1. Evaluation of PEG_{22}-b-$PTMC_{51}$ polymersome structure by laboratory SAXS acquisitions at rest within quartz capillaries. 203

3.2. Optimization of microfluidic device for Synchrotron SAXS acquisitions 206

3.3. Synchrotron SAXS measurements and data analysis 212

4. Conclusion 229

5. Appendix 231

5.1. Vesicle fitting model from SasView software 231

5.2. Elongated micelle fitting model 232

6. References 235

General conclusion and perspectives 239

Preliminary results on functionalized vesicle formulation 243

Preliminary results on DBCO function availability on vesicle surface 245

References 249

List of abbreviations

ABV	Doxorubicin, Bleomycin, Vincristine: standard chemotherapy combination
AIDS	Acquired Immuno Deficiency Syndrome
API	Active Pharmaceutical Ingredient
CBER	Center of Biologics Evaluation and Research
CDER	Center for Drug Evaluation and Research
CRPP	Centre de Recherche Paul Pascal
CWC	Critical Water Content
DLC	Drug Loading content
DLS	Dynamic Light Scattering
DMSO	Dimethylsulfoxide
DCR	Derived Count Rate
EDTA	Ethylene-diamine-tetraacetic acid
EE	Encapsulation Efficiency
EPR	Enhanced Permeability and Retention effect
FDA	Food and Drug Administration
FRET	Fluorescence Resonance Energy Transfer
FWR	Feed Weight Ratio
GCV	Ganciclovir
HEPES	2-[4-(2-hydroxyethyl)piperazin-1-yl]ethanesulfonic acid
ITO	Indium Tin Oxide
LNC	Lipid Nanocapsules
MALS	Multi Angle Light Scattering
MINT	Micro et Nanomédecines Translationnelles
MLVs, MVVs	Multi-Lamellar and Multivesicular Vesicles
NMs	Nanomedicines
NPs	Nanoparticles
PAA	Poly(acrylic acid)
PB	Poly(butadiene)
PBS	Phosphate Buffer Saline
PCL	Poly(caprolactone)
PDI	Poly dispersity index
PDMA	Poly(N,N'-dimethylacrylamide)

PDMS	Poly(dimethyl siloxane)
PDPA	Poly(2-(diisopropylamino)ethyl methacrylate))
PEG	Poly(ethylene glycol)
PGMEA	Propylene Glycol Methyl Ether Acetate
PHPMA	Poly([N-(2-hydroxypropyl)]methacrylamide)
PLA	Poly(lactic acid)
PLGA	Poly(lactid-*co*-glycolid acid)
PMPC	Poly(2-(methacryloyloxy)ethyl phosphorylcholine)
PNBA	Poly(*o*-nitrobenzyl acrylate)
PPLG	Poly(γ-R-glutamate)
PS	Poly(styrene)
PTFE	Poly(tetrafluoroethylene)
PTMC	Poly(trimethylene carbonate)
PTMBPEC	Poly(mono-2,4,6-trimethoxy benzyldiene-pentaerythriol carbonate-*co*-acryloyl carbonate)
PVA	Poly(vinyl alcohol)
ROS	Reactive Oxygen Species
SAXS	Small Angle X-ray Scattering
SDS	Sodium Dodecyl Sulfate
SLD	Scattering Light Density
SLS	Static Light Scattering
SUVs, LUVs, GUVs	Small, Large and Giant Unilamellar Vesicles
TAN	Temperature Assisted Nanoprecipitation
TEM	Transmission Electron Microscopy
TFR	Total Flow Rate
THF	Tetrahydrofurane
UV	Ultra Violet

List of symbols

a_0	Area occupied by hydrophilic group in copolymer
D	Coefficient diffusion
D_H	Hydrodynamic Diameter
$LogP$	Logarithm of the partition coefficient of a drug
$f_{Hydrophilic}$	Hydrophilic fraction in copolymer
F_t	Molar attraction function
F_p	Polar component of molar attraction function
k_B	Boltzmann constant
$I(q)$	Scattered light intensity
λ	Wavelenght
l_c	Length of molecule
M	Molar masses
N_A	Avogadro number
N_{agg}	Aggregation number
n_i	Refractive index
Pe	Peclet number
Pc	Packing parameter
Q_e, Q_i	External and internal flow rates
R^2	Correlation coefficient
q	Scattering vector
R_G	Radius of gyration
R_H	Hydrodynamic radius
R_c, R_i	Radius of channel, Radius of inner jet
R_{TEM}	Radius determined by measurement on Cryo-TEM images
U	Average flow speed ($m.s^{-1}$)
v	Volume
V	Molar volume
ρ	Shape factor
Δ	Distance through which diffusion of molecule occurs
$\Delta\delta_{P-S}$	Polymer-solvent solubility parameter
Δ_T	Lyderson correction for non-ideality
δ_p ; δ_d ; δ_H ; δ_t	Contributions of polar forces, dispersion forces and hydrogen to solubility parameter total
δ_{PTMC}	Polymersome membrane thickness
η	Dynamic Viscosity
ρb	Scattering light density
φ	Membrane volume fraction
χ^2	Fitting error

General introduction

Over the past few decades, the field of drug delivery has seen remarkable advances in improving therapeutic precision and efficacy for the treatment of various diseases, thanks to the drive to overcome the limitations of conventional "free" drug therapies by minimizing their side effects. In this context, nanoparticles have proven excellent candidates in improving the therapeutic efficacy of many drugs thanks to their contribution to the modification of pharmacokinetics and the opportunity to control their biodistribution. One promising strategy that has gained attention is the use of polymersomes as nano-carriers. Polymersomes are resulting from the self-assembly of amphiphilic block copolymers into vesicles with a structure similar to that of liposomes. These unique structures offer a wide range of advantages over conventional drug delivery systems, making them an interesting area of research with an important potential for improving therapeutics outcomes. Polymersome design and engineering provides a versatile platform for loading and delivering a diverse array of therapeutic agents, including small molecules, peptides, proteins, and nucleic acid. By tailoring the physicochemical properties of the polymersome components, such as copolymer composition, chain length, hydrophobicity, and surface change, researchers can precisely control their size, stability, drug-loading capacity and drug-release kinetics. These biocompatible polymeric vesicles have the unique advantage of being able to load hydrophilic and hydrophobic drugs into their inner aqueous core or membrane, respectively. This duality makes them suitable for a wide range of applications as a drug delivery system. These structures can also be modified with targeting ligand, such as antibodies or peptides, providing a spatial control over drug delivery by targeting specific cell lines, tissues or organs. Moreover, by incorporating stimuli-responsive elements such as pH-sensitive or temperature-sensitive polymers, these vesicles can be tailored to provide precise spatio-temporal control over drug release, thereby enabling site-specific drug delivery and reducing the risk of systemic toxicity.

In this context, this PhD project aims to develop drug-loaded vesicles ready to use for *in vitro / in vivo* assays and made with a biocompatible and biodegradable block copolymer: poly(ethylene glycol)-*block*-poly(trimethylene carbonate) or PEG-*b*-PTMC. The composition of the block copolymer has been chosen by selecting the hydrophilic PEG block for its biocompatibility (PEG is eliminated primarily through renal excretion) and its stealth effect: when nanoparticles are coated with PEG, the hydrophilic PEG chains on the surface of the particles create a hydrated layer, or "brush," that can sterically hinder the adsorption of serum proteins, especially the opsonins that are responsible for the activation of macrophages. This “PEGylation” results in a decrease in the rate of particle uptake by phagocytic cells and an increase in circulation time, which is desirable for drug delivery applications. On the other part, the choice of hydrophobic block PTMC is governed by its biodegradability. In the body PTMC undergoes hydrolysis or enzymatic degradation leading to the formation of trimethylene glycol which is further metabolized to form glycolic acid. The degradation products of PTMC are considered safe and non-toxic to the body, which makes PTMC a suitable material for biomedical applications.

The primary focus of this PhD project was to evaluate the self-assembly behavior of two PEG-*b*-PTMC copolymers, namely PEG_{22}-*b*-$PTMC_{51}$ and PEG_{46}-*b*-$PTMC_{119}$, which have been demonstrated to preferentially form vesicles. The use of “PEGylation” permit to escape the opsonization process, but the size of nanoparticle remains a key parameter to control, and the size can influence their circulation

time, liver and kidney uptake, and tissue accumulation. Among all the existing processes for the formulation of vesicles, and in particular polymersomes, microfluidics has been widely recognized as an ideal system for producing well-defined vesicles with high reproducibility, owing to its ability to provide easy access to process parameters that can be fine-tuned to precisely control vesicle size and other important characteristics. Aiming to produce vesicles with a low dispersity, we used microfluidic assisted self-assembly to produce and tune the size of PEG-*b*-PTMC vesicles.

Another objective of this PhD project is to improve our understanding on the encapsulation mechanisms of molecules inside polymersomes, with a particular focus on the ones of interest in this thesis based on PEG-*b*-PTMC. Concerning the drug encapsulation, one of the important characteristics to take into account is the preference of the drug for aqueous or organic media, given by the octanol/water partition coefficient (log P). This log P value might be a first parameter to consider in predicting whether the drug will go into the hydrophilic core or the hydrophobic membrane of the vesicle and will be evaluated during this PhD project. A more refined approach would be to use the Hansen parameters of the polymer and the drugs, which we did not consider here in a first approach.

Finally, the third objective of this PhD project is to take the advantage over the use of microfluidic processes to gain a deeper understanding of the mechanism of self-assembly of PEG-*b*-PTMC into vesicles. This will be achieved through the use of dynamic light scattering, confocal microscopy and *in operando* measurements X-Ray techniques. Thus, this final objective will allow us to optimize the drug encapsulation conditions by improving our understanding of the transition of block copolymers from the nucleation state to the growth state, ultimately leading to the formation of vesicles.

This thesis manuscript is organized in five chapters. First chapter will be dedicated to an overview of the literature on current strategies employed to produce vesicle and control their hydrodynamic diameter. An overview of drug loading strategies as well as detailed examples on how to spatio-temporally control drug release from polymersomes are compiled. Chapter II gathers optimization of microfluidic assisted self-assembly process of PEG-*b*-PTMC vesicles. Parameters influencing block copolymers self-assembly such as microfluidic chip choice, copolymer concentration and total flow rate will be discussed. In Chapter III, three molecules presenting different hydrophilicity were chosen as models for drug loading: Ganciclovir a hydrophilic antiviral used against human cytomegalovirus infections; Doxorubicin hydrochloride, as an amphiphilic chemotherapy drug; and Coumarin 6 a hydrophobic fluorescent probe which will play the role of hydrophobic drug. Passive and active drug loadings will be intended, comparing loading efficiency of vesicles presenting different membrane thicknesses. Chapter IV presents results obtained from the confocal microscopy observations of copolymer self-assembly, along with X-Ray measurements performed on *in operando* co-flow system for copolymer self-assembly, at Synchrotron Soleil. Finally, different perspectives of this PhD research project will be presented, toward the use of fluorescent PEG-*b*-PTMC vesicles as a model for polymersomes biodistribution evaluation. Another perspective of PEG-*b*-PTMC vesicles is their surface functionalization to create polymersome-cell conjugates with immune cells, with the aim of enhancing the local delivery of Ganciclovir when cytomegalovirus infection is present.

Chapter I.

Literature Review

Table of contents

1. Nanomedicine and the breakthrough of polymer nanoparticles 23

1.1. Presentation of the general concept of nanomedicine 23

1.2. Exploring nanomaterials based on lipids and polymers 25

1.3. The role of poly(ethylene glycol) for improving stealth properties 28

1.4. Controlled biodistribution of nanoparticles via passive and active targeting mechanism 30

1.5. Controlled drug release of nanoparticles via external stimuli 33

2. Vesicle formulation: the importance of process choice on size control 34

2.1. Film hydration processes 36

2.2. Solvent-displacement processes 39

3. Adjustment of the size of nanoparticles by post-processing recalibration 45

3.1. Extrusion 45

3.2. Sonication 46

3.3. Freeze-Thawing 47

4. State of the art of physico-chemical parameters allowing the control of the size and the morphology of polymer nanoparticles 48

4.1. The effect of solvent 48

4.2. The effect of copolymer concentration 48

4.3. Incorporation of chemical additives 49

4.4. The role of temperature 50

5. Polymersomes as drug delivery systems 51

5.1. General definitions of drug delivery systems 51

5.2. Drug encapsulation by passive loading 52

5.3. Drug encapsulation by active loading 54

5.4. Evaluation and control of the drug release from nanoparticles 58

Conclusion 62

References 63

1. Nanomedicine and the breakthrough of polymer nanoparticles

1.1. Presentation of the general concept of nanomedicine

From a general point of view, nanotechnologies are described as objects designed with at least one dimension in the nanometric range. They are findable in many applications, from electronic areas (with processors and carbon nanotubes exploitations) to medical field (as targeted delivery of drugs, imaging agents, and other therapeutic agents to specific cells or tissues in the body). Theses nano-scale objects exhibit promising properties that have generated significant interest in them.[1]

As previously mentioned, medicine hasn't been spared by the nanotechnology craze, as technological innovation of nano-size technologies within medicine are now referred as "nanomedicines" (NMs) by the National Institute of Health in USA.[2] Moreover, the European Science Foundation gives an extended definition as following : "the comprehensive monitoring, repair and improvement of all human biological systems, working from the molecular level using engineered devices and nanostructures to achieve medical benefit".[3]

With more than 150 companies developing nanoscale therapeutics in 2006, it is questionable why the field has generated a lot of interest.[4] Indeed, the development of those nanoscale devices tends to answer medicine issues. According to the biopharmaceutical classification system, which categorizes active pharmaceutical ingredient (API) based on their aqueous solubility and cellular permeability, around 40 % of the API present on the pharmaceutical market have low aqueous solubility. Concerning API under evaluation in clinical trials, 70 % of them have low aqueous solubility.[5] In addition, the possibility to be degraded and to be rapidly cleared may lead to poor half-life and poor distribution in human body for these API, implying repeated intake and numerous side effects.[6] The development of a delivery system that enhance solubility and biodistribution has thus become an urgent need.

As summarized by *Peer et al*[7], nanomedicine system have the heavy task to:

- "Protect drug from degradation,
- prevent drug from unwanted interacting with biological environment,
- enhance absorption of the drug into selected tissues,
- control pharmacokinetic and drugs tissues distribution profile,
- improve intracellular penetration." [7]

In addition to the aforementioned roles, precise specifications need to be filled by nanomedicines in order to be used safely in the human body. Therefore, nanomedicine must:

- be biocompatible, well characterized and easily functionalized,
- be stable under physiological aqueous conditions,
- exhibit higher uptake from targeted cells over normal ones,
- have an extended circulation half-life.[7]

To fulfill most or all of these requirements, various types of nanoparticles have been developed over time. Figure 1 illustrates the extensive range of micro and nanomedicines that have been developed over the past two centuries and demonstrates the growing diversity of nanoparticles designed for the healthcare sector since the 1950s. Firstly, they were designed to deliver drugs or

therapeutic agents to specific cells or tissues in the body, which can improve the effectiveness of treatment and reduce the risk of side effects.

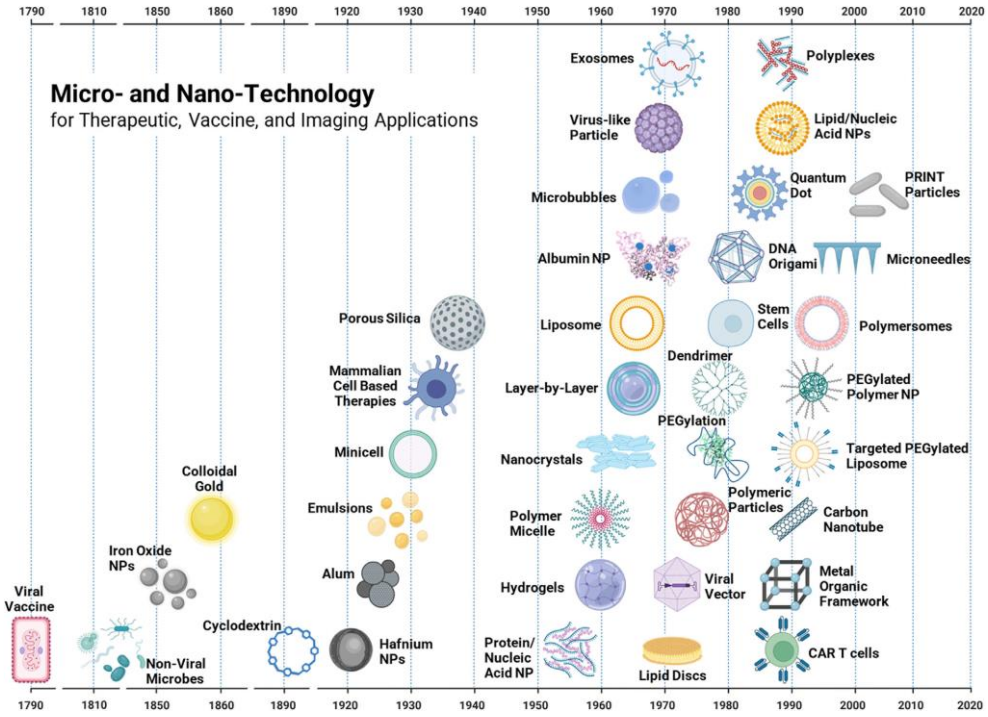

***Figure 1**: Timeline showing first time reported micro and nanomedicine. From Stiepel et al.[8]*

In recent years, increasingly versatile nanoparticles with the most complex functionality have been developed to offer nanomedicines combining diagnostics, imaging and targeted drug delivery. Nanoparticles (NPs) can be now engineered to have a range of different physical and chemical properties, such as composition, size, shape or surface chemistry (as shown in Figure 2)[9], which can be tailored to suit different applications and medical needs. Polymer nanoparticles play a major role in these new functionalization challenges. Thanks to this impressive “tool box” that offers these colloidal systems, the term of “personalized medicine” is today the issue in treatments that use nanomedicine technology.

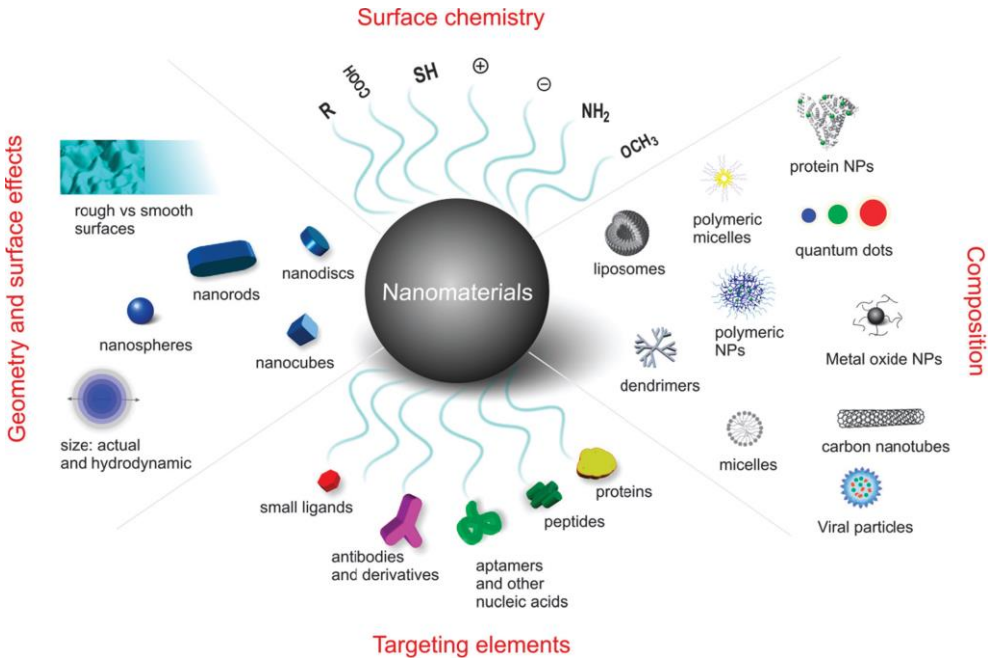

Figure 2: *Schematic representation of the multiple designs leading to nanoparticles. Variety comes from composition, targeting moieties, surface chemistry, size and shape, allowing to have a perfectly dedicated nanomedicine. From Kamaly et al.*[9]

1.2. Exploring nanomaterials based on lipids and polymers

Through the different types of colloidal systems present in nanomedicine, lipid vesicles and polymer nanoparticles are counting for a major part of nanoparticles approved for clinical use and investigational drugs, as represented by Figure 3.

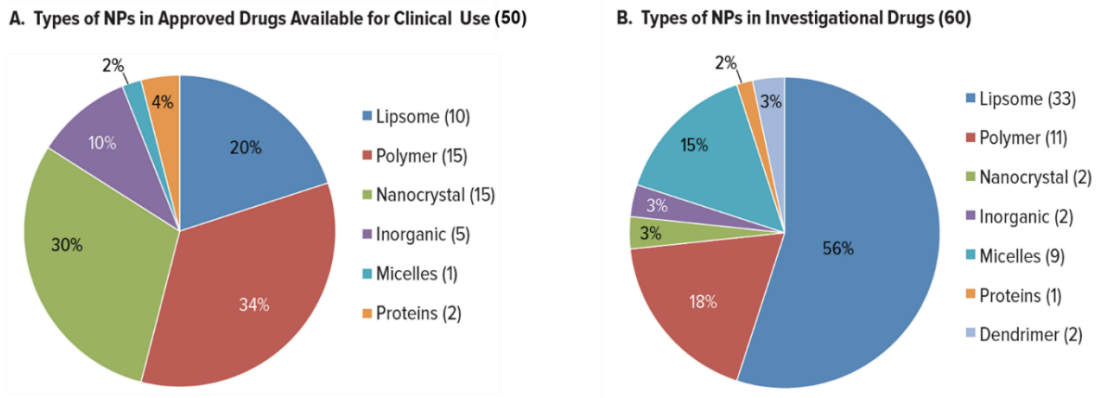

Figure 3: *Type repartition of NPs approved for clinical use and investigational drugs. Pie charts enhance the majority share occupied by liposomes and polymer NPs over other types of NMs as they represent more than 50% of approved NMs and close from ¾ of investigational drugs. From Ventola et al.*[10]

From the Greek suffix "-some" (body of), liposome are vesicles composed of a lipidic bilayer enclosing an aqueous core. Lipids are not the only molecules forming vesicles and an entire family of "-somes" object is now referred, such as polymersomes (polymeric vesicles)[11], niosome (nonionic

amphiphilic vesicles)[12], virosomes (viral protein decorated vesicles)[13], vesosomes (nested vesicles)[14] and some others. The first example of liposomes were described in 1964[15] paving the way to their polymeric counterparts, first reported 30 years later.[16,17] However, the path from first initial discovery to FDA (Food and drug administration) approval, is lined with clinical trials that often cause delays in their use as treatments. As an example, 30 years passed between the first report on liposomes and the FDA approval of Doxil®, the first liposomal nanomedicine approved on the pharmaceutical market to treat AIDS associated with Kaposi's Sarcoma[18]. Northefelt *et al.*[18] compared the efficiency and toxicity of the standard chemotherapy combination (doxorubicin, bleomycin, vincristine, named ABV) and doxorubicin loaded pegylated-liposomes. The study highlights the better response rate of liposomes compared to the free drug (45.9 % and 24.8 %) that may be attributed to an increased half-life of the loaded drug (55 h) compared to the free drug (1 h). They also report that well-known side effects such as alopecia, neuropathy and nausea occurred with a significant lower frequency to patients treated with the liposomal drug, which leads to a lower rate of patient discontinuing their participation in the study (11 % of patients quitting liposomal treatment against 37 % for ABV) [18]. This study shows how nanomedicines are used to increase efficiency of drug while decreasing side effects.

In the literature on polymeric nanomedicines, there are reports of multiple shapes and forms of these objects. From polymer-drug conjugates, micelles, dendrimer, nanoshells, to vesicles, the use of polymers leads to a lot of promising NMs, as shown in Figure 4. Indeed, polymers can be biocompatible, with a high versatility of composition and shape.[6]

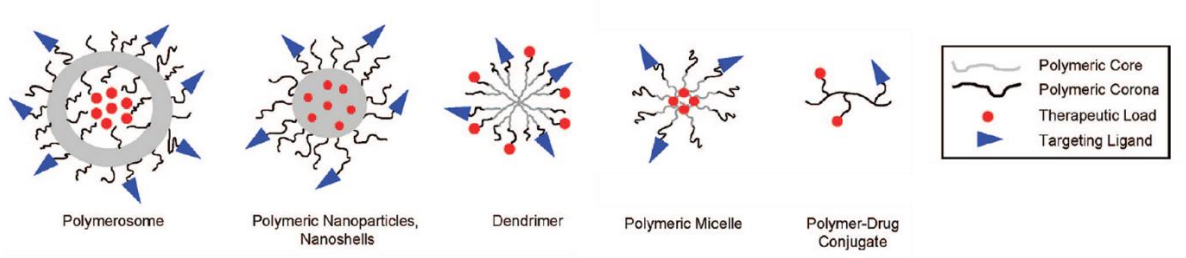

***Figure 4** : Polymeric nanoparticle platform. From Alexis et al.[6]*

At first, liposomes presented the great interest of being able to load both hydrophobic and hydrophilic drugs. Indeed, lipidic corona can accommodate hydrophobic drug while aqueous core can host hydrophilic drug. Following this lipidic example, polymer science developed polymersomes that keep similar structure, by using amphiphilic block copolymer. Figure 5 gives a schematic representation of both liposomes and polymersomes.

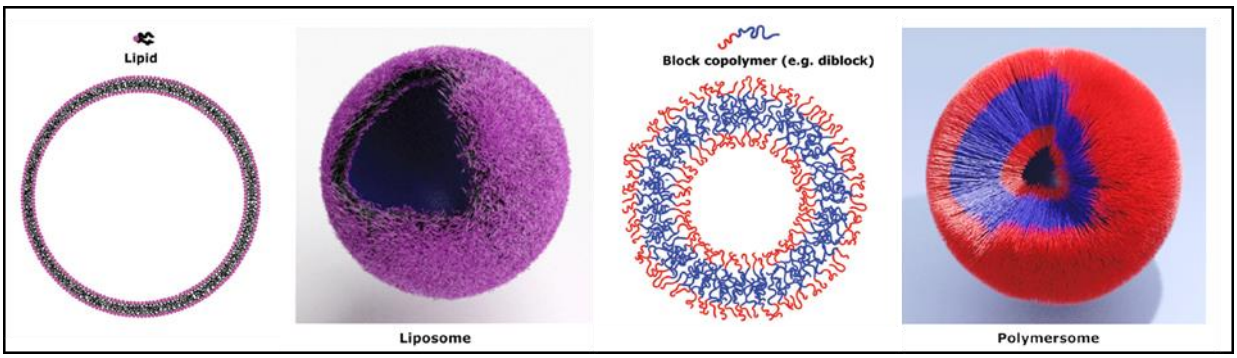

***Figure 5**: Schematic representation of liposome (left) and polymersome (right). From Rideau et al.[19]*

Polymersomes are composed of amphiphilic copolymers, with a hydrophilic block and a hydrophobic block, and are presenting the property to self-assemble in aqueous solution into various shapes. When block copolymer is in contact with aqueous solvent, hydrophobic block escaping water leads to self-assembly of the copolymer. Self-assembly of block copolymers in aqueous water is driven by a combination of thermodynamic and entropic forces. The hydrophobic blocks of the copolymers tend to associate with each other and form structures in order to reduce their exposure to the polar solvent, while the hydrophilic blocks interact favorably with the solvent and distribute evenly throughout the solution. This creates a balance of forces that drives the copolymer to self-assemble into specific nanoscale structures, such as micelles, lamellae or vesicles. The obtained shapes have been shown to be dependent on the packing parameter (*Pc*) of the polymer. *Pc* is definite following this equation (Equation I.1):

$$Pc = \frac{v}{a_0 l_c} \qquad I.1$$

with *v* as the volume of the hydrophobic chain, a_0 the area occupied by the hydrophilic group and l_c the length of the molecule. Depending on the *Pc* value, block copolymers are more willing to form either micelle, warm-like micelle or vesicle structure, as illustrated by Figure 6.[20]

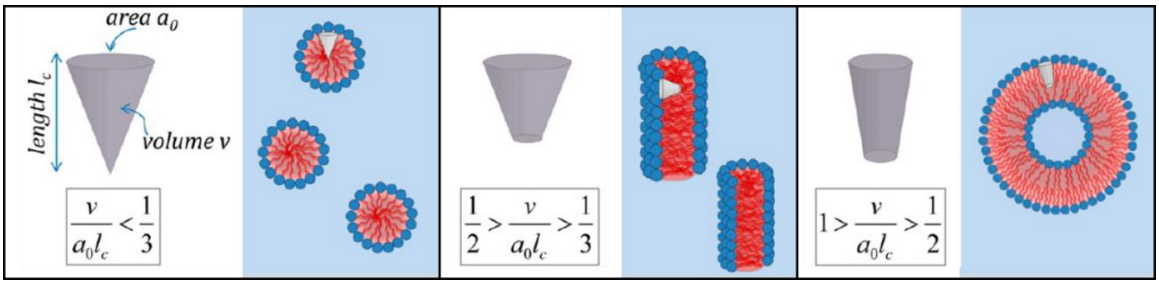

Figure 6: *Packing parameter theoretically predicting morphology of amphiphilic aggregates. (according to Israelachvili et al.[20]). From Bleul et al.[21]*

In addition to these driving forces, the microphase separation of the blocks can also be influenced by other factors such as the molecular weight, the temperature, the polymer concentration, or the ionic strength of the solution. These factors can influence the thermodynamics and kinetics of self-assembly and ultimately determine specific structures that are formed. This is why *Pc* parameter has progressively been replaced by a simpler parameter; the mass fraction of hydrophilic polymer, to predict the morphology resulting of the self-assembly. Discher *et al.*[11] proposed a starting point on the prediction of the shape, depending on the hydrophilic fraction of block copolymer ($f_{Hydrophilic}$). This study proposed that copolymer with $f_{Hydrophilic}$ between 25 % and 40 % will tend to form vesicles, those with $f_{Hydrophilic}$ between 40 % and 50 % will form cylinders and those being outside of those ranges will form micelles or invert micelles. This hypothesis is represented in Figure 7. However, despite the fact that $f_{Hydrophilic}$ is easier to chemically controlled during the polymerization of the block copolymer, the prediction of morphology could be influenced by the nature of the block copolymer used.

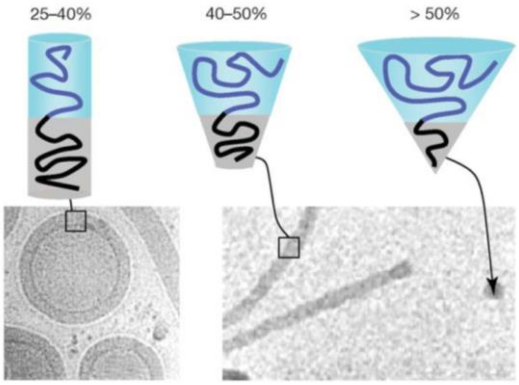

Figure 7 : *General rule to predict NPs shape regarding their hydrophilic fraction. From Discher et al.*[11]

As previously mentioned, polymersomes have a high potential as drug delivery system and has also the advantage of providing solutions to the main drawbacks of their lipidic counterparts, while keeping biocompatibility and capacity of loading both hydrophilic and hydrophobic drugs. Comparison of those two kind of vesicles has already been reviewed by Rideau *et al.*[19] and Matoori *et al.*[22] and is summarized in Figure 8.

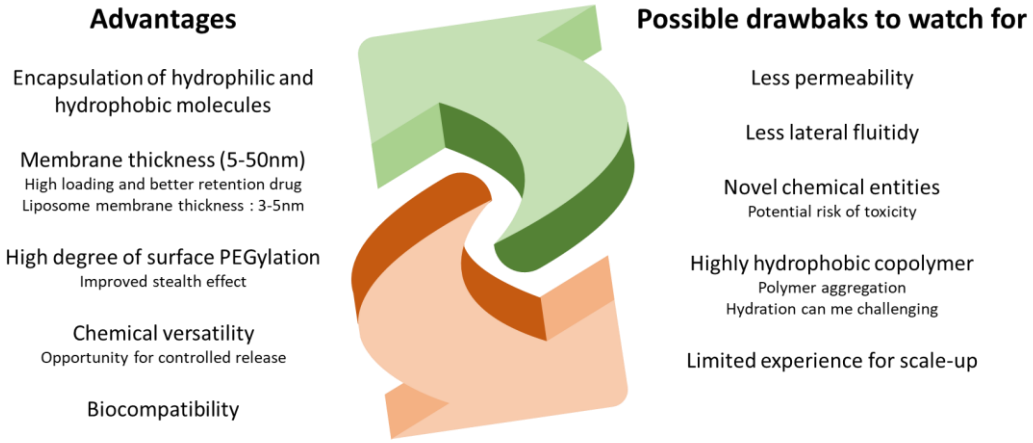

Figure 8: *Advantages and possible drawbacks of polymersomes compared to liposomes. Inspired of Matoori et al.*[22]*, completed with Rideau et al.*[19]

The first part of this chapter maintains a general understanding of the concept of nanomedicine while the second and third parts will concentrate primarily on vesicles, with a specific emphasis on polymersomes.

1.3. The role of poly(ethylene glycol) for improving stealth properties

Nanomedicines have been upgraded overtime to override issues such as fast clearance, low tissue specificity and accumulation or low effective amount of drug loaded. Nicolas *et al.* describe the evolution of nanoparticles for medicine through the description of four nanoparticles generations. [23]

First generation of nanoparticles were used to encapsulate drug and modify their kinetic of absorption. These nanoparticles were quickly covered by opsonins (plasma proteins responsible for the identification of foreign object) and captured by Kupffer's cells, which are liver macrophages used

for removing foreigner substances from the blood as it passes through the liver. This is done by engulfing and breaking down these substances and this process is called phagocytosis. Consequently, those nanoparticles (NPs) tend to accumulate in the liver before being cleared out of the body. This phenomenon has eventually been used to treat liver diseases such as liver cancer. Poly(cyanoacrylate) NPs encapsulating anti-cancer drug were first used to target liver cancer using the clearing role of Kupffer's cells for example.[24] To prevent the uptake of NPs, one potential solution could be avoiding the opsonization process by using poly(ethylene glycol) (PEG), a hydrophilic and flexible polymer, on the surface of NPs to sterically inhibit both electrostatic and hydrophobic interaction with plasma proteins. Chain length, shape and density of grafted PEG on NPs surface have been shown to be the main parameters effecting NPs surface hydrophilicity and phagocytosis[25]. Lee *et al.*[25] reported an assay on PEG conformation on proteins absorption. They reported that size and grafting density of PEG influenced the mushroom/brush conformation of PEG. Indeed, low grafting density leads to a mushroom conformation of PEG chain while high grafting density leads to extended brushes of PEG chains. Brush conformation seemed to be the conformation avoiding opsonization process. PEG regimes are illustrated in Figure 9.

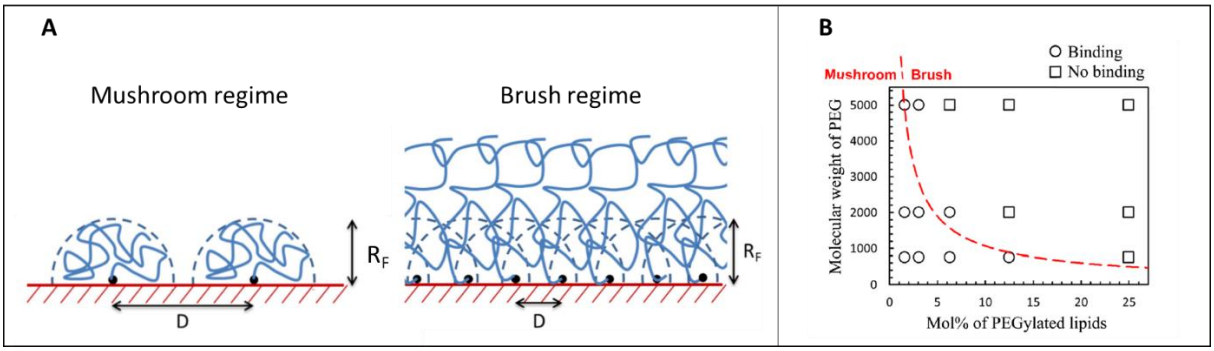

***Figure 9** : A) Representation of mushroom / brush regimes of polymer chains at the surface of a nanoparticles. D refers to grafting spacing and R_F to the coil radius of polymer chains, adapted from Dr Gauvin Hemery PhD thesis.[26] B) Binding of plasma protein on NPs depending on the molecular weight and grafting density of PEG chain on NPs from Lee et al.[25]*

Semple *et al.*[27] established a relation between the amount of proteins binding and the clearance of NPs. Gref *et al*.[28] shows similar behavior by comparing PEG-coated and uncoated poly(lactid-*co*-glycolid) acid (PLGA) NPs. They reported that five minutes after injection, 66 % of uncoated NPs were found in the liver, while only 15 % of coated ones were found after the same amount of time. They even reported that the number of PEG-coated NPs found in the liver after 5 h was not exceeding 30 % of the overall injected NPs. These studies established the benefit of NPs PEGylation for improving the biodistribution profile, and consequently, the enhancement of their therapeutic activity.

1.4. Controlled biodistribution of nanoparticles via passive and active targeting mechanism

1.4.1. Passive targeting and the EPR effect

The extended circulation time, given by the "*PEGylation*", has been the starting point of a passive accumulation strategy, mostly use in tumor treatment that enhanced a new biological process called "*Enhanced Permeability and Retention effect*" (EPR effect). The EPR effect was firstly described by Matsumura and Maeda in 1986[29]: Biomacromolecules accumulate in a higher concentration in tumor tissues than in healthy tissues or organs, as long as they circulate long enough in the bloodstream. This phenomenon must be the results of a combination of the following parameters (Figure 10) [30,31] :

- extensive angiogenesis of vessels with irregular shape and anomalous conformation around cells,
- lack of smooth muscle layer and sporadic blood flow,
- vascular leakage in response to AT-II-induced hypertension,
- defective vascular architecture leading to extensive leakage caused by large gap between endothelial cell-cell junction (6 to 12 nm for healthy vessels[32], 380 to 780 nm in tumor vessels[33]),
- impaired lymphatic clearance,
- extensive extravasation (vascular permeability) induced by vascular mediators[29].

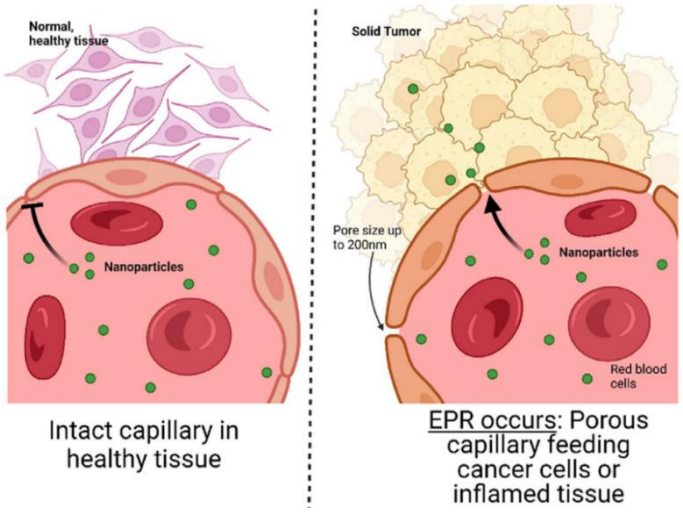

Figure 10: *Representation of nanoparticles penetration in intact endothelium of healthy tissue and in tumors tissue. The accumulation of nanoparticles in tumors tissue is represented through the EPR effect. From Stiepel et al.*[8]

To take advantage of this unhealthy vessel architecture, NMs only need to follow few parameters to take advantage of the EPR effect[34,35] :

- no interaction with blood component or blood vessels and no antigenicity,
- a molecular weight or size larger than 40 kDa, corresponding to a molecular weight above renal clearance threshold,
- an overall weakly negative to nearly neutrally charged surface,
- a circulation time longer than 6 to 7 hours in systemic circulation (for mice model).

It should be mentioned that particle size seems to influence accumulation through the EPR effect. Charrois *et al.*[36] tested the accumulation of four size of stealth liposomes on tumor 4T1 murine mammary carcinoma (82, 101, 154 and 241 nm). The study reported that the liposomes with a larger size present lower accumulation profile compared to the three others lower size evaluated in tissues of interest. Recently, the EPR effect has been shown to present some 'active targeting'. Indeed, Matsumoto *et al.*[37] reported a tendency for a "bursting effect" that occurs mainly in blood vessels found within and in close proximity to the tumor. They evaluated those bursts by using fluorescent polymeric nanoparticles and study their accumulation in human pancreatic tumor implanted in mice. They introduced the concept of "active pores", illustrated in Figure 11.

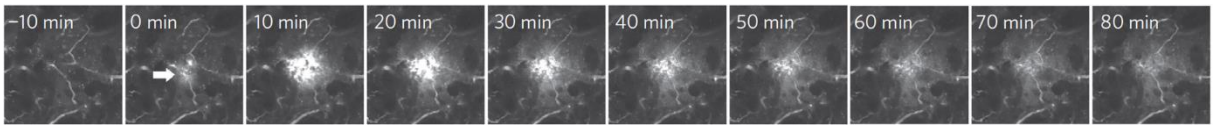

Figure 11: *Time-lapse images of an eruption in a mouse receiving fluorescent NPs, followed by intravital confocal laser scanning microscopy. Growth of the eruption and its dispersal are shown. Scale bar: 100 µm. From Matsumoto et al.*[37]

According to this report, 30 nm fluorescent NPs can diffuse trough endothelial pore passively and thus follow the EPR effect while 70 nm fluorescent NPs need active pores to diffuse, leading to a burst phenomenon. The EPR effect seemed a "gold standard" for cancer therapy. But with the presence of a large variety of tumors with different composition and structures, the EPR effectiveness becomes questionable.[8,38]

1.4.2. Active targeting and the role of grafting ligand

After "PEGylation", allowing to use a passive targeting, a third generation of nanomedicine attempted to provide an answer to target specific tissues with an active targeting mechanism. Thus stealth nanoparticles have been functionalized on the surface by ligands, such as vitamins, carbohydrates, peptides, antibodies and others.[7,37,39] that give to these systems and selective recognition of specific antigens or receptors which are overexpressed on the surface of targeted tissues via a "key-lock" interaction. Table 1 gives few examples of ligands used to functionalize polymersomes for targeted drug delivery[39,40].

To produce third generation NPs, following parameters should be considered:

- expressing an optimal quantity of ligands on the surface of NPs,
- conserving the chemical integrity of ligand and their ability to recognize the targeted site,
- preserving colloidal stability of NPs and their stealth once ligands are positioned. [36]

An example is presented by Mackiewicz *et al.*[41]. They studied the impact of grafting density of folic acid or biotin on polymeric NPs and reported an optimal functionalization density of 15-20 % of ligand. This grafting density allows a maximal affinity for tumor cells receptors when lower or upper grafting rate show less affinity. This case demonstrates the delicate art of ligand grafting, where more is not necessarily better.

Table 1 : *Examples of ligands used to functionalize polymersomes to achieve targeted delivery through the use of specific receptors and comparison of the obtained improvement compared to non-targeted drugs.*

Model	Target receptor	Ligand	Enhancement	Ref.
Breast cancer	Folate receptor	Folic acid	1.7-fold higher uptake	[42]
Dendritic cells	Cellular membrane	Tat	2 h reduction in time to obtain half-maximal fluorescent intensity; 7-fold increase maximal fluorescent intensity	[43]
Lung cancer	Epithelial cell-adhesion molecule	19-mer EpCAM RNA aptamer	Halved tumor volume	[44]
Blood–brain barrier	Transferrin receptor	Transferrin	2.3-fold increase in brain uptake	[45]
Inflamed epithelial	Endothelial cell adhesion molecules ICAM-1	Anti-ICAM1	7.5-fold increase in binding rate to inflamed versus uninflamed cells	[46]

1.5. Controlled drug release of nanoparticles via external stimuli

Development of NPs as drug delivery system has been described as allowing to protect the drug and to target site. Those allow to enhance the accumulation of drug in tissue of interest, but do not ensure the accessibility of drug. Therefore, the last generation of NMs has the aim to develop stimuli-responsive NMs with a space-time control on drug delivery. Several strategies have been developed, using endogenous specificities of diseased tissue such as temperature, pH, enzyme, or pressure. Exogenous stimuli, such as electricity, ultrasound, magnetism, or light have also been studied. All those stimuli responsive NMs have been widely reviewed. [19,47,48] Figure 12 illustrate the wild variety of stimuli that can be used to trigger drug release.

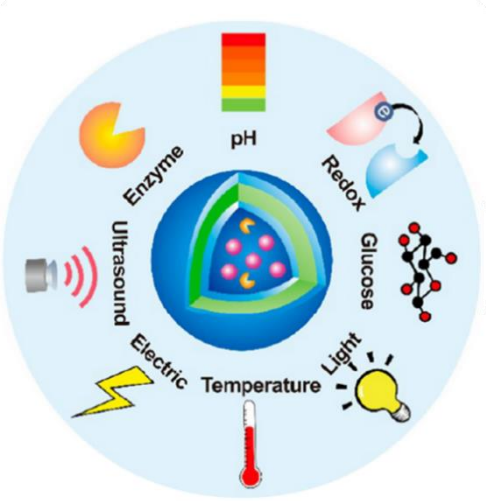

Figure 12 : *Schematic illustration of various stimulus for drug delivery, including endogenous and exogenous ones. Adapted from Hu et al.*[47]

NMs are continuously evolving to ensure an always more efficient delivery. From nude NPs, PEGylation, functionalization and stimuli responsiveness, progress seemed to be never ending, hope, for the best. The next step to target exclusively one specific organ of tissue seems to follow the exploration of cellular-conjugation by several chemical tools, including click chemistry[49,50].

2. Vesicle formulation: the importance of process choice on size control

When planning to use nanoparticle as drug delivery system, the impact of liver and kidneys, the organs that are responsible for withdrawing foreign substances from the bloodstream, are a major importance. The use of "PEGylation" permit to escape the opsonization process, but the size of nanoparticle remains a key parameter to control. As described earlier, their size can influence their circulation time, liver and kidney uptake, and tissue accumulation. Literature reports that nanoparticles with a size higher than 100 nm tend to be cleared faster by liver instead of those with a size below 100 nm. On the other hand, NPs smaller than 10 nm tend to be excreted rapidly by kidneys.[6] As an illustration, Brinkhuis *et al.*[51] studied the impact of the size of polymersomes on half-life circulation time . They reported that vesicles from 120 to 250 nm (in diameter size) are rapidly cleared from bloodstream after 4 h while 30 % of NPs with 90 nm in diameter are still in circulation after 24 h.

As previously described, among NPs, polymersomes have a high potential as nanomedicine applications. This part will focus on reviewing processes used to produce exclusively vesicles, depicting general processes, and giving examples of how finer parameters (e.g. copolymer concentration, temperature, solvents, or additives) could influence the size of the formed vesicles.

Processes used to produce vesicles were firstly developed on liposomes and adapted latterly for polymersomes. They can be divided into two main categories: i) film hydration processes, where a dry amphiphilic polymer is hydrated in aqueous solvent (Part II.2) and ii) solvent-displacement processes, where copolymer is solubilized in a good organic solvent and aqueous solvent is then added (Part II.3).

Vesicles are classified depending on their size (referring to hydrodynamic diameter D_H) and the multiplicity of bilayers forming the membrane: small unilamellar vesicles (SUVs), from 10 to 100 nm; large unilamellar vesicles (LUVs), from 100 nm to 1 µm and giant unilamellar vesicles (GUVs) with a size bigger than 1 µm. Vesicles composed of multiple concentric layers of copolymer are known as multilamellar vesicles (MLVs). MVVs are then used to name multivesicular vesicles when vesicles are entrapped in vesicles. Those last ones are also known as vesosomes.[12,19,52] This classification is illustrated in Figure 13.

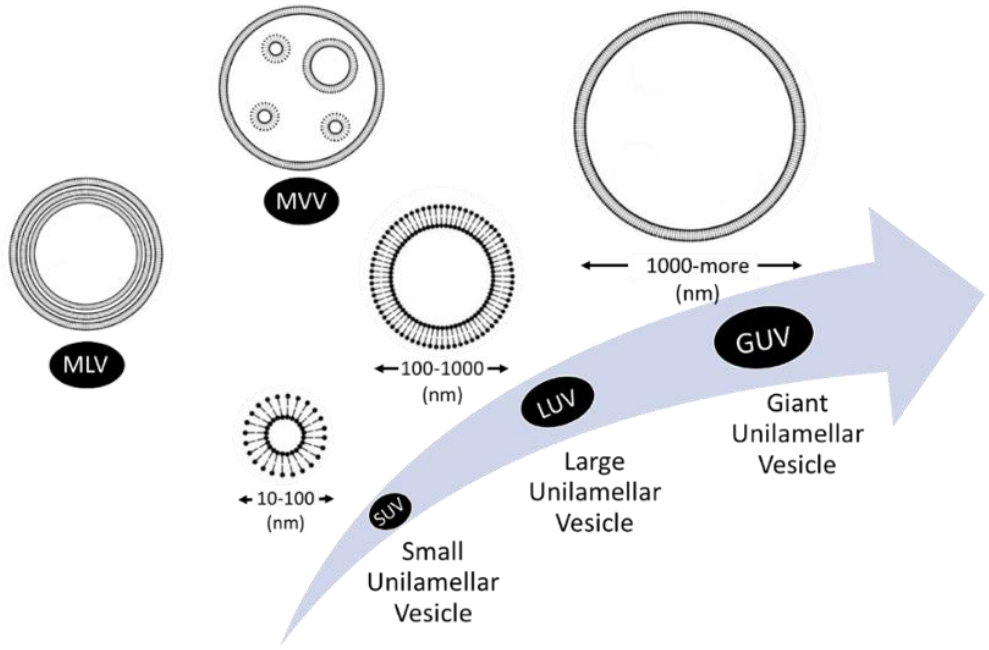

Figure 13: *Vesicle denomination depending on their diameter and lamellarity. Adapted from Moghassemi et al.[12], completed by Rideau et al.[19]*

2.1. Film hydration processes

Film hydration process remains one of the most used techniques to obtain vesicles with a great yield. It consists in dissolving block copolymer into a volatile solvent. The mixture is then poured in a flask and the solvent evaporates at room temperature, under nitrogen or by using rotary evaporator. A film of dry copolymer forms on the walls of the flask and aqueous solvent is poured on top of it. The film is hydrated with or without stirring and vesicles form slowly during the hydration of the bilayer film.[53–57] Figure 14 illustrates the process.

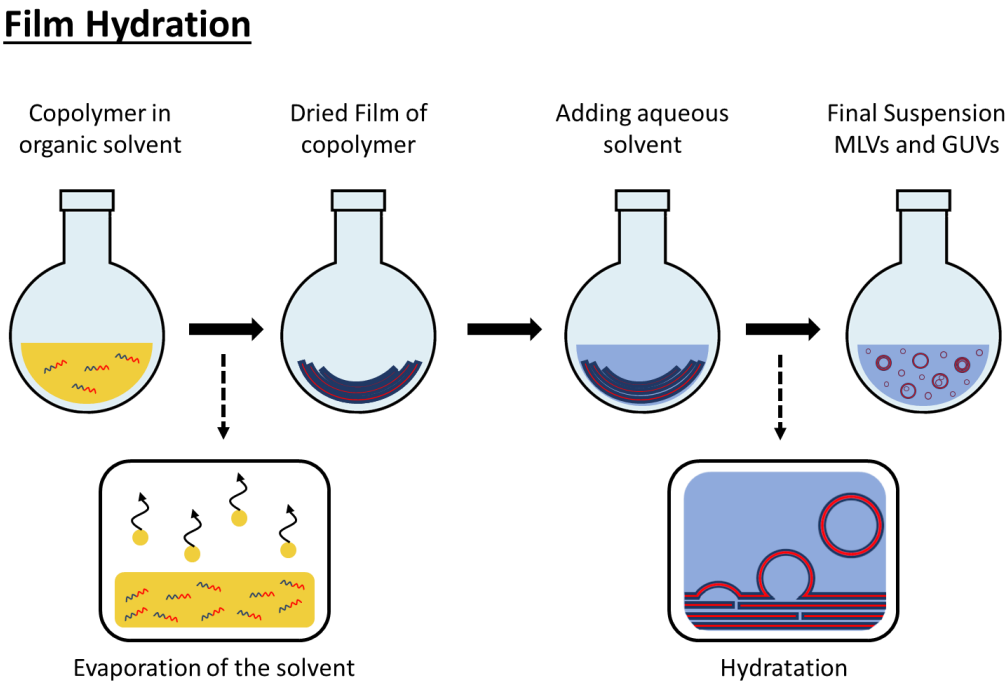

Figure 14: *Schematic representation of the different steps of film hydration. Drawing inspired by Moghassemi et al.*[12]

The process of rehydration can be divided into three stages : first, hydration of the solid copolymer film, then swelling of the copolymer film into polymersomes due to physical forces applied to the bilayer films, and lastly fusion of adjacent polymersomes due to mechanical stresses.[58] This process leads to the formation of GUVs with uncontrolled size, dispersity and some multilamellarity. Nevertheless, the ease of implementation, the applicability with large types of copolymers and the great yield of vesicles obtained allow this process to remain attractive as dispersity and size are tunable with post-formulation processes (see Part II.4). An elegant way to overcome polydispersity and to increase size control for film hydration process is the lithography process described by Howse *et al.* [59] Briefly, ultraviolet photolithography is performed through TEM grid that serves as a mask. The aim is to obtain square patterned surface of hydrophilic square on hydrophobic substrate. Thus, when pouring a mixture of copolymer in volatile solvent, dewetting of the hydrophobic surface leads to formation of well-defined copolymer coated squares (Figure 15). After drying, pattern is hydrated with water leading to a maximum diameter influenced by TEM grid size. Another advantage of this technique is that swelling of copolymer is eased from the sides of the squares patterned on the surface.

However, the article reported that even if the dispersity is reduced, it remains in certain cases important.

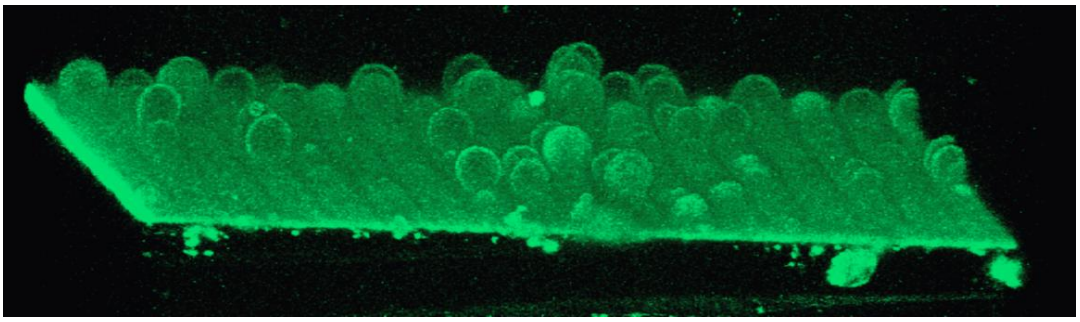

Figure 15: *3D image generated from a series of vertical slices of vesicles forming from a photolithographed surface allowing the pattern to influence vesicle size. From Howse et al.*[59]

2.1.1. Electroformation

Film hydration process has the drawback to be time consuming (several hours to days) and need in several cases mechanic stirring or ultrasound for a perfect swelling of the copolymer layer. One way to reduce formation time has been developed by using electric field to induce copolymer swelling and polymersome dewetting. Angelova end Dimitriov[60] firstly reported electroformation process in 1986, described for the formation of egg lecithin liposomes. They established few critical parameters:

- temperature needs to be above main phase transition,
- rate of formation depends on temperature,
- during formation, vesicles can internalize external solute, containing molecules such as sucrose or even larger particles,
- vesicles do not form in solutes with higher ionic strength (> 0.1 mM of monovalent salts concentration).

The electroformation process is similar to film hydration process, except that polymer film is formed on conductive surface. The film is spread on two ITO (indium tin oxide) covered glass slides and then dried. Slides that face each other are separated by a spacer and connected to electrodes. Slides and spacer form a chamber filled with aqueous solvent and placed in a temperature-controlled environment. Electric field is then applied between slides to destabilize copolymer swelling bilayers and detach them in order to form vesicles. Few mechanisms of destabilization have been hypothesized : electric field induces negative surface tension[61], electrokinetic flows may be involved[62], electric pressure and shear stress may be involved in the case of membrane separating solution of different conductivities[63]. The electroformation is represented on Figure 16.

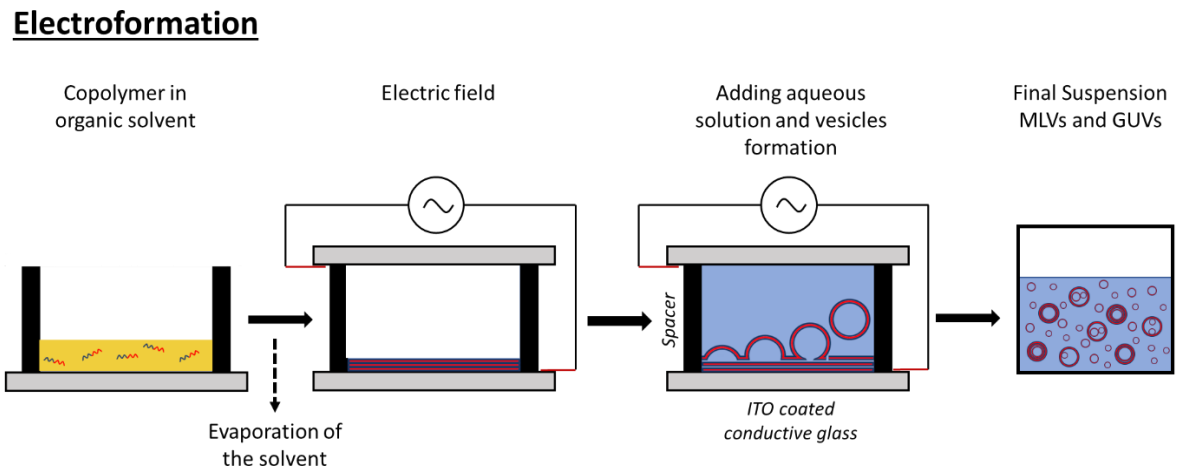

Figure 16: *Schematic representation of the different steps of electroformation.*

This technique is described here on conductive glass slide but has also been performed on platinum string. Thus, Menger *et al.*[64] poetically described vesicle formation on platinum string as the production of *"large unilamellar spheres lined up like pigeons on a telephone line".*

In 1986, electroformation seemed difficult to be used with solutions with higher ionic strength, but since then, progress have been done and scientists achieved to bypass this restriction. Solutions with higher ionic strength are believed to prohibit separation of copolymer bilayer due to an electrostatistical screening of repulsive charges.[65] The increase of the required forces needed to swell the copolymer film into vesicles have been then envisaged .[66,67] Li *et al.*[58] reported a screening of amplitude and frequency of electric field used to produce vesicles by electroformation in a 100 mM NaCl solution. They proved that, if electroformation is performed in salted solution at low amplitude [1-5V] and low frequency [~Hz], the increase of one or both of those parameters seems to be necessary to obtain vesicle formation. They reported that KHz-range frequency favors vesicle formation in saline solution by forbidding formation of electric double layer. Lefrançois *et al.* even reported the production of vesicles by electroformation in PBS solution by applying an alternative current, keeping a stable frequency and an increase of the amplitude over formation.[68]

2.2. Solvent-displacement processes

Solvent exchange processes are the second group of processes widely used to produce vesicles. Innovative processes which derive from the conventional process will be described below but these have all the common point to start with solubilization of the copolymer in an organic solvent wherein each block of the copolymer exhibits good solubility.

2.2.1. Nucleation-growth mechanism for the formation of vesicles

The mechanism of vesicle formation will be first discussed. If mechanism is quit visible for film hydration processes of GUVs, it is harder to visualize formation mechanism during solvent displacement processes.[69,70]Literature reports the following process : copolymer is firstly well solubilized in an organic solvent. Then, a counter solvent (typically water) is added gradually until reaching the critical water content (CWC). The CWC is the amount of water needed to start the initial stage of the nucleation, in which small clusters or particles form. Therefore, these particles will grow until the obtention of larger structures.[71]

In the case of block copolymer self-assembly, the particles formed at initial stage will be micelles. When water content increases, those micelles evolve in a second shape, which might be either swollen micelles or elongated micelles. Therefore, swollen micelles will expand to form a bilayer membrane with an aqueous core, while elongated micelles will flatten to fold up into vesicles.[21,72–75] Representation of supposed mechanisms for polymersomes formation is illustrated in Figure 17.

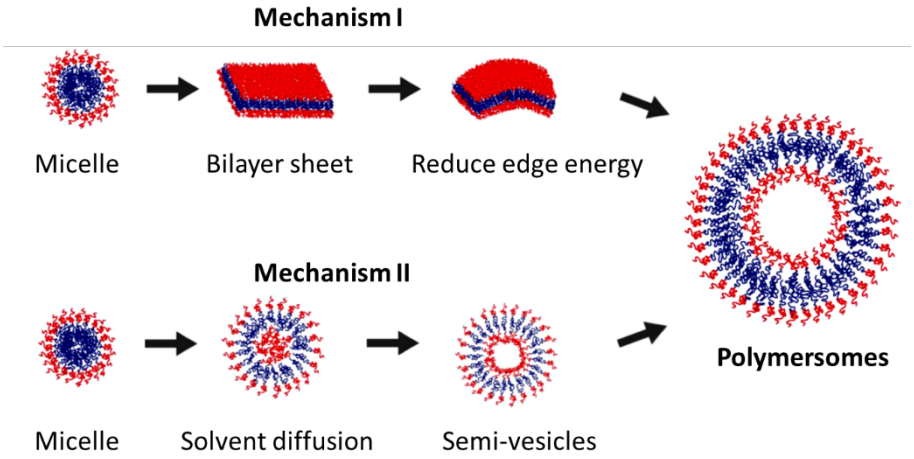

Figure 17: *Schematic representation of supposed mechanisms of vesicle formation. Adapted from Iqbal et al.* [75]

When block copolymers form vesicles, it may be difficult to predict exactly the mechanism of self-assembly (swelling of micelles and/or folding of elongated micelles). However, the self-assembly mechanism will influence the encapsulation process, especially for hydrophilic molecules. Indeed, hydrophilic molecules need to pass through the hydrophobic membrane in order to reach the core of swollen micelles. Nevertheless, literature indicates that the time allowed for nanoparticles to grow will indeed have an impact on their final size. Thus, mixing rate, water addition and interdiffusion of solvent / counter solvent become a key point for tuning size of vesicles. [76,77]

2.2.2. Nanoprecipitation

Nanoprecipitation has been patented in 1989 by Fessi *et al.*[78] and is one of the most used processes to produce LUVs and SUVs. While performing direct nanoprecipitation, copolymer is solubilized in a good organic solvent for both blocks of the amphiphilic copolymer. This solvent needs to be water miscible. While the solution is stirred, aqueous solvent is added dropwise. As water diffuses into organic solvent, the overall solvent mixture become a counter solvent for hydrophobic part of the copolymer, which leads to self-assembly. A supplementary post-formulation purification process (such as dialysis, evaporation or ultrafiltration) is required to withdraw organic solvent. Vesicle suspension in aqueous solvent is thus obtained.[79–81] Nanoprecipitation process is depicted in Figure 18.

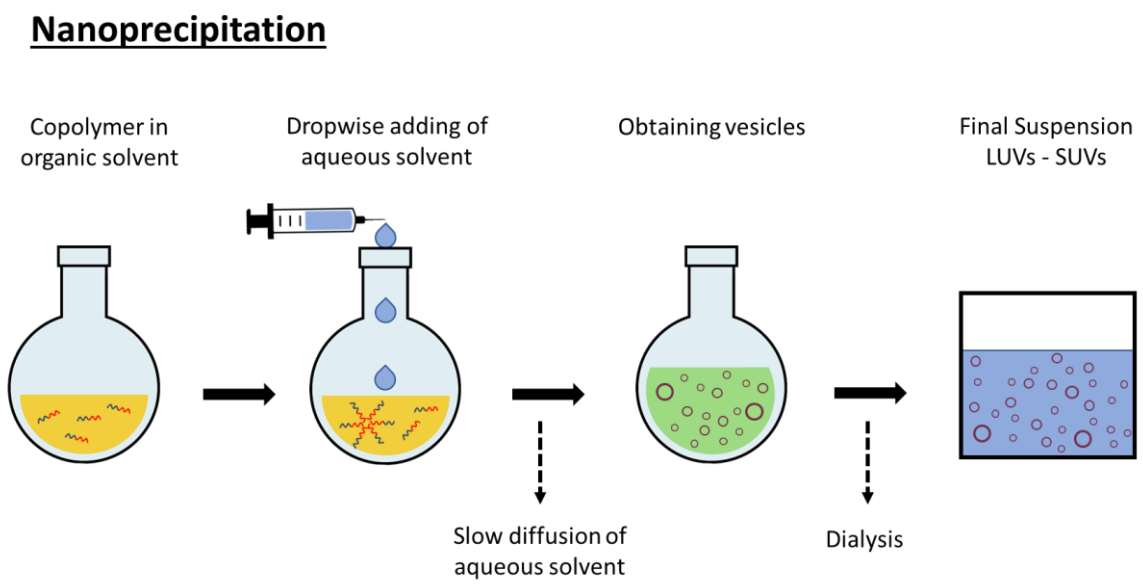

Figure 18: *Schematic representation of the different steps of direct nanoprecipitation. Inspired from Coralie Lebleu PhD manuscript.*[82]

In opposition to direct nanoprecipitation, inverse nanoprecipitation consist in the dropwise addition of polymer solubilized in organic solvent into water.[77] A supplementary nanoprecipitation technique, called flash nanoprecipitation can be used to produce nanoparticles and involves rapid mixing of a solution of a polymer with a high-volume of a counter solvent, typically water. This rapid mixing causes the polymer to rapidly precipitate, resulting in the formation of nanoparticles.[83–87]

2.2.3. Emulsification processes

Two types of processes use emulsification for GUVs production: double-emulsion technique and emulsion-centrifugation technique. Double-emulsion technique consists in solubilizing the copolymer in a volatile organic solvent immiscible with aqueous solvent. The aqueous solvent is then added under strong stirring to obtain a first invert water in oil emulsion (w/o emulsion). This emulsion is then added to water under stirring to obtain a double w/o/w emulsion. Copolymer stabilizes the emulsion by forming two monolayers on the surface of the droplets. Organic solvent is then withdrawn

by evaporation and as the organic layer gets thinner, monolayers of polymer join themselves to form a bilayer membrane.[14,88] Figure 19 depicts this process.

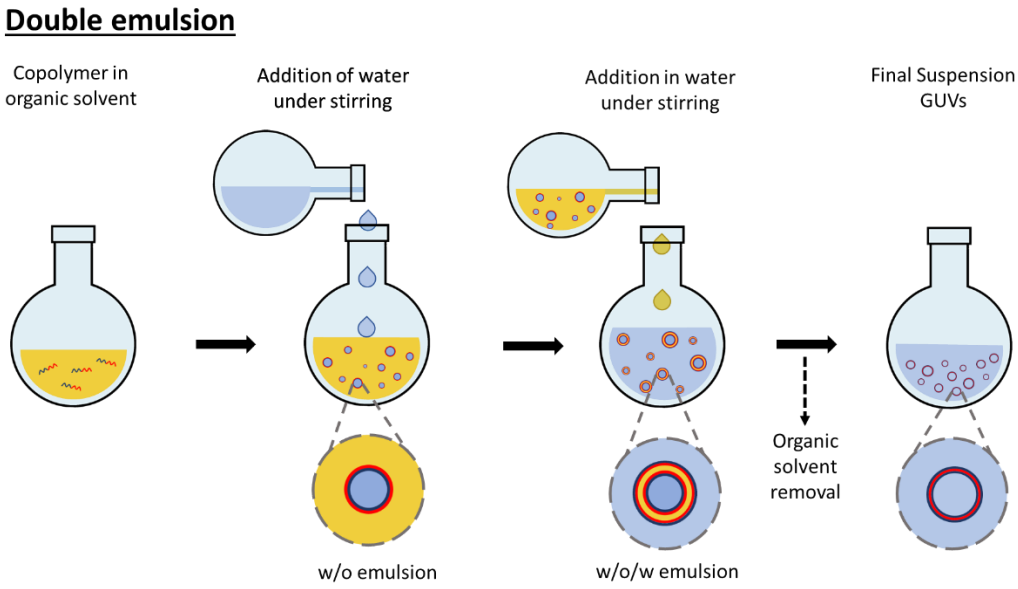

***Figure 19**: Schematic representation of the double emulsion process. Inspired from Dr Coralie Lebleu PhD thesis.[82]*

For emulsion-centrifugation formulation, the obtention of a first w/o emulsion is also performed. A biphasic system is then realized from an aqueous solution on top of which a small amount of solution containing w/o emulsion is poured. Block copolymers will align at the interface of water phase and phase that containing the first emulsion. This formulation is then centrifugated and droplets of the first emulsion will pass through the layer of copolymer of the biphasic system that will permit them to gain a second monolayer of copolymer. The organic solvent will then be withdrawn and vesicles will be obtained. [52,89,90] Emulsion-centrifugation process is represented in Figure 20.

The primary limitation of these processes is the lack of control over vesicle size or uniformity. Therefore, as the organic solvent evaporates and lead to a reduction of droplet size, an excess of copolymer may appear due to invaginations or expulsion of the excess polymer when vesicles are formed[90]. Besides, the addition of stabilizing polymer, for instance poly(vinyl alcohol) (PVA), is often necessary for the stabilization of the second bilayer in order to avoid aggregation of droplets. On the other hand, the main advantage of those processes will be the possibility to use different copolymers at each steps, leading to vesicle membrane composed of two monolayers with different copolymers[91].

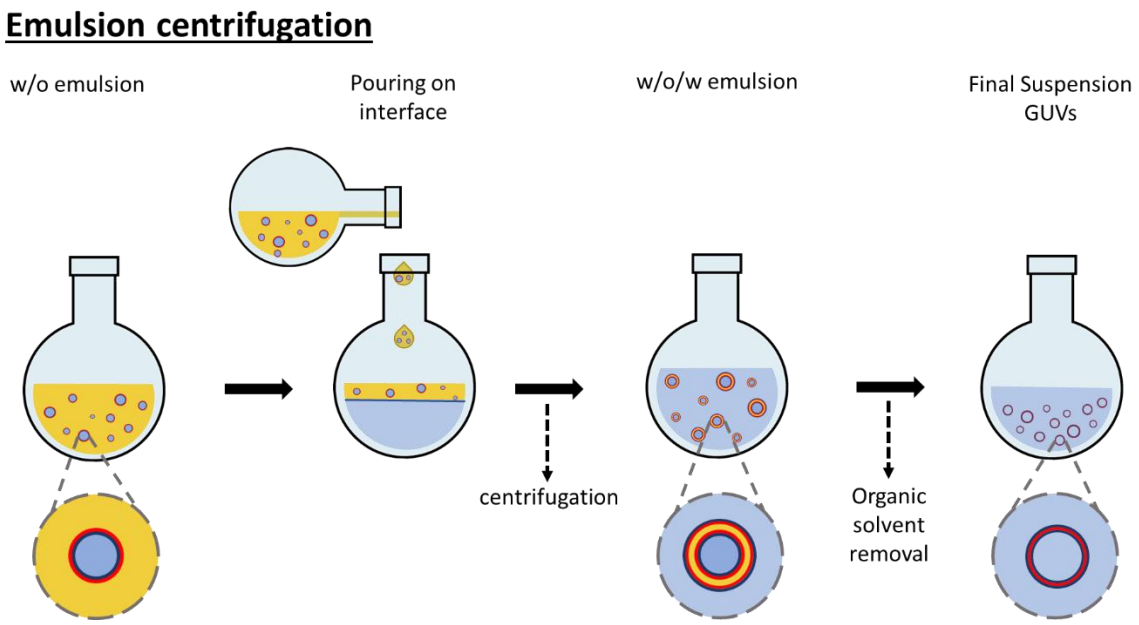

Figure 20: *Schematic representation of the emulsion centrifugation process. Inspired from Coralie Lebleu PhD thesis.*[82]

2.2.4. Solvent displacement controlled by microfluidic

Microfluidic has been described by Whitesides[92] as *"the science and technology of systems that process or manipulate small amounts of liquids, using channels with dimension of tens to hundreds of micrometers".* Microfluidic devices used in vesicle production have multiple configurations that are tailored from existing microfluidic processes. Nanoprecipitation and double-emulsion are two formulations that have been adapted to microfluidic devices[73,93–97] . Microfluidics has been employed to overcome the lake of control on vesicle size and dispersity from pre-existing processes. In the case of double emulsion, the two-steps procedure can be gathered in a simple microfluidic model, shown on Figure 21. Droplets of water are produced at the first junction in an organic solvent immiscible with water. Copolymer in the organic solvent is stabilizing at the interface, creating the first reverse emulsion. Those droplets cross the channel to the second junction where they converged at the outer aqueous phase, producing the w/o/w emulsion.[98]

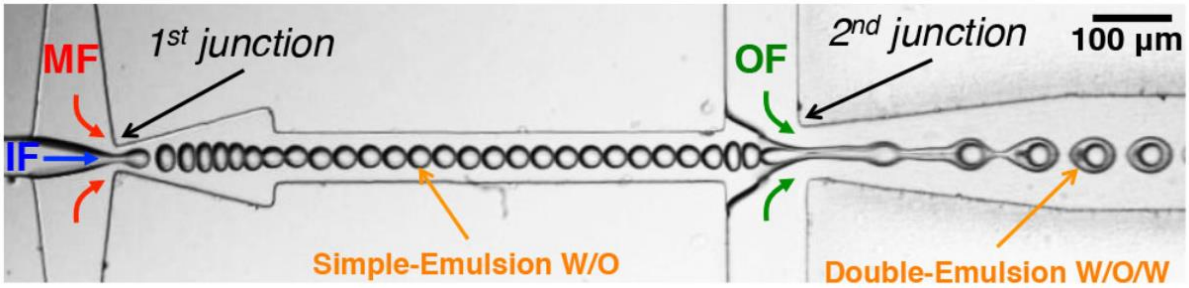

Figure 21: *Production of w/o/w double emulsion, IF and OF being aqueous solvent and MF an immiscible with water organic solvent. From Petit et al.*[93]

Microfluidic systems produce very regular sized droplets, leading to monodisperse vesicles. Droplet size is easily tunable via the choice of flow rates and solvents viscosity. For instance, Petit *et al*.[93] achieved to obtain vesicles from 7 to 58 µm only by changing both parameters. As other nanoparticles formulation methods, the removal of organic solvent is necessary. Therefore, as previously mentioned, an excess of copolymer and organic solvent must be expelled. This phenomenon has been depicted in Figure 22 and documented in the literature[73,99].

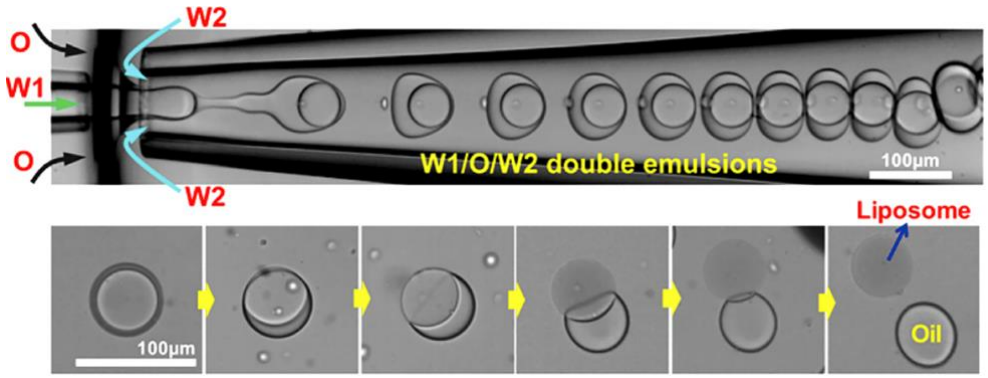

***Figure 22**: Production of liposome, from W/O/W microfluidic generated double-emulsion to expel of excess oil and polymer. From Seo et al.[99]*

Multiple design producing monodisperse double-emulsion droplets has been developed over time.[93,99,100] However, the obtention of monodisperse droplets often required the use of stabilizers, such as synperonic F108™[93], poly(vinhyl alcohol) (PVA)[73,98] or glycerol[98]. If microfluidic double emulsion allows to obtain monodispersed GUVs, the microfluidic adaptation for nanoprecipitation of monodispersed SUVs and LUVs is already established. Microfluidic assisted self-assembly through the control of solvent-displacement requires the precise control of mixing of organic solvent containing copolymer and aqueous solvent. A very simple design, shown in Figure 23, has been developed in which the mixing of both solvents is achieved through pure diffusion.[101]

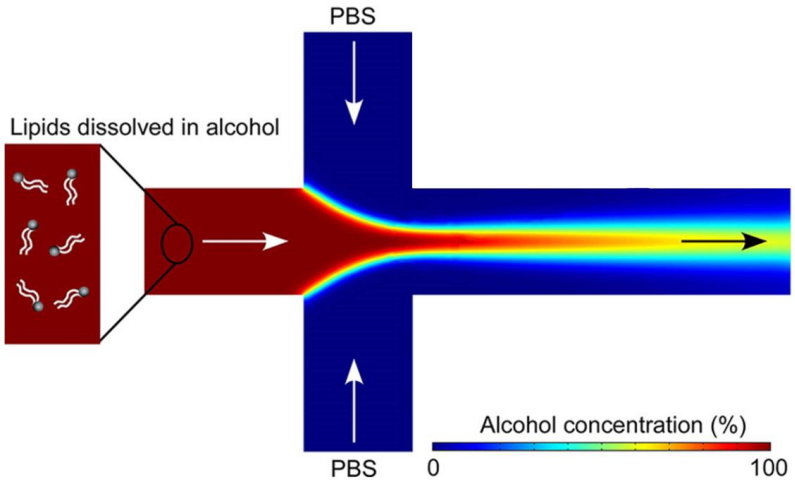

***Figure 23**: Schematic of interdiffusion of solvent in a flow focusing microfluidic devices. Adapted from Zhang et al.[73]*

The general idea of using microfluidic is an obtention of a precise control on mixing speed using flow rates.[102,103] As diffusion between laminar flows could be time-consuming, the specific design of microfluidic chips relying on interdiffusion time control was established. For instance, the reduction of diffusion time could be obtained by decreasing the thickness of solvent layer inside the chip in which interdiffusion occurs. Micromixer chips and Herringbone chips are good examples of this division of flows in thinner layers and are depicted in Figure 24 and allow the precise control of mixing through the fine tuning of flow rates.[104,105] Compared to classical ways, microfluidic set-ups have shown greater control concerning vesicles size and dispersity, and an easy industrial scale up as microfluidic can be continuously used.[106,107]

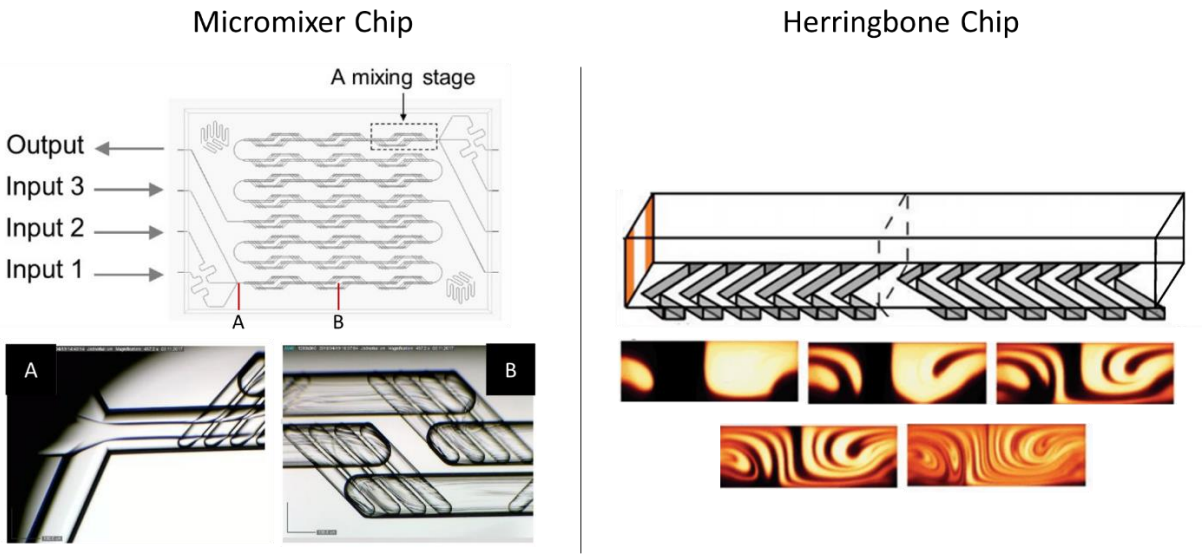

Figure 24: *Schematic representation and pictures of flow mixing. (left) Micromixer chip dividing flows using subdivided channels. Adapted from Albuquerque et al.[104] and Lebleu et al.[82] (right) Herringbone chip with steps inducing forces perpendicular to the main flow direction, creating whirlwinds that thinned flows. Adapted from Stroock et al.[105]*

3. Adjustment of the size of nanoparticles by post-processing recalibration

The formulation processes for obtaining vesicles suffer from a common issue: a lack of size specificity and a high degree of size dispersion among the objects produced. Recently, post process techniques have been developed including extrusion, sonication, and freeze-thawing.

3.1. Extrusion

Extrusion is widely used after processed that tend to form GUVs or MLVs.[108–111] This method was originally developed by Olson *et al.*[112] where they demonstrated the preparation of liposomes with reduced sizes through the use of extrusion under low pressure. They used nanoporous membrane and evaluated the decrease of pore size. They firstly obtained polydisperse liposomes with size from 3 to 0.2 µm by film hydration and used several membranes with a cut-off threshold from 3 µm to 200 nm. At the end, the obtention of a population of monodisperse liposomes with a size around 270 nm was performed, as shown in Figure 25.

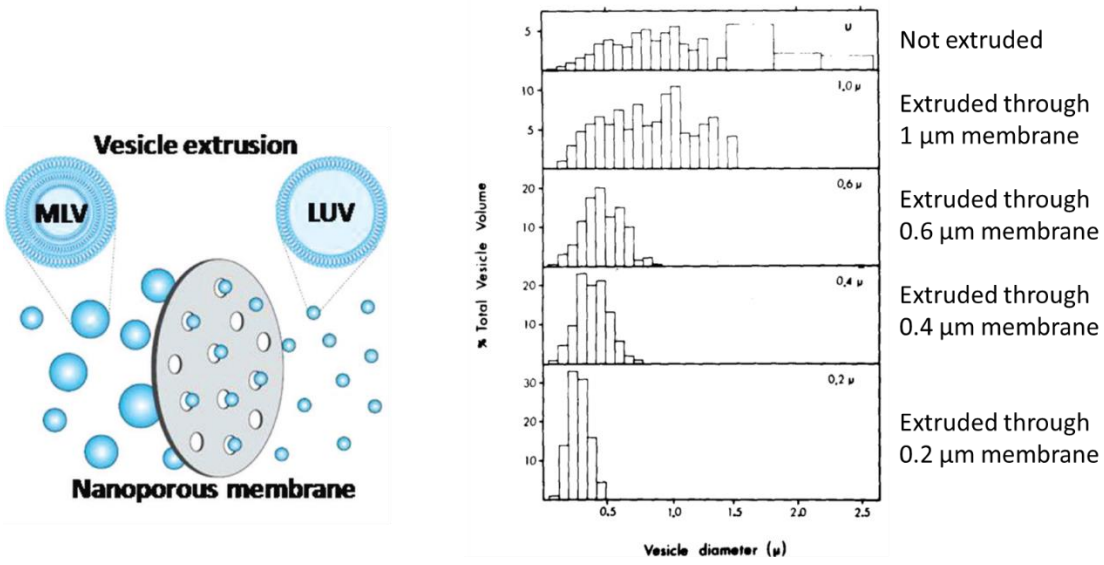

Figure 25: *(left) Schematic representation of extrusion process from Guo et al.[108] (right) Size distribution of vesicles determined by negative stain electron microscopy after extrusion through polycarbonate membrane. From Olson et al.[112]*

In order to facilitate the resizing of vesicles by extrusion, temperature may be used to add mobility to the polymer chains, but this increase in mobility could also lead to vesicles which are very flexible and consequently able to be deformed and pass through pores without being resized. Solvent can also be added as a plasticizer as demonstrated by *Men et al.*[113] They demonstrated that keeping 80 % or 67 % of organic solvent during their nanoprecipitation process and directly extruding those solution, favor the size decrease of final vesicles. When less organic solvent was added (around 33 %), no change in size between before and after extrusion was observed.

3.2. Sonication

By using sonication bath or probe, the reduction of vesicle size has been demonstrated by Woodbury *et al.* They reported that sonication time influences the efficiency of sonication as a size-reducer process for vesicles, as reported in Figure 26 (left).[114] The same phenomenon has been shown by Silva *et al.,* by using a ultrasonic probe. The impact of the power of probe on vesicles size was evaluated, as shown in Figure 26 (right).[115] Men *et al.*[113] also studied the effect of solvent as plasticizer. They reported that when the quantity of organic solvent was increased, a decrease of sonication time was required to reduce vesicles size. For instance, they reported that 30 seconds was enough to reduce the size of their vesicles from 480 to 100 nm, when 80 % of organic solvent was present. A longer time of 5 min was required with 50 % of organic solvent and 15 min was not enough to reduce size of vesicles with 30 % of organic solvent.

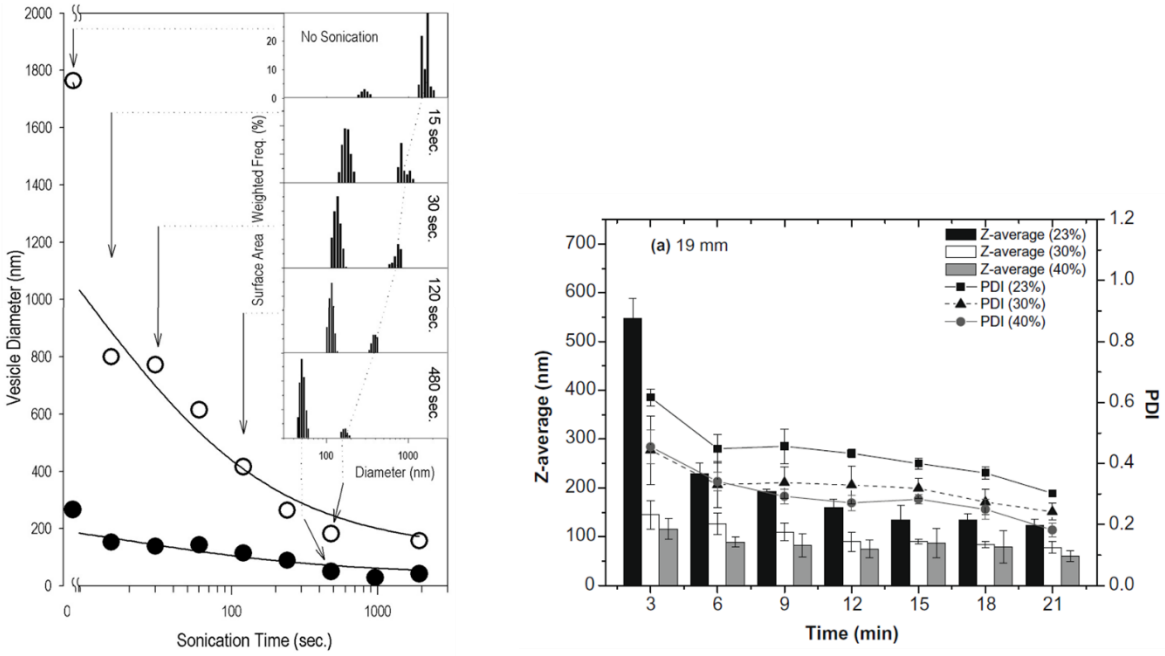

Figure 26: *(left) Representation of the size decrease of liposomes while using different sonication bath time. Two populations are detected and followed. Insert: DLS measurement at punctual sonication time. Rom Woodbury et al.[114] (right) Effect of sonication using a probe on liposomes with several amplitudes (23 %, 30 %, 40 %). From Silva et al.[115] Both experiments show a significant decrease in vesicles size over time.*

3.3. Freeze-Thawing

Freeze thawing has the interest of standardizing vesicle size but not necessarily reducing it. Indeed, freeze-thawing is used to reduce GUVs into LUVs and SUVs into LUVs[116,117] Sou *et al.*[117] reported a study on how liposomes are affected by freeze-thawing. They studied liposomes with a size in the nanometer and micrometer scale and proposed hypothesis on the mechanism of resizing. For vesicle with a size from 3 to 50 µm, they observed a size reduction when a freeze-thawing operation was applied. They proposed that this decrease in size should be due to dehydration and mechanical pressure on vesicle membrane due to the formation of ice crystals in the aqueous medium, in the vesicle core and outside of the vesicle, leading to breaking vesicle membrane during freezing period. This broken membrane would be able to be rehydrated and reclosed during thawing, forming smaller vesicles. They also reported that after one cycle of freeze-thawing, only 40 % of their vesicle previously larger than 3 µm remain larger than 3 µm. This proportion reduces with the number of freeze-thawing cycles, when the cooling rate is at -140°C.min^{-1}, as depicted by Figure 27. On the other hand, for smaller vesicles, they proposed a process based on fusion of vesicles. The efficiency of fusion is related to the average distance between vesicles. Indeed, a higher concentration of vesicle increases the chance of fusion. Also, they suggested that a slow cooling rate would promote the growth of larger ice crystal, resulting in a reduced distance between each vesicle and an increase of their local concentration. By using a vesicle formulation, with a size of vesicles smaller than 3 µm, they observed, after the first cycle of freeze-thawing with a cooling rate at -140°C.min^{-1}, 45 % of the vesicles appeared to be larger than 3 µm. This fraction of vesicles with a dimension higher than 3 µm seems to increase as cooling rate decreases, to reach 70 % of vesicle larger than 3 µm with a cooling rate of -1°C.min^{-1}, as shown in Figure 27. Reduction of GUVs size by freeze-thawing have also been studied by Sriwongsitanont *et al.* and Anzai *et al.* for complementary examples.[118–120]

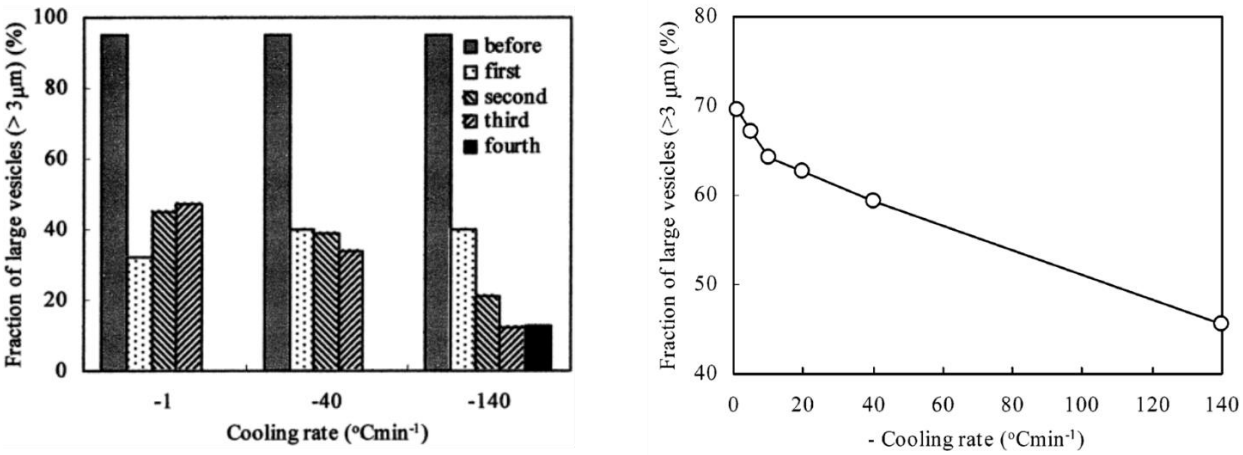

***Figure 27**: Effect of freeze-thawing cycles and cooling rate on liposomes size. (left) Initial vesicles larger than 3 µm are decreased in size with freeze-thawing. (right) Initial vesicles smaller than 3 µm are increased in size with freeze-thawing.*

4. State of the art of physico-chemical parameters allowing the control of the size and the morphology of polymer nanoparticles

The choice of copolymer appeared to be an evident parameter to pay attention to. Indeed, as discussed in the first part, ratio between hydrophobic and hydrophilic blocks has to be finely chosen to favor the formation of vesicles among other morphology (micelles, worm-like, etc). Mai and Eisenberg[121] deeply investigated the effect of PS-*b*-PAA (poly(styrene)-block-poly(acrylic acid)) composition and molecular weight on the copolymer self-assembly. We will discuss herein about few process parameters that can influence finely vesicles size.

4.1. The effect of solvent

The choice of solvent seemed an obvious parameter to consider. Solvents present intrinsic properties that can affect self-assembly, including solubility or viscosity for instance.[122,123] While working on vesicle self-assembly using nanoprecipitation, Sanson *et al.*[77] studied the impact of the choice of organic solvent on vesicle size. They also studied the influence of the addition of one phase to the other phase, on the vesicle size. In this article, when organic solvent is added dropwise in stirred water, vesicle formation and growth is quickly stopped as organic solvent diffuses rapidly in a large excess of water. This leads to the formation of SUVs. However, the choice of organic solvent seems to poorly influence the vesicle size. Otherwise, when water is added dropwise in stirred organic solvent, vesicles size is influenced by the solvent choice and the duration of addition. According to the authors, when organic solvent has a high affinity with water (meaning a low Flory-Huggins interaction parameter), interdiffusion between organic solvent and water is accelerated, which also lead to a rapid quenching of nanoparticles growth. This might explain why, when THF/Methanol is used as a solvent, vesicles show an average hydrodynamic diameter twice bigger than those produced with DMSO as an organic solvent. These results are in compliance with those published by Galindo *et al.*[124], that demonstrate a correlation between the solvent-water Flory-Huggins parameters and the average size of obtained nanoparticle. The influence of addition duration is also explained in the article of Sanson *et al.*[77].

4.2. The effect of copolymer concentration

Copolymer concentration has been shown to be one of the easiest ways to tune vesicle size. Obtaining larger vesicles, when a higher concentration of copolymer is applied, appears to be driven by at least three parameters with the consequence to increase the time for vesicle to growth[21,76,77]:

- increasing the copolymer concentration and consequently the ratio of organic/aqueous solvent tend to decrease the amount of aqueous solvent,
- increasing concentration also tends to increase solvent viscosity, slowing interdiffusion of aqueous and organic solvent,
- a higher copolymer concentration means more polymer chain available for the formation of larger vesicles.

Bleul *et a*l.[21] reported that PS-*b*-PAA (poly(styrene)-block-poly(acrylic acid)) vesicles grew from 90 to 124 nm when initial copolymer content varied from 0.6 to 5 wt%. Same behavior is reported for PTMC-*b*-PLA (poly(trimethylene carbonate)-block-poly(lactic acid)) : vesicles diameter increased from 72 to 176 nm when copolymer initial concentration increased from 1 to 100 $mg.mL^{-1}$. Concentration effect is even more obvious on polyion complexes (PIC) self-assembly. Anraku *et al.*[125] studied the self-assembly of PIC into vesicles and reported the possibility of obtaining vesicles, named "PICsomes", with a size four times larger by multiplying copolymer concentration by ten. Thus, they achieved to obtain vesicles with a size of 100 nm by using 1 $mg.mL^{-1}$ of copolymer in solution, and vesicles with a size of 400 nm when 10 $mg.mL^{-1}$ was used.

4.3. Incorporation of chemical additives

Additives can take various forms, ranging from molecules to nanoparticles. For example, Zhang *et al.*[126] reported the impact of HCl, NaOH and salts on PS-*b*-PAA (poly(styrene)-*block*-poly(acrylic acid)) object morphology and size. They proposed that self-assembly is governed by three factors [127] :

- stretching of PS block in the core,
- surface tension between solvent and core,
- repulsion among corona chains.

They studied first the impact of HCl on the morphology. A change of morphology was observed from sphere to bilayer, via a rod-like structure, as the HCl content was increased. They proposed that, in water, PAA blocks are partially ionized. In acidic condition, the protonation of PAA units decreases the charge density and thus the electrostatic repulsion among corona chain those consequently reduce entropy due to PS chain stretching. On the other hand, using NaOH had an antagonist effect, leading to a reverse behavior in term of morphology. Concerning the impact of salts, they compared calcium chloride, as a divalent ion, and sodium chloride, as a monovalent ion. They showed that the use of monovalent salt allows to change morphology from micelles to large vesicles, via the intermediate formation of cylinders and smaller vesicles, by increasing salt concentration. They highlighted the fact that divalent salts show the same behavior with a lower concentration is applied. For example, the transition from micelles to vesicles is possible with a concentration of $CaCl_2$ five time lower than NaCl.

Small inorganic nanoparticles can also be incorporated to help structuration of copolymer into vesicles. Hickey *et al.*[128] demonstrated that the PS-*b*-PAA self-assembly can be influenced by the use of oleic acid-stabilized iron oxide nanoparticles. Increasing the size and quantity of iron NPs favors the obtention of vesicles instead of micelles. They showed that polymersomes size gradually decrease from 513 +/- 76 nm to 257 +/- 90 nm by increasing the iron NPs size from 5.8 to 16.3 nm. This was explained by the change in membrane curvature of vesicles according to the size of the iron NPs. This phenomenon is illustrated in Figure 28.

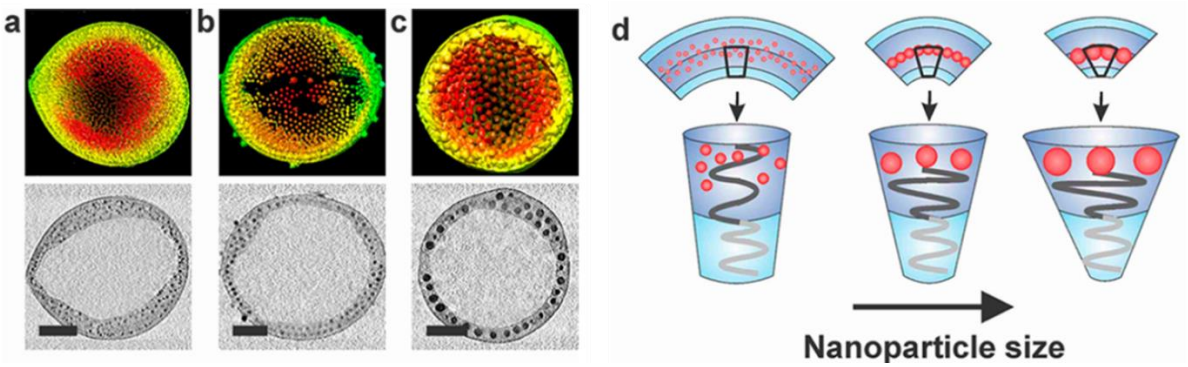

Figure 18: *3D surface reconstruction and TEM images of polymersomes assembles with (a) 5.8 nm, (b) 9.9 nm, (c) 16.3 nm iron oxide NPs. Scale bars: 100 nm. (d) Schematic representation of polymersomes membrane curvature affected by the iron NP size. From Hickey et al.*[128]

4.4. The role of temperature

Temperature is an important parameter to control during vesicle formation due to a modification of the properties of the solvent (such as viscosity), but also due to the impact on the behavior of the polymer chain (such as their mobility). These impacts could lead to a modification of the size and morphology of formed polymer nanoparticles. Zhou *et al.*[81] studied the effect of temperature during nanoprecipitation. They called this technique "temperature assisted nanoprecipitation" (TAN) and compared it to nanoprecipitation at room temperature and film hydration. By using PEG-*b*-PCL (poly(ethylene glycol)-*block*-poly(caprolactone)) as block copolymers, they proved that a certain temperature is required to obtain polymersomes by nanoprecipitation while no vesicles were formed with nanoprecipitation performed at room temperature . They also showed that above 50 °C, which was determined as the limit temperature to obtain vesicles, the increase of temperature leads to an increase of the size of the obtained vesicles.

Another illustration of the role of temperature is given by Desbaumes and Eisenberg[123], studying the effect of some parameters on self-assembly, among which temperature. They studied PS-*b*-PAA self-assembly through the single-solvent method. Briefly, PS-*b*-PAA block copolymer is solubilized in organic solvent at a high temperature, then temperature was decreased during the polymer self-assembly and the obtained suspension was dialyzed against aqueous solvent before being characterized. They showed that a dependance of initial temperature used to solubilize the copolymer on nanoparticle morphology is established. With butanol as organic solvent, copolymer was solubilized at 160 °C and spheres were formed during cooling. But when the solubilization temperature didn't exceed 115 °C, vesicles were formed when temperature was lowered.

5. Polymersomes as drug delivery systems

5.1. General definitions of drug delivery systems

In the field of nanomedicine, the interaction between molecules and entities that formed nanoparticles are investigated since the first trial of drug encapsulation inside nanosystem. Since then, a great number of publications is dedicated to the field of drug interaction with nanoparticles, as well as in the encapsulation or in the release process. As previously mentioned, polymersomes are of great interest due to their ability to load hydrophilic drugs in the core and hydrophobic drugs in the bilayer membrane. Compared to their lipidic counterpart, polymersomes tend to have a thicker membrane, enabling them to carry a greater quantity of hydrophobic drug. This has been previously observed with paclitaxel, a hydrophobic drug, with a loading content ten times higher in PEG-*b*-PLA / PEG-*b*-PB (poly(ethylene glycol)-b-poly(butadiene)) polymersomes[129] than in liposomes[130]. Additionally, polymersomes are known to be more stable[131], less leaky[132] and have a longer life-span than liposomes[19] , which can help to better control drug release.

The quantification of the drug encapsulation capacity is established by using two parameters : the drug loading content[133] (DLC) and the encapsulation efficiency[134] (EE). These parameters are calculated following equations that are detailed below (Equation I.2 and I.3):

$$DLC = \frac{weight\ of\ loaded\ drug}{weight\ of\ loaded\ polymersomes} \times 100 \qquad I.2$$

$$EE = \frac{weight\ of\ loaded\ drug}{weight\ of\ drug\ in\ feed} \times 100 \qquad I.3$$

Other equations could be used to qualify the loading capacity, such as the feed weight ratio (FWR), corresponding to the ratio between weight of feeding drug and weight of copolymer.[135,136] The drug loading content represents the ratio between the weight of the drug and the overall weight of loaded nanoparticles (copolymer + loaded drug). This information enables us to understand the distribution between drug and polymer in the nanoparticle and provides an idea of the maximum amount of drug that could be delivered *in vivo*. The encapsulation efficiency is more related to the formulation process, as it indicates the ratio between loaded and initially available drug during formulation. The perfect formulation system will thus tend to have the highest DLC and EE. The first drug loading method consists in addition of drug during the process of formation of nanoparticles, corresponding to a “passive encapsulation”. Passive loading involves drug dissolution in solutions that will be used during the nanocarrier assembly. In order to achieve a high yield of encapsulation in vesicles, a remote loading approach or “active encapsulation” might also be used. This method involves the addition of drug to preformed vesicles through a pH gradient or an ion gradient capable of generating a pH gradient.

5.2. Drug encapsulation by passive loading

Passive loading is a simple and convenient method for drug loading. This process involves loading drug simultaneously with the formation of polymersomes. Briefly, compound to be loaded is added either in the organic solvent with copolymer, or in aqueous solvent, depending on their solubility.[137] To illustrate the passive loading method, doxorubicin hydrochloride was chosen as an example of a rather hydrophilic drug and paclitaxel as an example of hydrophobic drug. Colley *et al.*[138] reported a film hydration process used to passively loaded doxorubicin and paclitaxel. Basically, $PMPC_{25}$-b-$PDPA_{70}$ (poly(2-(methacryloyloxyethylphosphorylcholine))-*block*-poly(2-(diisopropylamino)ethyl methacrylate)) is prepared to undergo film formation after solvent evaporation. Aqueous solvent is added and polymersomes self-assembly was observed. The critical factor in this process is dissolving doxorubicin in the aqueous solvent before the hydration of the polymer film so that polymersomes encapsulate the drug directly during their formation. Free drug is then removed from the polymersomes suspension by gel permeation chromatography. They reported an EE of 49.1 ± 4.4 % and the DLC was approximately 1.21 %. Similarly, paclitaxel was loaded by film hydration, except that paclitaxel was previously solubilized in organic solvent with polymer and allowed to form a film by solvent evaporation. The reported EE was 44.8 ± 8.6 % and the DLC can also be calculated and was about 1.11% (Table 2).

Table 2 : *Drug Loading Content and Encapsulation efficiency of Doxorubicin and Paclitaxel loading in $PMPC_{25}$-$PDPA_{70}$ polymersomes. Data from Colley et al.*[138]

Drug	DLC (%)	EE (%)
Doxorubicin	~ 1.21	49.1 ± 4.4
Paclitaxel	~ 1.11	44.8 ± 8.6
Doxorubicin	~ 0.92	37.1 ± 13.5
+ Paclitaxel	~ 1.07	42.7 ± 10.2

Paclitaxel has also been passively loaded during nanoprecipitation process as reported by Chen *et al.*[134] They reported a typical process of nanoprecipitation where an aqueous buffer is added dropwise to a solution composed of both PEG-*b*-PTMBPEC copolymer (poly(ethylene glycol)-*block*-poly(mono-2,4,6-trimethoxy benzylidene-pentaerythritol carbonate-*co*-acryloyl carbonate)) and paclitaxel drug, solubilized in Dioxane/DMSO solvent. Dialysis was then used to withdraw free drug and organic solvent. They reported a DLC of 3 to 7.5 %, depending on the initial amount of paclitaxel used, and an EE from 30 to 37.7 %. As another example of passive loading of Doxorubicin, Albuquerque *et al.*[104] reported the use of microfluidic assisted nanoprecipitation. Doxorubicin was also simply solubilized in the organic solvent that also contains $PHPMA_m$-*b*-$PDPA_n$ copolymer (poly([N-(2-hydroxypropyl)]methacrylamide)-*block*-poly[2-(diisopropylamino)ethyl methacrylate]). They experimented nanoprecipitation by using PBS buffer as aqueous solvent, completing by dialysis after vesicles formation to withdraw organic solvent and free drug. They reported a DLC of 9.8 % and an EE of 53.1 % (Table 3).

Table 3 : *Comparison of DLC and EE of Doxorubicin and Paclitaxel depending on the self-assembly process used during passive loading. Film hydration data from Colley et al.[138] Nanoprecipitation of doxorubicin from Albuquerque et al.[104], Nanoprecipitation of paclitaxel from Chen et al [134].*

Drug	Film hydration		Nanoprecipitation	
	DLC (%)	EE (%)	DLC (%)	EE (%)
Doxorubicin	~ 1.21	49.1 ± 4.4	9.8	53.1
Paclitaxel	~ 1.11	44.8 ± 8.6	3 to 7.5	30 to 37.7

Sanson *et al.*[80] proposed a novel method to enhanced doxorubicin passive loading by nanoprecipitation by exploring the pH sensitivity of doxorubicin. They compared the DLC and EE of nanoparticles done by nanoprecipitation using buffer at pH 7.4 or buffer at pH 10.5 as aqueous solvent. Following nanoprecipitation, both suspensions were purified by using dialysis techniques with a bath composed of buffer at pH 7.4. This approach overcomes the limitation of aggregation and enables surpassing the maximum doxorubicin encapsulation at pH 7.4. Notably, the authors were able to achieve a DLC of 47 % at pH 10.5, which is twice the maximum limit of 23 % observed at pH 7.4 (Table 4). Thus, this technique offers a promising approach to increase the effectiveness of doxorubicin delivery.

Table 4 *: Drug Loading Content and Encapsulation Efficiency of Doxorubicin, loaded by nanoprecipitation at pH 7.4 or pH 10.5 and with different Feed Weight Ratios (FWR). From Sanson et al.[80]*

FWR (wt.%)	pH 7.4		pH 10.5	
	DLC (wt.%)	EE (wt.%)	DLC (wt.%)	EE (wt.%)
10	5 ± 2	47 ± 3	5 ± 2	49 ± 3
20	10 ± 2	56 ± 3	9 ± 2	47 ± 3
30	23 ± 2	78 ± 3	13 ± 2	44 ± 3
40			20 ± 2	49 ± 3
50	Aggregation of polymer and doxorubicin		34 ± 2	68 ± 3
60			42 ± 2	71 ± 3
70			47 ± 2	67 ± 3

After reviewing these examples, we might be tempted to conclude that nanoprecipitation is a superior method for drug loading, given the higher DLC of paclitaxel and doxorubicin achieved through this process compared to the film hydration process (with comparable EE). However, it is difficult to draw firm conclusions on these processes due to the variability of copolymer used across these examples. In passive loading, the critical factor is to identify the optimal combination of process, copolymer, and drug to achieve maximum encapsulation. Furthermore, the feed weight ratio (FWR) of the drug has been reported to impact DLC and EE. In conclusion, it is more interesting to compare DLC and EE within the same study, where only a few parameters vary, rather than between studies that may differ in process, polymer, and feed weight ratio.

5.3. Drug encapsulation by active loading

Active drug loading, in contrast to passive loading, occurs after vesicle formation. The concept behind active loading is to establish a concentration gradient between the inner and outer aqueous phase of the membrane. This is achieved by assembling the vesicles in an aqueous solvent that differs from the one in which they will ultimately be placed (Figure 29). While there are few examples of active loading reported in the literature, some noteworthy ones will be discussed here.

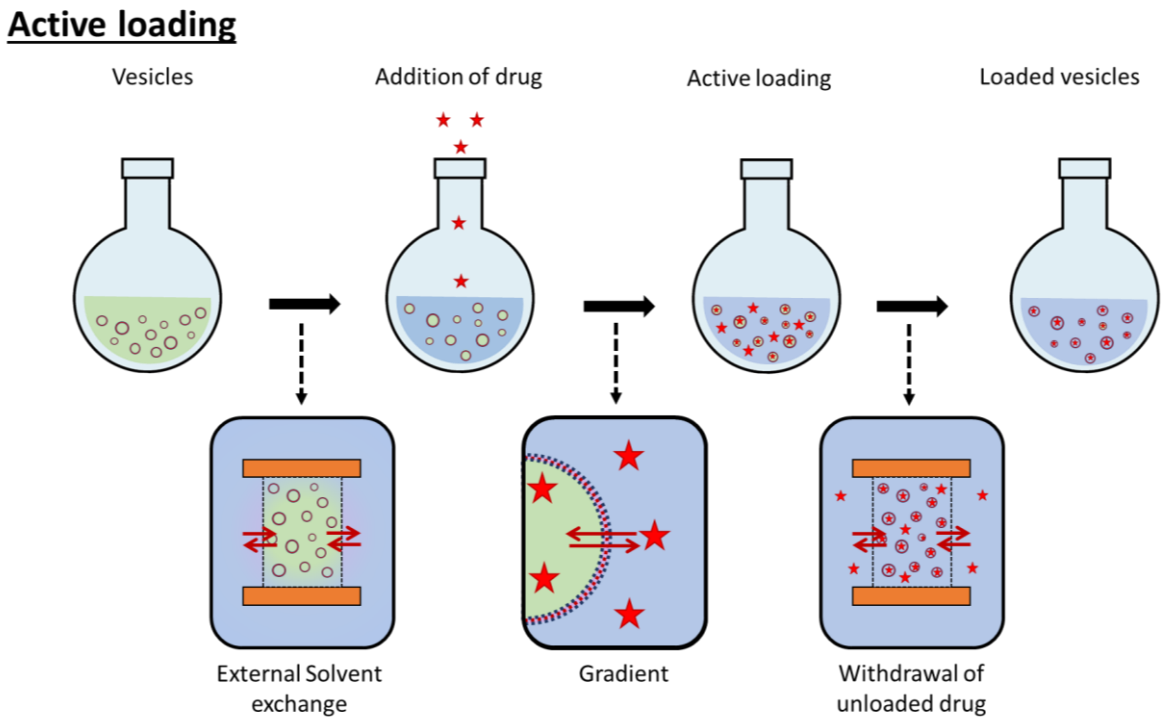

Figure 29: *Schematic representation of active loading. Active loading can use pH or ionic gradient for instance.*

5.3.1. pH gradient

pH gradient is a common method used to increase loading of doxorubicin in polymersomes. The process is described as follows: vesicles are formulated in an acidic aqueous buffer in order to obtain an acidic core inside the vesicles. A purification method (such as dialysis or column exchange) is then used to change the external solvent to a solvent with a neutral pH. The drug is then added in the external medium of the suspension. By using doxorubicin HCl as drug loading model, the proposed loading mechanism suppose that, due to the presence of an amine group, doxorubicin exists both in neutral and charged form in solution. At neutral pH, the doxorubicin is mainly neutral while at acidic pH, it exists primarily in the charged form. Neutral form assumes to be membrane permeable while the charged form is not membrane permeable. Transmembrane redistribution dictated by Henderson-Hasselbach relation thus occurs.[139,140] This phenomenon leads to accumulation of doxorubicin in the inner acidic core of vesicles[140–147]. As this method uses vesicles already preformed, membrane permeability may be an issue. To overcome this limitation, membrane permeability needs to be enhanced, by increasing the temperature of the overall suspension[141,144], or by using a specific solvent

that will increase membrane fluidity, called a plasticizer solvent, such as dioxane[139]. Choucair *et al.*[139] reported a study on the effect of pH gradient and also the use of dioxane as plasticize, on doxorubicin loading. After the self-assembly of PS-*b*-PAA block copolymers by nanoprecipitation using water at pH 2.5 and dioxane as organic solvent, the solution was purified to withdraw the organic solvent. The solution was then separated into multiple samples, each containing an external constant concentration of doxorubicin but with varying amounts of dioxane. The samples were then left to stir for four hours before the pH was adjusted to 6.3 and left to stir for three days. The samples were subsequently dialyzed to remove any unencapsulated drug. The researchers also studied the effect of dioxane on doxorubicin without a pH gradient, with vesicles self-assembled at pH 6.3. Their observations revealed that increasing the dioxane fraction improved permeability through the membrane, facilitating the diffusion of the drug and leading to faster loading, as shown in Figure 30. After three days of incubation, doxorubicin loading was found to be four times higher in samples with 48 % dioxane than in those with 22 % dioxane. However, when the system is given enough time to reach equilibrium, the degree of loading should be independent of the dioxane content. The graph represented on figure 30 only shows that the higher the dioxane content, the faster the loading process occurs.

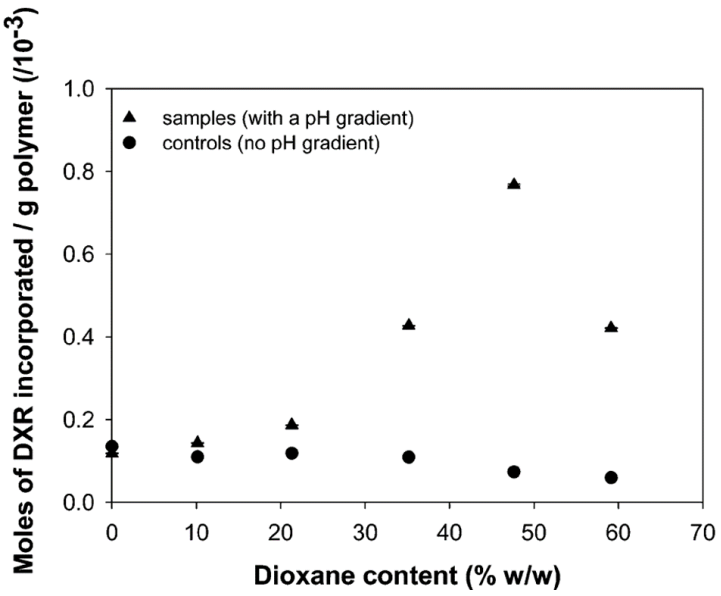

Figure 30: *Loading of doxorubicin in PS-b-PAA vesicles as a function of pH gradient and dioxane content. From Choucair et al.*[139]

The decrease in loading observed when dioxane content exceeds 48 % is attributed to the facilitated diffusion of protons through the membrane, which leads to a reduction of the pH gradient and ultimately a decrease in drug loading. In comparison, when no pH gradient is employed, drug loading is found to be independent of dioxane content. The study concludes by indicating that the pH gradient method allows for doxorubicin loading levels to be increased up to 10-fold compared to methods that do not utilize a pH gradient.

5.3.2. Ionic gradient

The active drug loading described with pH gradient has also been used with ionic gradients that use ammonium salts, sodium salts or manganese salts.[148–153] Cheung *et al.*[150] reported a study about doxorubicin loading via Mn^{2+} gradient. Vesicles were formulated in $MnSO_4$ buffer, and a gel permeation chromatography was then used to exchange the external media for an aqueous media composed of sucrose, HEPES and EDTA (hydroxyethyl-piperazineethane-sulfonic acid and ethylene-diamine-tetraacetic acid*)*. As discussed earlier, increasing fluidity of chain is necessary to facilitate the drug transport across the membrane. To investigate this, experiments were performed at 60 °C and the influence of feed weight ratio (FWR) and the internal concentration of $MnSO_4$ was evaluated on the drug loading. They reported a maximum FWR beyond which doxorubicin uptake decreased. Additionally, for a given FWR, using $MnSO_4$ to induce a gradient was found to significantly increase doxorubicin uptake, from 10 % of FWR without gradient, up to 85 % when using the ionic gradient. To explain this phenomenon, they studied the formation of complexes between doxorubicin and Mn^{2+} as depicted in Figure 31. They proved a complex formation in bulk by measuring a change in absorption spectra during active loading. As doxorubicin is known to change absorption spectra from red to blue when pH increases higher than pH 8, they also proved that this change in absorbance is not the consequence of a pH modification by measuring no pH change in bulk, meaning that complex formation is the only mechanism driving doxorubicin loading.

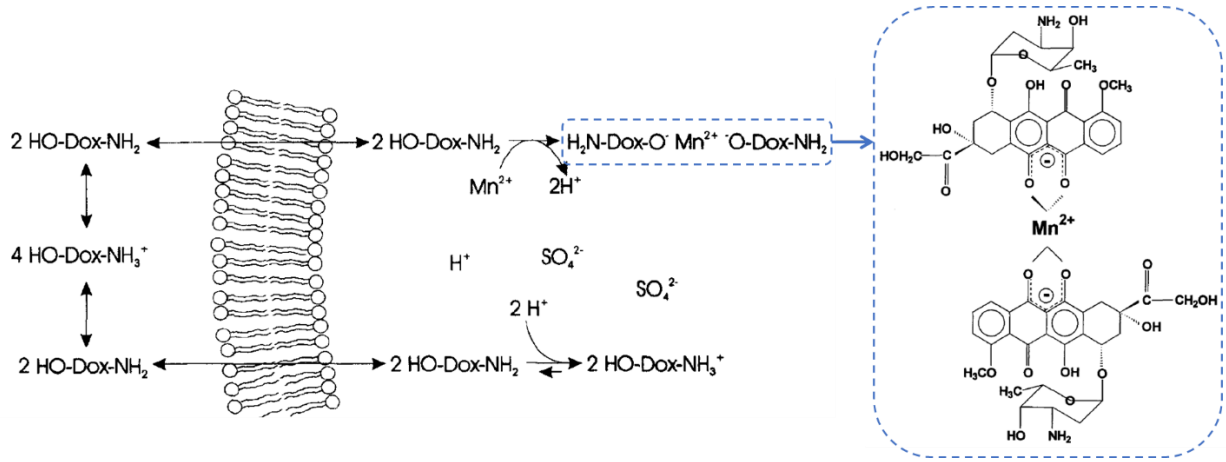

Figure 31: *Schematic representation of doxorubicin-Mn^{2+} complex formed during doxorubicin active loading by ionic gradient. Adapted from Cheung et al.*[150]

Studies on active loading have been performed using ionic gradient with salts others than manganese salts. Fritze *et al*.[148] compared effect of changing the counter ion of sodium and ammonium ions on doxorubicin loading, using citrate, phosphate, sulfate, or acetate counter ions. Vesicles were formulated using film hydration method with different buffer, followed by a change of the external media by gel permeation chromatography. For an identical salt concentration and doxorubicin concentration conditions, the salts were classified based on their efficiency to load doxorubicin, as shown in Figure 32.

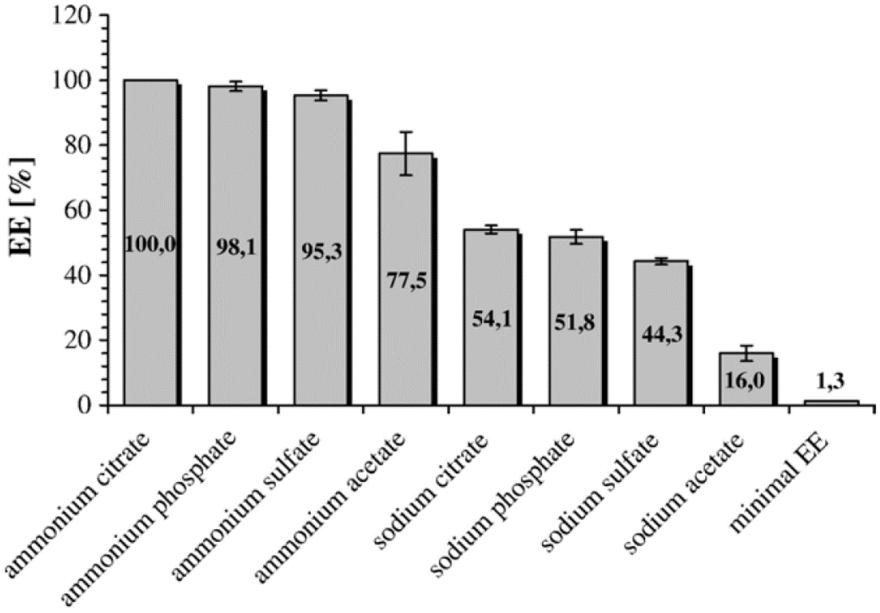

Figure 32: *Encapsulation efficiency of doxorubicin in vesicles driven by different salt gradients. From Fritze et al.*[148]

They also studied the influence of the salt concentration on active loading and showed an improve uptake with higher salt concentration. Fritze *et al.* reported that doxorubicin loading leads to overcoming the solubility of doxorubicin in the inner core of vesicle, thus doxorubicin crystals are formed. These crystals are visible by Cryo-TEM, as shown in Figure 33.[153–156]

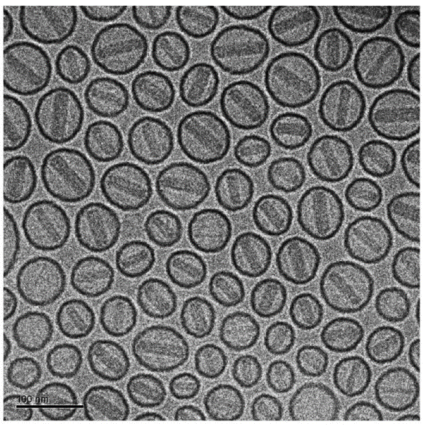

Figure 33*: Doxorubicin loaded vesicles in which inter doxorubicin concentration exceeded solubility limit, leading to doxorubicin precipitation/crystallization. From Andriyanov et al.*[155]

5.4. Evaluation and control of the drug release from nanoparticles

While achieving a good drug loading is important, delivering the drug effectively is equally crucial. As previously mentioned, several release strategies have been used taking the advantage of endogenous or exogenous stimuli to induce drug release at a given time.[47,48,157,158] While this part will not provide an exhaustive overview of techniques used to induce drug release, it will detail a few examples.

5.4.1. Endogenous stimuli

Endogenous stimuli take the advantage of a physiological change induced by an illness, to provoke drug delivery. The trigger can be a variation of pH, the presence of specific enzymes[159–161], or the use of an redox reaction[162–164] due to generation of reactive oxygen species (ROS), for instance.[158]pH is an interesting trigger when the goal of the developed drug delivery system is the treatment of tumors or inflammatory tissues, as these both tissues exhibit mildly acidic pH.[165] To use this trigger, one way will be to use a copolymer sensitive to hydrolysis. Chen *et al.*[134] used PEG-*b*-PTMBPEC (poly(ethylene glycol)-*block*-poly(mono-2,4,6-trimethoxy benzylidene-pentaerythritol carbonate)) as sensitive copolymer in acidic pH. They reported the influence of pH on the release of doxorubicin loaded in PEG-*b*- PTMBPEC vesicles. As shown in Figure 34, the pH decrease leads to faster release, reaching 95 % of release in 4 h at pH 4, when only 30% is reached at pH 7.4, proving the pH responsiveness of this system.

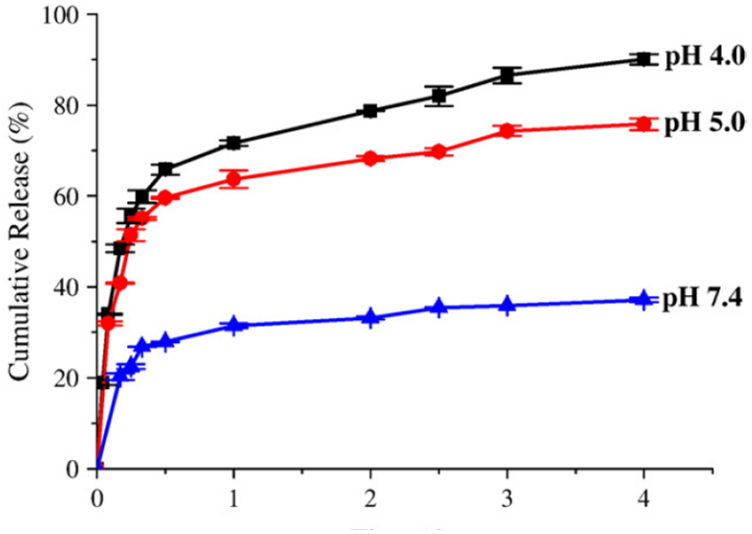

Figure 34: *pH triggered release of Doxorubicin from pH sensitive PEG-b-PTMBPEC polymersomes. From Chen et al.*[134]

Another strategies using pH trigger is described by Quadir *et al.*[166] with the use of PEG-*b*-PPLG (poly(ethylene glycol)-*block*-poly(γ-R-glutamate)) copolymers with amine pendant side chains. They first demonstrated the ability of these copolymer to self-assemble at pH 8 and showed, by performing fluorescence resonance energy transfer (FRET) assays, that the decrease of pH induced destabilization and disassembly of vesicles as amines became fully protonated.[167] Thus, after loading doxorubicin in PEG-*b*-PPLG vesicles, they showed a significant change in release profile according to the pH of the external media. What makes this study particularly interesting is that it was conducted on mice to

demonstrate the *in vivo* efficacy of pH-sensitive vesicles on cancer cells. The researchers compared untreated tumor with tumor treated with either free drug or drug loaded in vesicles, as shown in Figure 35. The results demonstrate that the loaded vesicles were more effective in limiting tumor growth compared to the free drug.

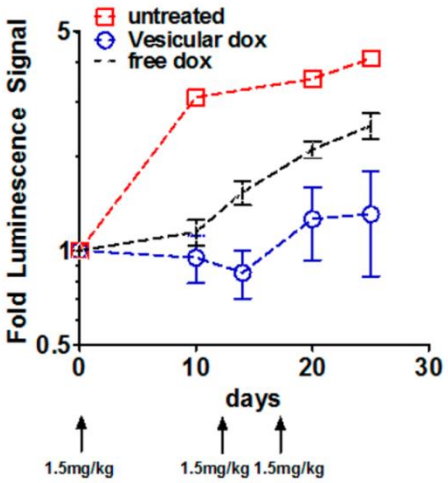

Figure 35: *Tumor remediation study against MDA-MB-469 xenografts in NCR nude mice comparing untreated tumor, tumor treated with free doxorubicin and tumor treated with vesicles loaded doxorubicin. From Quadir et al.*[166]

5.4.2. Exogenous stimuli

Exogenous triggers offer a way to control spatially and/or temporally the drug release coming from the polymer nanoparticles. This way uses an external stimulus, such as temperature[168–171], ultrasound[172–175], magnetic field[176–179] or light to induce the drug release[48]. Regarding the use of light, photo-sensitive polymersomes can undergo various mechanisms.[55,180–184]. A first proposition would be to synthesize a photo-sensitive copolymer able to self assemble into vesicles. Beauté *et al.*[180] and Hou *et al.*[185] proposed two different approches for this concept. Hou *et al.*[185] reported the synthesis of PDMA-*b*-PNBA (poly (*N,N'*-dimethylacrylamide) -*block*-poly (o-nitrobenzyl acrylate)) containing o-nitrobenzyl groups that react upon UV light irradiation. They demonstrated that under light irradiation at 365 nm, a cleaveage reaction between o-nitrobenzyl ester and the rest of the hydrophobic PNBA are formed and consequently generate o-nitrobenzhaldehyde and free carboxylic acides. In this case, the hydrophobic blocks became hydrophilic, leading to the disassembly of the vesicles due to the disparity in the amphiphilic properties of the block copolymers. Researchers followed this phenomenon on free chains in solution before achieving to use this copolymer to self-assemble into polymersomes.They studied the result of the cleavage under UV light on polymersomes shape. They then reported the delivery of doxorubicin and a hydrophobic dye (nile red) from their specific polymersomes. They compared release of both compounds with and without an exposition to UV light. As represented in figure 36 A, without irradiation, no decrease on the emission spectra of Nile red was observed while under irradiation at 365 nm, a signficant decrease was observed. Concerning the release of doxorubicine, they proved that the time of polymersomes exposition on UV irradiation has an influence on the quantity of drug released, as shown in figure 36 B.

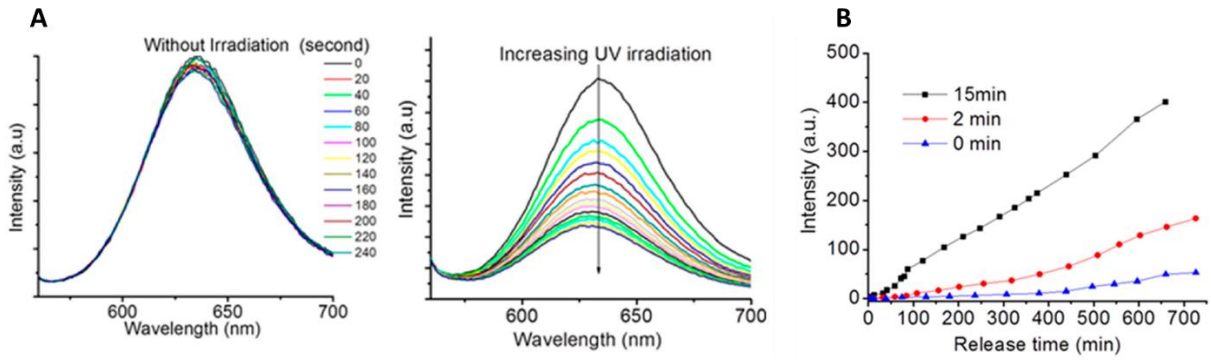

Figure 26: *A) Nile Red emission spectra of polymersome solution with and without UV irradiation of polymersomes at 365 nm. B) Doxorubicin emission intensity in polymersomes exposed to different irradiation time at 365nm. From Hou et al.*[185]

Beauté *et al.*[180] proposed a similar strategy consisting of using a photo-sensitive PEG-coumarin-b-PTMC (poly(ethylene glycol)-coumarin-*block*-poly(trimethylene carbonate)) able to self-assemble into polymersomes. Due to the presence of coumarin, a photo-sensitive dye, irradiation is supposed to break copolymer and consequently destabilizing vesicles.

Another way to use light as a release trigger is to use light-induced osmotic shock. By using compound able to increase the osmotic pressure, the low membrane permeability of polymersomes doesn't allow external solvent to counterbalance this osmolarity difference inside and outside the vesicles and the osmotic pressure remains imbalanced leading to a membrane destabilization and an "explosion" on the vesicles. To induce this phenomenon, Peyret *et al.* loaded light-sensitive molecules in vesicles, methylene blue or calcein, able to cleave under UV irradiation respectively at 633 nm and 488 nm and generate radical species that induce an increase of osmolarity. They were able to selectively trigger the explosion of vesicles based on the encapsulated molecule. Specifically, they demonstrated that vesicles loaded with methylene blue did not explode under 488 nm irradiation, but did under 633 nm irradiation, whereas the opposite is observed for calcein loaded vesicles. Both types of vesicles were subjected to laser irradiation, as shown in Figure 37. Therefore, co-encapsulating another drug with the photosensitive molecule can enable to control its release under precise irradiation conditions.

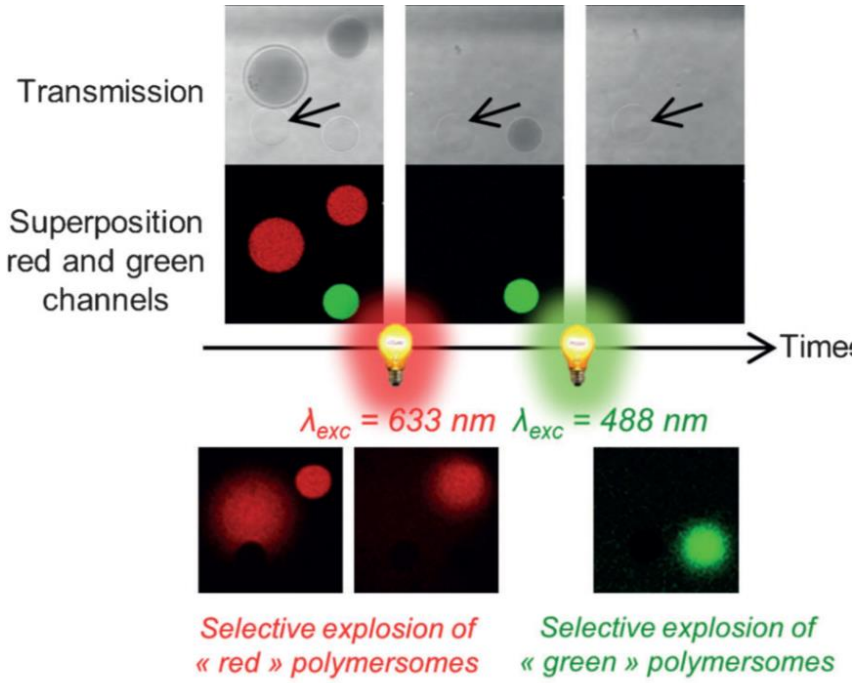

Figure 37: *Confocal observation of vesicles loaded with methylene blue (red) or calcein (green) or sucrose for control (arrow). Exposition to 633 nm leads to methylene blue loaded vesicles explosion while calcein loaded ones remain intact until 488 nm irradiation. Sucrose loaded ones remain intact.*

Conclusion

Through this chapter, polymersomes appeared to be a strong tool for drug delivery. Made from a large variety of amphiphilic block copolymers, robustness and versatility are two of their main advantages. Development of processes allowed to produce polymersomes from nano- to micro-scale that can nowadays been formulated with reduced size dispersity and improved reproducibility through the use of microfluidic processes. Their hollow structure is of great interest for drug loading as hydrophilic drug can be loaded in the aqueous core while hydrophobic drug can be loaded in the membrane of the vesicle. Spatiotemporal control over drug delivery as bee mentioned through the development of stimuli-responsive polymersomes of all kinds, enabling site-specific drug delivery and reduction of systemic toxicity.

My PhD research project fits in this context and had the objectives to: formulate polymersomes ready-to-use for *in vitro / in vivo* experiment with size control, study hydrophilic and hydrophobic drug loading and investigate mechanism of copolymer self-assembly into vesicles. The different steps of the project are detailed in each of the following chapters.

References

(1) Xia, Y. Are We Entering the Nano Era? *Angew. Chem. Int. Ed.* **2014**, *53*. https://doi.org/10.1002/anie.201406740.

(2) Singh, R.; Lillard, J. W. Nanoparticle-Based Targeted Drug Delivery. *Exp. Mol. Pathol.* **2009**, *86* (3), 215–223. https://doi.org/10.1016/j.yexmp.2008.12.004.

(3) Kreyling, W. *Nanomedicine : An ESF-European Medical Councils (EMRC) Forword Look Report 2005*; 2005.

(4) Wagner, V.; Dullaart, A.; Bock, A.-K.; Zweck, A. The Emerging Nanomedicine Landscape. *Nat. Biotechnol.* **2006**, *24* (10), 1211–1217. https://doi.org/10.1038/nbt1006-1211.

(5) Papich, M. G.; Martinez, M. N. Applying Biopharmaceutical Classification System (BCS) Criteria to Predict Oral Absorption of Drugs in Dogs: Challenges and Pitfalls. *AAPS J.* **2015**, *17* (4), 948–964. https://doi.org/10.1208/s12248-015-9743-7.

(6) Alexis, F.; Pridgen, E.; Molnar, L. K.; Farokhzad, O. C. Factors Affecting the Clearance and Biodistribution of Polymeric Nanoparticles. *Mol. Pharm.* **2008**, *5* (4), 505–515. https://doi.org/10.1021/mp800051m.

(7) Peer, D.; Karp, J.; Hong, S.; Farokhzad, O.; Margalit, R.; Langer, R. Nanocarriers as an Emerging Platform for Cancer Therapy. *Nat. Nanotechnol.* **2007**, *2*, 751–760. https://doi.org/10.1038/nnano.2007.387.

(8) Stiepel, R. T.; Duggan, E.; Batty, C. J.; Ainslie, K. M. Micro and Nanotechnologies: The Little Formulations That Could. *Bioeng. Transl. Med. n/a* (n/a), e10421. https://doi.org/10.1002/btm2.10421.

(9) Kamaly, N.; Xiao, Z.; Valencia, P. M.; Radovic-Moreno, A. F.; Farokhzad, O. C. Targeted Polymeric Therapeutic Nanoparticles: Design, Development and Clinical Translation. *Chem. Soc. Rev.* **2012**, *41* (7), 2971. https://doi.org/10.1039/c2cs15344k.

(10) Ventola, C. L. Progress in Nanomedicine: Approved and Investigational Nanodrugs. *Pharm. Ther.* **2017**, *42* (12), 742–755.

(11) Discher, D. E.; Ahmed, F. Polymersomes. *Annu. Rev. Biomed. Eng.* **2006**, *8*, 323–341. https://doi.org/10.1146/annurev.bioeng.8.061505.095838.

(12) Moghassemi, S.; Hadjizadeh, A. Nano-Niosomes as Nanoscale Drug Delivery Systems: An Illustrated Review. *J. Control. Release Off. J. Control. Release Soc.* **2014**, *185*, 22–36. https://doi.org/10.1016/j.jconrel.2014.04.015.

(13) Kaneda, Y. Virosomes: Evolution of the Liposome as a Targeted Drug Delivery System. *Adv. Drug Deliv. Rev.* **2000**, *43* (2–3), 197–205. https://doi.org/10.1016/s0169-409x(00)00069-7.

(14) Kim, S.-H.; Shum, H. C.; Kim, J. W.; Cho, J.-C.; Weitz, D. A. Multiple Polymersomes for Programmed Release of Multiple Components. *J. Am. Chem. Soc.* **2011**, *133* (38), 15165–15171. https://doi.org/10.1021/ja205687k.

(15) Bangham, A. D.; Horne, R. W. Negative Staining of Phospholipids and Their Structural Modification by Surface-Active Agents as Observed in the Electron Microscope. *J. Mol. Biol.* **1964**, *8* (5), 660-IN10. https://doi.org/10.1016/S0022-2836(64)80115-7.

(16) van Hest, J. C.; Delnoye, D. A.; Baars, M. W.; van Genderen, M. H.; Meijer, E. W. Polystyrene-Dendrimer Amphiphilic Block Copolymers with a Generation-Dependent Aggregation. *Science* **1995**, *268* (5217), 1592–1595. https://doi.org/10.1126/science.268.5217.1592.

(17) Zhang, L.; Eisenberg, A. Multiple Morphologies of "Crew-Cut" Aggregates of Polystyrene-b-Poly(Acrylic Acid) Block Copolymers. *Science* **1995**, *268* (5218), 1728–1731. https://doi.org/10.1126/science.268.5218.1728.

(18) Northfelt, D. W.; Dezube, B. J.; Thommes, J. A.; Miller, B. J.; Fischl, M. A.; Friedman-Kien, A.; Kaplan, L. D.; Du Mond, C.; Mamelok, R. D.; Henry, D. H. Pegylated-Liposomal Doxorubicin versus Doxorubicin, Bleomycin, and Vincristine in the Treatment of AIDS-Related Kaposi's Sarcoma:

Results of a Randomized Phase III Clinical Trial. *J. Clin. Oncol.* **1998**, *16* (7), 2445–2451. https://doi.org/10.1200/JCO.1998.16.7.2445.

(19) Rideau, E.; Dimova, R.; Schwille, P.; Wurm, F. R.; Landfester, K. Liposomes and Polymersomes: A Comparative Review towards Cell Mimicking. *Chem. Soc. Rev.* **2018**, *47* (23), 8572–8610. https://doi.org/10.1039/C8CS00162F.

(20) Israelachvili, J. N.; Mitchell, D. J.; Ninham, B. W. Theory of Self-Assembly of Hydrocarbon Amphiphiles into Micelles and Bilayers. *J. Chem. Soc. Faraday Trans. 2 Mol. Chem. Phys.* **1976**, *72* (0), 1525–1568. https://doi.org/10.1039/F29767201525.

(21) Bleul, R.; Thiermann, R.; Maskos, M. Techniques To Control Polymersome Size. *Macromolecules* **2015**, *48* (20), 7396–7409. https://doi.org/10.1021/acs.macromol.5b01500.

(22) Matoori, S.; Leroux, J.-C. Twenty-Five Years of Polymersomes: Lost in Translation? *Mater. Horiz.* **2020**, *7* (5), 1297–1309. https://doi.org/10.1039/C9MH01669D.

(23) Nicolas, J.; Couvreur, P. Les Nanoparticules Polymères Pour La Délivrance de Principes Actifs Anticancéreux. *médecine/sciences* **2017**, *33*, 11–17. https://doi.org/10.1051/medsci/20173301003.

(24) Chiannilkulchai, N.; Ammoury, N.; Caillou, B.; Devissaguet, J. P.; Couvreur, P. Hepatic Tissue Distribution of Doxorubicin-Loaded Nanoparticles after i.v. Administration in Reticulosarcoma M 5076 Metastasis-Bearing Mice. *Cancer Chemother. Pharmacol.* **1990**, *26* (2), 122–126. https://doi.org/10.1007/BF02897257.

(25) Lee, H.; Larson, R. G. Adsorption of Plasma Proteins onto PEGylated Lipid Bilayers: The Effect of PEG Size and Grafting Density. *Biomacromolecules* **2016**, *17* (5), 1757–1765. https://doi.org/10.1021/acs.biomac.6b00146.

(26) Hemery, G. Synthesis of Magnetic and Thermosensitive Iron Oxide Based Nanoparticles for Biomedical Applications. These de doctorat, Bordeaux, 2017. https://www.theses.fr/2017BORD0729 (accessed 2023-01-13).

(27) Semple, S. C.; Chonn, A.; Cullis, P. R. Interactions of Liposomes and Lipid-Based Carrier Systems with Blood Proteins: Relation to Clearance Behaviour in Vivo. *Adv. Drug Deliv. Rev.* **1998**, *32* (1), 3–17. https://doi.org/10.1016/S0169-409X(97)00128-2.

(28) Gref, R.; Domb, A.; Quellec, P.; Blunk, T.; Müller, R. H.; Verbavatz, J. M.; Langer, R. The Controlled Intravenous Delivery of Drugs Using PEG-Coated Sterically Stabilized Nanospheres. *Adv. Drug Deliv. Rev.* **1995**, *16* (2–3), 215–233. https://doi.org/10.1016/0169-409X(95)00026-4.

(29) Matsumura, Y.; Maeda, H. A New Concept for Macromolecular Therapeutics in Cancer Chemotherapy: Mechanism of Tumoritropic Accumulation of Proteins and the Antitumor Agent Smancs. *Cancer Res.* **1986**, *46* (12 Pt 1), 6387–6392.

(30) Greish, K. Enhanced Permeability and Retention of Macromolecular Drugs in Solid Tumors: A Royal Gate for Targeted Anticancer Nanomedicines. *J. Drug Target.* **2007**, *15*, 457–464. https://doi.org/10.1080/10611860701539584.

(31) Maeda, H. The Enhanced Permeability and Retention (EPR) Effect in Tumor Vasculature: The Key Role of Tumor-Selective Macromolecular Drug Targeting. *Adv. Enzyme Regul.* **2001**, *41*, 189–207. https://doi.org/10.1016/s0065-2571(00)00013-3.

(32) Sarin, H. Physiologic Upper Limits of Pore Size of Different Blood Capillary Types and Another Perspective on the Dual Pore Theory of Microvascular Permeability. *J. Angiogenesis Res.* **2010**, *2*, 14. https://doi.org/10.1186/2040-2384-2-14.

(33) Hobbs, S. K.; Monsky, W. L.; Yuan, F.; Roberts, W. G.; Griffith, L.; Torchilin, V. P.; Jain, R. K. Regulation of Transport Pathways in Tumor Vessels: Role of Tumor Type and Microenvironment. *Proc. Natl. Acad. Sci. U. S. A.* **1998**, *95* (8), 4607–4612. https://doi.org/10.1073/pnas.95.8.4607.

(34) Maeda, H. SMANCS and Polymer-Conjugated Macromolecular Drugs: Advantages in Cancer Chemotherapy. *Adv. Drug Deliv. Rev.* **2001**, *46* (1–3), 169–185. https://doi.org/10.1016/s0169-409x(00)00134-4.

(35) Maeda, H.; Tsukigawa, K.; Fang, J. A Retrospective 30 Years After Discovery of the Enhanced Permeability and Retention Effect of Solid Tumors: Next-Generation Chemotherapeutics and

Photodynamic Therapy--Problems, Solutions, and Prospects. *Microcirc. N. Y. N 1994* **2016**, *23* (3), 173–182. https://doi.org/10.1111/micc.12228.

(36) Charrois, G. J. R.; Allen, T. M. Rate of Biodistribution of STEALTH Liposomes to Tumor and Skin: Influence of Liposome Diameter and Implications for Toxicity and Therapeutic Activity. *Biochim. Biophys. Acta* **2003**, *1609* (1), 102–108. https://doi.org/10.1016/s0005-2736(02)00661-2.

(37) Matsumoto, Y.; Nichols, J. W.; Toh, K.; Nomoto, T.; Cabral, H.; Miura, Y.; Christie, R. J.; Yamada, N.; Ogura, T.; Kano, M. R.; Matsumura, Y.; Nishiyama, N.; Yamasoba, T.; Bae, Y. H.; Kataoka, K. Vascular Bursts Enhance Permeability of Tumour Blood Vessels and Improve Nanoparticle Delivery. *Nat. Nanotechnol.* **2016**, *11* (6), 533–538. https://doi.org/10.1038/nnano.2015.342.

(38) Huynh, E.; Zheng, G. Cancer Nanomedicine: Addressing the Dark Side of the Enhanced Permeability and Retention Effect. *Nanomed.* **2015**, *10* (13), 1993–1995. https://doi.org/10.2217/nnm.15.86.

(39) Nicolas, J.; Mura, S.; Brambilla, D.; Mackiewicz, N.; Couvreur, P. Design, Functionalization Strategies and Biomedical Applications of Targeted Biodegradable/Biocompatible Polymer-Based Nanocarriers for Drug Delivery. *Chem. Soc. Rev.* **2013**, *42* (3), 1147–1235. https://doi.org/10.1039/c2cs35265f.

(40) Leong, J.; Teo, J. Y.; Aakalu, V. K.; Yang, Y. Y.; Kong, H. Engineering Polymersomes for Diagnostics and Therapy. *Adv. Healthc. Mater.* **2018**, *7* (8), e1701276. https://doi.org/10.1002/adhm.201701276.

(41) Mackiewicz, N.; Nicolas, J.; Handké, N.; Noiray, M.; Mougin, J.; Daveu, C.; Lakkireddy, H. R.; Bazile, D.; Couvreur, P. Precise Engineering of Multifunctional PEGylated Polyester Nanoparticles for Cancer Cell Targeting and Imaging. *Chem. Mater.* **2014**, *26* (5), 1834–1847. https://doi.org/10.1021/cm403822w.

(42) Alibolandi, M.; Abnous, K.; Hadizadeh, F.; Taghdisi, S. M.; Alabdollah, F.; Mohammadi, M.; Nassirli, H.; Ramezani, M. Dextran-Poly Lactide-Co-Glycolide Polymersomes Decorated with Folate-Antennae for Targeted Delivery of Docetaxel to Breast Adenocarcinima in Vitro and in Vivo. *J. Controlled Release* **2016**, *241*, 45–56. https://doi.org/10.1016/j.jconrel.2016.09.012.

(43) Christian, N. A.; Milone, M. C.; Ranka, S. S.; Li, G.; Frail, P. R.; Davis, K. P.; Bates, F. S.; Therien, M. J.; Ghoroghchian, P. P.; June, C. H.; Hammer, D. A. Tat-Functionalized Near-Infrared Emissive Polymersomes for Dendritic Cell Labeling. *Bioconjug. Chem.* **2007**, *18* (1), 31–40. https://doi.org/10.1021/bc0601267.

(44) Alibolandi, M.; Ramezani, M.; Abnous, K.; Sadeghi, F.; Atyabi, F.; Asouri, M.; Ahmadi, A. A.; Hadizadeh, F. In Vitro and in Vivo Evaluation of Therapy Targeting Epithelial-Cell Adhesion-Molecule Aptamers for Non-Small Cell Lung Cancer. *J. Controlled Release* **2015**, *209*, 88–100. https://doi.org/10.1016/j.jconrel.2015.04.026.

(45) Pang, Z.; Gao, H.; Yu, Y.; Chen, J.; Guo, L.; Ren, J.; Wen, Z.; Su, J.; Jiang, X. Brain Delivery and Cellular Internalization Mechanisms for Transferrin Conjugated Biodegradable Polymersomes. *Int. J. Pharm.* **2011**, *415* (1), 284–292. https://doi.org/10.1016/j.ijpharm.2011.05.063.

(46) Robbins, G. P.; Saunders, R. L.; Haun, J. B.; Rawson, J.; Therien, M. J.; Hammer, D. A. Tunable Leuko-Polymersomes That Adhere Specifically to Inflammatory Markers. *Langmuir* **2010**, *26* (17), 14089–14096. https://doi.org/10.1021/la1017032.

(47) Hu, X.; Zhang, Y.; Xie, Z.; Jing, X.; Bellotti, A.; Gu, Z. Stimuli-Responsive Polymersomes for Biomedical Applications. *Biomacromolecules* **2017**, *18* (3), 649–673. https://doi.org/10.1021/acs.biomac.6b01704.

(48) Kauscher, U.; Holme, M. N.; Björnmalm, M.; Stevens, M. M. Physical Stimuli-Responsive Vesicles in Drug Delivery: Beyond Liposomes and Polymersomes. *Adv. Drug Deliv. Rev.* **2019**, *138*, 259–275. https://doi.org/10.1016/j.addr.2018.10.012.

(49) Ayer, M.; Klok, H.-A. Cell-Mediated Delivery of Synthetic Nano- and Microparticles. *J. Controlled Release* **2017**, *259*, 92–104. https://doi.org/10.1016/j.jconrel.2017.01.048.

(50) Anselmo, A. C.; Mitragotri, S. Cell-Mediated Delivery of Nanoparticles: Taking Advantage of Circulatory Cells to Target Nanoparticles. *J. Controlled Release* **2014**, *190*, 531–541. https://doi.org/10.1016/j.jconrel.2014.03.050.

(51) Brinkhuis, R. P.; Stojanov, K.; Laverman, P.; Eilander, J.; Zuhorn, I. S.; Rutjes, F. P. J. T.; van Hest, J. C. M. Size Dependent Biodistribution and SPECT Imaging of (111)In-Labeled Polymersomes. *Bioconjug. Chem.* **2012**, *23* (5), 958–965. https://doi.org/10.1021/bc200578s.
(52) Marguet, M.; Edembe, L.; Lecommandoux, S. Polymersomes in Polymersomes: Multiple Loading and Permeability Control. *Angew. Chem. Int. Ed.* **2012**, *51* (5), 1173–1176. https://doi.org/10.1002/anie.201106410.
(53) Sui, X.; Kujala, P.; Janssen, G.-J.; Jong, E. de; Zuhorn, I. S.; Hest, J. C. M. van. Robust Formation of Biodegradable Polymersomes by Direct Hydration. *Polym. Chem.* **2015**, *6* (5), 691–696. https://doi.org/10.1039/C4PY01288G.
(54) O'Neil, C. P.; Suzuki, T.; Demurtas, D.; Finka, A.; Hubbell, J. A. A Novel Method for the Encapsulation of Biomolecules into Polymersomes via Direct Hydration. *Langmuir* **2009**, *25* (16), 9025–9029. https://doi.org/10.1021/la900779t.
(55) Peyret, A.; Ibarboure, E.; Tron, A.; Beauté, L.; Rust, R.; Sandre, O.; McClenaghan, N. D.; Lecommandoux, S. Polymersome Popping by Light-Induced Osmotic Shock under Temporal, Spatial, and Spectral Control. *Angew. Chem. Int. Ed Engl.* **2017**, *56* (6), 1566–1570. https://doi.org/10.1002/anie.201609231.
(56) Xu, H.; Cui, W.; Zong, Z.; Tan, Y.; Xu, C.; Cao, J.; Lai, T.; Tang, Q.; Wang, Z.; Sui, X.; Wang, C. A Facile Method for Anti-Cancer Drug Encapsulation into Polymersomes with a Core-Satellite Structure. *Drug Deliv.* **2022**, *29* (1), 2414–2427. https://doi.org/10.1080/10717544.2022.2103209.
(57) Rideau, E.; Wurm, F. R.; Landfester, K. Giant Polymersomes from Non-Assisted Film Hydration of Phosphate-Based Block Copolymers. *Polym. Chem.* **2018**, *9* (44), 5385–5394. https://doi.org/10.1039/C8PY00992A.
(58) Li, Q.; Wang, X.; Ma, S.; Zhang, Y.; Han, X. Electroformation of Giant Unilamellar Vesicles in Saline Solution. *Colloids Surf. B Biointerfaces* **2016**, *147*, 368–375. https://doi.org/10.1016/j.colsurfb.2016.08.018.
(59) Howse, J. R.; Jones, R. A. L.; Battaglia, G.; Ducker, R. E.; Leggett, G. J.; Ryan, A. J. Templated Formation of Giant Polymer Vesicles with Controlled Size Distributions. *Nat. Mater.* **2009**, *8* (6), 507–511. https://doi.org/10.1038/nmat2446.
(60) Angelova, M. I.; Dimitrov, D. S. Liposome Electroformation. *Faraday Discuss. Chem. Soc.* **1986**, *81* (0), 303–311. https://doi.org/10.1039/DC9868100303.
(61) Sens, P.; Isambert, H. Undulation Instability of Lipid Membranes under an Electric Field. *Phys. Rev. Lett.* **2002**, *88* (12), 128102. https://doi.org/10.1103/PhysRevLett.88.128102.
(62) Lacoste, D.; Lagomarsino, M. C.; Joanny, J.-F. Fluctuations of a Driven Membrane in an Electrolyte. *EPL - Europhys. Lett.* **2007**, *77* (1), 18006. https://doi.org/10.1209/0295-5075/77/18006.
(63) Seiwert, J.; Vlahovska, P. M. Instability of a Fluctuating Membrane Driven by an Ac Electric Field. *Phys. Rev. E Stat. Nonlin. Soft Matter Phys.* **2013**, *87* (2), 022713. https://doi.org/10.1103/PhysRevE.87.022713.
(64) Menger, F. M.; Angelova, M. I. Giant Vesicles: Imitating the Cytological Processes of Cell Membranes. *Acc. Chem. Res.* **1998**, *31* (12), 789–797. https://doi.org/10.1021/ar970103v.
(65) Yamashita, Y.; Oka, M.; Tanaka, T.; Yamazaki, M. A New Method for the Preparation of Giant Liposomes in High Salt Concentrations and Growth of Protein Microcrystals in Them. *Biochim. Biophys. Acta* **2002**, *1561* (2), 129–134. https://doi.org/10.1016/s0005-2736(02)00338-3.
(66) Angelova, M.; Dimitrov, D. S. A Mechanism of Liposome Electroformation. In *Trends in Colloid and Interface Science II*; Degiorgio, V., Ed.; Progress in Colloid & Polymer Science; Steinkopff: Darmstadt, 1988; pp 59–67. https://doi.org/10.1007/BFb0114171.
(67) D'Onofrio, T. G.; Hatzor, A.; Counterman, A. E.; Heetderks, J. J.; Sandel, M. J.; Weiss, P. S. Controlling and Measuring the Interdependence of Local Properties in Biomembranes. *Langmuir* **2003**, *19* (5), 1618–1623. https://doi.org/10.1021/la026133a.
(68) Lefrançois, P.; Goudeau, B.; Arbault, S. Electroformation of Phospholipid Giant Unilamellar Vesicles in Physiological Phosphate Buffer. *Integr. Biol.* **2018**, *10* (7), 429–434. https://doi.org/10.1039/C8IB00074C.

(69) Landman, J.; Ouhajji, S.; Prévost, S.; Narayanan, T.; Groenewold, J.; Philipse, A. P.; Kegel, W. K.; Petukhov, A. V. Inward Growth by Nucleation: Multiscale Self-Assembly of Ordered Membranes. *Sci. Adv.* **2018**, *4* (6), eaat1817. https://doi.org/10.1126/sciadv.aat1817.
(70) Ilhan-Ayisigi, E.; Yaldiz, B.; Bor, G.; Yaghmur, A.; Yesil-Celiktas, O. Advances in Microfluidic Synthesis and Coupling with Synchrotron SAXS for Continuous Production and Real-Time Structural Characterization of Nano-Self-Assemblies. *Colloids Surf. B Biointerfaces* **2021**, *201*, 111633. https://doi.org/10.1016/j.colsurfb.2021.111633.
(71) Lim Soo, P.; Eisenberg, A. Preparation of Block Copolymer Vesicles in Solution. *J. Polym. Sci. Part B Polym. Phys.* **2004**, *42* (6), 923–938. https://doi.org/10.1002/polb.10739.
(72) Förster, S.; Zisenis, M.; Wenz, E.; Antonietti, M. Micellization of Strongly Segregated Block Copolymers. *J. Chem. Phys.* **1996**, *104* (24), 9956–9970. https://doi.org/10.1063/1.471723.
(73) Zhang, G.; Sun, J. Lipid in Chips: A Brief Review of Liposomes Formation by Microfluidics. *Int. J. Nanomedicine* **2021**, *Volume 16*, 7391–7416. https://doi.org/10.2147/IJN.S331639.
(74) Jabbari, V.; Banner, D. J.; Phakatkar, A. H.; Shahbazian-Yassar, R. Nucleation and Growth Visualization of Self-Assembled Polymeric Micelles/Vesicles Using in Situ Liquid Cell-TEM. *Microsc. Microanal.* **2020**, *26* (S2), 2576–2578. https://doi.org/10.1017/S1431927620022084.
(75) Iqbal, S.; Blenner, M.; Alexander-Bryant, A.; Larsen, J. Polymersomes for Therapeutic Delivery of Protein and Nucleic Acid Macromolecules: From Design to Therapeutic Applications. *Biomacromolecules* **2020**, *21* (4), 1327–1350. https://doi.org/10.1021/acs.biomac.9b01754.
(76) Thiermann, R.; Mueller, W.; Montesinos-Castellanos, A.; Metzke, D.; Löb, P.; Hessel, V.; Maskos, M. Size Controlled Polymersomes by Continuous Self-Assembly in Micromixers. *Polymer* **2012**, *53*, 2205–2210. https://doi.org/10.1016/j.polymer.2012.03.058.
(77) Sanson, C.; Schatz, C.; Le Meins, J.-F.; Brûlet, A.; Soum, A.; Lecommandoux, S. Biocompatible and Biodegradable Poly(Trimethylene Carbonate)-b-Poly(l-Glutamic Acid) Polymersomes: Size Control and Stability. *Langmuir* **2010**, *26* (4), 2751–2760. https://doi.org/10.1021/la902786t.
(78) Fessi, H.; Puisieux, F.; Devissaguet, J. Ph.; Ammoury, N.; Benita, S. Nanocapsule Formation by Interfacial Polymer Deposition Following Solvent Displacement. *Int. J. Pharm.* **1989**, *55* (1), R1–R4. https://doi.org/10.1016/0378-5173(89)90281-0.
(79) Barreras-Urbina, C. G.; Ramírez-Wong, B.; López-Ahumada, G. A.; Burruel-Ibarra, S. E.; Martínez-Cruz, O.; Tapia-Hernández, J. A.; Rodríguez Félix, F. Nano- and Micro-Particles by Nanoprecipitation: Possible Application in the Food and Agricultural Industries. *Int. J. Food Prop.* **2016**, *19* (9), 1912–1923. https://doi.org/10.1080/10942912.2015.1089279.
(80) Sanson, C.; Schatz, C.; Le Meins, J.-F.; Soum, A.; Thévenot, J.; Garanger, E.; Lecommandoux, S. A Simple Method to Achieve High Doxorubicin Loading in Biodegradable Polymersomes. *J. Control. Release Off. J. Control. Release Soc.* **2010**, *147* (3), 428–435. https://doi.org/10.1016/j.jconrel.2010.07.123.
(81) Zhou, J.; Ni, R.; Chau, Y. Polymeric Vesicle Formation via Temperature-Assisted Nanoprecipitation. *RSC Adv.* **2017**, *7* (29), 17997–18000. https://doi.org/10.1039/C7RA01959A.
(82) Lebleu, C. Polymersomes Based on PEG-b-PTMC towards Cell-Mediated Delivery of Nanomedicines. phdthesis, Université de Bordeaux, 2019. https://tel.archives-ouvertes.fr/tel-03463393 (accessed 2022-04-20).
(83) Pustulka, K. M.; Wohl, A. R.; Lee, H. S.; Michel, A. R.; Han, J.; Hoye, T. R.; McCormick, A. V.; Panyam, J.; Macosko, C. W. Flash Nanoprecipitation: Particle Structure and Stability. *Mol. Pharm.* **2013**, *10* (11), 4367–4377. https://doi.org/10.1021/mp400337f.
(84) Massella, D.; Celasco, E.; Salaün, F.; Ferri, A.; Barresi, A. A. Overcoming the Limits of Flash Nanoprecipitation: Effective Loading of Hydrophilic Drug into Polymeric Nanoparticles with Controlled Structure. *Polymers* **2018**, *10* (10), 1092. https://doi.org/10.3390/polym10101092.
(85) Zhu, Z. Flash Nanoprecipitation: Prediction and Enhancement of Particle Stability via Drug Structure. *Mol. Pharm.* **2014**, *11* (3), 776–786. https://doi.org/10.1021/mp500025e.
(86) Tao, J.; Chow, S. F.; Zheng, Y. Application of Flash Nanoprecipitation to Fabricate Poorly Water-Soluble Drug Nanoparticles. *Acta Pharm. Sin. B* **2019**, *9* (1), 4–18. https://doi.org/10.1016/j.apsb.2018.11.001.

(87) Pagendarm, H. M.; Stone, P. T.; Baljon, J. J.; Aziz, M. H.; Pastora, L. E.; Wilson, J. T. Flash Nanoprecipitation for the Production of Endosomolytic Polymersomes for Cytosolic Drug Delivery. ChemRxiv October 21, 2021. https://doi.org/10.26434/chemrxiv-2021-7jfp9.
(88) Hayward, R. C.; Utada, A. S.; Dan, N.; Weitz, D. A. Dewetting Instability during the Formation of Polymersomes from Block-Copolymer-Stabilized Double Emulsions. *Langmuir* **2006**, *22* (10), 4457–4461. https://doi.org/10.1021/la060094b.
(89) Pautot, S.; Frisken, B. J.; Weitz, D. A. Production of Unilamellar Vesicles Using an Inverted Emulsion. *Langmuir* **2003**, *19* (7), 2870–2879. https://doi.org/10.1021/la026100v.
(90) Kamat, N. P.; Lee, M. H.; Lee, D.; Hammer, D. A. Micropipette Aspiration of Double Emulsion-Templated Polymersomes. *Soft Matter* **2011**, *7* (21), 9863–9866. https://doi.org/10.1039/C1SM06282D.
(91) Peyret, A.; Ibarboure, E.; Le Meins, J.-F.; Lecommandoux, S. Asymmetric Hybrid Polymer–Lipid Giant Vesicles as Cell Membrane Mimics. *Adv. Sci.* **2018**, *5* (1), 1700453. https://doi.org/10.1002/advs.201700453.
(92) Whitesides, G. M. The Origins and the Future of Microfluidics. *Nature* **2006**, *442* (7101), 368–373. https://doi.org/10.1038/nature05058.
(93) Petit, J.; Polenz, I.; Baret, J.-C.; Herminghaus, S.; Bäumchen, O. Vesicles-on-a-Chip: A Universal Microfluidic Platform for the Assembly of Liposomes and Polymersomes. *Eur. Phys. J. E* **2016**, *39* (6), 59. https://doi.org/10.1140/epje/i2016-16059-8.
(94) Pilkington, C. P.; Seddon, J. M.; Elani, Y. Microfluidic Technologies for the Synthesis and Manipulation of Biomimetic Membranous Nano-Assemblies. *Phys. Chem. Chem. Phys.* **2021**, *23* (6), 3693–3706. https://doi.org/10.1039/D0CP06226J.
(95) Trantidou, T.; Friddin, M.; Salehi-Reyhani, A.; Ces, O.; Elani, Y. Droplet Microfluidics for the Construction of Compartmentalised Model Membranes. *Lab. Chip* **2018**, *18*. https://doi.org/10.1039/C8LC00028J.
(96) Whitesides, G. M.; Stroock, A. D. Flexible Methods for Microfluidics. *Phys. Today* **2001**, *54* (6), 42.
(97) Liu, Z.; Fontana, F.; Python, A.; Hirvonen, J. T.; Santos, H. A. Microfluidics for Production of Particles: Mechanism, Methodology, and Applications. *Small Weinh. Bergstr. Ger.* **2020**, *16* (9), e1904673. https://doi.org/10.1002/smll.201904673.
(98) Shum, H. C.; Lee, D.; Yoon, I.; Kodger, T.; Weitz, D. A. Double Emulsion Templated Monodisperse Phospholipid Vesicles. *Langmuir ACS J. Surf. Colloids* **2008**, *24* (15), 7651–7653. https://doi.org/10.1021/la801833a.
(99) Seo, H.; Lee, H. Recent Developments in Microfluidic Synthesis of Artificial Cell-like Polymersomes and Liposomes for Functional Bioreactors. *Biomicrofluidics* **2021**, *15* (2), 021301. https://doi.org/10.1063/5.0048441.
(100) Yousofvand, R.; Ghasemi, K. A Novel Microfluidic Device for Double Emulsion Formation: The Effects of Design Parameters on Droplet Production Performance. *Colloids Surf. Physicochem. Eng. Asp.* **2022**, *635*, 128059. https://doi.org/10.1016/j.colsurfa.2021.128059.
(101) Thiele, J.; Steinhauser, D.; Pfohl, T.; Förster, S. Preparation of Monodisperse Block Copolymer Vesicles via Flow Focusing in Microfluidics. *Langmuir* **2010**, *26* (9), 6860–6863. https://doi.org/10.1021/la904163v.
(102) Bonhomme, O. Étude de La Formation de Fibres En Microfluidique : Compétition Entre Mise En Forme et Gélification de Fluides Complexes Sous Écoulement. These de doctorat, Bordeaux 1, 2011. https://www.theses.fr/2011BOR14306 (accessed 2023-01-17).
(103) Jahn, A.; Stavis, S. M.; Hong, J. S.; Vreeland, W. N.; DeVoe, D. L.; Gaitan, M. Microfluidic Mixing and the Formation of Nanoscale Lipid Vesicles. *ACS Nano* **2010**, *4* (4), 2077–2087. https://doi.org/10.1021/nn901676x.
(104) Albuquerque, L. J. C.; Sincari, V.; Jäger, A.; Konefał, R.; Pánek, J.; Černoch, P.; Pavlova, E.; Štěpánek, P.; Giacomelli, F. C.; Jäger, E. Microfluidic-Assisted Engineering of Quasi-Monodisperse PH-Responsive Polymersomes toward Advanced Platforms for the Intracellular Delivery of Hydrophilic Therapeutics. *Langmuir* **2019**, acs.langmuir.9b01009. https://doi.org/10.1021/acs.langmuir.9b01009.

(105) Stroock, A. D.; Dertinger, S. K. W.; Ajdari, A.; Mezić, I.; Stone, H. A.; Whitesides, G. M. Chaotic Mixer for Microchannels. *Science* **2002**, *295* (5555), 647–651. https://doi.org/10.1126/science.1066238.

(106) Swaay, D. van; deMello, A. Microfluidic Methods for Forming Liposomes. *Lab. Chip* **2013**, *13* (5), 752–767. https://doi.org/10.1039/C2LC41121K.

(107) Streck, S.; Neumann, H.; Nielsen, H.; Rades, T.; McDowell, A. Comparison of Bulk and Microfluidics Methods for the Formulation of Poly-Lactic-Co-Glycolic Acid (PLGA) Nanoparticles Modified with Cell-Penetrating Peptides of Different Architectures. *Int. J. Pharm. X* **2019**, *1*, 100030. https://doi.org/10.1016/j.ijpx.2019.100030.

(108) Guo, P.; Huang, J.; Zhao, Y.; Martin, C. R.; Zare, R. N.; Moses, M. A. Nanomaterial Preparation by Extrusion through Nanoporous Membranes. *Small Weinh. Bergstr. Ger.* **2018**, *14* (18), e1703493. https://doi.org/10.1002/smll.201703493.

(109) Zhu, T. F.; Szostak, J. W. Preparation of Large Monodisperse Vesicles. *PloS One* **2009**, *4* (4), e5009. https://doi.org/10.1371/journal.pone.0005009.

(110) Parnell, A. J.; Tzokova, N.; Topham, P. D.; Adams, D. J.; Adams, S.; Fernyhough, C. M.; Ryan, A. J.; Jones, R. a. L. The Efficiency of Encapsulation within Surface Rehydrated Polymersomes. *Faraday Discuss.* **2009**, *143* (0), 29–46. https://doi.org/10.1039/B902574J.

(111) Patty, P. J.; Frisken, B. J. The Pressure-Dependence of the Size of Extruded Vesicles. *Biophys. J.* **2003**, *85* (2), 996–1004.

(112) Olson, F.; Hunt, C. A.; Szoka, F. C.; Vail, W. J.; Papahadjopoulos, D. Preparation of Liposomes of Defined Size Distribution by Extrusion through Polycarbonate Membranes. *Biochim. Biophys. Acta* **1979**, *557* (1), 9–23. https://doi.org/10.1016/0005-2736(79)90085-3.

(113) Men, Y.; Peng, F.; Tu, Y.; Hest, J. C. M. van; Wilson, D. A. Methods for Production of Uniform Small-Sized Polymersome with Rigid Membrane. *Polym. Chem.* **2016**, *7* (24), 3977–3982. https://doi.org/10.1039/C6PY00668J.

(114) Woodbury, D.; Grigg, A.; Welling, R.; Knudson, B. Reducing Liposome Size with Ultrasound: Bimodal Size Distributions. *J. Liposome Res.* **2006**, *16*, 57–80. https://doi.org/10.1080/08982100500528842.

(115) Silva, R.; Ferreira, H.; Little, C.; Cavaco-Paulo, A. Effect of Ultrasound Parameters for Unilamellar Liposome Preparation. *Ultrason. Sonochem.* **2010**, *17* (3), 628–632. https://doi.org/10.1016/j.ultsonch.2009.10.010.

(116) Pick, U. Liposomes with a Large Trapping Capacity Prepared by Freezing and Thawing of Sonicated Phospholipid Mixtures. *Arch. Biochem. Biophys.* **1981**, *212* (1), 186–194. https://doi.org/10.1016/0003-9861(81)90358-1.

(117) Sou, K.; Naito, Y.; Endo, T.; Takeoka, S.; Tsuchida, E. Effective Encapsulation of Proteins into Size-Controlled Phospholipid Vesicles Using Freeze-Thawing and Extrusion. *Biotechnol. Prog.* **2003**, *19* (5), 1547–1552. https://doi.org/10.1021/bp0201004.

(118) Sriwongsitanont, S.; Ueno, M. Effect of a PEG Lipid (DSPE-PEG2000) and Freeze-Thawing Process on Phospholipid Vesicle Size and Lamellarity. *Colloid Polym Sci* **2004**, *282*, 753–760. https://doi.org/10.1007/s00396-003-1015-x.

(119) Sriwongsitanont, S.; Ueno, M. Effect of Freeze-Thawing and Polyethylene Glycol (PEG) Lipid on Fusion and Fission of Phospholipid Vesicles. *Chem. Pharm. Bull. (Tokyo)* **2004**, *52* (5), 641–642. https://doi.org/10.1248/cpb.52.641.

(120) Anzai, K.; Yoshida, M.; Kirino, Y. Change in Intravesicular Volume of Liposomes by Freeze-Thaw Treatment as Studied by the ESR Stopped-Flow Technique. *Biochim. Biophys. Acta BBA - Biomembr.* **1990**, *1021* (1), 21–26. https://doi.org/10.1016/0005-2736(90)90378-2.

(121) Mai, Y.; Eisenberg, A. Self-Assembly of Block Copolymers. *Chem. Soc. Rev.* **2012**, *41* (18), 5969–5985. https://doi.org/10.1039/C2CS35115C.

(122) Yu, Y.; Zhang, L.; Eisenberg, A. Morphogenic Effect of Solvent on Crew-Cut Aggregates of Apmphiphilic Diblock Copolymers. *Macromolecules* **1998**, *31* (4), 1144–1154. https://doi.org/10.1021/ma971254g.

(123) Desbaumes, L.; Eisenberg, A. Single-Solvent Preparation of Crew-Cut Aggregates of Various Morphologies from an Amphiphilic Diblock Copolymer. *Langmuir* **1999**, *15* (1), 36–38. https://doi.org/10.1021/la980632n.

(124) Galindo-Rodriguez, S.; Allémann, E.; Fessi, H.; Doelker, E. Physicochemical Parameters Associated with Nanoparticle Formation in the Salting-out, Emulsification-Diffusion, and Nanoprecipitation Methods. *Pharm. Res.* **2004**, *21* (8), 1428–1439. https://doi.org/10.1023/b:pham.0000036917.75634.be.

(125) Anraku, Y.; Kishimura, A.; Oba, M.; Yamasaki, Y.; Kataoka, K. Spontaneous Formation of Nanosized Unilamellar Polyion Complex Vesicles with Tunable Size and Properties. *J. Am. Chem. Soc.* **2010**, *132* (5), 1631–1636. https://doi.org/10.1021/ja908350e.

(126) Zhang, L.; Eisenberg, A. Morphogenic Effect of Added Ions on Crew-Cut Aggregates of Polystyrene-b-Poly(Acrylic Acid) Block Copolymers in Solutions. *Macromolecules* **1996**, *29* (27), 8805–8815. https://doi.org/10.1021/ma961376t.

(127) Zhang, L.; Eisenberg, A. Multiple Morphologies and Characteristics of "Crew-Cut" Micelle-like Aggregates of Polystyrene-b-Poly(Acrylic Acid) Diblock Copolymers in Aqueous Solutions. *J. Am. Chem. Soc.* **1996**, *118* (13), 3168–3181. https://doi.org/10.1021/ja953709s.

(128) Hickey, R. J.; Koski, J.; Meng, X.; Riggleman, R. A.; Zhang, P.; Park, S.-J. Size-Controlled Self-Assembly of Superparamagnetic Polymersomes. *ACS Nano* **2014**, *8* (1), 495–502. https://doi.org/10.1021/nn405012h.

(129) Ahmed, F.; Pakunlu, R. I.; Srinivas, G.; Brannan, A.; Bates, F.; Klein, M. L.; Minko, T.; Discher, D. E. Shrinkage of a Rapidly Growing Tumor by Drug-Loaded Polymersomes: PH-Triggered Release through Copolymer Degradation. *Mol. Pharm.* **2006**, *3* (3), 340–350. https://doi.org/10.1021/mp050103u.

(130) Immordino, M. L.; Brusa, P.; Arpicco, S.; Stella, B.; Dosio, F.; Cattel, L. Preparation, Characterization, Cytotoxicity and Pharmacokinetics of Liposomes Containing Docetaxel. *J. Control. Release Off. J. Control. Release Soc.* **2003**, *91* (3), 417–429. https://doi.org/10.1016/s0168-3659(03)00271-2.

(131) Chandrawati, R.; Caruso, F. Biomimetic Liposome- and Polymersome-Based Multicompartmentalized Assemblies. *Langmuir* **2012**, *28* (39), 13798–13807. https://doi.org/10.1021/la301958v.

(132) Che, H.; Hest, J. C. M. van. Stimuli-Responsive Polymersomes and Nanoreactors. *J. Mater. Chem. B* **2016**, *4* (27), 4632–4647. https://doi.org/10.1039/C6TB01163B.

(133) Danafar, H.; Rostamizadeh, K.; Davaran, S.; Hamidi, M. PLA-PEG-PLA Copolymer-Based Polymersomes as Nanocarriers for Delivery of Hydrophilic and Hydrophobic Drugs: Preparation and Evaluation with Atorvastatin and Lisinopril. *Drug Dev. Ind. Pharm.* **2014**, *40* (10), 1411–1420. https://doi.org/10.3109/03639045.2013.828223.

(134) Chen, W.; Meng, F.; Cheng, R.; Zhong, Z. PH-Sensitive Degradable Polymersomes for Triggered Release of Anticancer Drugs: A Comparative Study with Micelles. *J. Control. Release Off. J. Control. Release Soc.* **2010**, *142* (1), 40–46. https://doi.org/10.1016/j.jconrel.2009.09.023.

(135) Sun, B.; Chiu, D. T. Determination of the Encapsulation Efficiency of Individual Vesicles Using Single-Vesicle Photolysis and Confocal Single-Molecule Detection. *Anal. Chem.* **2005**, *77* (9), 2770–2776. https://doi.org/10.1021/ac048439n.

(136) Liu, G.-Y.; Lv, L.-P.; Chen, C.-J.; Liu, X.-S.; Hu, X.-F.; Ji, J. Biocompatible and Biodegradable Polymersomes for PH-Triggered Drug Release. *Soft Matter* **2011**, *7* (14), 6629–6636. https://doi.org/10.1039/C1SM05308F.

(137) Messager, L.; Gaitzsch, J.; Chierico, L.; Battaglia, G. Novel Aspects of Encapsulation and Delivery Using Polymersomes. *Curr. Opin. Pharmacol.* **2014**, *18*, 104–111. https://doi.org/10.1016/j.coph.2014.09.017.

(138) Colley, H. E.; Hearnden, V.; Avila-Olias, M.; Cecchin, D.; Canton, I.; Madsen, J.; MacNeil, S.; Warren, N.; Hu, K.; McKeating, J. A.; Armes, S. P.; Murdoch, C.; Thornhill, M. H.; Battaglia, G. Polymersome-Mediated Delivery of Combination Anticancer Therapy to Head and Neck Cancer

Cells: 2D and 3D *in Vitro* Evaluation. *Mol. Pharm.* **2014**, *11* (4), 1176–1188. https://doi.org/10.1021/mp400610b.

(139) Choucair, A.; Lim Soo, P.; Eisenberg, A. Active Loading and Tunable Release of Doxorubicin from Block Copolymer Vesicles. *Langmuir* **2005**, *21* (20), 9308–9313. https://doi.org/10.1021/la050710o.

(140) Mayer, L. D.; Bally, M. B.; Cullis, P. R. Uptake of Adriamycin into Large Unilamellar Vesicles in Response to a PH Gradient. *Biochim. Biophys. Acta* **1986**, *857* (1), 123–126. https://doi.org/10.1016/0005-2736(86)90105-7.

(141) Abraham, S.; McKenzie, C.; Masin, D.; Ng, R.; Harasym, T.; Mayer, L.; Bally, M. In Vitro and in Vivo Characterization of Doxorubicin and Vincristine Coencapsulated within Liposomes through Use of Transition Metal Ion Complexation and PH Gradient Loading. *Clin. Cancer Res. Off. J. Am. Assoc. Cancer Res.* **2004**, *10*, 728–738. https://doi.org/10.1158/1078-0432.CCR-1131-03.

(142) Madden, T. D.; Harrigan, P. R.; Tai, L. C.; Bally, M. B.; Mayer, L. D.; Redelmeier, T. E.; Loughrey, H. C.; Tilcock, C. P.; Reinish, L. W.; Cullis, P. R. The Accumulation of Drugs within Large Unilamellar Vesicles Exhibiting a Proton Gradient: A Survey. *Chem. Phys. Lipids* **1990**, *53* (1), 37–46. https://doi.org/10.1016/0009-3084(90)90131-a.

(143) Nichols, J. W.; Deamer, D. W. Catecholamine Uptake and Concentration by Liposomes Maintaining p/ Gradients. *Biochim. Biophys. Acta* **1976**, *455* (1), 269–271. https://doi.org/10.1016/0005-2736(76)90169-3.

(144) Mayer, L. D.; Bally, M. B.; Hope, M. J.; Cullis, P. R. Uptake of Antineoplastic Agents into Large Unilamellar Vesicles in Response to a Membrane Potential. *Biochim. Biophys. Acta* **1985**, *816* (2), 294–302. https://doi.org/10.1016/0005-2736(85)90497-3.

(145) Ahmed, F.; Pakunlu, R. I.; Brannan, A.; Bates, F.; Minko, T.; Discher, D. E. Biodegradable Polymersomes Loaded with Both Paclitaxel and Doxorubicin Permeate and Shrink Tumors, Inducing Apoptosis in Proportion to Accumulated Drug. *J. Control. Release Off. J. Control. Release Soc.* **2006**, *116* (2), 150–158. https://doi.org/10.1016/j.jconrel.2006.07.012.

(146) Mayer, L. D.; Tai, L. C.; Bally, M. B.; Mitilenes, G. N.; Ginsberg, R. S.; Cullis, P. R. Characterization of Liposomal Systems Containing Doxorubicin Entrapped in Response to PH Gradients. *Biochim. Biophys. Acta* **1990**, *1025* (2), 143–151. https://doi.org/10.1016/0005-2736(90)90091-2.

(147) Maurer, N.; Fenske, D. B.; Cullis, P. R. Developments in Liposomal Drug Delivery Systems. *Expert Opin. Biol. Ther.* **2001**, *1* (6), 923–947. https://doi.org/10.1517/14712598.1.6.923.

(148) Fritze, A.; Hens, F.; Kimpfler, A.; Schubert, R.; Peschka-Süss, R. Remote Loading of Doxorubicin into Liposomes Driven by a Transmembrane Phosphate Gradient. *Biochim. Biophys. Acta BBA - Biomembr.* **2006**, *1758* (10), 1633–1640. https://doi.org/10.1016/j.bbamem.2006.05.028.

(149) Haran, G.; Cohen, R.; Bar, L. K.; Barenholz, Y. Transmembrane Ammonium Sulfate Gradients in Liposomes Produce Efficient and Stable Entrapment of Amphipathic Weak Bases. *Biochim. Biophys. Acta* **1993**, *1151* (2), 201–215. https://doi.org/10.1016/0005-2736(93)90105-9.

(150) Cheung, B. C.; Sun, T. H.; Leenhouts, J. M.; Cullis, P. R. Loading of Doxorubicin into Liposomes by Forming Mn2+-Drug Complexes. *Biochim. Biophys. Acta* **1998**, *1414* (1–2), 205–216. https://doi.org/10.1016/s0005-2736(98)00168-0.

(151) Abraham, S. A.; Edwards, K.; Karlsson, G.; MacIntosh, S.; Mayer, L. D.; McKenzie, C.; Bally, M. B. Formation of Transition Metal-Doxorubicin Complexes inside Liposomes. *Biochim. Biophys. Acta* **2002**, *1565* (1), 41–54. https://doi.org/10.1016/s0005-2736(02)00507-2.

(152) Bolotin, E.; Cohen, R.; Bar, L.; Emanuel, N.; Ninio, S.; Barenholz, Y.; Lasic, D. Ammonium Sulfate Gradients for Efficient and Stable Remote Loading of Amphipathic Weak Bases into Liposomes and Ligandoliposomes. *J. Liposome Res.* **2008**, *4*, 455–479. https://doi.org/10.3109/08982109409037057.

(153) Li, X.; Cabral-Lilly, D.; Janoff, A.; Perkins, W. Complexation of Internalized Doxorubicin into Fiber Bundles Affects Its Release Rate from Liposomes. *J. Liposome Res. - J LIPOSOME RES* **2000**, *10*, 15–27. https://doi.org/10.3109/08982100009031092.

(154) Nordström, R.; Zhu, L.; Härmark, J.; Levi-Kalisman, Y.; Koren, E.; Barenholz, Y.; Levinton, G.; Shamrakov, D. Quantitative Cryo-TEM Reveals New Structural Details of Doxil-Like PEGylated

Liposomal Doxorubicin Formulation. *Pharmaceutics* **2021**, *13* (1), 123. https://doi.org/10.3390/pharmaceutics13010123.

(155) Andriyanov, A.; Koren, E.; Barenholz, Y.; Goldberg, S. Therapeutic Efficacy of Combining PEGylated Liposomal Doxorubicin and Radiofrequency (RF) Ablation: Comparison between Slow-Drug-Releasing, Non-Thermosensitive and Fast-Drug-Releasing, Thermosensitive Nano-Liposomes. *PloS One* **2014**, *9*, e92555. https://doi.org/10.1371/journal.pone.0092555.

(156) Wibroe, P.; Ahmadvand, D.; Oghabian, M.; Yaghmur, A.; Moghimi, S. An Integrated Assessment of Morphology, Size, and Complement Activation of the PEGylated Liposomal Doxorubicin Products Doxil®, Caelyx®, DOXOrubicin, and SinaDoxosome. *J. Control. Release Off. J. Control. Release Soc.* **2015**, *221*. https://doi.org/10.1016/j.jconrel.2015.11.021.

(157) Onaca, O.; Enea, R.; Hughes, D. W.; Meier, W. Stimuli-Responsive Polymersomes as Nanocarriers for Drug and Gene Delivery. *Macromol. Biosci.* **2009**, *9* (2), 129–139. https://doi.org/10.1002/mabi.200800248.

(158) Oliveira, H.; Thevenot, J.; Lecommandoux, S. Smart Polymersomes for Therapy and Diagnosis: Fast Progress toward Multifunctional Biomimetic Nanomedicines. *Wiley Interdiscip. Rev. Nanomed. Nanobiotechnol.* **2012**, *4*, 525–546. https://doi.org/10.1002/wnan.1183.

(159) Jang, W.-S.; Park, S. C.; Reed, E. H.; Dooley, K. P.; Wheeler, S. F.; Lee, D.; Hammer, D. A. Enzymatically Triggered Rupture of Polymersomes. *Soft Matter* **2016**, *12* (4), 1014–1020. https://doi.org/10.1039/C5SM01881A.

(160) Lee, J. S.; Groothuis, T.; Cusan, C.; Mink, D.; Feijen, J. Lysosomally Cleavable Peptide-Containing Polymersomes Modified with Anti-EGFR Antibody for Systemic Cancer Chemotherapy. *Biomaterials* **2011**, *32* (34), 9144–9153. https://doi.org/10.1016/j.biomaterials.2011.08.036.

(161) Wang, S.; Chen, Z.-R. Fluorescence Lifetime-Based Sensing of Polymersome Leakage. *Photochem. Photobiol. Sci.* **2017**, *16* (2), 155–158. https://doi.org/10.1039/C6PP00296J.

(162) Zou, Y.; Meng, F.; Deng, C.; Zhong, Z. Robust, Tumor-Homing and Redox-Sensitive Polymersomal Doxorubicin: A Superior Alternative to Doxil and Caelyx? *J. Control. Release Off. J. Control. Release Soc.* **2016**, *239*. https://doi.org/10.1016/j.jconrel.2016.08.022.

(163) Cerritelli, S.; Velluto, D.; Hubbell, J. A. PEG-SS-PPS: Reduction-Sensitive Disulfide Block Copolymer Vesicles for Intracellular Drug Delivery. *Biomacromolecules* **2007**, *8* (6), 1966–1972. https://doi.org/10.1021/bm070085x.

(164) Cheng, R.; Meng, F.; Ma, S.; Xu, H.; Liu, H.; Jing, X.; Zhong, Z. Reduction and Temperature Dual-Responsive Crosslinked Polymersomes for Targeted Intracellular Protein Delivery. *J. Mater. Chem.* **2011**, *21* (47), 19013–19020. https://doi.org/10.1039/C1JM13536H.

(165) Ulbrich, K.; Subr, V. Polymeric Anticancer Drugs with PH-Controlled Activation. *Adv. Drug Deliv. Rev.* **2004**, *56* (7), 1023–1050. https://doi.org/10.1016/j.addr.2003.10.040.

(166) Quadir, M. A.; Morton, S. W.; Deng, Z. J.; Shopsowitz, K. E.; Murphy, R. P.; Epps, T. H.; Hammond, P. T. PEG–Polypeptide Block Copolymers as PH-Responsive Endosome-Solubilizing Drug Nanocarriers. *Mol. Pharm.* **2014**, *11* (7), 2420–2430. https://doi.org/10.1021/mp500162w.

(167) Engler, A. C.; Bonner, D. K.; Buss, H. G.; Cheung, E. Y.; Hammond, P. T. The Synthetic Tuning of Clickable PH Responsive Cationic Polypeptides and Block Copolypeptides. *Soft Matter* **2011**, *7* (12), 5627–5637. https://doi.org/10.1039/C1SM05064H.

(168) Liu, F.; Kozlovskaya, V.; Medipelli, S.; Xue, B.; Ahmad, F.; Saeed, M.; Cropek, D.; Kharlampieva, E. Temperature-Sensitive Polymersomes for Controlled Delivery of Anticancer Drugs. *Chem. Mater.* **2015**, *27* (23), 7945–7956. https://doi.org/10.1021/acs.chemmater.5b03048.

(169) Kozlovskaya, V.; Liu, F.; Yang, Y.; Ingle, K.; Qian, S.; Halade, G. V.; Urban, V. S.; Kharlampieva, E. Temperature-Responsive Polymersomes of Poly(3-Methyl-N-Vinylcaprolactam)-Block-Poly(N-Vinylpyrrolidone) To Decrease Doxorubicin-Induced Cardiotoxicity. *Biomacromolecules* **2019**, *20* (10), 3989–4000. https://doi.org/10.1021/acs.biomac.9b01026.

(170) Bixner, O.; Kurzhals, S.; Virk, M.; Reimhult, E. Triggered Release from Thermoresponsive Polymersomes with Superparamagnetic Membranes. *Materials* **2016**, *9* (1), 29. https://doi.org/10.3390/ma9010029.

(171) Xu, H.; Meng, F.; Zhong, Z. Reversibly Crosslinked Temperature-Responsive Nano-Sized Polymersomes: Synthesis and Triggered Drug Release. *J. Mater. Chem.* **2009**, *19* (24), 4183–4190. https://doi.org/10.1039/B901141B.

(172) Li, W.-P.; Su, C.-H.; Chang, Y.-C.; Lin, Y.-J.; Yeh, C.-S. Ultrasound-Induced Reactive Oxygen Species Mediated Therapy and Imaging Using a Fenton Reaction Activable Polymersome. *ACS Nano* **2016**, *10* (2), 2017–2027. https://doi.org/10.1021/acsnano.5b06175.

(173) Wei, P.; Sun, M.; Yang, B.; Xiao, J.; Du, J. Ultrasound-Responsive Polymersomes Capable of Endosomal Escape for Efficient Cancer Therapy. *J. Control. Release Off. J. Control. Release Soc.* **2020**, *322*, 81–94. https://doi.org/10.1016/j.jconrel.2020.03.013.

(174) Wei, P.; Cornel, E. J.; Du, J. Ultrasound-Responsive Polymer-Based Drug Delivery Systems. *Drug Deliv. Transl. Res.* **2021**, *11* (4), 1323–1339. https://doi.org/10.1007/s13346-021-00963-0.

(175) Chen, W.; Du, J. Ultrasound and PH Dually Responsive Polymer Vesicles for Anticancer Drug Delivery. *Sci. Rep.* **2013**, *3* (1), 2162. https://doi.org/10.1038/srep02162.

(176) Sanson, C.; Diou, O.; Thévenot, J.; Ibarboure, E.; Soum, A.; Brûlet, A.; Miraux, S.; Thiaudière, E.; Tan, S.; Brisson, A.; Dupuis, V.; Sandre, O.; Lecommandoux, S. Doxorubicin Loaded Magnetic Polymersomes: Theranostic Nanocarriers for MR Imaging and Magneto-Chemotherapy. *ACS Nano* **2011**, *5* (2), 1122–1140. https://doi.org/10.1021/nn102762f.

(177) Oliveira, H.; Pérez-Andrés, E.; Thevenot, J.; Sandre, O.; Berra, E.; Lecommandoux, S. Magnetic Field Triggered Drug Release from Polymersomes for Cancer Therapeutics. *J. Control. Release Off. J. Control. Release Soc.* **2013**, *169*. https://doi.org/10.1016/j.jconrel.2013.01.013.

(178) Ryzhkov, A.; Raikher, Y. Size-Dependent Properties of Magnetosensitive Polymersomes: Computer Modelling. *Sensors* **2019**, *19* (23), 5266. https://doi.org/10.3390/s19235266.

(179) Liu, J. F.; Jang, B.; Issadore, D.; Tsourkas, A. Use of Magnetic Fields and Nanoparticles to Trigger Drug Release and Improve Tumor Targeting. *Wiley Interdiscip. Rev. Nanomed. Nanobiotechnol.* **2019**, *11* (6), e1571. https://doi.org/10.1002/wnan.1571.

(180) Beaute, L. Single synthetic cell microreactor for the fundamental understanding of NOS enzymatic activity and its implication in system biology. 280.

(181) Kamat, N. P.; Robbins, G. P.; Rawson, J. S.; Therien, M. J.; Dmochowski, I. J.; Hammer, D. A. A Generalized System for Photo-Responsive Membrane Rupture in Polymersomes. *Adv. Funct. Mater.* **2010**, *20* (16), 2588–2596. https://doi.org/10.1002/adfm.201000659.

(182) Mabrouk, E.; Cuvelier, D.; Brochard-Wyart, F.; Nassoy, P.; Li, M.-H. Bursting of Sensitive Polymersomes Induced by Curling. *Proc. Natl. Acad. Sci. U. S. A.* **2009**, *106* (18), 7294–7298. https://doi.org/10.1073/pnas.0813157106.

(183) Amstad, E.; Kim, S.-H.; Weitz, D. A. Photo- and Thermoresponsive Polymersomes for Triggered Release. *Angew. Chem. Int. Ed Engl.* **2012**, *51* (50), 12499–12503. https://doi.org/10.1002/anie.201206531.

(184) Beauté, L.; McClenaghan, N.; Lecommandoux, S. Photo-Triggered Polymer Nanomedicines: From Molecular Mechanisms to Therapeutic Applications. *Adv. Drug Deliv. Rev.* **2019**, *138*, 148–166. https://doi.org/10.1016/j.addr.2018.12.010.

(185) Hou, W.; Liu, R.; Bi, S.; He, Q.; Wang, H.; Gu, J. Photo-Responsive Polymersomes as Drug Delivery System for Potential Medical Applications. *Molecules* **2020**, *25* (21), 5147. https://doi.org/10.3390/molecules25215147.

Chapter II.

Microfluidic-assisted self-assembly of polymersomes: *in vitro/in vivo* “ready to use” method with size control

Table of contents

Introduction **79**

1. Experimental section **80**
1.1. Materials 80
1.2. Methods 80

2. Study of parameters for PEG-*b*-PTMC microfluidic-assisted self-assembly **85**
2.1. Effect of osmotic pressure on vesicles 85
2.2. Organic solvents choice towards *in vitro / in vivo* experiments 87
2.3. Nucleation of self-assembly system: critical water content assays 88

3. Microfluidic assisted self-assembly processes **92**
3.1. Microfluidic chip design 92
3.2. Optimization of the organic / aqueous solvent ratio in micromixer chip 95
3.3. Optimization of the organic / aqueous solvent ratio in Herringbone chip 98

4. Fine tuning vesicle size with microfluidic parameters **100**
4.1. Variation of initial copolymer concentration 100
4.2. Variation of total flow rate as a way to influence solvents mixing speed 103
4.3. Impact on solvent removal conditions on vesicle formation 105
4.4. Measuring mixing time in microfluidic chips 106

5. Conclusion **111**

6. Appendix **113**
6.1. Viscosity and refractive index of DMSO/PBS and Acetone/Glucose mixtures 113
6.2. Solubility Parameters 114
6.3. Scattered intensity of 100 nm latex under several stirring rate 117
6.4. Multi-Angle Light Scattering, calculations and methods 118
6.5. Dynamic light scattering 124
6.6. Multi Angle Light scattering 126

7. References **131**

Introduction

In recent years, polymers for drug delivery have been investigated for their ability to be used as drug carriers.[1–4] Among all the nanoparticles formed from polymer and drug, polymersomes have encountered a wide interest as they presented the ability to load both hydrophilic and hydrophobic drug. They also presented better mechanical properties than liposomes, leading to an increased circulation time and less premature leakage[3,5]. As described in Chapter 1.I.1-2, polymersomes have been developed to be more and more efficient, gaining the ability to escape body clearance[6–9] and to be able to release loaded drug at a desired location and time. [10,11]

In a previous work, Coralie Lebleu investigated the self-assembly of an amphiphilic copolymer: PEG_n-*b*-$PTMC_m$ (poly(ethylene glycol)-*block*-poly(trimethylene carbonate)). This type of biocompatible and biodegradable polymer has been demonstrated to be highly interesting for biomaterials design, due to their low toxicity, biodegradability and potential functionality.[12–16] Study was focused on obtaining polymersomes from PEG_n-*b*-$PTMC_m$. To do so, several compositions of block copolymer were synthetized to identify a composition forming vesicles prior to micelles or wormlike micelles.[16,17] As mentioned in Ch1.I.1, PEG fraction is a key parameter influencing the type of colloidal system obtained after self-assembly[18,19]. Ideal PEG fraction was identified as being around 16 wt% for PEG-*b*-PTMC. Starting from this point, this chapter focuses on using PEG_n-*b*-$PTMC_m$ with this ideal PEG fraction. A copolymer was synthetized by ring opening polymerization as previously described: PEG_{22}-*b*-$PTMC_{51}$.[16]

As described in Chapter 1.II., multiples processes can be used to produce vesicles.[20–26] Most of them present the disadvantage of producing vesicles with a low control over size and dispersity. To overcome these drawbacks, microfluidic processes were developed to produce either micron-size vesicles or nano-size vesicles with a good control over size and dispersity (Ch 1.II.3.d).[24,27–30] Aiming to produce vesicles with a low dispersity, we used microfluidic assisted self-assembly to produce our vesicles.

This chapter particularly focuses on studying parameters allowing to produce vesicle suspension ready to use both *in vitro* and *in vivo*, with a fine tuning of the size of produced vesicles. Indeed, as described in Ch 1.II.1, the size of vesicle plays an important role in biodistribution profile by tuning the half-life of vesicles according to their size[31,32]. The influence of organic and aqueous solvent, the influence of mixing strategies using two distinct microfluidic devices (Micromixer and Herringbone) and the impact of flow rate and copolymer concentration will be studied in detail.

1. Experimental section

1.1. Materials

Solvents: Dimethylsulfoxide (DMSO) was purchased from Sigma-Aldrich, Acetonitrile from Fischer Chemicals, Tetrahydrofuran (THF) from Thermo Scientific and Acetone from Acros Organics.

Aqueous solutions: PBS 10x was purchased from Euromedex and diluted ten times to obtain PBS 1x. Glucose and Sucrose were purchased from Sigma-Aldrich and solubilized in osmosis water.
pH and osmolarity of aqueous solution were adjusted using a pH meter *inoLab® pH 730 WTW* and an osmometer *Löser automatic TypM 10-25µL*, to reach pH=7.4 ± 0.1 and an osmolarity of 300 ± 4 mOsm.L^{-1}.

Amphiphilic block copolymer synthesis: PEG_{22}-*b*-$PTMC_{51}$ was synthetized by ring-opening polymerization of TMC using MeO-PEG_n-OH as macroinitiator (f_{PEG}=16.1%, D = 1.04, M_n=6200 g.mol^{-1}). This synthesis was already reported by Coralie Lebleu[17] and was performed by Pierre Lalanne.

TEM staining agents: Samarium Acetate was purchased from Sigma-Aldrich, Phototungstic acid from Acros Organics, Uranyl Acetate from from TAAB, Uranyless from em-grade.com.

1.2. Methods

Microfluidic system: Dolomite microfluidics system was used to induce microfluidic assisted self-assembly of PEG_{22}-*b*-$PTMC_{51}$. The system is composed of two Mitos pressure pumps (3200175) equipped with flowmeters (3200097) allowing flows to run in a micromixer chip of 12 mixing stages (3200401), connection is ensured by ethylene propylene tubing (1/16" x 0.25 mm, 3200063). All DMSO solutions were filtered with Polytetrafluoroethylene (PTFE) syringe filter of 0.45 µm, acetone solutions were filtered with Nylon syringe filter of 0.45 µm and aqueous solution were filtered with Cellulose Acetate (CA) syringe filters of 0.22 µm. Additional filters were also connected at pump outlets, between pumps and chip. Pump containing organic solution was connected to first and third inputs using a T-connector. Aqueous solvent pump being connected directly to second input of the chip. Camera was used to ensure that chip is dust and air bubble free before sample production. Under nitrogen pressure, flow rates were controlled using Mitos Flow Control Center 2.5.17 software. As water is already a solvent entered in the software, water calibration was used. For organic solvent (DMSO and Acetone), specific solvent calibrations were performed.

Fluid calibration: To obtain a calibration curve for each organic solvent, both pumps were filled with the solvent of interest. *Mineral oil* was used as fluid calibration on Mitos Flow Control Center 2.5.17 software. Flow rates from 30 to 800 µL.min^{-1} were set in each pump simultaneously. 3 mL of solvent were collected at the outlet of the chip. Weight of collected solvent was then measured. Volume of solvent obtained was calculated from the solvent mass using solvent density at 25°C (Acetone: 0.7789, DMSO: 1.095). Obtained flow rates were plotted versus expected flow rates and a linear regression was obtained (with R^2 = 0.99). The leading coefficient of the linear regression was used to modify the flow rate of the organic pump. For DMSO, the obtained flow rates were 0.71 times lower than expected and for acetone, flow rates obtained were 1.16 times higher than expected using *mineral oil* as fluid

calibration in the software. These coefficients will be used to obtained desired flow rates in the following experiments. Figure 1 shows calibration curves obtained from this method.

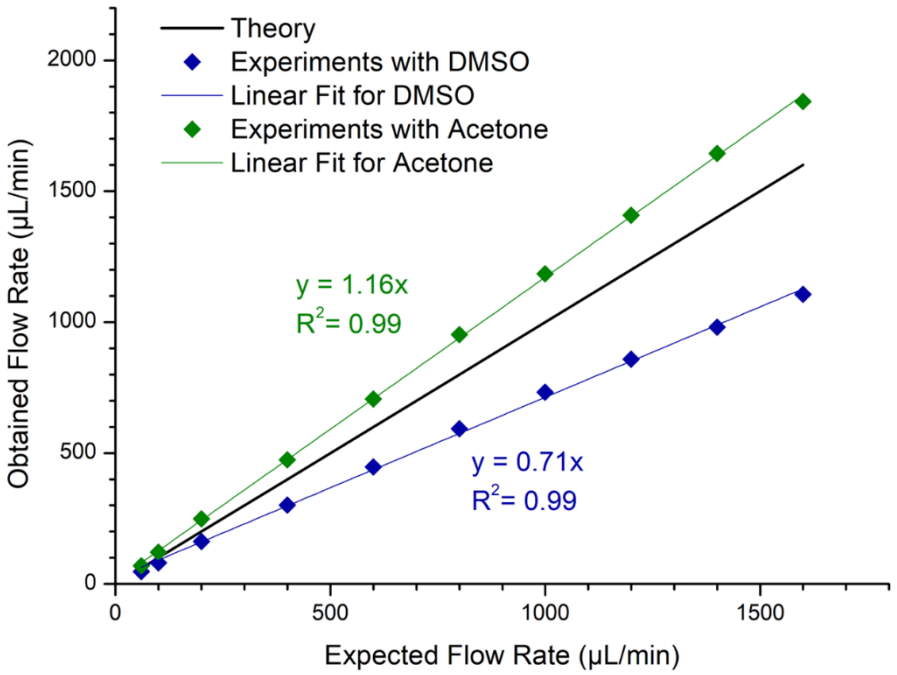

***Figure 1**: Calibration curves and linear regression obtained for organic solvents (DMSO in blue and Acetone in green) using microfluidic system composed of a micromixer chip, two Mitos pumps and Mineral Oil calibration on Mitos Flow Control Center 2.5.17 software.*

Herringbone microfluidic chip: Herringbone chip (from Darwin Microfluidics) was used to induce copolymer self-assembly. Harvard Apparatus 33 Syringe Pump Dual Infuse was used to control flow rates. Syringe driver and chip were connected with fluorinated ethylene propylene tubing (1/16" x 0.25mm, 3200063). The accuracy of flow rates delivered by the syringe driver was verified within a specific range of flow rates studied.

PDMS Chip: Polydimethylsiloxane (PDMS) reproduction of the glass herringbone chip from Darwin Microfluidics was done by photolithography. Masks and a UV curing resin were used to produce a negative of the channel to cast PDMS chip on top of it. Briefly, two masks were drawn using CleWin3 software. The first mask represents the main channel, and the second mask only shows the asymmetric chevrons, typical of the herringbone chip, as shown in Figure 2. The main channel has a dimension of 200 µm in width and 3.1 cm in length. A "drop" shape was designed in the first mask, allowing to have 2 inlets one inlet dedicated for the first solvent which is divided in two channels so that the two flows coming from the first solvent surround the single flow coming from the second solvent at the beginning of the straight channel. Asymmetric chevrons have a dimension of 50 µm in width, separated by a distance of 50 µm. They form a 45° angle with the main channel and have an arrow shape which tip is located at 1/3 of main channel's width. Every 6 steps, asymmetry changes for the tip to be at 1/3 at the other side of the main channel as shown in figure 2. 12 septs represent a mixing unit, the entire chip is composed of 15 mixing units. Photomasks are produced by Artnet Pro company.

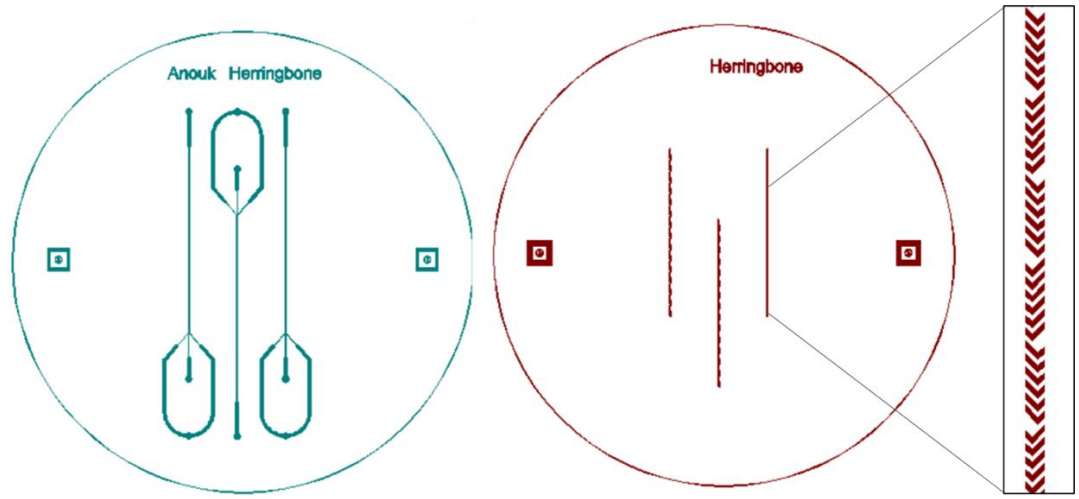

Figure 2: *Masks representation made with Clewin3 software. (Left) Main channel (Right) asymmetric chevrons forming one mixing chamber. Masks are used to obtain a negative photolithography of the PDMS herringbone chip.*

We aimed to reproduce the glass herringbone chip with following dimensions: 80 µm canal depth and 30 µm step depth. SU-8 3050 resin from Microchem was spin coated at 2000 rpm on a silica wafer. Resin was then soft-baked at 95 °C for 30 min on a hotplate. Mask of main channel was placed between wafer and UV light and UV was turned on during 10 s at 25 mW. Resin underwent a post exposure bake at 95 °C for 5 min. Without washing uncured resin, SU-8 3025 resin from Microchem was spin coated on top of the first layer at 3000 rpm and soft-baked at 95 °C for 14 min. Resin was then exposed to UV light through the mask of the steps for 8 s at 25 mW. Resin was post-baked during 5 min at 95 °C. Wafer was then immersed in a bath of *PGMEA* (propylene glycol methyl ether acetate) for 12 min to withdraw uncured resin. Wafer was then rinsed with isopropanol and dried. It underwent a plasma treatment before being exposed to hexamethyldisilazane vapors. This treatment helps to demold PDMS once cured.

Channel and steps depth were measured using an optical profilometer SNeox from Sensofar, doing an acquisition in wave optics, with the interferometric mode. We obtained a channel depth of 78,6 µm (for 80 µm targeted) and step depth of 37 µm (for 30 µm targeted). Figure 3 shows wafer on top of which the negative chip is built.

***Figure 3**: Silica wafer on top of which herringbone pattern has been created using UV curing resin in order to be used as a negative for PDMS chip.*

This wafer was then placed in a petri dish and a mixture of homogenized and degassed SYLGARD™ 184 Silicone Elastomer Base and 10 %wt of SYLGARD™ 184 Silicone elastomer curing agent was poured on top of the wafer. PDMS was let to cross-linked during 1h30 at 65 °C. Cured PDMS was demolded from wafer. Holes were dug to create inputs and outputs of the chip. PDMS underwent plasma treatment to allow it sticking to the glass plate that will forms the bottom of the chip. PDMS on glass was put few hours at 65 °C and final PDMS chip obtained is shown in Figure 4.

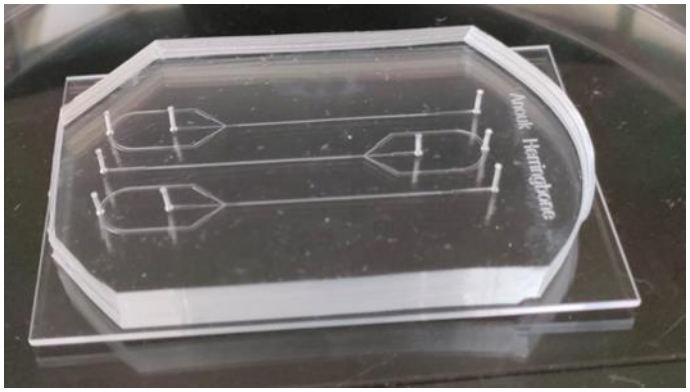

***Figure 4**: PDMS reproduction of Herringbone glass chip from Darwin Microfluidics. PDMS chip exhibit 3 Herringbone Chips.*

Mobile DLS: VASCO KIN™ from Courdouan Technologies was loaned by the laboratory "Centre de Recherche Paul Pascal" (CRPP). VASCO KIN™ is a Dynamic Light Scattering (DLS) apparatus composed of a mobile head that proceed in a continuous measurement at 170°, to obtain size distribution, scattered intensity or correlograms from solution analyzed. Laser source is a high stability laser diode (λ = 638 nm) which will be used at 70% of its power. Measurements are controlled using NanoKin® software.

DLS 90 °: Dynamic Light Scattering (DLS) will be used as first intention to measure hydrodynamic diameter (D_H) and polydispersity index (PDI) of objects. Measurements were carried out using a Malvern Zetasizer Nano ZS equipped with a He-Ne laser (λ = 633 nm) at 25 °C and a scattering angle of 90 °. Quartz cell of 10 mm optical path length was used. Values of viscosity and refractive index were

corrected according to the mixture of organic/aqueous solvent used (Appendix Figure A1 and A2). DLS measurement were acquired from the average of three different measurements of 8 runs of 8 s each. D_H and PDI were calculated from autocorrelation functions using cumulant methods and were averaged. DLS measurement theory is developed in appendix.

MALS: Multi-Angle Light Scattering (MALS) measurements were performed using ALV/CGS3 equipment composed of an ALV-5000 goniometer with a He-Ne laser (λ = 633 nm) and an ALV-5000/EPP multiple τ digital correlator. Solutions to be analyzed were placed in cylindrical glass tubes and immersed in a filtered toluene bath maintained at 25 °C. Static light scattering (SLS) was performed from 25 ° to 149 ° by step of 2 ° and DLS on the same range of angle, by steps of 6 °. Samples were diluted up to 500 times, when necessary, to obtain an almost constant attenuator all along measurement. R_G was determined using Berry second order model on SLS measurements and R_H using Stroke-Einstein model on DLS measurements. Data were normalized with the signals obtained for pure toluene and pure aqueous solvent. Calculations and methods are provided in appendix (Figure A4 to A13). Using R_G and R_H, we can calculate shape factor $\rho=R_G/R_H$. This factor allows to know the nature of the nanoparticle depending on its value. If ρ = 1, objects are more likely to be vesicles, ρ=2 is a sign of cylindrical objects and if ρ=0.8, objects are more likely to be spheres or micelles.[33–36]

TEM: Transmission electron microscopy was used to observe PEG_{22}-*b*-$PTMC_{51}$ nanoparticles. Samples were sprayed on TEM grids using a glassware device allowing to spray fine droplets of solution, under nitrogen flow. Grids were then dried for 5 min and 40 µL of a 1 % solution of staining agent was deposited on top of the grid during 1 min before being absorbed by a KimTech tissue. Staining agent used were phosphotungstic acid, samarium acetate, uranyl acetate or uranyless. TEM observations were performed on a MET HITACHI 120kV – H7650 in Bordeaux Imaging Center. Images obtained were either not significant or showing full spheres and not hollowed vesicles as shown on Figure 5. However, Cryo-TEM will confirm that objects exhibit a core-shell structure. This seems to be an artefact of staining agent. We tried to decrease concentration of staining agent in solution, or to reduce exposure time to staining agent, but we didn't achieve to obtain significant images. Thus, Cryo-TEM analysis will be preferred.

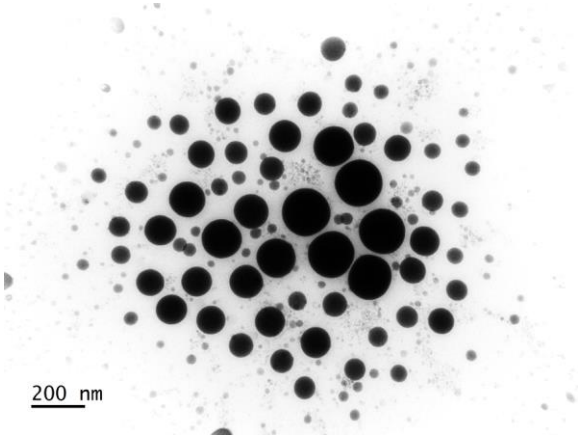

***Figure 5**: TEM images obtained from objects of self-assembled PEG_{22}-b-$PTMC_{51}$. Objects seem to full spheres. Staining agent: Samarium Acetate deposited at 1% during 1 min.*

Cryo-TEM: Cryo-Transmission Electron Microscopy (Cryo-TEM) images were recorded at the Institut de Minéralogie, de Physique des matériaux et de Cosmochimie (Paris) on a Lab6 by Jean-Michel Guinier.

2. Study of parameters for PEG-*b*-PTMC microfluidic-assisted self-assembly

2.1. Effect of osmotic pressure on vesicles

Polymer self-assembly into polymersomes leads to the formation of an aqueous core surrounded by a polymeric bilayer. This represents one of their best advantages as it allows them to load hydrophilic drugs into the aqueous lumen and hydrophobic drugs into the bilayer formed by the hydrophobic block of the copolymer. However, this aqueous core is also one of their main weaknesses. Contrary to their filled counterpart (micelles or spherical nanoparticles), vesicles are sensitive to osmotic pressure variation. Osmotic pressure occurs when osmolarity of the inner aqueous core is different to the one of the external medium[37]. This phenomenon can lead to vesicle deformation, or membrane rupture, as illustrated in Figure 6.

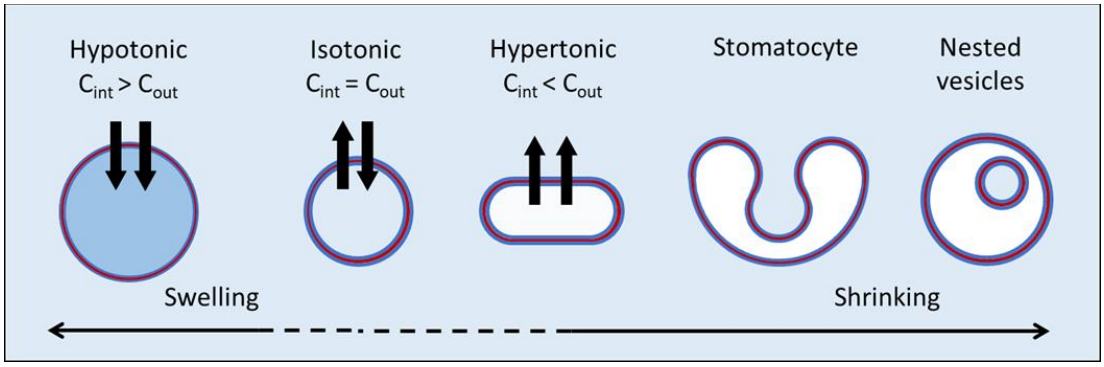

***Figure 6**: Schematic representation of osmotic pressure on vesicle membrane. Inspired by Coralie Lebleu PhD thesis[17] and Liu et al.[37]*

The choice of aqueous solvent used during formulation of nanoparticles determines the composition of aqueous core. Many articles report vesicles production for therapeutic purposes[38] with some vesicles formulated in pure water[39–41]. This choice of aqueous solvent is questionable because the osmolarity of pure water (~0 $Osm.L^{-1}$) does not correspond to the physiological osmolarity (~286 $mOsm.L^{-1}$)[42]. When administrated intravenously, vesicles may undergo strong osmotic pressure and hypertonic shock, which can lead to vesicle deformation.

Vesicles of PEG_{22}-*b*-$PTMC_{51}$ were obtained by microfluidic assisted self-assembly using the micromixer chip. 10 $mg.mL^{-1}$ copolymer solution solubilized in DMSO and ultrapure water were used for formulation with an organic/aqueous solvent ratio of 20/80 %vol and a total flow rate of 1000 $\mu L.min^{-1}$. Dialysis against osmosed water was used to withdraw organic solvent (24 h, 3 bath changes of 2 L, using a dialysis membrane with a 25kDa cut-off). Three ultrafiltration cycles from 10 to 2 mL were performed for replacing the external aqueous media of suspension from pure water to PBS with an osmolarity of 281 $mOsm.L^{-1}$. Nanoparticles placed in water and in PBS were analyzed by cryo-TEM to observe any effect of osmotic pressure on their size and shape. Vesicle size was measured on Cryo-TEM images using Image-J software on 150 vesicles for each sample. Cryo-TEM acquisitions and distribution size are represented in Figure 7.

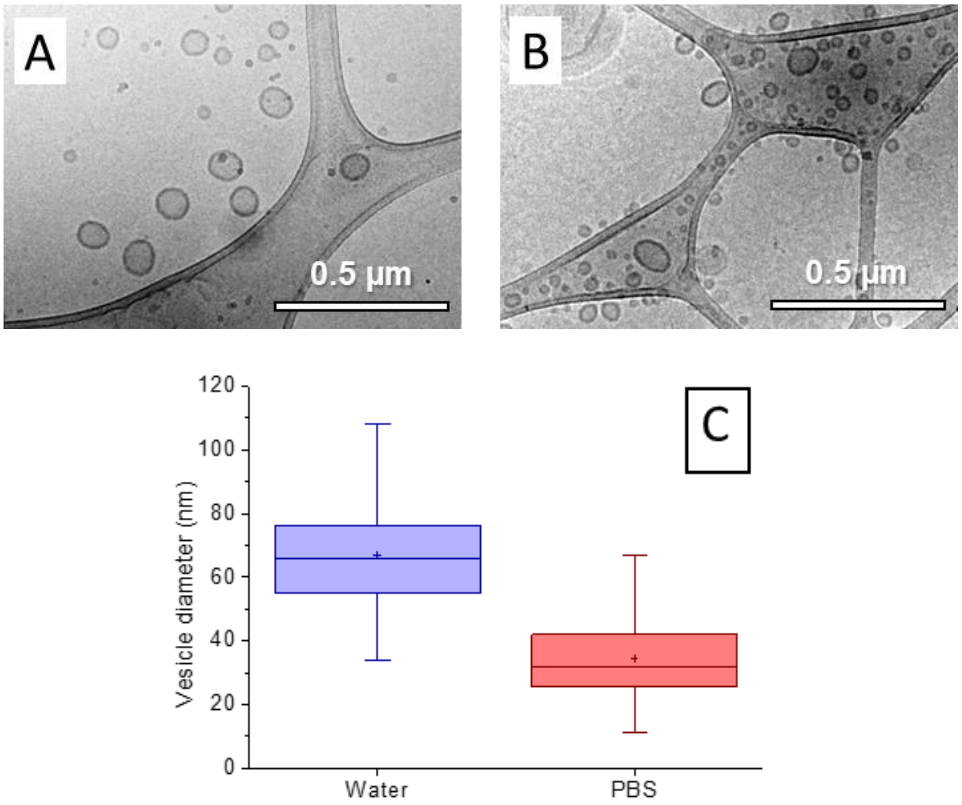

Figure 7: *A) Cryo-TEM image of PEG_{22}-b-$PTMC_{51}$ vesicles formulated in pure water. B) Cryo-TEM image of PEG_{22}-b-$PTMC_{51}$ vesicles formulated in pure water after external solvent exchange (external solvent: PBS, 281 $mOsm.L^{-1}$). C) Box chart showing vesicle distribution before and after external medium change, measured on 150 vesicles per conditions. Box chart shows maximum and minimum size (extremities), 25 and 75 percentiles (box), mean (cross) and median (line in the box).*

As predicted, vesicles formulated in pure water underwent a strong hypertonic shock when the external solvent exchange was performed with a physiological-like solvent. Indeed, the average value of vesicle diameter measured by Cryo-TEM goes from 67 nm, in water, to 34 nm, in PBS. This shrinking effect must be the result of hypertonic shock that causes elongation and splitting of the vesicles. If we consider the use of vesicle for drug loading, shape and size transformation may induce leakage and an uncontrolled burst release of the encapsulated drug. These results emphasize the critical role of aqueous solvent choice when colloidal systems, such as vesicles, are used for biological applications. Therefore, we decided to produce vesicles directly in PBS as aqueous solvent, with an osmolarity of 300 $mOsm.L^{-1}$, to prevent any possible premature drug leakage or colloidal destabilization during *in vitro / in vivo* assays.

2.2. Organic solvents choice towards *in vitro / in vivo* experiments

Historically, Coralie Lebleu developed PEG_{22}-*b*-$PTMC_{51}$ self-assembly with a solvent-exchange process between DMSO and water.[16] Indeed, DMSO is a good solvent to use when aiming medical application. According to Q3C- Tables and List Guidance for Industry from FDA, CDER and CBER, DMSO is part of "Class 3" solvents which "*may be regarded as less toxic and of lower risk to human health. Class 3 includes no solvent known as a human health hazard at levels normally accepted in pharmaceuticals. […] It is considered that amounts of these residual solvents of 50 mg per day or less would be acceptable without justification.*"[43]

Despite its usefulness in vesicle formulation, DMSO still requires post-formulation purification steps by using dialysis or ultrafiltration. To avoid these purification steps and prevent drug leakage, the use of another solvent was investigated in order to find a volatile solvent that will be evaporated at ambient temperature after formulation. Several solvents were tested including THF, acetonitrile and acetone. Compatibility of organic solvent and aqueous solvent in the microfluidic chip was also verified. Several aqueous solvents were tested to find the compatible couple, including PBS, sucrose and glucose solutions, all of them with an osmolarity at 300 $mOsm.L^{-1}$ and a pH = 7.4. Mixing organic and aqueous solvents in the microfluidic chip resulted in aggregate formation for most combinations, as shown in Figure 8. However, the mix of acetone and glucose was found as usable in the microfluidic chip. Acetone is also considered as a "Class 3" solvent according to Q3C- Tables and List Guidance for Industry from FDA, making it an ideal organic solvent for medical applications when used in small quantities. Thus, future experiments will involve the DMSO/PBS couple or Acetone/Glucose couple.

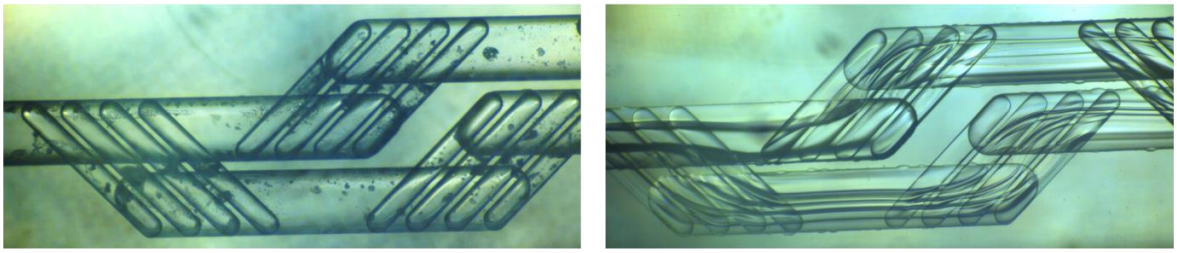

***Figure 8**: (Left) Out-of-flow appearance of microfluidic micromixer chip, with a focus on the first micromixer unit, after the mixing of acetonitrile and PBS solvent. Solid aggregates appear all over the chip. (Right) In-flow appearance of microfluidic micromixer chip, with a focus on the first micromixer unit, after the mixing of DMSO and PBS solvent.*

2.3. Nucleation of self-assembly system: critical water content assays

Before performing self-assembly experiments using microfluidics, it is important to determine the critical water content required for copolymer to self-assembly, as described Ch1.II.3.a. We define the critical water content (CWC) as the minimum amount of water that must be added in an organic solution containing block copolymers to initiate the formation of self-assembled structures.

To measure the CWC for PEG_{22}-*b*-$PTMC_{51}$, we decided to measure the intensity of light scattered by a copolymer solution solubilized in organic solvent while adding aqueous solvent. Indeed, free copolymer chains in organic solvent have almost no scattering signal, but water addition leads to copolymer self-assembly into colloidal structures and an increase of scattered light is observed[44]. Critical water content is thus defined at the inflection point of the curve that represented the intensity as a function of the aqueous solvent content. We first performed *ex-situ* measurements of scattered signals with a PEG_{22}-*b*-$PTMC_{51}$ solution in organic solvent (5 $mg.mL^{-1}$ initially in DMSO or Acetone) and after the addition of different fractions of aqueous solvent, as represented in Figure 9. The CWC for copolymer in acetone was found to be between 20 and 30 %vol of glucose solution addition, while for copolymer in DMSO, it was estimated between 0 and 10 % vol of PBS addition. It is important to note that the precision for the determination of the value of CWC depends on the volume of addition chosen for aqueous solvent and thus provide only an approximative idea. To improve the accuracy of this study, we used the VASCO KIN™ apparatus for *in-situ* measurement during the addition of aqueous solvent. The proposed home-made set up used to conduct the experiment is represented in Figure 10A.

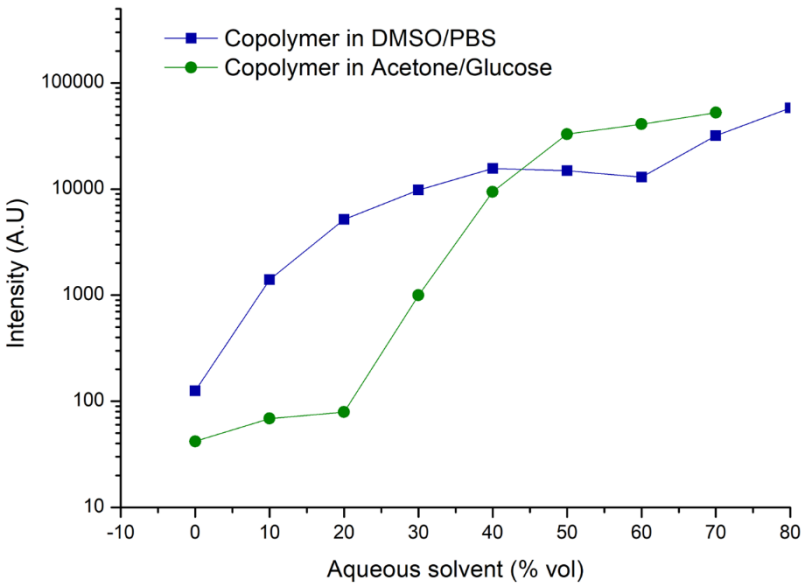

***Figure 9**: Representation of the derived count rates (DCR) as a function of the aqueous solvent content (in %vol). The inflexion point of the curve represents the CWC. PEG_{22}-b-$PTMC_{51}$ was dissolved at 5 $mg.mL^{-1}$ in DMSO (blue line) or in acetone (green line) and stirred 1 min before the addition of PBS or glucose solution. Volumes of addition were calculated to allow measurements every 10% vol addition of aqueous solvent.*

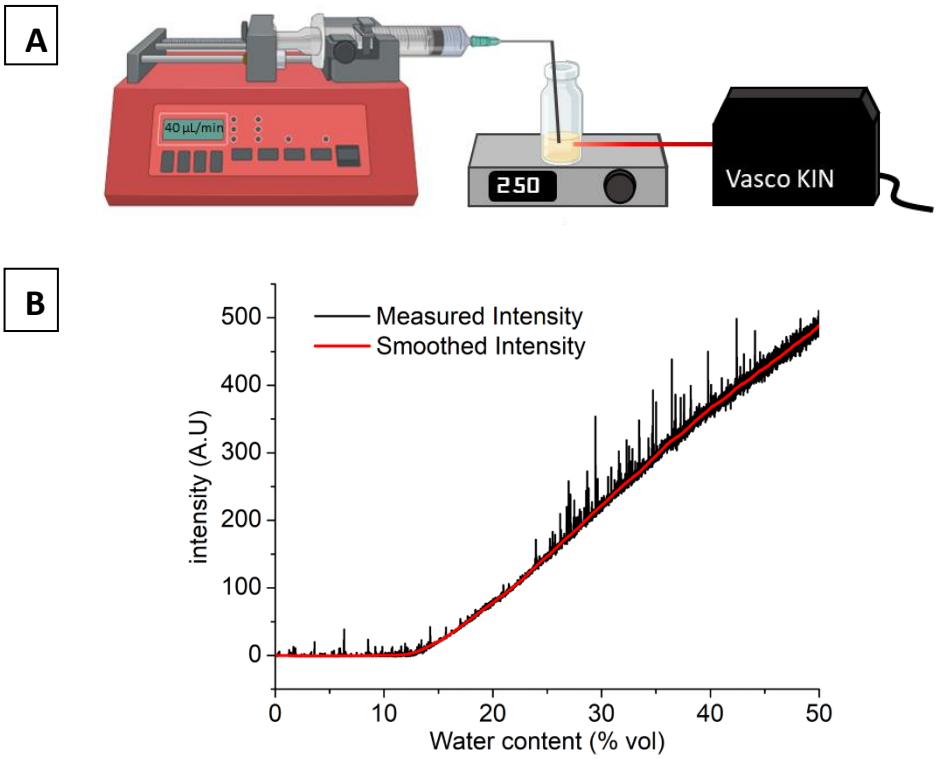

***Figure 10**: A) Schematic representation of "home-made" mobile DLS set-up. B) Scattered light intensity measured during the PEG_{22}-b-$PTMC_{51}$ self-assembly, when aqueous solvent is added to copolymer dissolved in the organic solvent (initial copolymer concentration at 2.5 mg.mL^{-1}).Black line : raw measured intensity. Red line: Smoothing of the data given by Savitzky-Golay method (Window 200 pts, Polynomial order 2) with Origin85 software.*

While measuring scattered intensity *in-situ*, an aqueous solvent was added using a Harvard Apparatus syringe driver, with a needle immersed in the copolymer solution under magnetic stirring at 250 rpm. This speed allows homogenization of the solute while positioning the laser between the magnetic stirrer and meniscus due to agitation. We obtained a curve of scattered intensity represented in Figure 10B. As the experiment is not protected by an enclosure, dusts in the air and light pollution might interfere with the laser. The Savitzky-Golay smoothing function was used to remove noise and was applied on curves, represented by the red line of Figure 10B. The CWC was determined at the inflection point of the curve. Those experiments aimed to measure only the scattered intensity, without considering the size of the objects. However, due to the use of magnetic stirring in the experiment, these measurements were not able to provide accurate correlograms or diameters. Supplementary results present on appendix show evidence that this set-up is not suitable for measuring object size, as demonstrated by the impact of stirring on the size measurement of latex particles of 100 nm.

We began the CWC experiment by determining the stirring speed required to mix the entire height of the vial with a maximum water content of 70%. We found that 250 rpm was the ideal stirring rate. We then prepared a solution of PEG_{22}-*b*-$PTMC_{51}$ at 2.5 mg.mL^{-1} in DMSO and examined the effect of the flow rate addition of added aqueous content on CWC. Figure 11 shows curves obtained at flow rate of 20, 40, 80 and 160 µL.min^{-1}. The observed results confirm that slope break occurs at the same amount of PBS regardless of the flow rate.

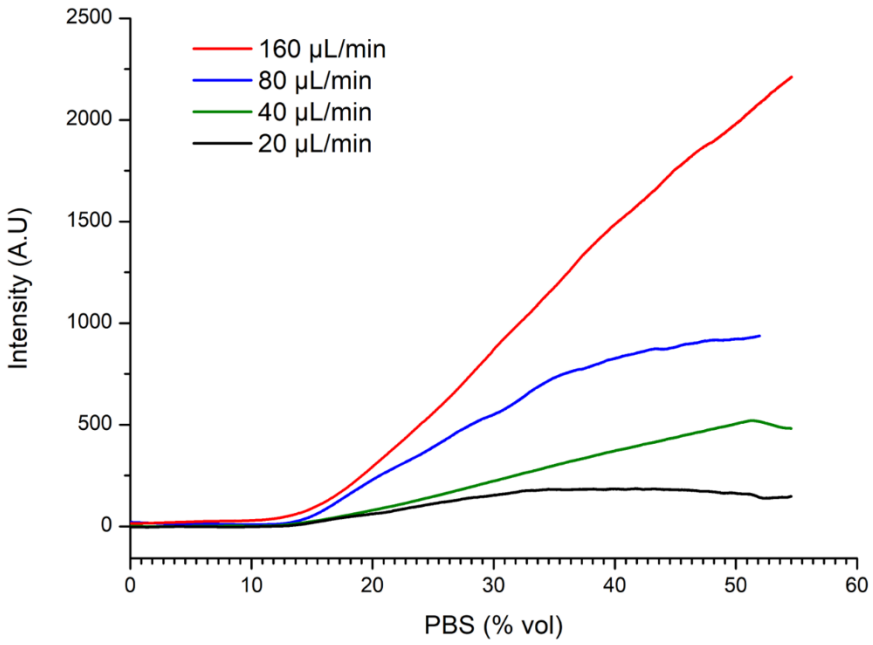

***Figure 11**: Scattering intensity measured from a PEG_{22}-b-$PTMC_{51}$ solution of 2.5 mg.mL^{-1} in DMSO during PBS addition at different flow rates. Curves represents an average of signals from experiments done in triplicate. Smoothing of the data are given by Savitzky-Golay method.*

The CWC depends on several parameters, including the choice of the aqueous/organic solvent and the copolymer concentration. The CWC was measured for each organic/aqueous solvent pair: DMSO/PBS and Acetone/Glucose. Figure 12 shows the curves obtained from the CWC measurements using a copolymer solution at 2.5 mg.mL^{-1} in organic solvent. Compared to the CWC measured through punctual addition of aqueous solvent, results are similar with the CWC in acetone being higher compared to DMSO. The theoretical values of Hildebrand solubility parameters of PEG and PTMC in solvent mixtures along water addition also predicted these results. Both copolymer blocks were found to be in bad solvent condition at 10% vol of water in DMSO and at 26% vol of water in acetone. (Calculations available in appendix).[45] This is consistent with the respective 14% vol and 25% vol CWCs measured for DMSO and acetone during *in-situ* acquisitions.

We also varied the initial copolymer concentration from 1 to 10 mg.mL^{-1} and measured the CWC with the organic/aqueous solvent pair of DMSO/PBS. Figure 13 shows that decreasing copolymer concentration slightly increases CWC from 10.5% vol at 10 mg.mL^{-1} to 12.5% vol at 1 mg.mL^{-1}.

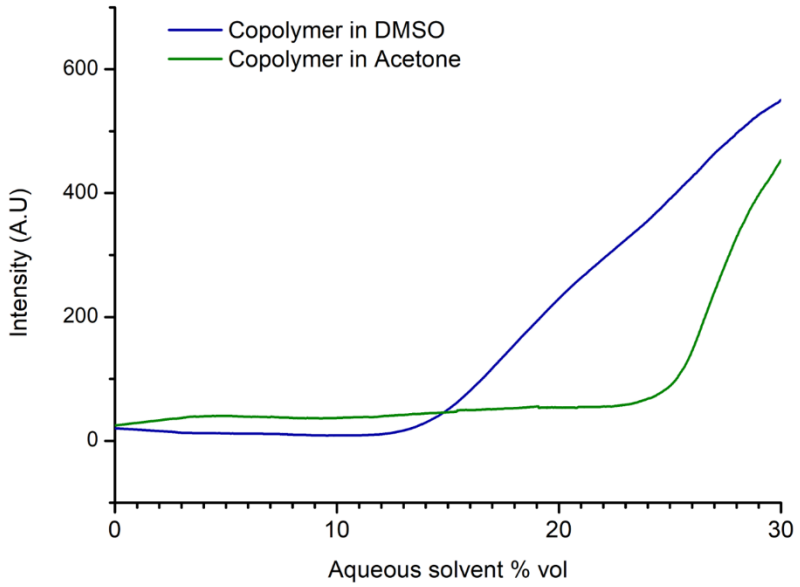

***Figure 12**: Scattered light intensity as measured by DLS during PEG_{22}-b-$PTMC_{51}$ self-assembly when PBS or glucose solution is added to polymer dissolved in DMSO (blue line) or Acetone (green line) for a copolymer concentration of 2.5 mg.mL^{-1}. Represented curves are the average result of experiments carried out in triplicate and are smoothed by Savitzky-Golay method.*

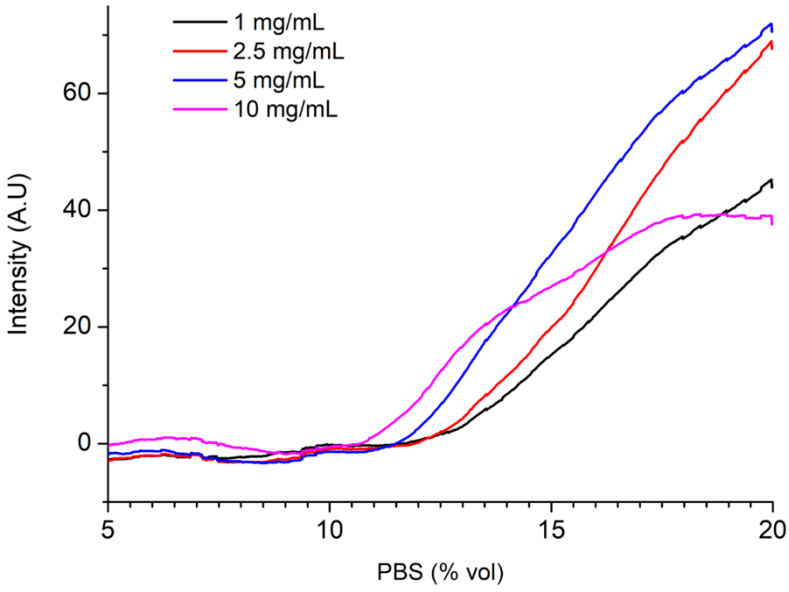

***Figure 13**: Scattered light intensity as measured by DLS during PEG_{22}-b-$PTMC_{51}$ self-assembly when PBS is added to polymer dissolved in DMSO and for a copolymer concentration range from 1 to 10 mg.mL^{-1}. Represented curves are the average result of experiments carried out in triplicate and are smoothed by Savitzky-Golay method.*

To ensure the kinetical entrapment of our nanoparticles growth[19] during microfluidic experiment, we decided to use an organic/aqueous ratio with a water content far above the CWC threshold. Indeed, by maintaining a minimum of aqueous solvent of 40 %vol, we ensure a stable self-assembly that shouldn't be disrupted by post-formulation processes, such as dialysis purification.

3. Microfluidic assisted self-assembly processes

In this section, we will briefly discuss the factors that affect the self-assembly of block copolymers, including copolymer concentration, nature of the solvent, water content in the solvent mixture and mixing rate of solvent. Nanoprecipitation was mainly carried out by manually adding organic phase in a large excess of aqueous phase. This process of self-assembly is quenched by adding a large excess of water, which limits chain mobility and freezes the current morphology. Besides, the manual nanoprecipitation process is often limited by poor reproducibility and repeatability, leading to the formation of nanoparticles with a relatively high polydispersity index (PDI > 0.2). The thermodynamic equilibrium allowed for a copolymer to self-assembly is only reachable under certain preparation conditions, such as the content of common solvent, which enable sufficient chain mobility and faster morphologic transitions during the addition of water. In many cases, the thermodynamic equilibrium is unreachable over the experimental time scale, resulting in aggregate formation under kinetic control, which strongly depends on the mechanism of aggregate formation[46]. The implementation of processes allowing a better control of the mixing and the solvent flow rate allowed to solve the problem of the homogeneity of the nanoparticles. Specifically, microfluidic systems enable automated formulation of nanoparticles with high reproducibility and also offer the ability to continuously produce larger volumes of suspension for scale-up purposes. Besides, in typical microfluidic system, the flow is highly organized due to the small size of the channels. This results in mixing occurring primarily through diffusion, a slow process that leads to a low mixing speed, represented by classical chips with a ratio length / diameter of the channel that are very high. To overcome this limitation, various types of microfluidic mixers have been developed with three main strategies to increase the mixing speed[47]: (1) using multilaminar mixers (or micromixers) that create a subdivision of the initial flow into multiple sub-flows, reducing the width of the laminar flow phases and decreasing diffusion distances; (2) introducing transversal flow elements that create partially chaotic mixing, as seen in the case of herringbone mixers; and (3) causing flow collisions, resulting in smaller fluid segments and, in some cases, even turbulent mixing, as seen in impact-jet and vortex mixers.

3.1. Microfluidic chip design

3.1.1. Micromixer Chip

In this chapter, we will study two microfluidic chips, the primary one being the Micromixer chip from Dolomite Microfluidics. This commercial glass chip is composed of two paths, each containing twelve micromixers. The overall micromixer chip, also called the “split and recombine” chip, is designed to divide flows into thinner layers and then recombine them. The goal of this chip is to reduce inter-diffusion time by reducing layer thickness, as represented in Figure 14. In more details, the flow is split into two or more streams as it enters the micromixer, with each stream passing through a separate channel. These channels are designed to induce a mixing process that promotes rapid diffusion of the fluids across the channel under pseudo-laminar regime. After passing through the mixing region, the individual streams are recombined to form a single, well-mixed output stream. The resulting mixture is highly homogeneous. Overall, the split and recombine micromixer is a highly effective way of achieving rapid and efficient mixing in microfluidic systems, thanks to its use of diffusion-driven mixing processes. Representation of the global chip is given in Figure 16.

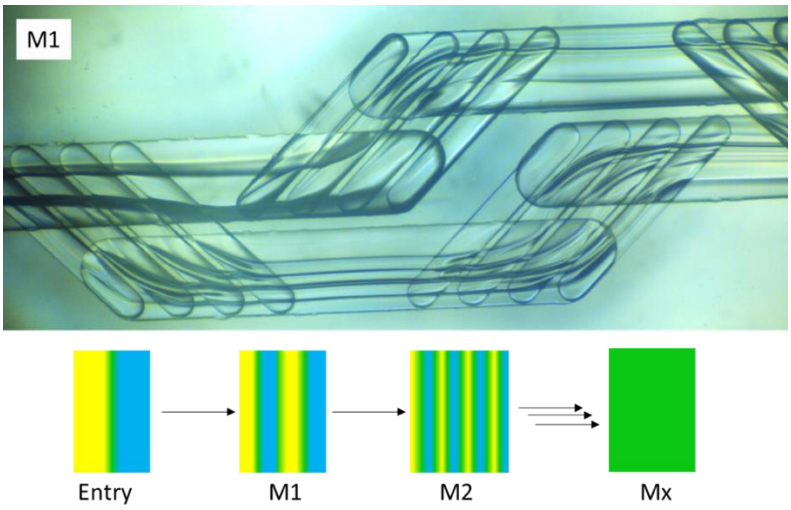

Figure 14: *Picture and schematic representation of flows present inside Micromixer chip, dividing flows to reduce their thickness and interdiffusion time after each mixing chamber, represented by the letter "M", with M1 the first mixing chamber and M2 the second mixing chamber. At the end of the twelve mixing chambers, the two fluids are perfectly mixed together due the formation of thinner layer after each passage in a mixing chamber.*

3.1.2. Herringbone Chip

The second chip that will be used is the Herringbone Chip from Darwin Microfluidic. As described by Stroock *et al.*[29], this chip is composed of a straight channel hollowed out with steps in the form of asymmetrical spikes, that generate forces perpendicular to current flow. When fluids are introduced into the herringbone chip, the herringbone pattern creates a series of vortices and recirculation zones that promote mixing between the fluids. Specifically, as the fluids flow through the grooves, they experience a combination of shearing and rotational forces that cause them to mix and intermingle. The herringbone pattern also generates secondary flow patterns, such as vortices and eddies, that help to break up any remaining laminar flow and promote mixing. Thus, whirlpool is formed, and divides flows into thinner layers, leading to a faster interdiffusion of solvents, as represented in Figure 15. Overall, the flow of fluids inside a herringbone chip is highly complex and depends on a variety of factors, such as the channel geometry, flow rate, and viscosity of the fluids. However, the herringbone pattern is specifically designed to promote mixing and achieve rapid and efficient fluid mixing.

Figure 16 gives a representation of the overall microfluidic system composed of two pumps, the microfluidic chip and a purification step, in this case dialysis.

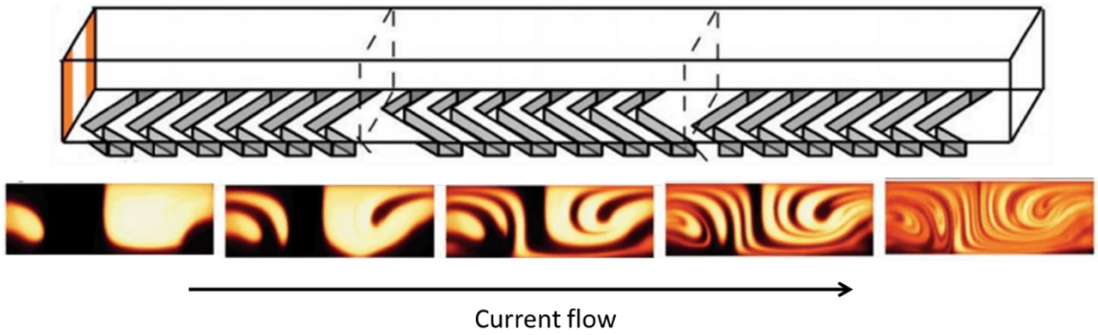

***Figure 15**: Pictures and schematic representation flows circulation inside a Herringbone chip. Whirlpool created by perpendicular forces allows to reduce flows thickness and interdiffusion time, adapted from Stroock et al.*[29]

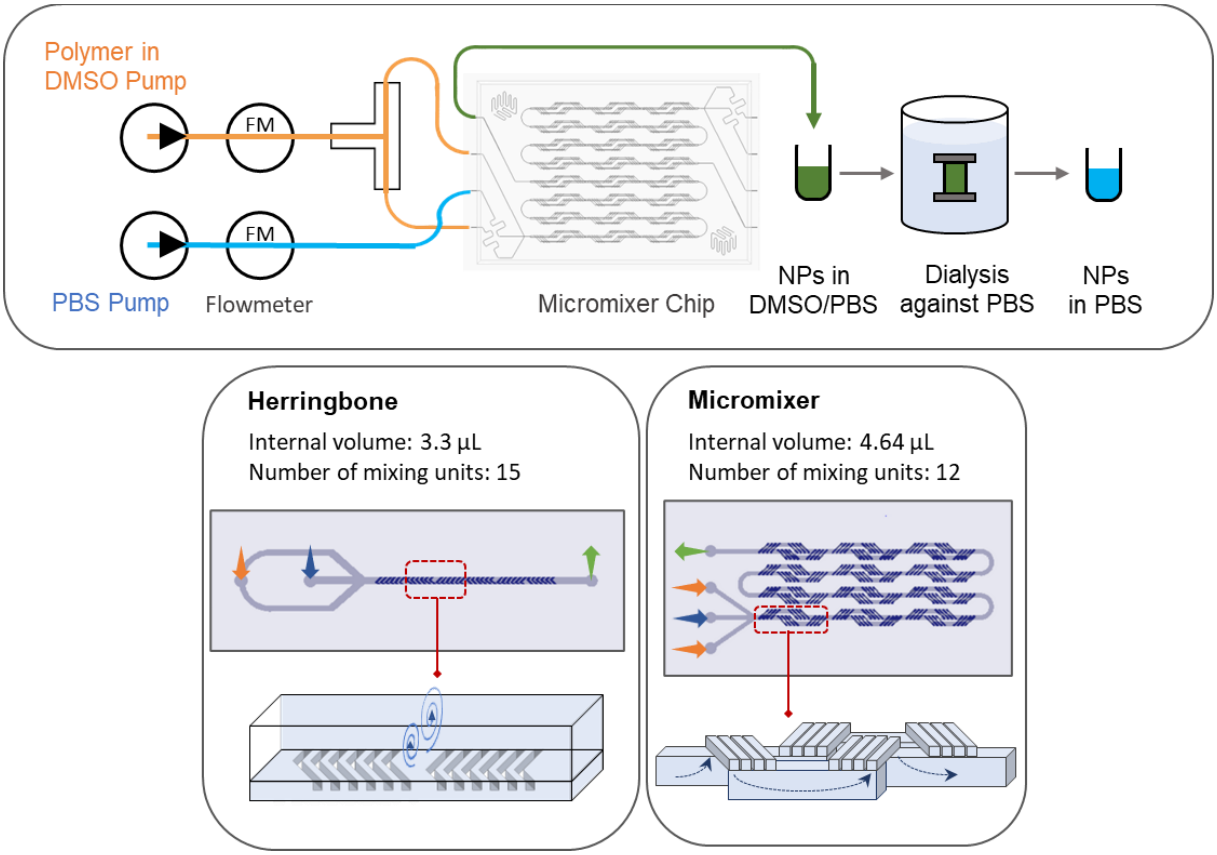

***Figure 16**: Schematic representation of microfluidic assisted formulation of polymersomes followed by an overview of the microfluidic chips used for their preparation (Herringbone and Micromixer).*

3.2. Optimization of the organic / aqueous solvent ratio in micromixer chip

The initial microfluidic experiment aims to identify the key parameters necessary to produce consistently sized vesicles with low diameter dispersity (PDI < 0.15). Micromixer chip was used to adjust organic/aqueous solvent ratio. A solution of 10 $mg.mL^{-1}$ of PEG_{22}-*b*-$PTMC_{51}$ in organic solvent (DMSO or Acetone) was prepared and the organic/aqueous solvent ratio was adjusted from 50/50 to 20/80% v/v. The total flow rate was set at 1000 $\mu L.min^{-1}$. Suspensions obtained from DMSO/PBS were then purified by using dialysis against PBS while suspensions obtained from acetone/glucose were evaporated under nitrogen bubbling, until acetone mass was withdrawn. Hydrodynamic diameter (D_H) and PDI were systematically measured by dynamic light scattering, as represented in Figure 17 and Figure 18. As a result, microfluidic assisted self-assembly enables to form nanoparticles with a D_H between 100 and 300 nm for both solvent pair.

If any ratio of DMSO / PBS produces homogenous population of nanoparticles (with a PDI < 0.15), acetone /glucose solvent requires an organic content higher than 50% vol to reach a low PDI (<0.15). When organic solvent fraction was increased from 20 to 50% v/v, an increase of D_H was observed for experiment involving DMSO as an organic solvent, from 152 to 283 nm. On the other hand, a decrease of D_H was observed for experiments done in Acetone, from 245 to 126 nm.

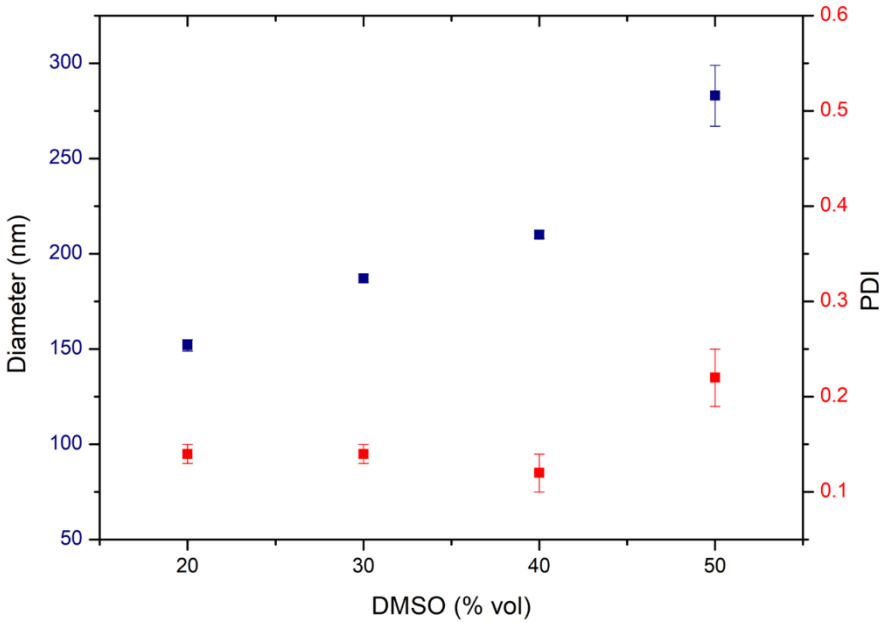

***Figure 17**: Hydrodynamic diameter and PDI measured by DLS 90° for purified PEG_{22}-b-$PTMC_{51}$ nanoparticles formulated by varying the ratio of organic/aqueous solvent of DMSO / PBS, from 20 to 50% v/v of DMSO in the suspension after self-assembly in microfluidic using micromixer. Each value corresponds to the mean size value of 3 experiments and error bars correspond to standard deviation.*

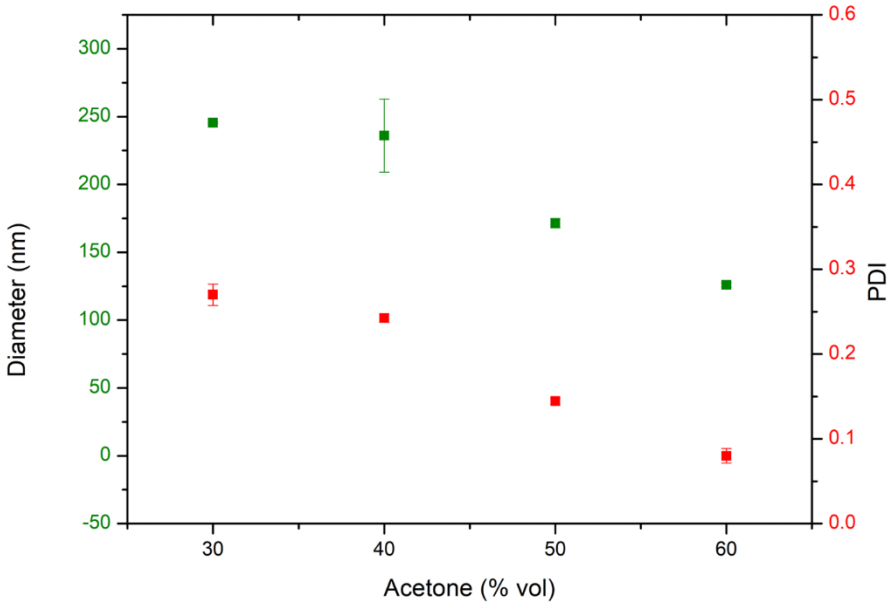

***Figure 18**: Hydrodynamic diameter and PDI measured by DLS 90° for purified PEG_{22}-b-$PTMC_{51}$ nanoparticles formulated by varying the ratio of organic/aqueous solvent of acetone / glucose, from 30 to 60% v/v of Acetone, in the suspension after self-assembly in microfluidic using micromixer. Each value corresponds to the mean size value of 3 experiments and error bars correspond to standard deviation.*

Increasing the organic fraction in the suspension results in a higher final concentration of copolymer prior to purification. The concentration of copolymer in the suspension varies from 2 $mg.mL^{-1}$, when 20% of organic solvent is used, to 5 $mg.mL^{-1}$, when 50% of organic solvent is used. To elucidate whether the change in size is due to the ratios of solvent or the final concentration of copolymer, the same experiment was repeated with a final copolymer concentration set at 2 $mg.mL^{-1}$, as represented in Figure 19 and Figure 20. The results show that the size of the nanoparticles remains stable at around 155 nm for both organic solvents, indicating that the final polymer concentration is the key parameter to control the size of the nanoparticles.

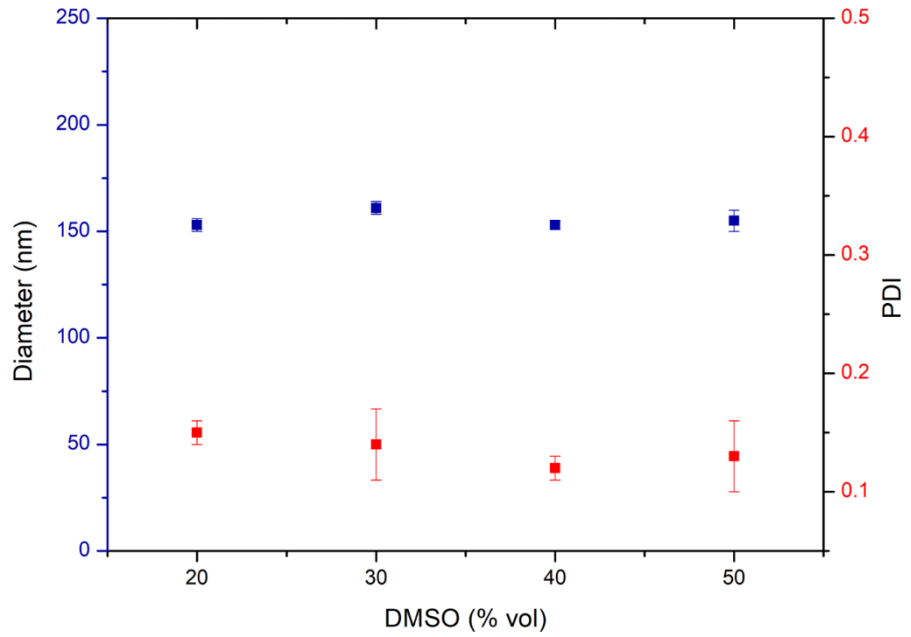

***Figure 19**: Hydrodynamic diameter and PDI measured by DLS 90° for purified nanoparticles formulated by varying the ratio of DMSO / PBS solvent from 20 to 50% v/v organic solvent in the suspension after self-assembly in microfluidic using micromixer and with a final PEG_{22}-b-$PTMC_{51}$ concentration in the suspension of 2 mg.mL^{-1}. Each value corresponds to the mean size value of 3 experiments and error bars correspond to standard deviation.*

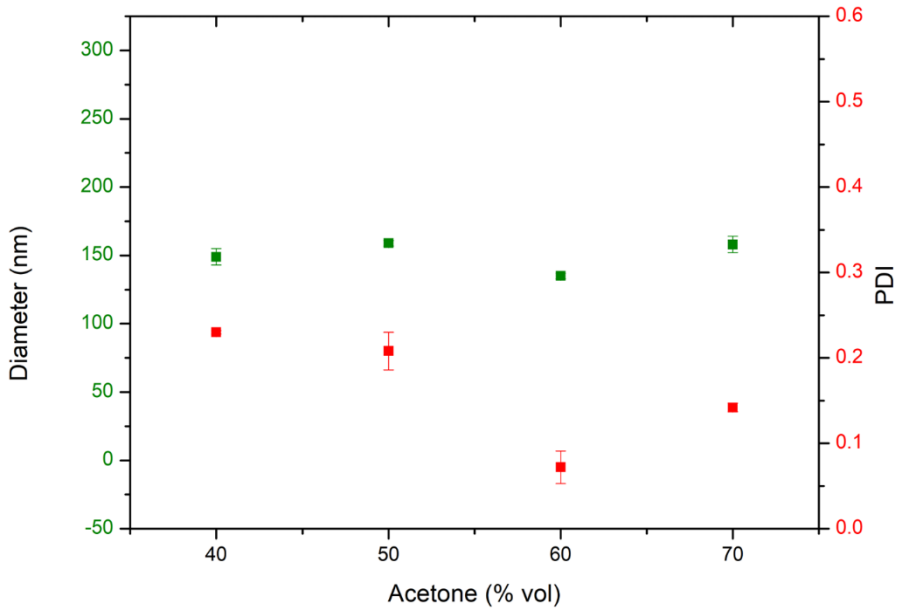

***Figure 20**: Hydrodynamic diameter and PDI measured by DLS 90° for purified nanoparticles formulated by varying the ratio of acetone / glucose solvent from 30 to 60% v/v organic solvent in the suspension after self-assembly in microfluidic using micromixer and with a final PEG_{22}-b-$PTMC_{51}$ concentration in the suspension of 2 mg.mL^{-1}. Each value corresponds to the mean size value of 3 experiments and error bars correspond to standard deviation.*

In order to confirm the formation of vesicular structures, the suspension formulated by using 20/80 % v/v DMSO/PBS and 60/40 % v/v acetone / glucose were characterized by Cryo-TEM (Figure 21). Cryo-TEM images confirms that these operating conditions allow to produce reproductible and homogeneous population of vesicles.

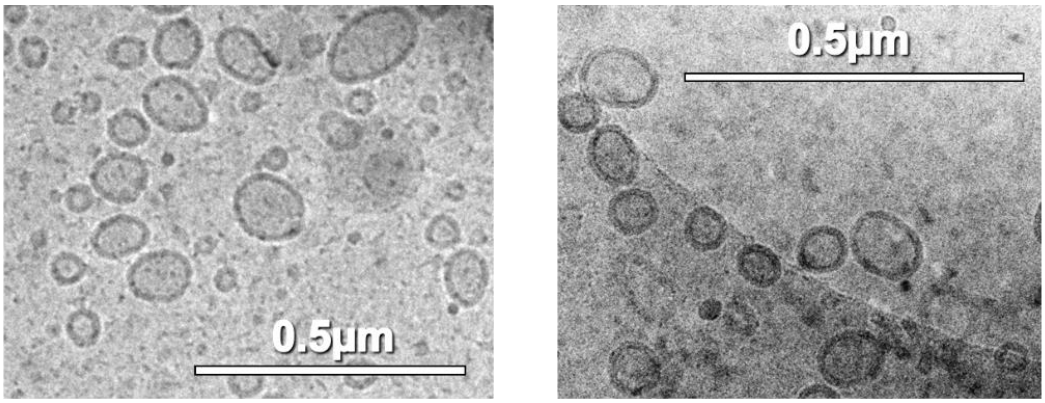

Figure 21: *Cryo-TEM images showing that microfluidic assisted self-assembly of PEG_{22}-b-$PTMC_{51}$ in micromixer chip successfully formed vesicles, whether using DMSO/PBS (20/80 %vol) pair (left) or Acetone/Glucose pair (60/40 % vol) (right).*

3.3. Optimization of the organic / aqueous solvent ratio in Herringbone chip

The ideal ratios of organic/aqueous solvent were investigated on the Herringbone chip to compare the effect of mixing strategy with that of a micromixer chip. Initial copolymer concentration was set at 10 $mg.mL^{-1}$ and total flow rate kept at 1000 $\mu L.min^{-1}$. DMSO/PBS ratio was adjusted from 20/80 %vol to 50/50 %vol. Hydrodynamic diameter and PDI were systematically measured by DLS (Figure 22). Both mixing strategies showed the same behavior, with an increase in hydrodynamic diameter observed on the Herringbone chip (from 113 to 274 nm), when the organic solvent fraction was increased from 20% to 50% v/v, probably impacted by the variation of final copolymer concentration, as explained for micromixer chip. In order to confirm the formation of vesicular structures, the suspension formulated with 20/80 % v/v ratio was characterized by Cryo-TEM (Figure 23). These results demonstrate that the mix between flows plays a critical role in determining the homogeneity of the resulting mixture and, consequently, in controlling the obtained structures. For the two chips presenting different circulating flow regimes, the mixing time seems to be well-controlled, leading to the production of monodisperse vesicular structures.

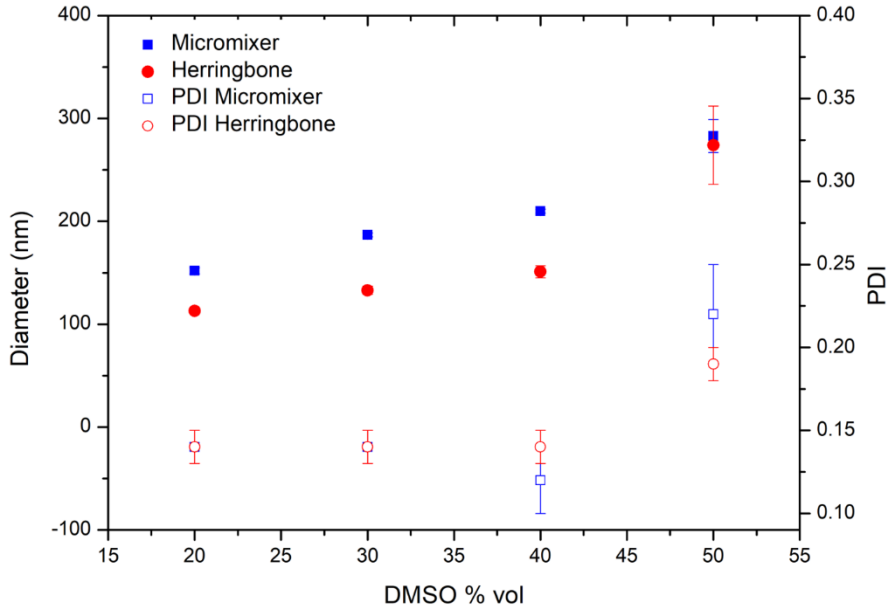

***Figure 22**: Hydrodynamic diameter and PDI measured by DLS 90° for purified objects made in Herringbone chip varying ratio of organic/aqueous solvent DMSO / PBS, from 20 to 50% v/v organic solvent. Each value corresponds to the mean size value of 3 experiments and error bars correspond to standard deviation.*

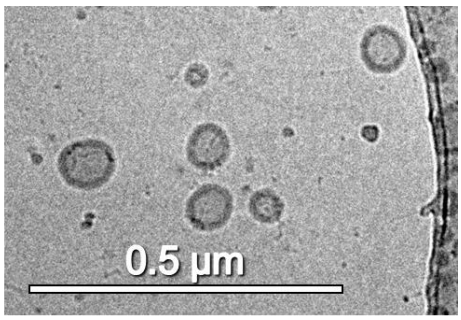

***Figure 23**: Cryo-TEM images showing that microfluidic assisted self-assembly of PEG_{22}-b-$PTMC_{51}$ in Herringbone chip successfully formed vesicles using DMSO/PBS (20/80 %vol) as organic/aqueous solvent.*

4. Fine tuning vesicle size with microfluidic parameters

4.1. Variation of initial copolymer concentration

As demonstrated previously with preliminary results, the copolymer concentration seems to be a key parameter to play with for tuning the size of the obtained vesicles when using microfluidic. We decided to investigate further this effect, by adjusting copolymer initial concentration in organic solvent. PEG_{22}-*b*-$PTMC_{51}$ was solubilized at 1 to 30 mg.mL^{-1} in DMSO and at 1 to 20 mg.mL^{-1} in acetone. Ratio of 20/80 % vol was set with DMSO/PBS, 60/40 % vol with acetone/glucose and the total flow rate was set at 1000 µL.min^{-1} in a micromixer chip. Organic solvent was removed after microfluidic solvent displacement, by dialysis for DMSO and evaporation for acetone, and the solution was filtered with 0.45 µm syringe filter cellulose acetate prior to DLS analysis. Hydrodynamic diameter and PDI were systematically measured by DLS (Figure 24 and Figure 25).

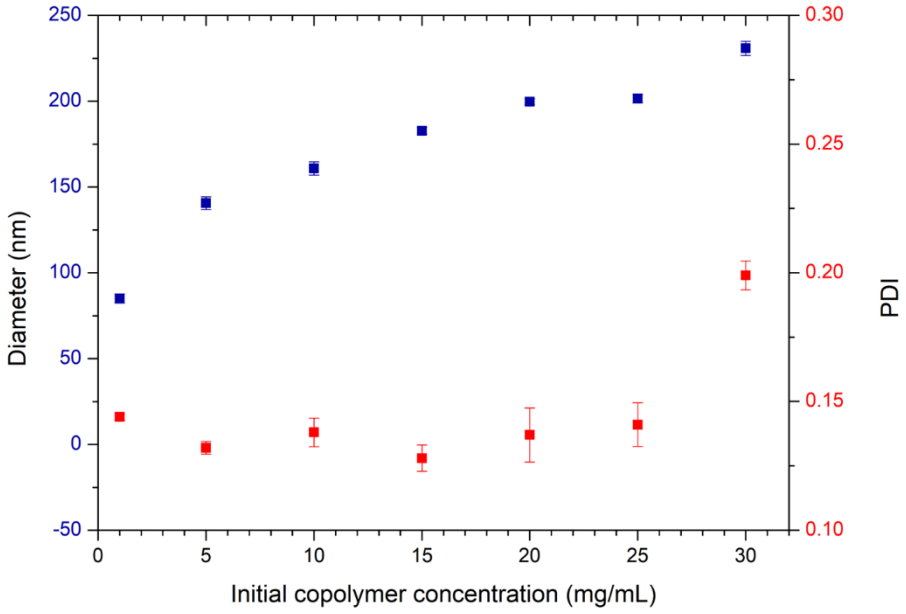

***Figure 24**: Hydrodynamic diameter and PDI measured by DLS 90° for purified PEG_{22}-b-$PTMC_{51}$ nanoparticles formulated by varying initial copolymer concentration in DMSO solvent, setting ratios of DMSO/ PBS solvent at 20/80 %vol. Each value corresponds to the mean size value of 3 experiments and error bars correspond to standard deviation.*

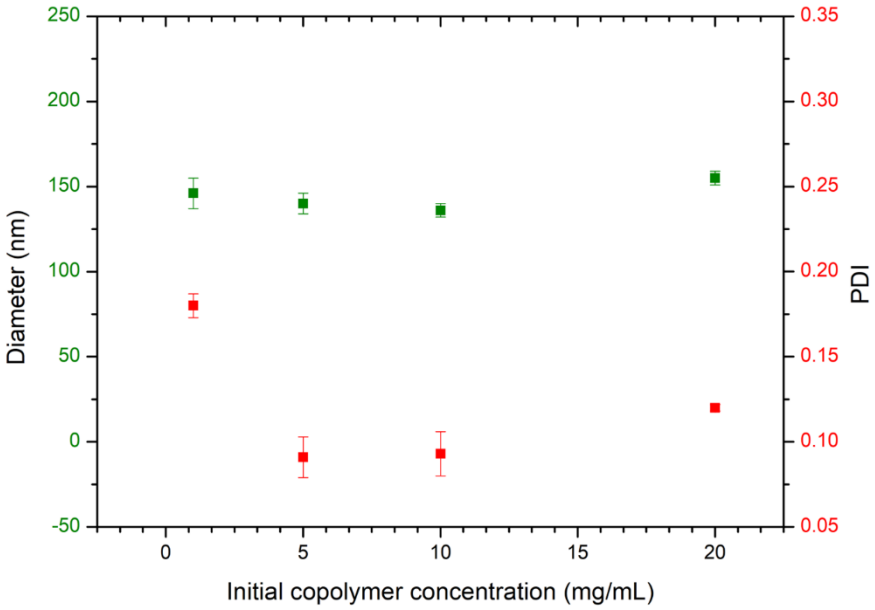

Figure 25: *Hydrodynamic diameter and PDI measured by DLS 90° for purified PEG_{22}-b-$PTMC_{51}$ nanoparticles formulated by varying initial copolymer concentration in acetone solvent, setting ratios of acetone/glucose solvent at 40/60 %vol. Each value corresponds to the mean size value of 3 experiments and error bars correspond to standard deviation.*

When formulated with acetone/glucose, the initial copolymer concentration presents no influence on final vesicle size as D_H remains around 150 nm whereas nanoparticles formulated with DMSO/PBS, present an increase in diameter observed according to the initial copolymer concentration. For instance, nanoparticles with a size of 76 nm were obtained with 1 $mg.mL^{-1}$ as initial copolymer concentration while nanoparticles of 192 nm were obtained with 20 $mg.mL^{-1}$. However, copolymer concentration up to 30 $mg.mL^{-1}$ seems to increase PDI upper than 0.15, meaning vesicle population are less homogenous. However, a linear trend between size and copolymer concentration can be observed between 5 and 25 $mg.mL^{-1}$, following the equation (Equation II.1) :

$$D_H = 3.37c + 127.03 \qquad II.1$$

with D_H the hydrodynamic diameter measured by DLS (in nm), and c the initial copolymer concentration (in $mg.mL^{-1}$). The coefficient of determination for this linear trend is R^2=0.9678

To ensure vesicular shape of nanoparticles, Multi Angle Light Scattering (MALS) was performed to measure R_G, R_H, and deducting shape factor $\rho = R_G/R_H$. The SLS and DLS curves, as well as the fitting equations, can be found in the appendix (Figure A4 to A9). The results obtained from both the DLS 90° measurement and MALS measurement were compiled in Table 1. The shape factor obtained ranged between 0.95 and 1.40 confirms a vesicular shape. Cryo-TEM was performed for suspensions formulated with initial minimum and maximum copolymer concentrations (Figure 26).

Table 5: *Hydrodynamic radius and radius or gyration of polymersomes (determined by DLS 90°, MALS and Cryo-TEM) obtained by microfluidic-assisted self-assembly with different PEG_{22}-b-$PTMC_{51}$ initial copolymer concentration. [a] Radius R_{TEM} is determined by an average measurement from approximately 50 vesicles.*

Total flow rate	**DLS 90°**		**MALS Measurements**			**Cryo-TEM**
mg/mL	R_H (nm)	PDI	R_G (nm)	R_H (nm)	$\rho=R_G/R_H$	R_{TEM}[a]
1	38	0.14	33	35	0.95	49 ± 9
5	65	0.13	72	60	1.21	
10	83	0.14	82	67	1.22	
15	85	0.13	102	75	1.36	
20	96	0.14	101	76	1.3	
25	104	0.14	111	87	1.27	
30	112	0.2	117	84	1.40	101 ± 18

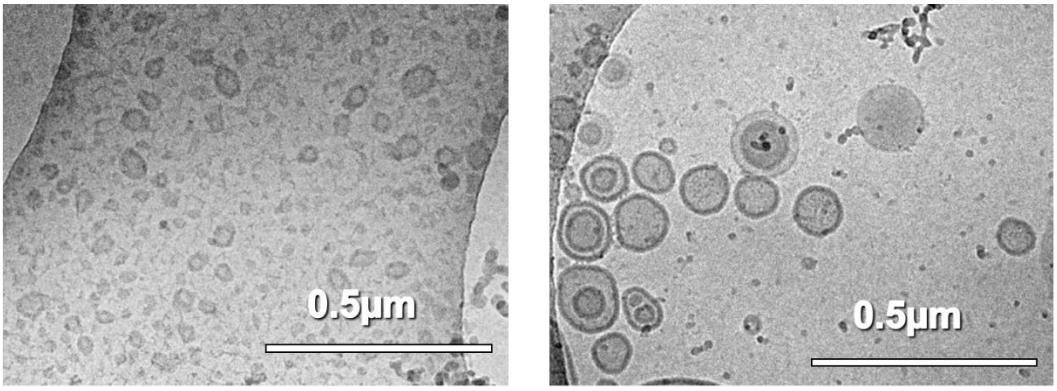

Figure 26*: Representative Cryo-TEM images for different conditions of PEG_{22}-b-$PTMC_{51}$ polymersomes formulation when using a micromixer system and DMSO/PBS as organic/aqueous solvent with two extremes initial copolymer concentrations of 1 mg.mL^{-1}(left) and 30 mg.mL^{-1}(right). Scale bar corresponds to 0.5 µm.*

The behavior of vesicles diameter growing with copolymer concentration is in agreement with a nucleation-growth mechanism[48,49], described in chapter 1.II.3.a. The increase in diameter while increasing copolymer concentration could be the consequence of two combined phenomena. First, a higher concentration of copolymer leads to a higher number of chains available for self-assembly. Then, by increasing copolymer concentration, viscosity of organic phase is increased, providing a higher mass transfer resistance and consequently, interdiffusion of solvent is slowed down. Those two phenomena contribute to the formation of larger nanoparticles.[15,19]

The results of this study demonstrate the successful formation of vesicles through PEG_{22}-*b*-$PTMC_{51}$ microfluidic assisted self-assembly. Furthermore, by adjusting the initial copolymer concentration, the hydrodynamic diameter of the vesicles can be tuned between 76 and 224 nm when DMSO/PBS couple is selected as organic/aqueous solvent. The same effect was demonstrated with poly(trimethylene carbonate)-*b*-poly(L-glutamic acid) $PTMC_{24}$-*b*-PGA_{12} polymersomes starting from copolymer concentrations in DMSO from 1 to 100 mg.mL^{-1}, resulting in hydrodynamic radius ranged between 72 and 176 nm.[15] This size control can be achieved without requiring any post-microfluidic processes, making this technique advantageous.

4.2. Variation of total flow rate as a way to influence solvents mixing speed

In a microfluidic system, the mixing speed can have a significant influence on the size of the vesicles formed. Mixing speed affects the rate and efficiency of the diffusion-controlled self-assembly process that leads to the formation of vesicles. At lower mixing speeds, the interdiffusion of solvent is slower, leading to the formation of larger vesicles. On the other hand, higher mixing speeds can increase the rate of solvent interdiffusion and result in the formation of smaller vesicles. Therefore, controlling the mixing speed in a microfluidic system can provide a means to regulate the size of vesicles formed during self-assembly[47]. Microfluidic self-assembly formulation using micromixer was performed with a variation of total flow rate (TFR) of 100, 200, 500 and 1000 µL.min^{-1}. Initial copolymer concentration was set at 10 mg.mL^{-1} in organic solvent, and organic/aqueous solvent ratios were set at 20/80 %vol for DMSO/PBS and 60/40 %vol for Acetone/Glucose. Hydrodynamic diameter and PDI were systematically measured by DLS after purification (Figure 27 and Figure 28). When acetone/glucose was used as organic/aqueous pair, no impact on hydrodynamic diameter is observed according to the TFR. However, for DMSO/PBS condition, a trend is visible with an increase of vesicles diameter when TFR is decreased. Range of vesicle size reachable by variation of TFR goes from 166 nm, with a TFR of 1000 µL.min^{-1}, to 218 nm, with a TFR of 100 µL.min^{-1}. Slower flow rates are hard to reach from Mitos pumps as they cannot deliver lower flow rates lower than 20 µL.min^{-1} each. To reach lower TFR for DMSO/PBS conditions, syringe driver from Harvard apparatus was used instead of Mitos pump. It was used to reproduce the 100 µL.min^{-1} to ensure that injecting apparatus doesn't change experiment results, and to reach a minimum TFR of 50 µL.min^{-1}. Observed tendency is confirmed with the highest D_H obtained at 242 nm for the minimal TFR of 50 µL.min^{-1}.

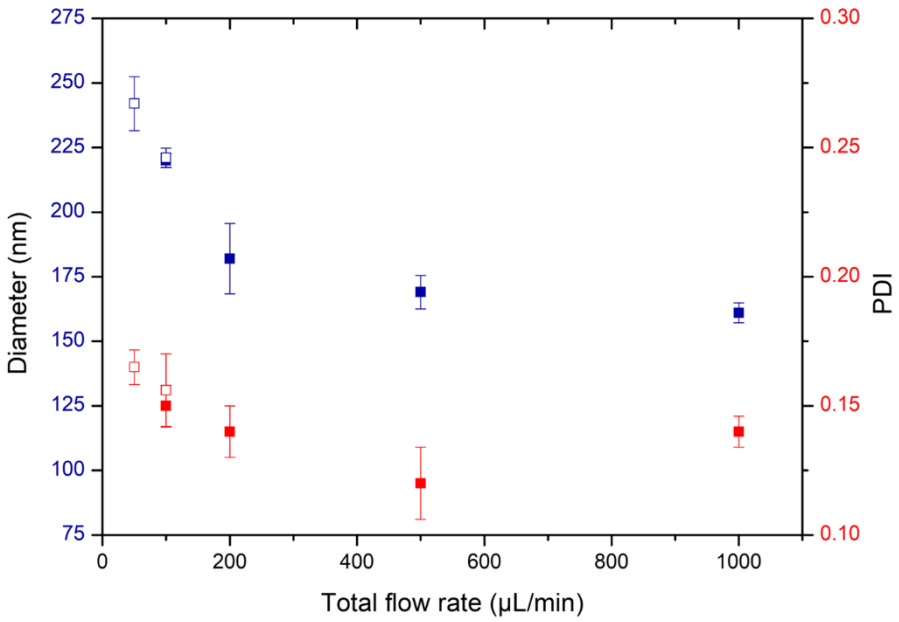

***Figure 27**: Hydrodynamic diameter and PDI measured by DLS 90° for purified PEG_{22}-b-$PTMC_{51}$ nanoparticles formulated by varying TFR in DMSO/PBS solvent, setting a TFR from 100 to 1000 µL.min^{-1}. Each value corresponds to the mean size value of 3 experiments and error bars correspond to standard deviation. Full squares represent experiments done with Mitos pumps and empty ones with Harvard syringe driver.*

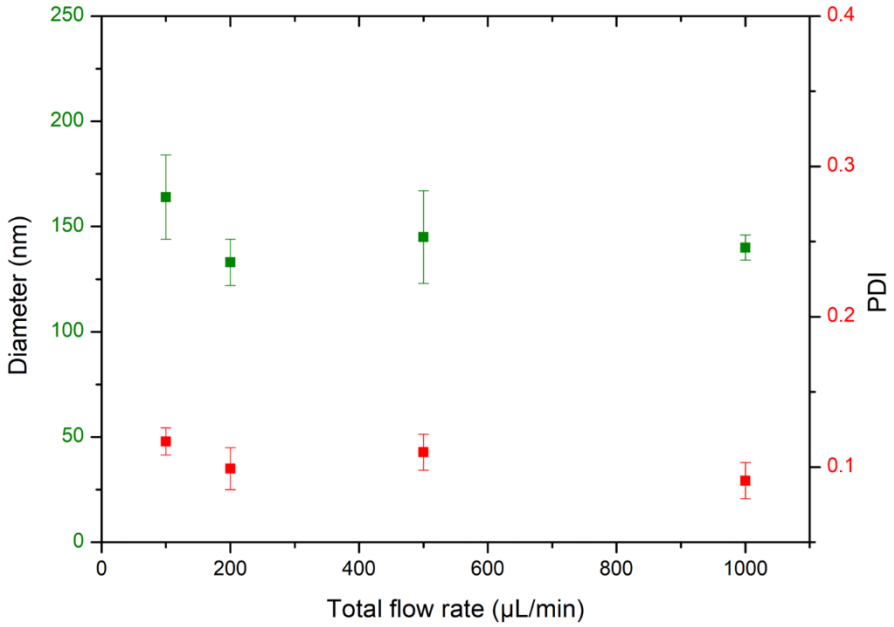

***Figure 28**: Hydrodynamic diameter and PDI measured by DLS 90° for purified PEG_{22}-b-$PTMC_{51}$ nanoparticles formulated by varying TFR in Acetone/glucose solvent, setting a TFR from 100 to 1000 µL.min^{-1}. Each value corresponds to the mean size value of 3 experiments and error bars correspond to standard deviation.*

To ensure vesicular shape of nanoparticles, Multi Angle Light Scattering (MALS) was performed to measure R_G, R_H, and deducting shape factor $\rho = R_G/R_H$. The SLS and DLS curves, as well as the fitting equations, can be found in the appendix (Figure A5, A10-A12). The results obtained from both the DLS 90° measurement and MALS measurement were compiled in Table 2. The shape factors obtained between 1.10 and 1.22 are in agreement with a vesicular shape. Cryo-TEM was performed for samples with minimum and maximum TFR to confirm the formation of polymersomes. (Figure 29)

***Table 6 :** Hydrodynamic radius and radius or gyration of polymersomes (determined by DLS 90°, MALS and Cryo-TEM) obtained by microfluidic-assisted self-assembly with different TFR. [a] Radius R_{TEM} is determined by an average measurement from approximately 50 vesicles.*

Total flow rate	**DLS 90°**		**MALS Measurements**			**Cryo-TEM**
µL.min^{-1}	R_H (nm)	PDI	R_g (nm)	R_H (nm)	$\rho=R_G/R_H$	R_{TEM}[a]
1000	83	0.14	82	67	1.22	72 ± 16
500	85	0.11	90	76	1.19	
200	104	0.13	75	68	1.10	
100	109	0.13	90	77	1.17	113 ± 25

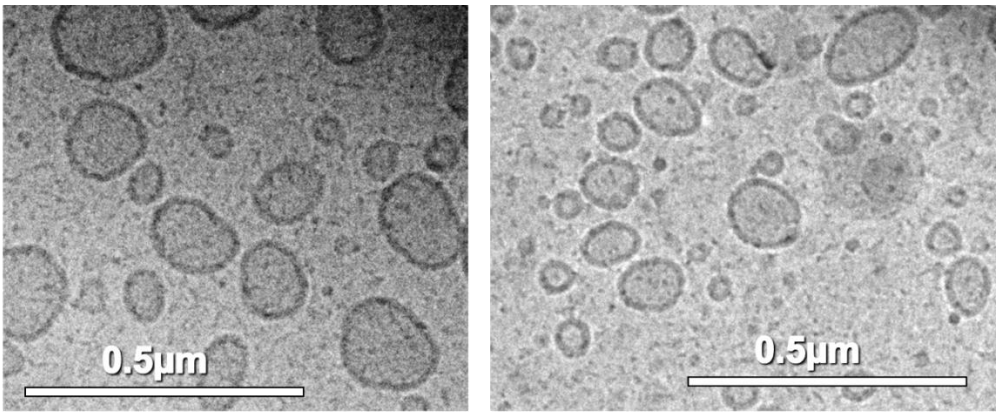

Figure 29: *Representative TEM images for different conditions of PEG_{22}-b-$PTMC_{51}$ polymersomes formulation when using a micromixer system and DMSO/PBS as organic/aqueous solvent with two extremes initial TFR of 100 µL.min^{-1}(left) and 1000 µL.min^{-1} (right). Scale bar corresponds to 0.5 µm.*

This behavior is once again in agreement with a nucleation-growth mechanism where a longer mixing rates allows more time for pre-formed colloidal systems to grow before being kinetically trapped.[15,50] By decreasing the TFR, a slower interdiffusion of solvent is obtained delaying the time to reach water content that kinetically trap the structure. Thus, when increasing interdiffusion time, copolymer chains self-assembly takes place for a longer time. Consequently, nanoparticles with larger aggregation number and larger diameters are obtained. This study confirms that two parameters have a major role to tune vesicle diameter using microfluidic assisted self-assembly of PEG_{22}-*b*-$PTMC_{51}$. As copolymer concentration, total flow rate is also an interesting parameter to play with.

4.3. Impact on solvent removal conditions on vesicle formation

As previously demonstrated, the self-assembly of PEG_{22}-b-$PTMC_{51}$ vesicles formulated in acetone/glucose leads to the formation of vesicles with a size around 150 nm that are not influenced by the initial copolymer concentration or the TFR. In the case of this formulation conditions, the impact of organic solvent removal was evaluated on the nucleation-growth mechanism for vesicle formation.

Solution of copolymer at 10 mg.mL^{-1} in acetone was used in microfluidic assisted self-assembly experiment. Ratio was kept at 60/40 % v/v and TFR at 1000 µL.min^{-1}. Analysis of these suspensions before acetone evaporation was evaluated by DLS 90°C and a mean hydrodynamic diameter of 65 ± 10 nm and a PDI of 0.21 ± 0.05 was measured. After acetone removal, the hydrodynamic diameter was increased twice compared to those obtained before acetone removal. It seems that the shape and the size of formed nanoparticle is not kinetically immobilized after the passage inside the microfluidic chip, and that vesicle growth continue to occur during organic solvent removal. We investigated the impact of evaporation on final size of obtained vesicles. Acetone was evaporated with and without the presence of nitrogen flows with different pressures, giving us different evaporation times: 30 min, 2h15 and 4h15. Evaporation is considered complete when acetone mass is withdrawn from sample. Hydrodynamic diameter and PDI were systematically measured by DLS after purification (as represented Figure 30). The increase of evaporation time leads to the formations of larger vesicles,

with a minimal size of 140 nm after 30 min of evaporation and a maximal size of 280 nm after 4h15 of evaporation.

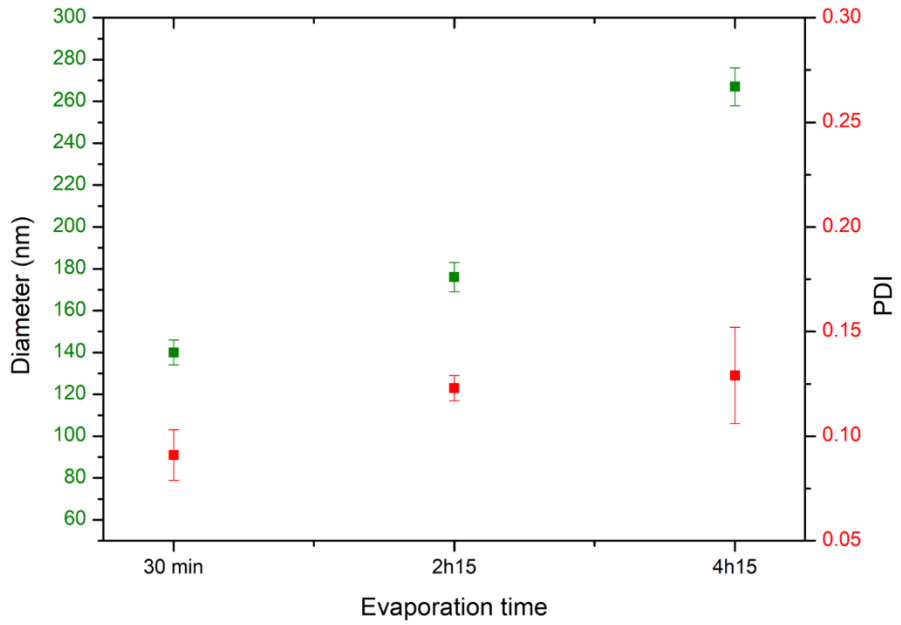

Figure 30: *Hydrodynamic diameter and PDI measured by DLS 90° for purified PEG_{22}-b-$PTMC_{51}$ nanoparticles formulated by varying the evaporation time during evaporation when Acetone/glucose (60/40 %vol) solvent are used for formulation. Each value corresponds to the mean size value of 3 experiments and error bars correspond to standard deviation.*

The observed phenomenon is consistent with a nucleation growth mechanism, in which microfluidics serves as the nucleation process, and removal of the organic solvent leads to vesicle growth. Evaporation of acetone results in an increase in water content, and as previously demonstrated, the rate at which the solvent transitions from a good solvent to a bad one is crucial for controlling vesicle size. As microfluidic chips may seem unnecessary for vesicle growth, we attempted manual nanoprecipitation by mixing a 10 $mg.mL^{-1}$ solution of PEG_{22}-b-$PTMC_{51}$ in a 60/40 % v/v acetone/glucose solution under magnetic stirring at 150 rpm. However, after acetone evaporation, we obtained a suspension with a PDI higher than 0.15, indicating a polydisperse population of nanoparticles. Microfluidic chips, on the other hand, create a controlled nucleation process that leads to well-defined nanoparticles, resulting in a homogenous population of vesicles. However, it is crucial to control the conditions of organic solvent removal to prevent modification of the shape and size of the suspensions after controlled self-assembly by microfluidic. In conclusion, microfluidics remains the most efficient process to obtain a homogenous population of vesicles, but organic solvent removal conditions must be still controlled to ensure reproducibility.

4.4. Measuring mixing time in microfluidic chips

We first thought that micromixer chip presents interdiffusion of solvent by keeping a constant laminar regime. The time for solvent interdiffusion to occur in laminar regime is given by Stokes-Einstein diffusion equation (Equation II.2.):

$$t = \frac{\Delta^2}{D} \qquad II.2$$

were Δ (m) is the distance through which diffusion is occurring and D ($m^2.s^{-1}$) the coefficient diffusion.[51,52]

This equation shows that interdiffusion is not dependent on flow rate. Consequently, the TFR in microfluidic experiment has no influence on interdiffusion time and vesicle size should remain constant along flow rate variation. We decided to verify the laminar nature of flows in micromixer chip.

4.4.1. Laminar or chaotic flows in micromixer chip

In order to establish a correlation between flow rate and mixing time in the micromixer chip, we conducted an experiment in which we measured the mixing time while varying the TFR. To track the progress of the mixing process, we observed unmixed solvent lines visible in Figure 31. Interdiffusion is supposed to be complete when lines are no longer visible. We used a mixture of DMSO/PBS 20/80% v/v while total flow rate was varied from 100 to 1000 µL.min^{-1}.

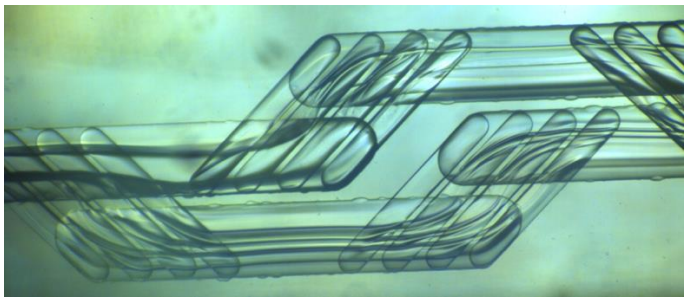

Figure 31 : *Observable flow lines in first micromixer unit of the micromixer chip.*

For the condition using a TFR of 1000 µL.min^{-1}, lines were not visible after the 4th micromixer unit, corresponding to an interdiffusion time of 89 ms (each mixing step having a volume of 0.37 µL) while for the condition with a TFR of 100 µL.min^{-1}, 8 micromixer units were necessary to obtain the same vanishing effect of lines running 100 µL.min^{-1}, corresponding to an interdiffusion time of 1,78 s. This observation is in agreement with previous results suggesting that at a higher flow rate, the formation of smaller nanoparticles is observed due to a faster kinetical entrapment, corresponding to a faster interdiffusion time of solvents.

To better understand this phenomenon, DMSO and solution of fluorescein in water was used as circulating flow and those were observed in the first micromixer unit by using a fluorescent microscope (OLYMPUS IX83 microscope using a filter to follow fluorescein fluorescence (λ_{ex} \ λ_{em} = 488\560 nm). Figure 32 compares lines obtained at 100 and 400 µL.min^{-1}. Although laminar flow lines are observed for lower TFR; the increase of TFR leads to the observation of flow lines that don't present laminar shapes anymore. It seems that inertial forces are involved in mixing process at higher flow rates as shown on figure 32, 400 µL.min^{-1}, leading to constrained flow lines. Inertial forces are supposed to be neglectable in laminar flow, this is not the case at higher TFR, and those additional forces will explain a better mixing at higher flow rate. In accordance with our explanation, Dolomite microfluidics reported that for micromixer chip : "At high flow rates, swirling occurs in the flow streams, reducing mixing time further."[53] The reduction of vesicle size with the increase of flow rate is confirmed to be the consequence of an increased mixing speed of solvent due to supplementary inertial forces. The

mix of both solvents at high TFR is not only the consequence of purely diffusive mechanism but also the combination with some chaotic regimes.

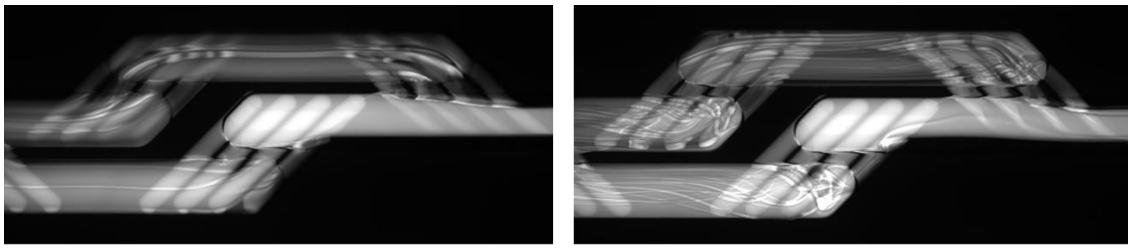

***Figure 32** : Pictures showing flow lines in the first micromixer unit of the micromixer chip. DMSO and fluoresceine solution 20/80 %vol are circulating in the chip with a TFR of 100 µL.min-1 (left) or 400 µL.min-1 (right). Fluorescent observation of laminar-like flow line at 100 µL.min-1and constrained flow lines at 400 µL.min-1 highlights the presence of inertial forces. OLYMPUS IX83 microscope equipped with a filter was used to follow fluoresceine fluorescence (λ_{ex}/ λ_{em} = 488/560 nm).*

4.4.2. Mixing speed influenced by flow rate in herringbone chip

To measure the mixing time in Herringbone glass chip from Darwin microfluidic, the fluorescence uniformization of a fluorescein solution was also performed by using an OLYMPUS IX83 microscope equipped with a filter to follow fluoresceine fluorescence (λ_{ex} \ λ_{em} = 488\560 nm). Unfortunately, the glass chip from Darwin Microfluidics exhibits significant roughness, which prevents the follow up of the uniformization of fluorescence, as illustrated in Figure 33. To overcome this issue, we decided to produce a PDMS Herringbone chip, as described in Ch 2.I.2. We used this PDMS reproduction to follow the interdiffusion of a solution of fluoresceine in water and DMSO. Figure 34 shows the interdiffusion throughout the chip. Pure DMSO, represented in black color on Figure 34, disappears along herringbone channel. However, no significant change in interdiffusion was observed throughout the length of the chip, when using 100 or 1000 µL.min^{-1} as TFR.

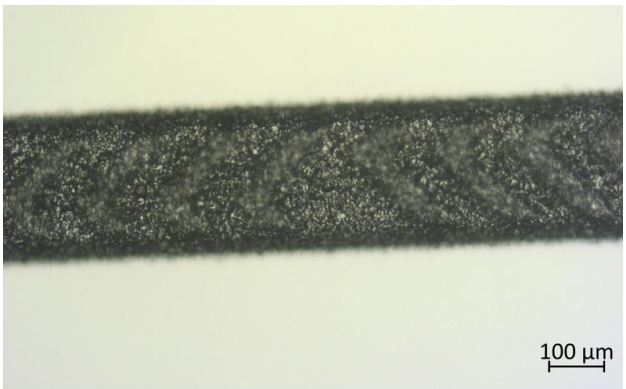

***Figure 33:** Roughness observed in Herringbone chip purchased from Darwin Microfluidics using an Axioskop 40 Zeiss microscope equipped with a AxioCam 105 color camera connected to a computer for acquisition.*

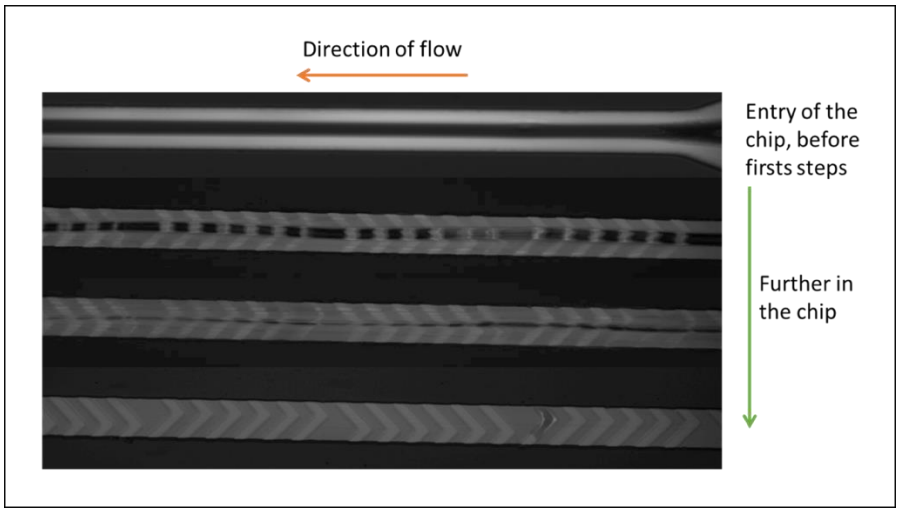

***Figure 34**: Following fluorescence uniformization in Herringbone chip to follow interdiffusion of solvents. We can see the disappearance of DMSO (dark in the middle) throughout the chip. OLYMPUS IX83 microscope equipped with a filter to follow fluoresceine fluorescence (λ_{ex} = 488 nm; λ_{em} = 560 nm).*

Stroock *et al.*[29] reports that the distance necessary for mixing to occur depends on Peclet number (Equation II.3) :

$$Pe = \frac{Ul}{D} \qquad II.3$$

with U as the average flow speed ($m.s^{-1}$), l (m) the cross-section dimension and D ($m^2.s^{-1}$) the diffusion coefficient.

They reported that multiplying Peclet number by a factor of ten do not drastically change distance necessary for complete inter diffusion to occur. If the distance is kept identical while decreasing flow rate, mixing time is thus increased. In the case of herringbone chip, the increase of Peclet number by ten has the consequence to divided by ten the time necessary for interdiffusion to occur. Thus, as herringbone chip is composed of 15 mixing units of 0.47 µL each and because uniform fluorescence is observed after approximately 14.5 mixers for both flow rates, we assume that interdiffusion time is 4.09 s at 100 $\mu L.min^{-1}$ and 409 ms at 1000 $\mu L.min^{-1}$. In conclusion, the impact of TFR with Herringbone chip will theoretically have a more important effect on vesicle size than the one observed using micromixer chip.

5. Conclusion

In this chapter, we explored several ways for the self-assembly of PEG_{22}-b-$PTMC_{51}$ into vesicles, also called polymersomes, with tunable size, in conditions allowing them to be ready to use for *in vivo*/ *in vitro* experiments.

We first proved the importance of choosing a physiological-like aqueous buffer when performing vesicle self-assembly. The sensitivity of polymersomes to osmotic pressure variation has been demonstrated by a significant decrease in their size when an external solvent exchange is performed from pure water to a medium mimicking physiological condition, going from 65 nm in water to 35 nm in physiological conditions. This transformation due to hypertonic shock could lead to uncontrolled bursting effect if drug loaded vesicles are placed in biological fluids with osmolarity disparities.

We succeeded in obtaining polymersomes prepared in buffer close to physiological conditions (pH = 7.4, 300 $mOsm.L^{-1}$) which will guarantee polymersomes integrity when administrated. The choice of organic solvents for polymersome self-assembly were evaluated to be the most biocompatible, by a selection of organic solvents present on the list of Class 3 solvents by Q3C- Tables and List Guidance for Industry from FDA, meaning a low toxicity when present in small quantities.

Critical water content to induce PEG_{22}-b-$PTMC_{51}$ self-assembly were measured through light scattering measurement for both organic solvents (Acetone and DMSO) and were used to optimize a minimal organic/aqueous solvent ratio to ensure formation of vesicles during all processes of formulation in microfluidic experiments. CWC in DMSO was measured around 11 %vol of aqueous solvent, depending on copolymer concentration, and CWC in Acetone was measured around 20 %vol aqueous solvent, in agreement with theoretical values of Hildebrand solubility parameters.

To develop a microfluidic method to produce polymersomes with the highest reliability and reproducibility, optimal aqueous/organic solvent ratio were evaluated for two pairs: acetone/glucose and DMSO/PBS pair. Advantage was taken over this study to compare two microfluidic chips with a fast-mixing process (Micromixer and Herringbone chip). Both microfluidic chip designs showed similar behavior, with a formation of vesicles with a low value for the polydispersity index under evaluated conditions.

We modified parameters in our microfluidic assisted process to study their influence on PEG_{22}-b-$PTMC_{51}$ polymersomes formation: influence of the choice of organic solvent, of aqueous/organic solvent ratio, of initial PEG_{22}-b-$PTMC_{51}$ concentration and of total flow rate.

Concerning the choice of organic solvent, no impact has been observed on polymersomes formation, as both DMSO and acetone lead to vesicle formation with a low value for the PDI. Study on variation of organic/aqueous ratio also shows no effect on vesicle formation. Concerning the influence of copolymer concentration, experiments were performed with DMSO/PBS as aqueous/organic solvent and an increase in size of obtained nanoparticles was observed according to copolymer concentration, with diameters ranging from 76 to 224 nm with a range of initial copolymer concentration from 1 to 30 $mg.mL^{-1}$. Concerning the impact of total flow rate on copolymer self-assembly, our process conditions enhanced an increase in vesicle size when the total flow rate is decreased, from 160 nm for the highest flow rate (1000 $\mu L.min^{-1}$), to 242 nm for the lowest one (50 $\mu L.min^{-1}$). Polydispersity index that remains below PDI = 0.15 for all conditions, highlights the

homogeneity of nanoparticle population, which were proven to keep a vesicular shape using multi angle light scattering and Cryo-TEM characterizations.

For the vesicles formulated with acetone/glucose as organic/aqueous solvent, no impact has been observed on vesicles size with the variation of copolymer concentration or total flow rate. However, our study highlighted that in the case of this organic/aqueous solvent pair, microfluidic system only allows nucleation step, and the step of nanoparticles growth occurs during acetone evaporation. Thus, the key parameter for tuning the size of vesicles, when working with acetone/glucose at 60/40 %vol in microfluidic assisted self-assembly, is the time for acetone evaporation. For instance, a fast evaporation (during 30 min) led to polymersomes with a size of 140 nm while a slow evaporation (during 4h15) led to a size of 280 nm.

In addition to providing a highly reproducible process for polymersome formation in terms of size and polydispersity index, microfluidic assisted self-assembly provides access to easily adjustable parameters to fine-tune their diameter. The proposed approach for the production of reproductible, monodisperse and ready to use polymersomes for *in vitro / in vivo* assays is a major advance in the production of nanocarriers, allowing for scale-up manufacturing while respecting pharmaceutical constraints.

6. Appendix

6.1. Viscosity and refractive index of DMSO/PBS and Acetone/Glucose mixtures

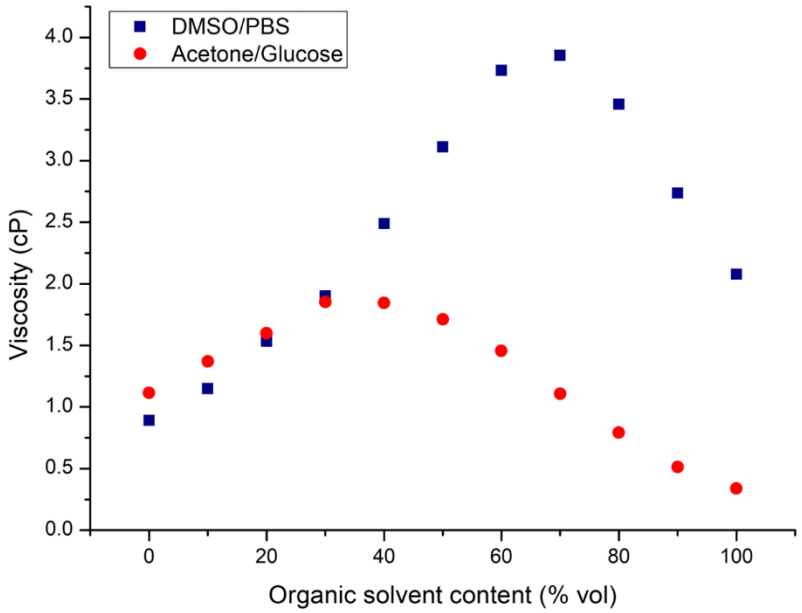

Figure A1: *Evolution of viscosity of DMSO/PBS and Acetone/Glucose mixtures depending on the organic solvent content, measured using a falling ball viscosimeter Microviscosimeter Lovis 2000 m/ME.*

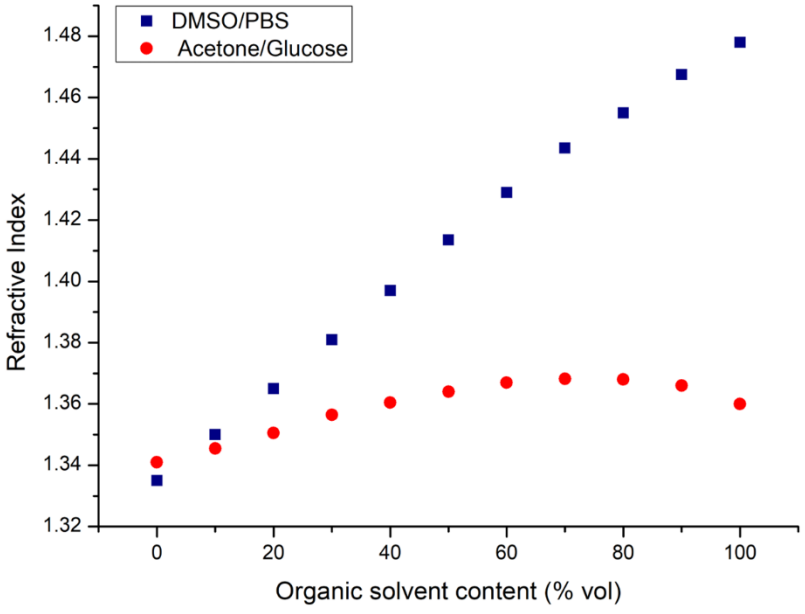

Figure A2: *Evolution of Refractive Index of DMSO/PBS and Acetone/Glucose mixtures depending on the organic solvent content, measured using a Carl Zeiss refractometer.*

Values of viscosity and refractive index were measured according to the mixture of organic/aqueous solvent: DMSO/PBS and acetone/glucose. Viscosity was measured with a falling ball viscosimeter *Microviscosimeter Lovis 2000 m/ME* and refractive index with a Carl Zeiss refractometer. Values were used in DLS measurement.

6.2. Solubility Parameters

Theoretical values for Hildebrand solubility parameters for PEG and PTMC along DMSO/PBS and acetone/glucose mixtures were calculated to be compared with critical water content measured for PEG_{22}-b-$PTMC_{51}$ self-assembly.

Function necessary to calculate solubility parameters are given as follow:

Molar attraction function:

$$F_t = \sum N_i \, F_{t,i} \qquad II.A.1$$

Molar Volume:

$$V = \sum N_i \, V_i \qquad II.A.2$$

Polar component of molar attraction function:

$$F_p = \sum N_i \, F_{p,i} \qquad II.A.3$$

Lyderson correction for non-ideality:

$$\Delta_T = \sum N_i \, \Delta_{T,i} \qquad II.A.4$$

Where N_i is the number of occurrences of a functional group i, V_i is the molar volume of the functional group i, $F_{t,i}$ is the molar attraction of the functional group i, $F_{p,i}$ is the polar component of the molar attraction function of a functional group i, and $\Delta_{T,i}$ is the Lyderson correction for non-ideality per functional group.[45] These parameters are calculated for both blocks of copolymer in Table A1:

***Table A1**: Molar attraction function, molar volume, polar content of molar attraction function and Lyderson correction for non-ideality given per chemical functional group leading to the calculation of those parameters for PEG and PTMC blocks. Green data are given from Hoy's system, blue ones are calculated using green data and above equations also coming from Van Krevelen[45].*

	F_t ($J^{1/2}.cm^{3/2}.mol^{-1}$)	F_p ($J^{1/2}.cm^{3/2}.mol^{-1}$)	Δ_T	V ($cm^3.mol^{-1}$)
$-CH_2-$	269	0	0.02	15.55
-O-	235	216	0.018	6.45
-COO-	640	528	0.05	23.7
PEG	773	216	0.058	37.55
PTMC	1682	744	0.128	76.8

Solubility parameters are then calculated using the following equations [45] :

Contribution of dispersion forces (polymer):

$$\delta_d = \left(\delta_t^2 - \delta_p^2 - \delta_H^2\right)^{1/2} \qquad II.A.5$$

Contribution of polar forces (polymer):

$$\delta_p = \delta_t \left(\frac{1}{\alpha} \frac{F_p}{F_T + \frac{277}{\bar{n}}} \right) \qquad II.A.6$$

$$\alpha = \frac{777\,\Delta_T}{V} \qquad II.A.7$$

Contribution of hydrogen bonding (polymer):

$$\delta_H = \delta_t \left(\frac{\alpha - 1}{\alpha}\right)^{1/2} \qquad II.A.8$$

Solubility parameter (polymer):

$$\delta = \delta_t = \frac{F_t + \frac{277}{\bar{n}}}{V} \qquad II.A.9$$

$$\delta = \left(\delta_p^2 + \delta_H^2 + \delta_d^2\right)^{1/2} \qquad II.A.10$$

$$\bar{n} = \frac{0.5}{\Delta_T} \qquad II.A.11$$

Contribution to solubility parameter for a mixture of 2 solvents:

$$\delta_n = x\,\delta_{n_{S1}} + (1 - x)\delta_{n_{S2}} \qquad II.A.12$$

Polymer – Solvent solubility:

$$\Delta\delta_{P-S} = \begin{pmatrix} \left(\delta_{d,P} - \delta_{d,S}\right)^2 + \\ \left(\delta_{p,P} - \delta_{p,S}\right)^2 + \\ \left(\delta_{H,P} - \delta_{H,S}\right)^2 \end{pmatrix}^{1/2} \qquad II.A.13$$

Calculations are gathered in table A2.

***Table A2**: Contribution of dispersion forces, polar forces and hydrogen bonding in addition with solubility parameter calculates for solvents and PEG and PTMC blocks. Green data are from Subrahmanyam et al.[54] and Hansen-solubility website, blue ones are calculated using green data and above equations also coming from Van Krevelen.*

	δ_d ($J^{1/2}/cm^{3/2}$)	δ_p ($J^{1/2}/cm^{3/2}$)	δ_h ($J^{1/2}/cm^{3/2}$)	δ ($J^{1/2}/cm^{3/2}$)
Water	15.5	16	42.3	47.8
Acetone	15.5	10.4	7	19.9
DMSO	18.4	16.4	10.2	26.7
PEG	16.7	10.1	8.8	21.4
PTMC	15.2	13.1	10.9	22.8

Van Krevelen *et al*.[45] reported that polymers are considered soluble in solvents when polymer-solvent solubility parameter : $\Delta\delta_{P\text{-}S} < 5$. We calculated here solubility parameters of DMSO/water and acetone/water mixtures as well as compatibility between solvents and blocks of copolymer (PEG and PTMC) along water addition in organic solvent. Here we are looking for water content leading to $\Delta\delta_{P\text{-}S} = 5$ for both blocks of copolymer which may predict CWC for PEG-*b*-PTMC self-assembly. (Table A3 and A4)

***Table A3**: Contribution of dispersion forces, polar forces and hydrogen bonding in addition with solubility parameter calculates for solvents and PEG and PTMC blocks in acetone / water mixture, in addition with copolymer block-solvent solubility parameters.*

Water content	δ_d	δ_p	δ_h	$\delta_{Solvent}$	$\Delta\delta_{S\text{-}P}$ PEG	$\Delta\delta_{S\text{-}P}$ PTMC
%vol	($J^{1/2}/cm^{3/2}$)	($J^{1/2}/cm^{3/2}$)	($J^{1/2}/cm^{3/2}$)	($J^{1/2}/cm^{3/2}$)		
2%	15.5	10.5	7.7	20.3	1.7	4.1
4%	15.5	10.6	8.4	20.6	1.4	3.5
6%	15.5	10.7	9.1	20.9	1.4	2.9
8%	15.5	10.8	9.8	21.3	1.8	2.5
10%	15.5	11.0	10.5	21.7	2.3	2.2
12%	15.5	11.1	11.2	22.1	2.9	2.0
14%	15.5	11.2	11.9	22.5	3.6	2.2
16%	15.5	11.3	12.6	23.0	4.2	2.5
18%	15.5	11.4	13.4	23.4	4.9	3.0
20%	15.5	11.5	14.1	23.9	5.6	3.5
22%	15.5	11.6	14.8	24.4	6.3	4.1
24%	15.5	11.7	15.5	24.9	7.0	4.8
26%	15.5	11.9	16.2	25.3	7.7	5.4

***Table A4**: Contribution of dispersion forces, polar forces and hydrogen bonding in addition with solubility parameter calculates for solvents and PEG and PTMC blocks in DMSO / Water mixture, in addition with copolymer block-solvent solubility parameters.*

Water content	δ_d	δ_p	δ_h	$\delta_{Solvent}$	$\Delta\delta_{S-P}$ PEG	$\Delta\delta_{S-P}$ PTMC
%vol	$(J^{1/2}/cm^{3/2})$	$(J^{1/2}/cm^{3/2})$	$(J^{1/2}/cm^{3/2})$	$(J^{1/2}/cm^{3/2})$		
2%	18.3	16.4	10.8	26.9	6.8	4.6
4%	18.3	16.4	11.5	27.1	7.0	4.6
6%	18.2	16.4	12.1	27.3	7.2	4.6
8%	18.2	16.4	12.8	27.6	7.5	4.8
10%	18.1	16.4	13.4	27.8	7.9	5.1

CWC of PEG-*b*-PTMC in DMSO is theoretically around 10% of water and CWC of PEG-*b*-PTMC in Acetone is theoretically around 26%. These water content represent the moment to which both blocks appear to be not soluble anymore in the organic/aqueous solvent mixture.

6.3. Scattered intensity of 100 nm latex under several stirring rate

Critical water content for copolymer self-assembly was measured using light scattering experiment (Vasco Kin mobile DLS) under magnetic stirring. Here we prove that only scattered intensity is relevant in such study under magnetic stirring. Analysis of a sample of polystyrene latex with a real size of 100 nm and with several magnetic stirring conditions shows that obtaining accurate particle sizes under magnetic stirring is not feasible. For instance, measurements report particle sizes as small as 14 nm under 100 rpm of agitation, whereas measurements taken without agitation report particle sizes of 99 nm. These findings suggest that DLS measurements under magnetic stirring may produce inconsistent and unreliable results, which should be considered when interpreting such data.

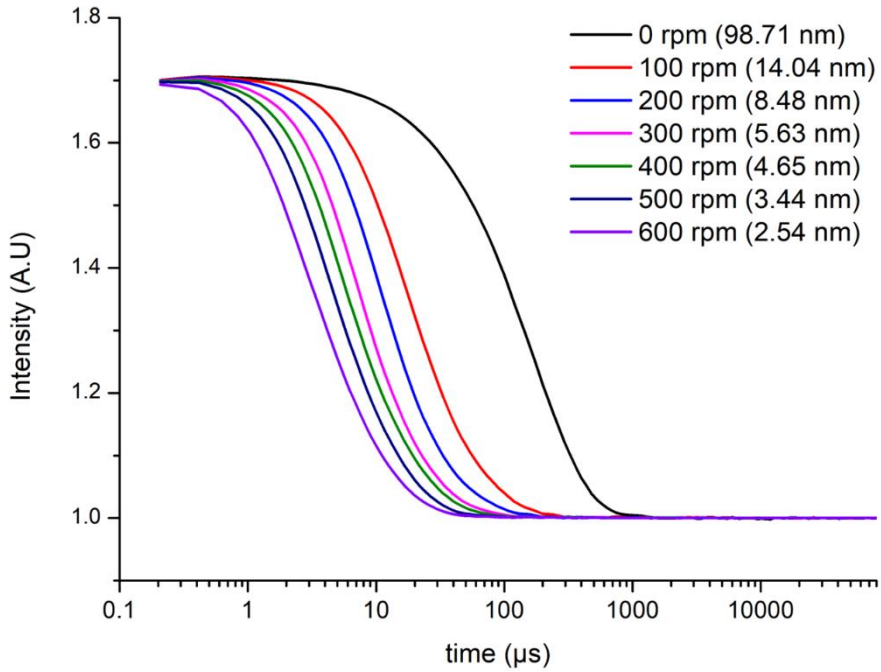

***Figure A3**: Correlograms of 100 nm latex particles under different stirring conditions and related diameters, measured with VascoKin DLS, highlighting the impact of stirring on nanoparticle size measurement.*

6.4. Multi-Angle Light Scattering, calculations and methods

MALS was used to ensure vesicular shape of object made with microfluidic assisted self-assembly of PEG-*b*-PTMC. SLS and DLS measurement were performed as described above and collected data as following:

Static Light Scattering results were fitted with a Berry plot where[55,56].

$$\sqrt{I(q)} = \sqrt{I(0)}\left(\frac{1-q^2R_G^2}{6}\right) \qquad II.A.14$$

Equation of second order was used to fit the non-linear behavior of the data that might be due to polydispersity. In this case, $\sqrt{I(x)} = A + Bx + Cx^2$ with x = q².

The radius of gyration R_G can be isolated using the following relation: $R_G = \sqrt{\frac{-6B}{A}}$.

Dynamic light scattering was plotted as Γ= Dq² according to Fick's law of diffusion where D ($m^2.s^{-1}$) is the particles diffusion coefficient connected to R_H by the Stokes-Einstein relation: $R_H = k_bT/(6\pi\eta D)$ with k_b the Boltzmann constant, T the temperature (K) and η the solvent viscosity (cP).

Figure A4 to A13 shows SLD and DLS measurements for samples of PEG-*b*-PTMC self-assembled nanoparticles.

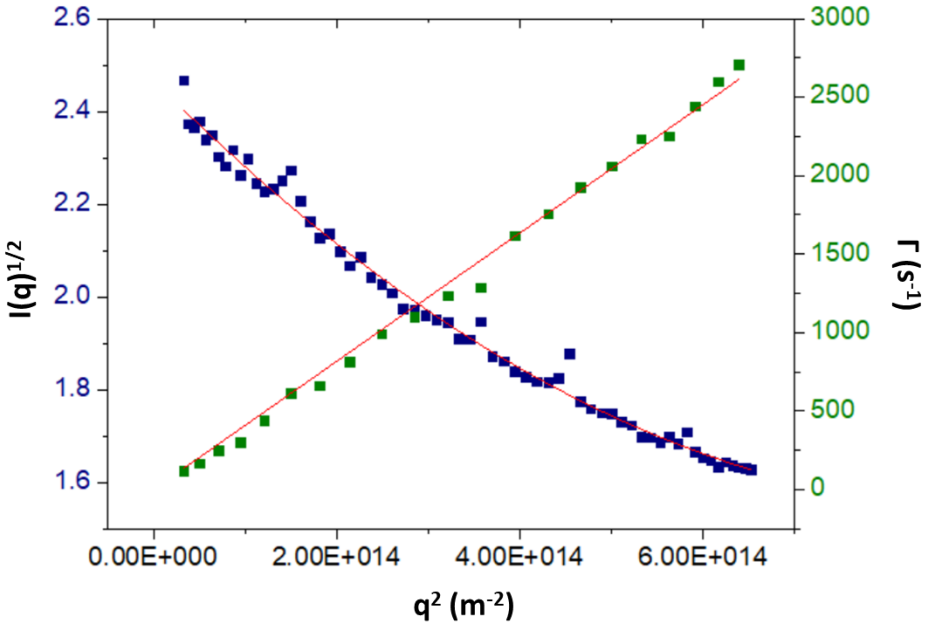

***Figure A4**: SLS (blue) and DLS (green) measurements obtained from MALS analyze of a nanoparticles solution obtained from microfluidic assisted self-assembly of PEG-b-PTMC copolymer. Initial copolymer concentration 5 mg/mL, total flow rate 1000 µL/min. (red) trends. SLS trend : $\sqrt{I(x)}$ = 2.47 – 1.97E-15 x + 1.05E-30 x² ; R² = 0.9907. DLS trend : Γ(x) = 4.07E-12 x ; R² = 0.9982.*

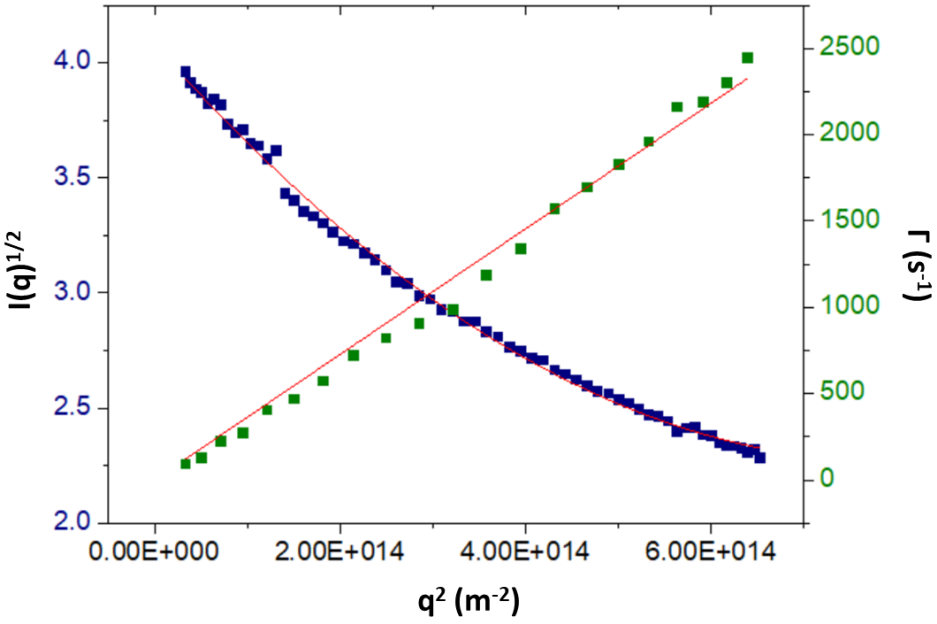

***Figure A5**: SLS (blue) and DLS (green) measurements obtained from MALS analyze of a nanoparticles solution obtained from microfluidic assisted self-assembly of PEG-b-PTMC copolymer. Initial copolymer concentration 10 mg/mL, total flow rate 1000 µL/min. (red) trends. SLS trend : $\sqrt{I(x)}$ = 4.079 – 4.55E-15 x + 2.86E-30 x² ; R² = 0.9968. DLS trend : Γ(x) = 3.64E-12 x ; R² = 0.9965.*

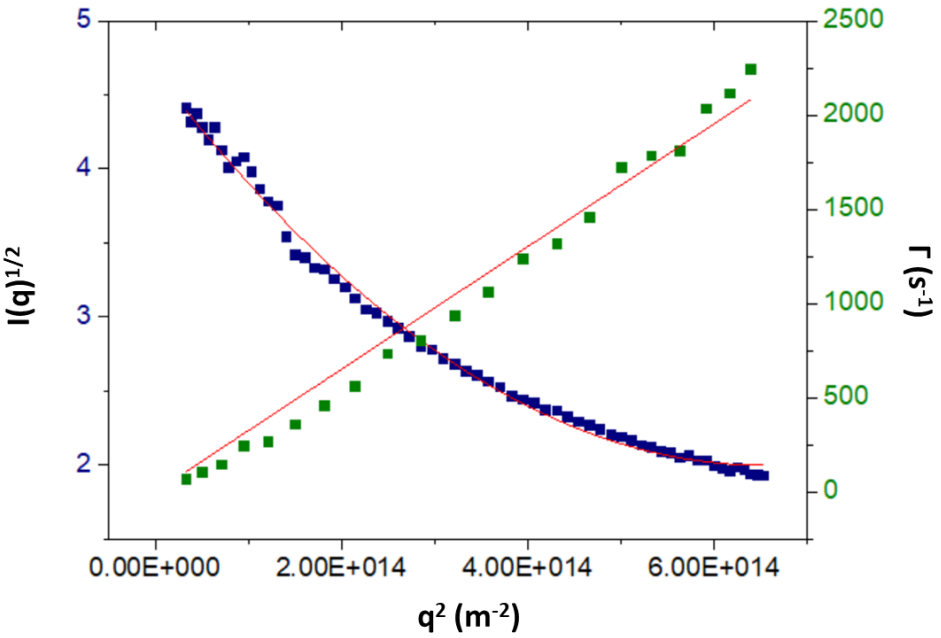

***Figure A6**: SLS (blue) and DLS (green) measurements obtained from MALS analyze of a nanoparticles solution obtained from microfluidic assisted self-assembly of PEG-b-PTMC copolymer. Initial copolymer concentration 15 mg/mL, total flow rate 1000 µL/min. (red) trends. SLS trend : $\sqrt{I(x)}$ = 4.65 – 8.13E-15 x + 6.61E-30 x² ; R² = 0.9949. DLS trend : Γ(x) = 3.26E-12 x ; R² = 0.9935.*

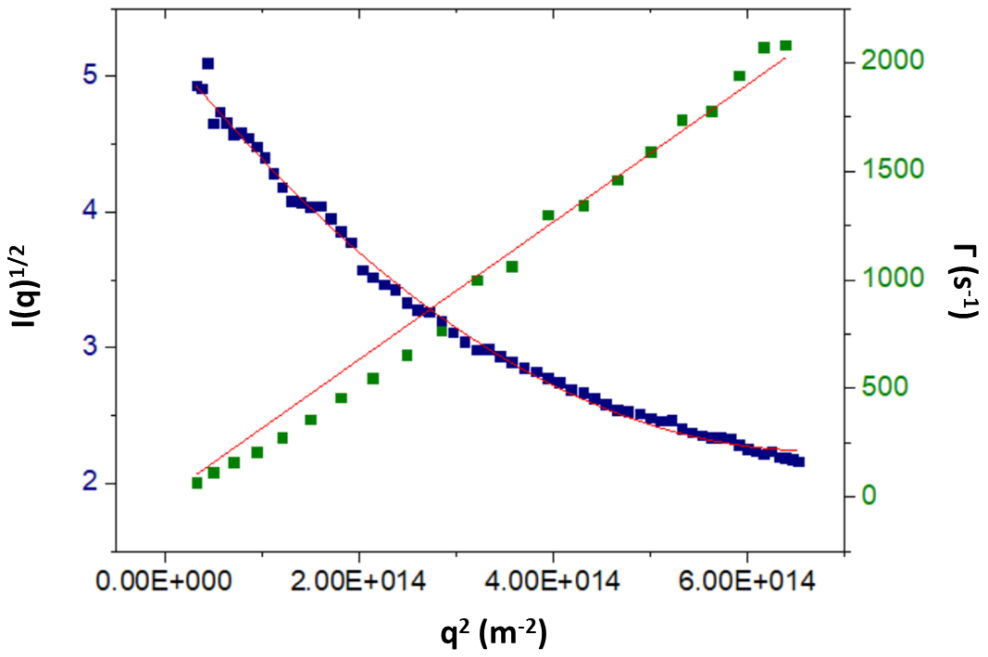

***Figure A7**: SLS (blue) and DLS (green) measurements obtained from MALS analyze of a nanoparticles solution obtained from microfluidic assisted self-assembly of PEG-b-PTMC copolymer. Initial copolymer concentration 20 mg/mL, total flow rate 1000 µL/min. (red) trends. SLS trend : $\sqrt{I(x)}$ = 5.21 – 8.86E-15 x + 6.61E-30 x² ; R² = 0.9952. DLS trend : Γ(x) = 3.16E-12 x ; R² = 0.9952.*

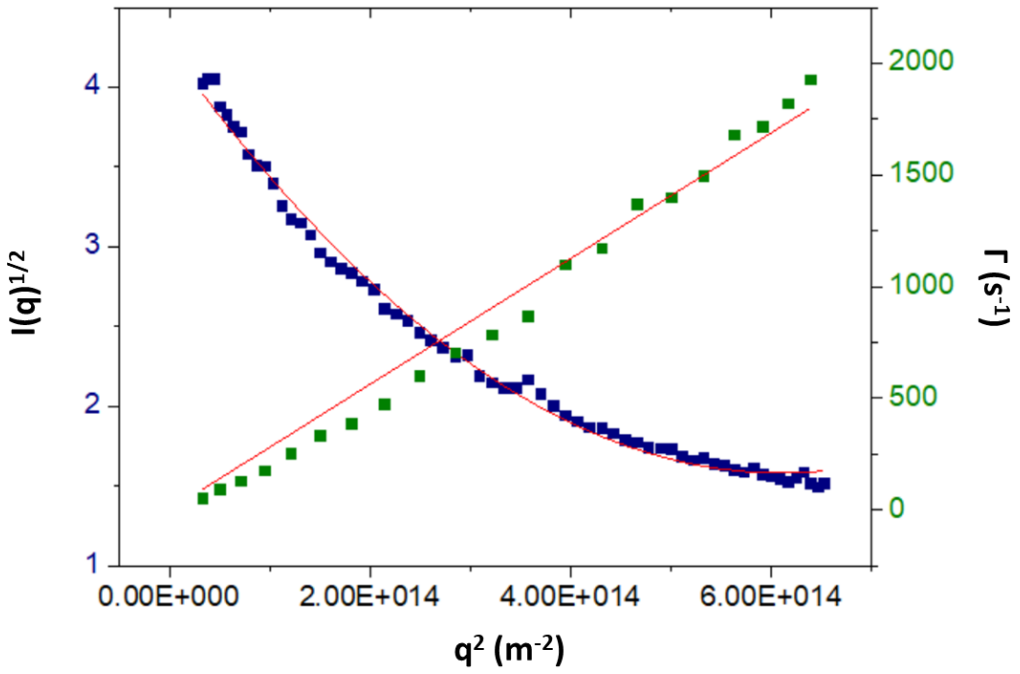

***Figure A8**: SLS (blue) and DLS (green) measurements obtained from MALS analyze of a nanoparticles solution obtained from microfluidic assisted self-assembly of PEG-b-PTMC copolymer. Initial copolymer concentration 25 mg/mL, total flow rate 1000 µL/min. (red) trends. SLS trend : $\sqrt{I(x)}$ = 4.24 – 8.70E-15 x + 7.13E-30 x² ; R² = 0.9933. DLS trend : Γ(x) = 2.82E-12 x ; R² = 0.9933.*

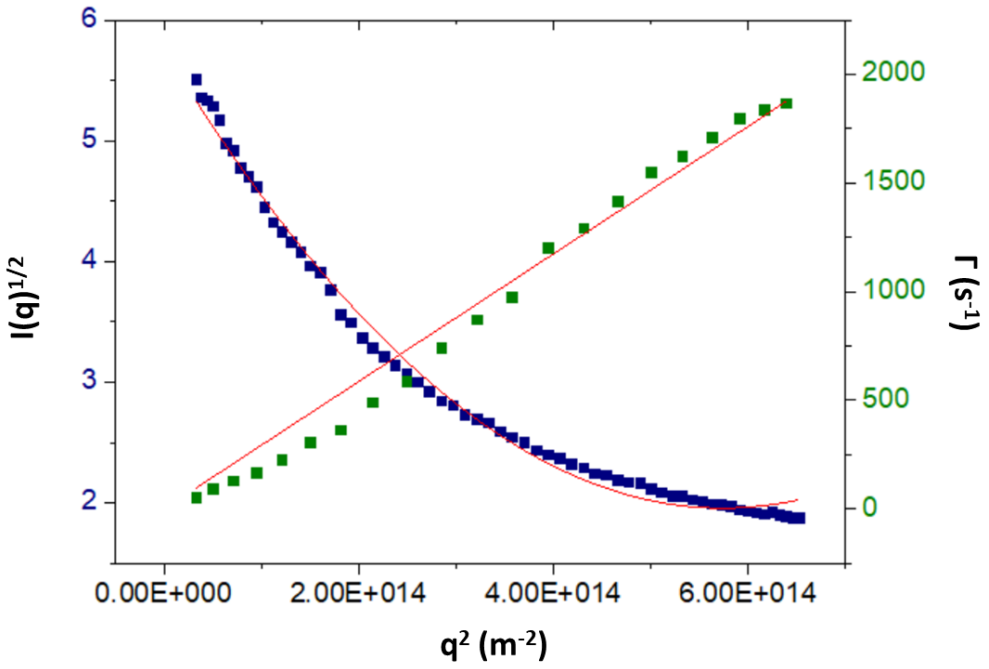

***Figure A9**: SLS (blue) and DLS (green) measurements obtained from MALS analyze of a nanoparticles solution obtained from microfluidic assisted self-assembly of PEG-b-PTMC copolymer. Initial copolymer concentration 30 mg/mL, total flow rate 1000 µL/min. (red) trends. SLS trend : $\sqrt{I(x)}$ = 5.75 – 1.32E-14 x + 1.15E-29 x² ; R² = 0.9930. DLS trend : Γ(x) = 2.93E-12 x ; R² = 0.9934.*

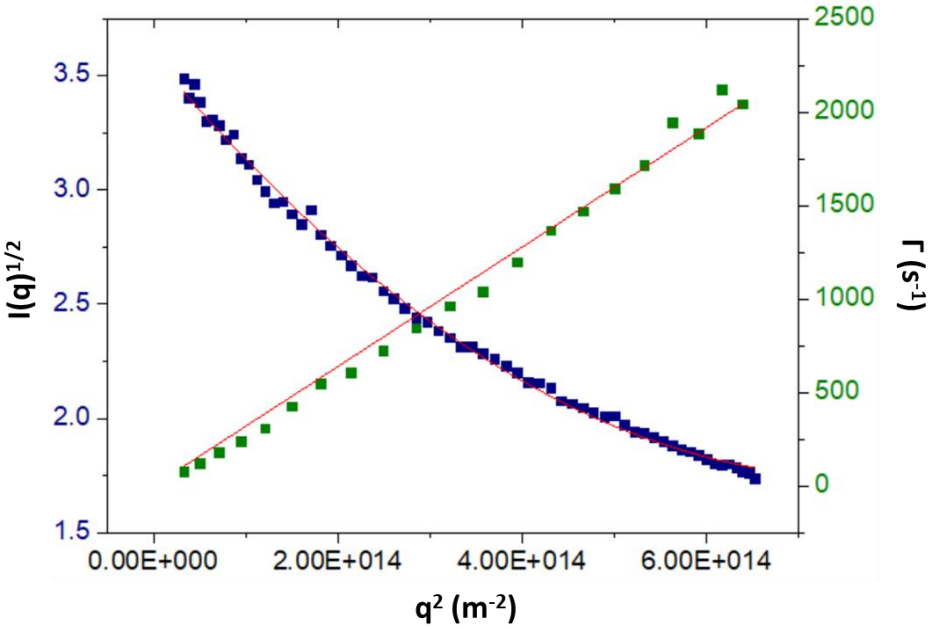

***Figure A10**: SLS (blue) and DLS (green) measurements obtained from MALS analyze of a nanoparticles solution obtained from microfluidic assisted self-assembly of PEG-b-PTMC copolymer. Initial copolymer concentration 10 mg/mL, total flow rate 100 µL/min. (red) trends. SLS trend : $\sqrt{I(x)}$ = 3.58 – 4.79E-15 x + 3.13E-30 x² ; R² = 0.9969. DLS trend : Γ(x) = 3.19E-12 x ; R² = 0.9968.*

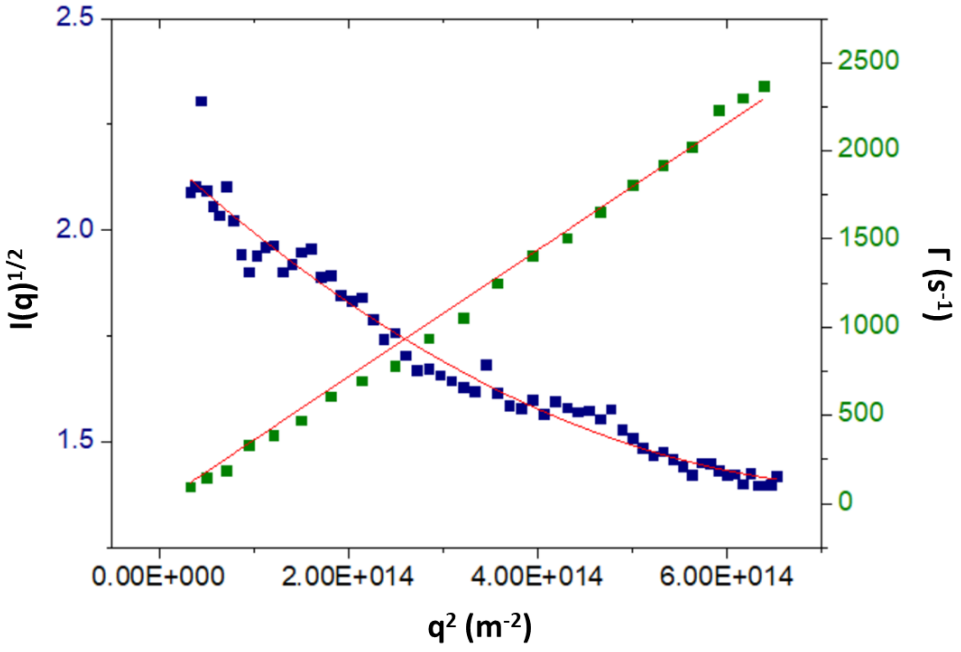

***Figure A11**: SLS (blue) and DLS (green) measurements obtained from MALS analyze of a nanoparticles solution obtained from microfluidic assisted self-assembly of PEG-b-PTMC copolymer. Initial copolymer concentration 10 mg/mL, total flow rate 200 µL/min. (red) trends. SLS trend : $\sqrt{I(x)}$ = 2.19 – 2.05E-15 x + 1.32E-30 x² ; R² = 0.9677. DLS trend : Γ(x) = 3.59E-12 x ; R² = 0.9980.*

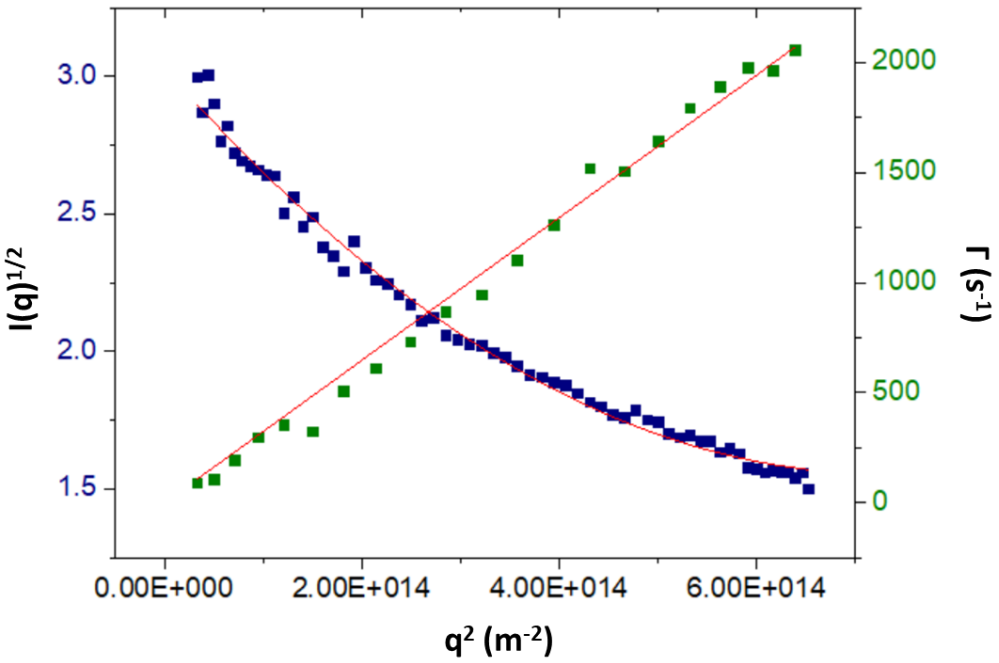

***Figure A12**: SLS (blue) and DLS (green) measurements obtained from MALS analyze of a nanoparticles solution obtained from microfluidic assisted self-assembly of PEG-b-PTMC copolymer. Initial copolymer concentration 10 mg/mL, total flow rate 500 µL/min. (red) trends. SLS trend : $\sqrt{I(x)}$ = 3.03 – 4.06E-15 x + 2.79E-30 x² ; R² = 0.9906. DLS tend : Γ(x) = 3.24E-12 x ; R² = 0.9969.*

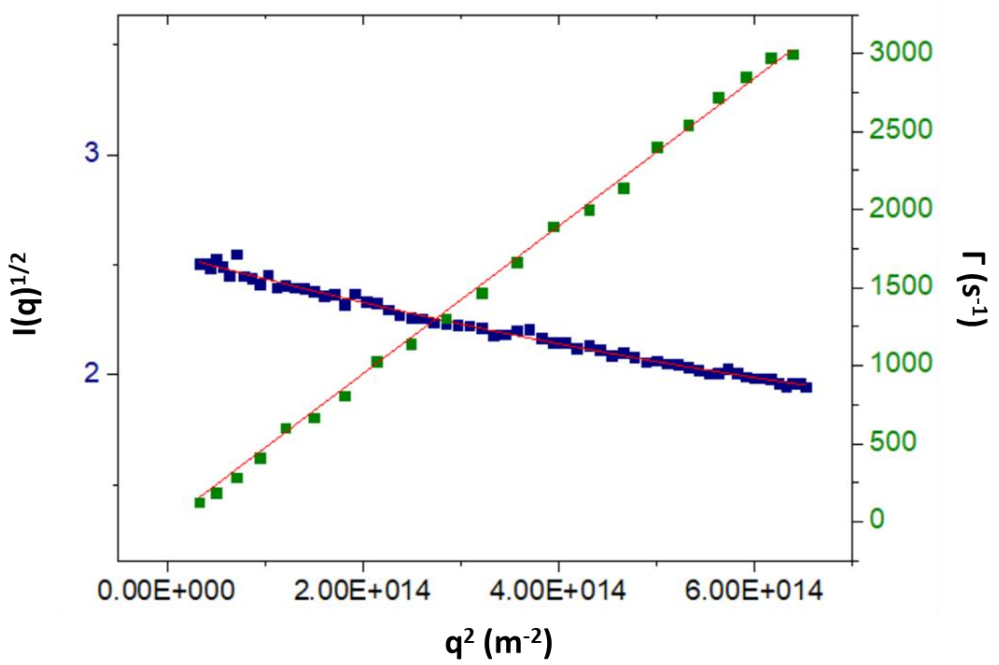

***Figure A13**: SLS (blue) and DLS (green) measurements obtained from MALS analyze of a nanoparticles solution obtained from microfluidic assisted self-assembly of PEG-b-PTMC copolymer in an Herringbone chip. Initial copolymer concentration 10 mg/mL, total flow rate 1000 µL/min. (red) trends. SLS trend : $\sqrt{I(x)}$ = 2.55 – 1.19E-15 x + 4.25E-31 x² ; R² = 0.9900. DLS trend : Γ(x) = 4.74E-12 x ; R² = 0.9994.*

6.5. Dynamic light scattering

DLS measurement is a non-destructive analysis allowing to measure hydrodynamic radius (R_h) and size distribution (represented as polydispersity index PDI) of particles in a suspension. Measurement relies on Brownian movement of particles in solution, with a random movement of particles in a fluid due to collisions with the surrounding molecules with a consequence for particles with smaller size to move faster than larger particles. This movement can cause particles to spread out over time, which is known as the diffusion D. When particles are exposed to a laser light, light diffused by particle fluctuate over time due to Brownian motion. This result in a fluctuating signal and which intensity of fluctuation depending on particle size. When particles are small, light is diffused rapidly, leading to a fast fluctuation in scattered intensity. For larger particles, a scattered intensity with a slower fluctuation in intensity is produced (Figure A14).

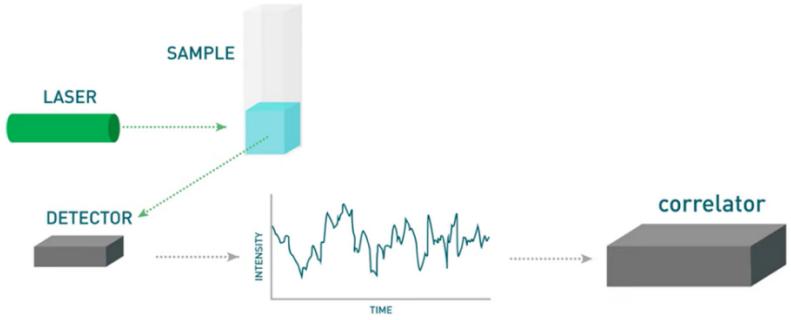

***Figure A14**: General representation of DLS measurement (from MalverPanalytical)*[57]

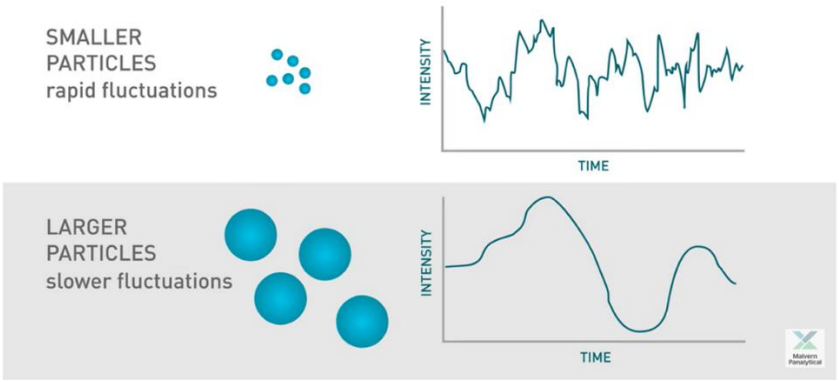

***Figure A15**: Scattered signal given by nanoparticles showing the evolution of signal fluctuation with particle size ((from MalverPanalytical)*[57]

During DLS measurement, several acquisitions of scattered signal are taken and compared to the first signal measured. Scattered signal separated by milliseconds are more similar than those separated by seconds. The evolution of signal being less and less similar to the first one measured is represented by the autocorrelation function (Figure A15).

The autocorrelation function reflects the rate at which particles move in and out of the detection volume over time. The correlation decreases as the time difference between the two measurements increases. The shape of the autocorrelation function provides information about the

size distribution of the particles, with larger particles producing slower fluctuations and broader autocorrelation functions than smaller particles. In particular, the decay rate of the autocorrelation function is related to the diffusion coefficient of the particles, which in turn is related to their hydrodynamic size. Smaller particles diffuse faster and produce a faster decay rate in the autocorrelation function, while larger particles diffuse more slowly and produce a slower decay rate (Figure A16).

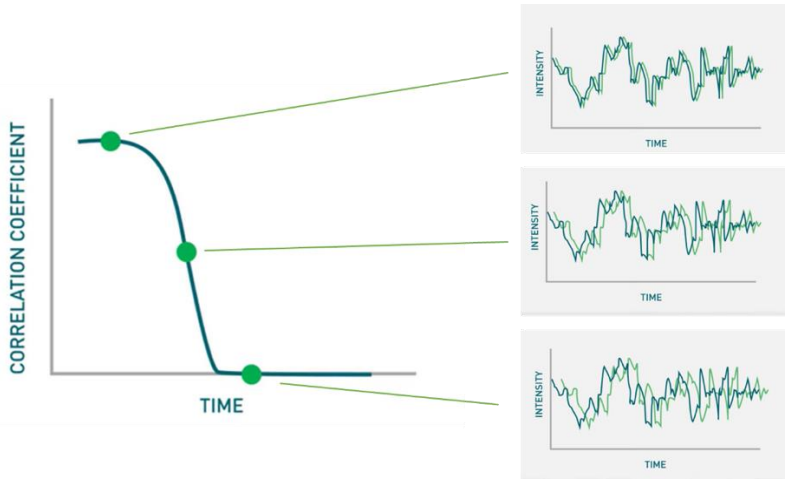

***Figure A16**: Evolution of scattered signal with time leading to autocorrelation function (from MalverPanalytical)*[57]

Method have been developed to extract diffusion coefficient from autocorrelation shape. Cumulant method will be used for monomodal size distribution when CONTIN method will be more adapted for polymodal size distribution. Those methods are used to determine the relaxation frequency Γ associated with nanoparticles movement. Fick's law gives the following relation between coefficient diffusion and relaxation frequency:

$$D = \Gamma q^2 \qquad II.A.15$$

where q is the norm of the scattering vector resulting from the difference between incident wave vector and scattered vector. (Figure A17)

$$\vec{q} = \overrightarrow{k_d} - \overrightarrow{k_i} \quad \text{with} \quad \|\overrightarrow{k_{i,d}}\| = \frac{2\pi}{\lambda_{i,d}}$$

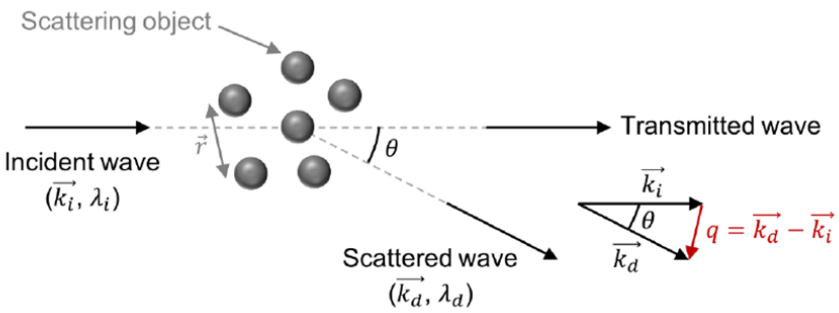

***Figure A17**: Schematic representation of scattering vector q, from Coralie Lebleu PhD manuscript*[17]

Hydrodynamic radius can finally be determined by Stokes-Einstein relationship:

$$R_h = \frac{k_B\, T}{6\pi\eta D} \qquad II.A.16$$

where kBT is the Boltzmann energy factor with T (K) the temperature and η (cP) the solvent viscosity.

DLS data is usually represented with an intensity distribution (intensity as a function of R_h). However, the scattering intensity is proportional to nanoparticle size and their concentration [NPs][58]:

$$I(q) \propto \mathrm{R_h^6}\,;[NPs] \qquad II.A.17$$

It's important to note that DLS measurements can be biased due to the influence of particle size. Larger particles can produce stronger signals than smaller ones, which can lead to an inaccurate interpretation of the result. This phenomenon can also make DLS more sensitive to factors such as aggregation and dust pollution, which may require filtering of the sample before analysis. Additionally, the hydrodynamic diameter measured by DLS cannot give us more information about the shape of particles, as the hydrodynamic diameter measured is the one of a spherical object having the same diffusion than the object measured. Anisotropy is not considered. Therefore, it's crucial to consider these limitations when analyzing DLS data.

In order to evaluate homogeneity of obtained particles populations, polydispersity index (PDI) will be considered, following next equation:

$$PDI = \left(\frac{SD}{Mean}\right)^2 \qquad II.A.18$$

where SD is the standard deviation in size.

A PDI close to 0 indicates that all the particles have the same size, while a higher PDI indicates a broader range of particle sizes. Therefore, a lower PDI value indicates a more narrow and homogeneous size distribution of nanoparticles, meaning that the particles are more similar in size to each other. In contrast, a higher PDI value suggests a greater variation in particle sizes, indicating a more heterogeneous suspension. Generally, NPs formed with PDI values smaller than 0.15 are considered as well-defined in size.

6.6. Multi Angle Light scattering

Multi-angle dynamic light scattering: Nanoparticle larger than $\lambda/20$ may present a change in scattered intensity depending on the angle of observation θ. Multi angle light scattering allows to measure scattered intensity at different angles and thus, at different values of scattering vector q.

Relaxation frequency Γ is measured at each angle allowing to draw Γ as a function of q. Then diffusion coefficient (D) of the nanoparticles is determined by the slope of the linear fit Γ = f(q^2) and Stokes-Einstein equation is used to deduce hydrodynamic radius of the nanoparticles R_h.

Multi-angle static light scattering: SLS measurements allow to measure radius of gyration of nanoparticles. The absolute scattering intensity I(q) of a sample measured during SLS analysis is

deduced by subtracting the scattering intensity of the solvent and by using a solvent of reference for which Rayleigh ratio is known (here we will use toluene as a reference, $R_{toluene}$=1.35×10^{-5} cm^{-1}).

$$I(q) = \frac{I_{measured} - I_{solvent}}{I_{toluene}} \times \left(\frac{n_{sample}}{n_{toluene}}\right)^2 \times R_{toluene} \qquad II.A.19$$

where I, $I_{solvent}$ and $I_{toluene}$ are respectively the scattering intensities of the sample, the solvent and toluene and with n_{sample}, $n_{toluene}$ are respectively the refractive indexes of the sample and toluene ($n_{toluene}$=1.496 at 25 °C).

The slope of the fit of $\sqrt{I(q)}$ as a function of q^2 (Berry plot)[55,58] allows the determination of the radius of gyration (R_G) of the NPs according to the following relationship:

$$\sqrt{I(q)} = \sqrt{I(0)}\ \frac{1 - q^2 R_G^2}{6} \qquad II.A.20$$

Equation of second order was used to better fit the non-linear behavior of the data that might be due to polydispersity. In this case, $\sqrt{I(x)} = A + Bx + Cx^2$ with x = q².

Then, we can isolate:

$$R_g = \sqrt{\frac{-6B}{A}} \qquad II.A.21$$

Multi-angle SLS allows the determination of the weight average molar mass of one particle $Mw(particle)$ using the following expression in a dilute regime:

$$\frac{Kc}{\Delta R} = \frac{1}{M_w}\left(1 + \frac{1}{3}R_g^2 q^2\right) + 2A_2 c \qquad II.A.22$$

Where c is the copolymer concentration, A_2 the second virial coefficient, which describe the particle-solvent interaction and K is the following constant:

$$K = \frac{4\pi^2 n_0^2 \left(\frac{dn}{dc}\right)^2}{N_A \lambda^4} \qquad II.A.23$$

Where n_0 is the refractive index of the solvent, (dn/dc) the refractive index increment, characterizing the change of refractive index with copolymer concentration, N_A Avogadro's number (N_A = 6.022 × 10^{23} mol^{-1}) and λ the wavelength of the light source.

To obtain M_w(particle) and R_g, scattering intensity of a sample was measured at different angle (θ) and copolymer concentration (c). Concentration of copolymer in vesicle solution was measured through a dry-extract using a freeze-dryer, with withdrawing PBS salt mass.

Data can be displayed with a Berry plot[59] following next equation and illustrated in Figure A18 :

$$\left[\frac{Kc}{\Delta R}\right]^{\frac{1}{2}} = f(q^2 + kc) \qquad II.A.24$$

Where k is an arbitrary constant. Extrapolation at until angle θ = 0° for each concentration is done to determine A_2 and an extrapolation at c = 0 is done at different angle to obtain R_g. The intercept of the two projections allow to obtain $\frac{1}{M_w(particle)}$.

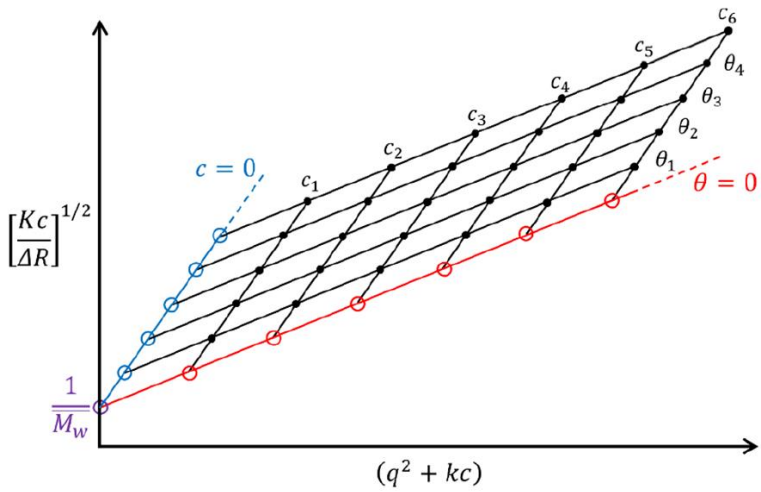

***Figure A18**: Berry plot representing multi-angle SLS data allowing to determine M_w (particle)*

When studying self-assemble particles of amphiphilic copolymer, three others parameters are interesting to know: the aggregation number (N_{agg}): average number of copolymer chains that composes one particle, the average area per copolymer chain ($A_{copolymer}$) and the concentration of NPs ([NPs]).

The aggregation number can be deduced from the ratio between the weight molar mass of one particle (M_w(particle)) and the weight molar mass of a copolymer chain (M_w(copolymer)):

$$N_{agg} = \frac{M_w(particle)}{M_w(copolymer)} \qquad II.A.25$$

By knowing copolymer dispersity Đ:

$$M_w = M_n \times Đ \qquad II.A.26$$

The area per copolymer chain in the polymersome can be expressed as:

$$A_{copolymer} = 2 \times \frac{4\pi \times R_g^2}{N_{agg}} \qquad II.A.27$$

This formula relies on the strong hypothesis that the membrane of polymersomes is a bilayer of copolymer chain without interdigitation or entanglement, which is probably not the case. This calculation is thus an estimation of reality.

Finally, concentration of NPs can be estimated from copolymer mass concentration as follows:

$$[NPs] = \frac{[copolymer]}{M_w(copolymer) \times N_{agg}} \qquad II.A.28$$

7. References

(1) Anajafi, T.; Mallik, S. Polymersome-Based Drug-Delivery Strategies for Cancer Therapeutics. *Ther Deliv* **2015**, *6* (4), 521–534. https://doi.org/10.4155/tde.14.125.

(2) Peer, D.; Karp, J.; Hong, S.; Farokhzad, O.; Margalit, R.; Langer, R. Nanocarriers as an Emerging Platform for Cancer Therapy. *Nature nanotechnology* **2007**, *2*, 751–760. https://doi.org/10.1038/nnano.2007.387.

(3) Rideau, E.; Dimova, R.; Schwille, P.; Wurm, F. R.; Landfester, K. Liposomes and Polymersomes: A Comparative Review towards Cell Mimicking. *Chem. Soc. Rev.* **2018**, *47* (23), 8572–8610. https://doi.org/10.1039/C8CS00162F.

(4) Stiepel, R. T.; Duggan, E.; Batty, C. J.; Ainslie, K. M. Micro and Nanotechnologies: The Little Formulations That Could. *Bioengineering & Translational Medicine n/a* (n/a), e10421. https://doi.org/10.1002/btm2.10421.

(5) Matoori, S.; Leroux, J.-C. Twenty-Five Years of Polymersomes: Lost in Translation? *Mater. Horiz.* **2020**, *7* (5), 1297–1309. https://doi.org/10.1039/C9MH01669D.

(6) Lee, H.; Larson, R. G. Adsorption of Plasma Proteins onto PEGylated Lipid Bilayers: The Effect of PEG Size and Grafting Density. *Biomacromolecules* **2016**, *17* (5), 1757–1765. https://doi.org/10.1021/acs.biomac.6b00146.

(7) Cullis, null; Chonn, null; Semple, null. Interactions of Liposomes and Lipid-Based Carrier Systems with Blood Proteins: Relation to Clearance Behaviour in Vivo. *Adv Drug Deliv Rev* **1998**, *32* (1–2), 3–17. https://doi.org/10.1016/s0169-409x(97)00128-2.

(8) Semple, S. C.; Chonn, A.; Cullis, P. R. Interactions of Liposomes and Lipid-Based Carrier Systems with Blood Proteins: Relation to Clearance Behaviour in Vivo. *Advanced Drug Delivery Reviews* **1998**, *32* (1), 3–17. https://doi.org/10.1016/S0169-409X(97)00128-2.

(9) Gref, R.; Domb, A.; Quellec, P.; Blunk, T.; Müller, R. H.; Verbavatz, J. M.; Langer, R. The Controlled Intravenous Delivery of Drugs Using PEG-Coated Sterically Stabilized Nanospheres. *Adv Drug Deliv Rev* **1995**, *16* (2–3), 215–233. https://doi.org/10.1016/0169-409X(95)00026-4.

(10) Kamaly, N.; Xiao, Z.; Valencia, P. M.; Radovic-Moreno, A. F.; Farokhzad, O. C. Targeted Polymeric Therapeutic Nanoparticles: Design, Development and Clinical Translation. *Chem. Soc. Rev.* **2012**, *41* (7), 2971. https://doi.org/10.1039/c2cs15344k.

(11) Hu, X.; Zhang, Y.; Xie, Z.; Jing, X.; Bellotti, A.; Gu, Z. Stimuli-Responsive Polymersomes for Biomedical Applications. *Biomacromolecules* **2017**, *18* (3), 649–673. https://doi.org/10.1021/acs.biomac.6b01704.

(12) WANG, H.; DONG, J. H.; QIU*, A. Y.; GU, Z. W. Studies on Properties and Drug Delivery Systems of PTMC-b-PEG-b-PTMC Block Copolymers. *Journal of Macromolecular Science, Part A* **1998**, *35* (5), 811–820. https://doi.org/10.1080/10601329808002013.

(13) Ajiro, H.; Haramiishi, Y.; Chanthaset, N.; Akashi, M. Polymer Design Using Trimethylene Carbonate with Ethylene Glycol Units for Biomedical Applications. *Polym J* **2016**, *48* (7), 751–760. https://doi.org/10.1038/pj.2016.35.

(14) Fukushima, K. Poly(Trimethylene Carbonate)-Based Polymers Engineered for Biodegradable Functional Biomaterials. *Biomaterials science* **2015**, *4*. https://doi.org/10.1039/c5bm00123d.

(15) Sanson, C.; Schatz, C.; Le Meins, J.-F.; Brûlet, A.; Soum, A.; Lecommandoux, S. Biocompatible and Biodegradable Poly(Trimethylene Carbonate)-b-Poly(l-Glutamic Acid) Polymersomes: Size Control and Stability. *Langmuir* **2010**, *26* (4), 2751–2760. https://doi.org/10.1021/la902786t.

(16) Lebleu, C.; Rodrigues, L.; Guigner, J.-M.; Brûlet, A.; Garanger, E.; Lecommandoux, S. Self-Assembly of PEG-b-PTMC Copolymers: Micelles and Polymersomes Size Control. *Langmuir* **2019**, *35* (41), 13364–13374. https://doi.org/10.1021/acs.langmuir.9b02264.

(17) Lebleu, C. Polymersomes Based on PEG-b-PTMC towards Cell-Mediated Delivery of Nanomedicines. phdthesis, Université de Bordeaux, 2019. https://tel.archives-ouvertes.fr/tel-03463393 (accessed 2022-04-20).

(18) Israelachvili, J. N.; Mitchell, D. J.; Ninham, B. W. Theory of Self-Assembly of Hydrocarbon Amphiphiles into Micelles and Bilayers. *J. Chem. Soc., Faraday Trans. 2* **1976**, *72* (0), 1525–1568. https://doi.org/10.1039/F29767201525.

(19) Bleul, R.; Thiermann, R.; Maskos, M. Techniques To Control Polymersome Size. *Macromolecules* **2015**, *48* (20), 7396–7409. https://doi.org/10.1021/acs.macromol.5b01500.

(20) Moghassemi, S.; Hadjizadeh, A. Nano-Niosomes as Nanoscale Drug Delivery Systems: An Illustrated Review. *J Control Release* **2014**, *185*, 22–36. https://doi.org/10.1016/j.jconrel.2014.04.015.

(21) Howse, J. R.; Jones, R. A. L.; Battaglia, G.; Ducker, R. E.; Leggett, G. J.; Ryan, A. J. Templated Formation of Giant Polymer Vesicles with Controlled Size Distributions. *Nature Mater* **2009**, *8* (6), 507–511. https://doi.org/10.1038/nmat2446.

(22) Angelova, M. I.; Dimitrov, D. S. Liposome Electroformation. *Faraday Discuss. Chem. Soc.* **1986**, *81* (0), 303–311. https://doi.org/10.1039/DC9868100303.

(23) Fessi, H.; Puisieux, F.; Devissaguet, J. Ph.; Ammoury, N.; Benita, S. Nanocapsule Formation by Interfacial Polymer Deposition Following Solvent Displacement. *International Journal of Pharmaceutics* **1989**, *55* (1), R1–R4. https://doi.org/10.1016/0378-5173(89)90281-0.

(24) Petit, J.; Polenz, I.; Baret, J.-C.; Herminghaus, S.; Bäumchen, O. Vesicles-on-a-Chip: A Universal Microfluidic Platform for the Assembly of Liposomes and Polymersomes. *Eur. Phys. J. E* **2016**, *39* (6), 59. https://doi.org/10.1140/epje/i2016-16059-8.

(25) Hayward, R. C.; Utada, A. S.; Dan, N.; Weitz, D. A. Dewetting Instability during the Formation of Polymersomes from Block-Copolymer-Stabilized Double Emulsions. *Langmuir* **2006**, *22* (10), 4457–4461. https://doi.org/10.1021/la060094b.

(26) Pautot, S.; Frisken, B. J.; Weitz, D. A. Production of Unilamellar Vesicles Using an Inverted Emulsion. *Langmuir* **2003**, *19* (7), 2870–2879. https://doi.org/10.1021/la026100v.

(27) Seo, H.; Lee, H. Recent Developments in Microfluidic Synthesis of Artificial Cell-like Polymersomes and Liposomes for Functional Bioreactors. *Biomicrofluidics* **2021**, *15* (2), 021301. https://doi.org/10.1063/5.0048441.

(28) Albuquerque, L. J. C.; Sincari, V.; Jäger, A.; Konefał, R.; Pánek, J.; Černoch, P.; Pavlova, E.; Štěpánek, P.; Giacomelli, F. C.; Jäger, E. Microfluidic-Assisted Engineering of Quasi-Monodisperse PH-Responsive Polymersomes toward Advanced Platforms for the Intracellular Delivery of Hydrophilic Therapeutics. *Langmuir* **2019**, acs.langmuir.9b01009. https://doi.org/10.1021/acs.langmuir.9b01009.

(29) Stroock, A. D.; Dertinger, S. K. W.; Ajdari, A.; Mezić, I.; Stone, H. A.; Whitesides, G. M. Chaotic Mixer for Microchannels. *Science* **2002**, *295* (5555), 647–651. https://doi.org/10.1126/science.1066238.

(30) Zhang, G.; Sun, J. Lipid in Chips: A Brief Review of Liposomes Formation by Microfluidics. *International Journal of Nanomedicine* **2021**, *Volume 16*, 7391–7416. https://doi.org/10.2147/IJN.S331639.

(31) Alexis, F.; Pridgen, E.; Molnar, L. K.; Farokhzad, O. C. Factors Affecting the Clearance and Biodistribution of Polymeric Nanoparticles. *Mol. Pharmaceutics* **2008**, *5* (4), 505–515. https://doi.org/10.1021/mp800051m.

(32) Brinkhuis, R. P.; Stojanov, K.; Laverman, P.; Eilander, J.; Zuhorn, I. S.; Rutjes, F. P. J. T.; van Hest, J. C. M. Size Dependent Biodistribution and SPECT Imaging of (111)In-Labeled Polymersomes. *Bioconjug Chem* **2012**, *23* (5), 958–965. https://doi.org/10.1021/bc200578s.

(33) Ferji, K.; Nouvel, C.; Babin, J.; Li, M.-H.; Gaillard, C.; Nicol, E.; Chassenieux, C.; Six, J.-L. Polymersomes from Amphiphilic Glycopolymers Containing Polymeric Liquid Crystal Grafts. *ACS Macro Lett.* **2015**, *4* (10), 1119–1122. https://doi.org/10.1021/acsmacrolett.5b00471.

(34) Ikkene, D.; Arteni, A. A.; Ouldali, M.; Six, J.-L.; Ferji, K. Self-Assembly of Amphiphilic Copolymers Containing Polysaccharide: PISA versus Nanoprecipitation, and the Temperature Effect. *Polym. Chem.* **2020**, *11* (29), 4729–4740. https://doi.org/10.1039/D0PY00407C.

(35) Houga, C.; Giermanska, J.; Lecommandoux, S.; Borsali, R.; Taton, D.; Gnanou, Y.; Le Meins, J.-F. Micelles and Polymersomes Obtained by Self-Assembly of Dextran and Polystyrene Based Block Copolymers. *Biomacromolecules* **2009**, *10* (1), 32–40. https://doi.org/10.1021/bm800778n.

(36) Dautzenberg, H. Advances in Polymer Science. Vol. 48. Light Scattering from Polymers. Hg. von H.-J. CANTOW u. a. ; Berlin/Heidelberg/New York: Springer-Verlag 1982, 167 S., Lwd., DM 98,–. *Acta Polymerica* **1984**, *35* (5), 433–433. https://doi.org/10.1002/actp.1984.010350518.

(37) Liu, X.; Stenhammar, J.; Wennerström, H.; Sparr, E. Vesicles Balance Osmotic Stress with Bending Energy That Can Be Released to Form Daughter Vesicles. *J. Phys. Chem. Lett.* **2022**, *13* (2), 498–507. https://doi.org/10.1021/acs.jpclett.1c03369.

(38) Pallavi, P.; Harini, K.; Gowtham, P.; Girigoswami, K.; Girigoswami, A. Fabrication of Polymersomes: A Macromolecular Architecture in Nanotherapeutics. *Chemistry* **2022**, *4* (3), 1028–1043. https://doi.org/10.3390/chemistry4030070.

(39) Besada, L. N.; Peruzzo, P.; Cortizo, A. M.; Cortizo, M. S. Preparation, Characterization, and in Vitro Activity Evaluation of Triblock Copolymer-Based Polymersomes for Drugs Delivery. *J Nanopart Res* **2018**, *20* (3), 67. https://doi.org/10.1007/s11051-018-4169-7.

(40) Hou, W.; Liu, R.; Bi, S.; He, Q.; Wang, H.; Gu, J. Photo-Responsive Polymersomes as Drug Delivery System for Potential Medical Applications. *Molecules* **2020**, *25* (21), 5147. https://doi.org/10.3390/molecules25215147.

(41) Zhou, Y.; Chen, R.; Yang, H.; Bao, C.; Fan, J.; Wang, C.; Lin, Q.; Zhu, L. Light-Responsive Polymersomes with a Charge-Switch for Targeted Drug Delivery. *J. Mater. Chem. B* **2020**, *8* (4), 727–735. https://doi.org/10.1039/C9TB02411E.

(42) Brinkman, J. E.; Dorius, B.; Sharma, S. Physiology, Body Fluids. In *StatPearls*; StatPearls Publishing: Treasure Island (FL), 2023.

(43) Q3C — Tables and List Guidance for Industry.

(44) Lim Soo, P.; Eisenberg, A. Preparation of Block Copolymer Vesicles in Solution. *Journal of Polymer Science Part B: Polymer Physics* **2004**, *42* (6), 923–938. https://doi.org/10.1002/polb.10739.

(45) Van Krevelen, D. W. COHESIVE PROPERTIES AND SOLUBILITY. In *Properties of Polymers*; Elsevier, 1997; pp 189–225. https://doi.org/10.1016/B978-0-444-82877-4.50014-7.

(46) Mai, Y.; Eisenberg, A. Self-Assembly of Block Copolymers. *Chem. Soc. Rev.* **2012**, *41* (18), 5969–5985. https://doi.org/10.1039/C2CS35115C.

(47) Agha, A.; Waheed, W.; Stiharu, I.; Nerguizian, V.; Destgeer, G.; Abu-Nada, E.; Alazzam, A. A Review on Microfluidic-Assisted Nanoparticle Synthesis, and Their Applications Using Multiscale

Simulation Methods. *Nanoscale Res Lett* **2023**, *18* (1), 18. https://doi.org/10.1186/s11671-023-03792-x.

(48) Jabbari, V.; Banner, D. J.; Phakatkar, A. H.; Shahbazian-Yassar, R. Nucleation and Growth Visualization of Self-Assembled Polymeric Micelles/Vesicles Using in Situ Liquid Cell-TEM. *Microsc Microanal* **2020**, *26* (S2), 2576–2578. https://doi.org/10.1017/S1431927620022084.

(49) Förster, S.; Zisenis, M.; Wenz, E.; Antonietti, M. Micellization of Strongly Segregated Block Copolymers. *J. Chem. Phys.* **1996**, *104* (24), 9956–9970. https://doi.org/10.1063/1.471723.

(50) Thiermann, R.; Mueller, W.; Montesinos-Castellanos, A.; Metzke, D.; Löb, P.; Hessel, V.; Maskos, M. Size Controlled Polymersomes by Continuous Self-Assembly in Micromixers. *Polymer* **2012**, *53*, 2205–2210. https://doi.org/10.1016/j.polymer.2012.03.058.

(51) Miller, C. C. The Stokes-Einstein Law for Diffusion in Solution. *Proceedings of the Royal Society of London. Series A, Containing Papers of a Mathematical and Physical Character* **1924**, *106* (740), 724–749.

(52) Bonhomme, O. Étude de La Formation de Fibres En Microfluidique : Compétition Entre Mise En Forme et Gélification de Fluides Complexes Sous Écoulement. These de doctorat, Bordeaux 1, 2011. https://www.theses.fr/2011BOR14306 (accessed 2023-01-17).

(53) Dolomite. *Micromixer Chip*. Dolomite Microfluidics. https://www.dolomite-microfluidics.com/product/micromixer-chip/ (accessed 2023-02-13).

(54) Subrahmanyam, R.; Gurikov, P.; Dieringer, P.; Sun, M.; Smirnova, I. On the Road to Biopolymer Aerogels—Dealing with the Solvent. *Gels* **2015**, *1*, 291–313. https://doi.org/10.3390/gels1020291.

(55) Podzimek, S. *Light Scattering, Size Exclusion Chromatography and Asymmetric Flow Field Flow Fractionation: Powerful Tools for the Characterization of Polymers, Proteins and Nanoparticles*; John Wiley & Sons, 2011.

(56) Buchholz, B. A.; Barron, A. E. The Use of Light Scattering for Precise Characterization of Polymers for DNA Sequencing by Capillary Electrophoresis. *Electrophoresis* **2001**, *22* (19), 4118–4128. https://doi.org/10.1002/1522-2683(200111)22:19<4118::AID-ELPS4118>3.0.CO;2-Q.

(57) *Dynamic Light Scattering DLS | Malvern Panalytical*. https://www.malvernpanalytical.com/en/products/technology/light-scattering/dynamic-light-scattering (accessed 2023-03-28).

(58) Lawler, D. M. SPECTROPHOTOMETRY | Turbidimetry and Nephelometry. In *Encyclopedia of Analytical Science (Second Edition)*; Worsfold, P., Townshend, A., Poole, C., Eds.; Elsevier: Oxford, 2005; pp 343–351. https://doi.org/10.1016/B0-12-369397-7/00718-4.

(59) Berry, G. C. Thermodynamic and Conformational Properties of Polystyrene. I. Light-Scattering Studies on Dilute Solutions of Linear Polystyrenes. *J. Chem. Phys.* **1966**, *44* (12), 4550–4564. https://doi.org/10.1063/1.1726673.

Chapter III.

Drug loading in PEG-*b*-PTMC polymersomes

Table of contents

Introduction 141

1. Experimental Section 143

1.1. Materials 143

1.2. Methods 143

2. Critical water content measurement for copolymer and drug compatibility 157

2.1. Evaluation of the critical water content of ganciclovir 157

2.2. Evaluation of the critical water content of Coumarin 6 159

2.3. Evaluation of the critical water content of Doxorubicin 161

3. Microfluidic assisted passive loading of drugs 162

3.1. Towards PEG_{22}-b-$PTMC_{51}$ loaded vesicles 162

3.2. Improving Ganciclovir passive loading by tuning the CWC of PEG_{22}-b-$PTMC_{51}$ 164

3.3. Towards PEG_{46}-*b*-$PTMC_{119}$ loaded vesicles 168

4. Active loading using PEG_{22}-*b*-$PTMC_{51}$ 175

4.1. Active loading through the use of pH gradient 175

4.2. Active loading through the use of ionic gradient 178

5. Conclusion 181

6. Appendix 183

6.1. Temperature measurement during solvent exchange processes 183

6.2. DLS measurement of PEG_{44}-b-$PTMC_m$ self-assemble nanoparticles 183

7. References 185

Introduction

The development of carriers for drug delivery was driven by the need to overcome the drawbacks associated to the delivery of free drugs. Carriers used at the nanometer scale were developed to limit premature degradation of the drug, reduce undesirable interactions with biological components, promote targeted drug absorption in certain type of tissues, and enable better control of pharmacokinetic parameters and more generally, biodistribution profile of drug[1]. These advances are of great interest for the reduction of drug doses and their associated side effects. Various forms of polymer carriers have been developed, including polymeric nanoshells, dendrimers, micelles and polymer-drug conjugates.[2] Among these, polymersomes have attracted great interest due to their superior properties.[3] Inspired by liposomes, polymersomes combine the benefits of loading both hydrophilic and hydrophobic drugs, while possessing a thicker membrane that imparts better mechanical properties and reduces drug leakage.[4,5] Consequently, they are versatile capsules with tunable size and composition, which can be loaded with a range of drug cargoes and researches on drug loading in vesicular systems are abundant[6,7]. The objective of this chapter is to improve our understanding of the encapsulation mechanisms of molecules in polymersomes, with a particular focus on the ones of interest in this thesis based on PEG-*b*-PTMC.

Concerning the drug encapsulation, another important characteristic to take into account is the preference of the drug for aqueous or organic media, given by the octanol/water partition coefficient (log P). The log P of a drug is a measure of its lipophilicity and is generally used to evaluate the tendency of a molecule to dissolve in a lipid or organic solvent. It is defined as the logarithm of the partition coefficient (P) of a drug, which is the ratio of its solubility in a nonpolar solvent (such as octanol) to its solubility in a polar solvent (such as water) at equilibrium[8]. A drug with a high log P value is more hydrophobic and tends to have affinity for hydrophobic layer. Conversely, a drug with a lower log P value (below zero) is more hydrophilic and tends to have poor affinity for hydrophobic membrane but is usually more easily solubilized in aqueous medium[9]. This log P value might be a first parameter to consider in predicting whether the drug will go into the hydrophilic core or the hydrophobic membrane of the vesicle. A more refined approach would be to use the Hansen parameters of the polymer and the drugs, which we did not consider here in a first approach.

After the development of microfluidic assisted self-assembly process for the formulation of poly(ethylene glycol)-*block*-poly(trimethylene carbonate) PEG_{22}-*b*-$PTMC_{51}$ polymer nanoparticles, the second part of this thesis concerns the evaluation of the capacity of these vesicles for drug encapsulation. Ganciclovir (log P = -1,66), a hydrophilic antiviral drug used to treat Cytomegalovirus infections[10,11] and Doxorubicin HCl, an amphiphilic chemotherapy drug (log P = 1,41) [12,13] were first tested. The mechanism of drug loading to PEG_{22}-b-$PTMC_{51}$ polymer vesicles was extended to the loading of Coumarin 6 (LogP = 4.9), a fluorescent molecule which will play the role of a hydrophobic drug.[14,15] Molecular structures of the three molecules are presented in Figure 1.

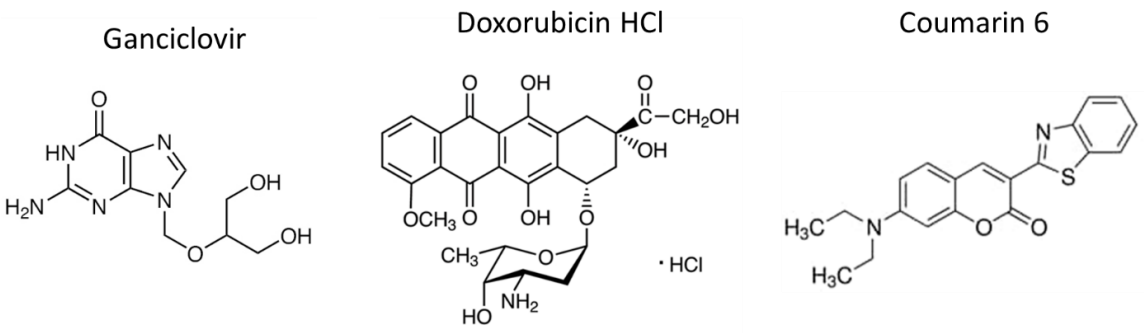

***Figure 1**: Representation of model molecules to be loaded: Ganciclovir (log P = - 1.66), Doxorubicin Hydrochloride (log P = 1.41) and Coumarin 6 (log P = 4.9).*

Evaluation of the critical water content (CWC) was first established for the three molecules to ensure that no precipitation of the drug occurs at a lower water content and before the self-assembly of the block copolymer. By determining the CWC of both the copolymer and the drug, the optimal conditions can be identified to ensure efficient and effective encapsulation of the drug within the copolymer vesicles.

After determining the most appropriate protocol for the quantification of Ganciclovir, Coumarin 6 and Doxorubicin loaded in polymersomes, we tried passive loading of the drug by adding it during the microfluidic assisted self-assembly process of PEG-*b*-PTMC. Two block copolymers that gave different membrane thickness and consequently membrane permeability were tested: PEG_{22}-*b*-$PTMC_{51}$ and PEG_{46}-*b*-$PTMC_{119}$. We finally intended active loading of Ganciclovir using both ionic[16–18] and pH gradient methods[19–21] to improve drug loading content of Ganciclovir in our PEG_{22}-*b*-$PTMC_{51}$ polymersomes.

1. Experimental Section

1.1. Materials

Solvents: Dimethylsulfoxide (DMSO) was purchased from Sigma-Aldrich, Phosphate Buffer Saline (PBS) concentrated ten times (10X) was purchased from Euromedex and diluted to obtain PBS 1X.
To obtain 100 mL of ammonium sulfate solution, 1.887 g of ammonium sulfate from Sigma Aldrich was solubilized in water. Osmolarity was adjusted and pH is not adjusted, finally measured at pH = 5.3. Citric acid buffer was made at 10 mM with 150 mM of NaCl to reach an osmolarity of 300 $mOsm.L^{-1}$ and a pH of 3. For 100 mL of acidic buffer, 936 mg of NaCl from Thermo Scientific, 174 mg of citric acid from Alfa Aesar and 28 mg of sodium citrate from Alfa Aesar are solubilized in water. pH and osmolarity was adjusted. pH and osmolarity of aqueous solution were adjusted using the pH meter *inoLab® pH 730 WTW* and the osmometer *Löser automatic TypM 10 – 25 µL*, to reach pH = 7.4 ± 0.1 and an osmolarity of 300 ± 4 $mOsm.L^{-1}$.

PEG_{22}-*b*-$PTMC_{51}$ and PEG_{46}-*b*-$PTMC_{119}$ were synthetized by ring-opening polymerization of TMC using MeO-PEG_n-OH as macroinitiator. This synthesis was already reported by Coralie Lebleu[22] and was performed by Pierre Lalanne and Eloïse Equy.

Surfactants: Sodium dodecyl sulfate (SDS) was purchased from VWR, Triton X-100 from Acros Organics and Hellmanex III from Hellma™.
Drug models: Doxorubicin HCl was purchased from EDQM, Coumarin 6 and Ganciclovir from Sigma Aldrich.
Purification: Sephadex G100 was purchased from Cytiva. Spectra/Por®6 dialysis membrane 25kDa were purchased from VWR and Ultracel® Ultrafiltration Discs were purchased from Merck.

1.2. Methods

1.2.1. Passive Loading

Passive loading was performed by adding the drug-to-load in organic solvent, with the copolymer, while performing microfluidic experiment as previously described. Briefly, drug (Ganciclovir, Doxorubicin Hydrochloride or Coumarin 6) was solubilized at a desired concentration with 10 $mg.mL^{-1}$ of PEG_n-*b*-$PTMC_m$ in DMSO. This organic solution was placed in a Mitos pressure pumps (3200175) equipped with flowmeters (3200097), connected to first and third inputs of Micromixer chip using a T-connector. Second pump, containing PBS at 300 $mOsm.L^{-1}$, pH=7.4, was connected to second input of the Micromixer chip. Flow rates were controlled using Mitos Flow Control Center 2.5.17 software and calibration reported in Chapter 2 was used for DMSO. Attention was paid on turning off microscope light during collecting to avoid Doxorubicin HCl or Coumarin 6 to bleach.

1.2.2. Ultrafiltration purification

Three purification processes were compared among which Dialysis, Ultrafiltration and Sephadex Column (gel permeation column). Ultrafiltration process uses pressure to force a liquid to go through a membrane with a certain cut-off, allowing molecules under this cut off to escape the tank with the solvent. Larger objects remain in ultrafiltration tank and can be collected. Ultrafiltration process was performed as follow: 2 mL of sample is placed in an ultrafiltration tank of 10 mL then 6 mL of PBS is added. Ultrafiltration is proceeded through a 30 kDa membrane at 2 bars, until volume is reduced back to 2 mL. This dilution – ultrafiltration represents a cycle, and 4 cycles are done to complete purification process.

To estimate the quantity of free drugs that would not be withdrawn by this process, we imagined that none of the drug was encapsulated. A classic experiment of passive loading will involve 10 $mg.mL^{-1}$ of drug in organic solvent and a ratio or organic/aqueous solvent used in microfluidic chip of 20/80 %vol. Thus, we can do the estimate purification follow-up as detailed in Figure 2. Experiments showed that the loaded drug measured after other purification processes appeared to have the same magnitude as the residual free drug after ultrafiltration. Therefore, the ultrafiltration process was discarded.

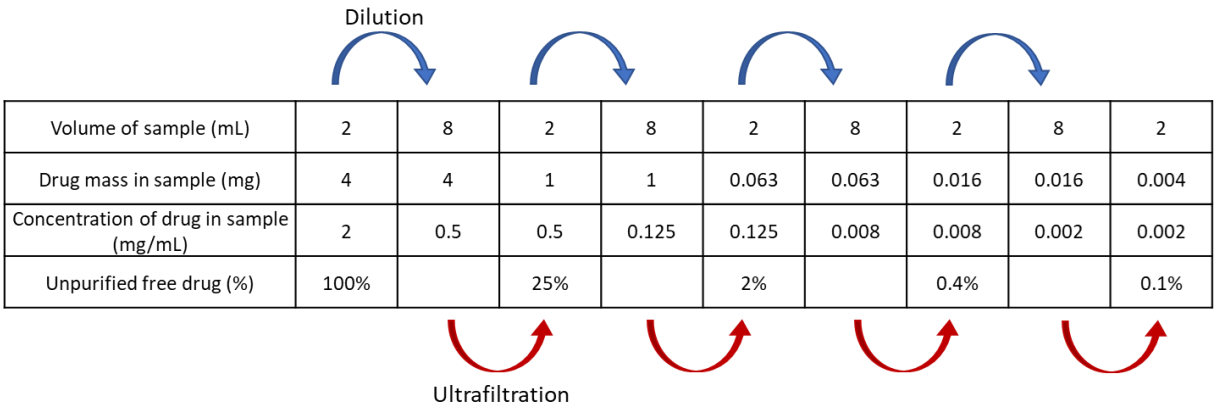

Volume of sample (mL)	2	8	2	8	2	8	2	8	2
Drug mass in sample (mg)	4	4	1	1	0.063	0.063	0.016	0.016	0.004
Concentration of drug in sample (mg/mL)	2	0.5	0.5	0.125	0.125	0.008	0.008	0.002	0.002
Unpurified free drug (%)	100%		25%		2%		0.4%		0.1%

Figure 2: *Theoretical follow up of ultrafiltration process made in order to estimate potential amount of unpurified free drug.*

1.2.3. Sephadex purification

Sephadex columns, are exclusion size column. Sephadex column is made as follows: 1.3 g of Sephadex G100 per column are let to swell in an excess of ultrapure water of 100 mL for 72 h (supplier's protocol). Swollen beads of crosslinked dextran are degassed for 30 min under vacuum. Beads are poured in a 25 cm column and let to pack, avoiding any drying. 45 mL of PBS 300 $mOsm.L^{-1}$ is then passed in the column until the solvent coming out of the column reach the osmolarity of the initial PBS. A 2 mL sample is then poured on top of the beads and let to go across. 15 aliquots of 1 mL each are collected at the output of the column while PBS is added on top to ensure sample progress down the column. Aliquots are then analyzed by Malvern Zetasizer DLS 90°, 1 measurement of 1 run of 5 s,

to get an idea of scattered intensity. Aliquots containing nanoparticles will scatter light while the others will not. Figure 3 illustrates how we identified aliquots of interest.

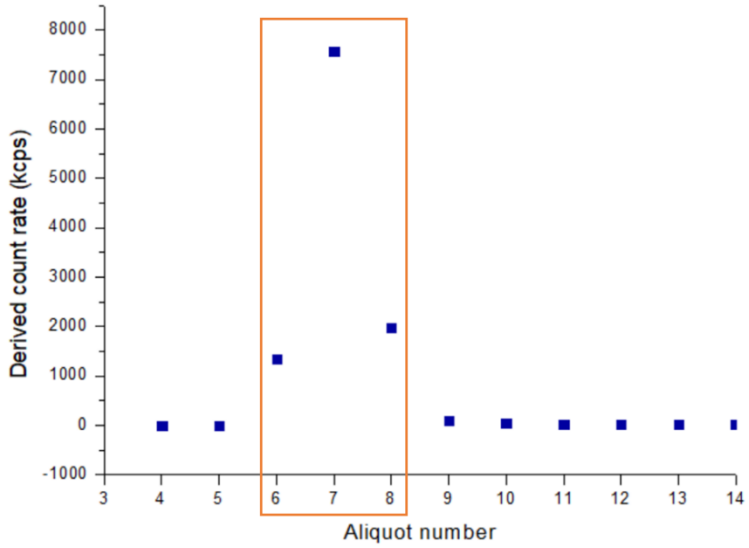

Figure 3: *Scattered intensity measured by DLS 90° of aliquots taken from a Sephadex column during purification. Aliquots 6, 7 and 8 show a higher Derived Count Rate than other aliquots, in agreement with the presence of nanoparticles.*

When doing Sephadex column, it is also important to ensure that unloaded free drug is separated from loaded one by the column. To do so, aliquots are also analyzed by UV spectroscopy using an *Agilent Technologies Cary Series UV-Vis spectrophotometer*. Figure 4 shows the absorbance of aliquots of a sample purified by sephadex after passive loading of Ganciclovir.

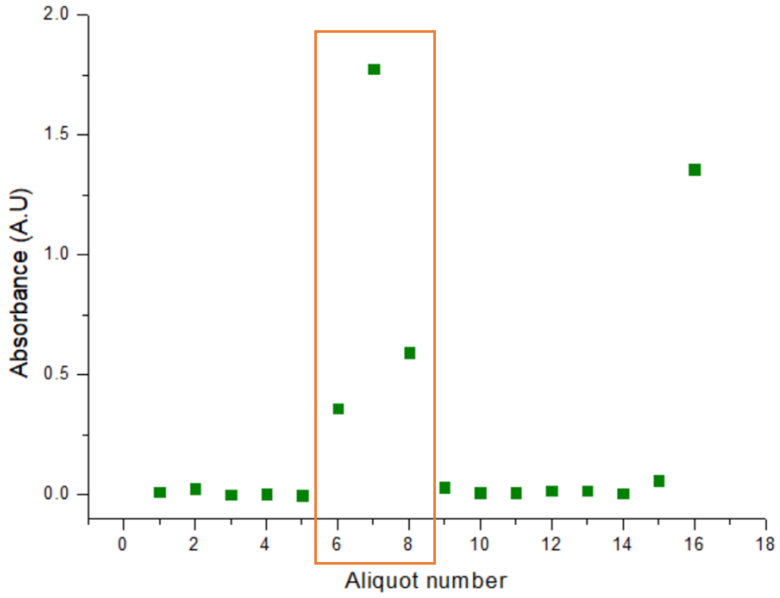

Figure 4: *UV absorbance at 254 nm of aliquots taken after sephadex column used to purify a sample made by passive loading of ganciclovir using microfluidic assisted self-assembly of PEG_{22}-b-$PTMC_{51}$. Aliquot 6 to 8 contain loaded drug. Aliquot 16 shows free drug, meaning that loaded and free drug are well separated by the Sephadex column.*

1.2.4. Particular case of Coumarin 6

Coumarin 6 is the most hydrophobic molecule used as a drug model in this work. When used in microfluidic assisted self-assembly, passive loading, samples taken at the end of microfluidics should be allowed to rest for 15 min so that unloaded coumarin 6 can flocculate. Indeed, the amount of water leads to drug precipitation. 15 min allow Coumarin 6 to flocculate and to form large aggregates easier to withdraw with a cotton filtration. Briefly, a small amount of cotton is packed in a glass Paster pipette and used as a filter. Sample is passed through this coarse filter which appears to be efficient. This step is used before dialysis or Sephadex column to avoid dialysis membrane or column clogging.

Figure 5: *Before and after cotton filtration of Coumarin 6 at high concentration in a 20/80 % vol DMSO/PBS mix, without copolymer in solution.*

1.2.5. Drug Loading quantification

As introduced in chapter 1, the Drug Loading Content (DLC) is a key parameter to measure and is defined as the weight given by the drug in the overall mass of the nanoparticle. To measure this parameter, we first collected samples from microfluidic, we then purified them to withdraw unloaded drug, and then managed to break nanoparticles for the loaded drug to be solubilized again and

quantified. Intrinsic properties of the loaded molecules were used for appropriate quantification, such as their UV absorbance (Ganciclovir) and Fluorescence (Doxorubicin HCl and Coumarin 6).

1.2.5.1. Ganciclovir

1.2.5.1.1. UV Calibration curve

Ganciclovir is known to have a signal by UV absorbance at 252 nm[23]. We thus tried to see which solvent suits the best to create a calibration curve for Ganciclovir. Two options were available: DMSO or PBS. Figure 6 shows absorbance spectrum of DMSO, PBS and Ganciclovir at 0.01 mg.mL^{-1} in each solvent.

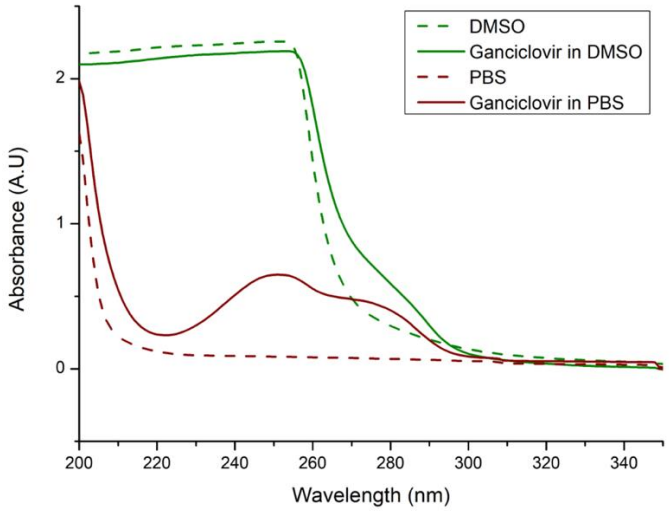

Figure 6: *Absorbance spectra of DMSO, PBS and Ganciclovir at 0.01 mg.mL^{-1} in DMSO or PBS as solvent.*

Figure 6 shows that DMSO already emits a signal in the UV absorbance, making the Ganciclovir signal not very visible. Nevertheless, PBS is having a much lower signal, allowing Ganciclovir signal to be visible. Calibration curve was thus made in PBS, measuring absorbance intensity, at 252 nm, of solutions with a known concentration of ganciclovir from 0.25 µg.mL^{-1} to 10 µg.mL^{-1}. Signal saturation is reached for 100 µg.mL^{-1}. After subtracting the PBS and cuvette signals, a calibration curve is obtained (Figure 7), giving the following equation after linear fitting (Equation III.1):

$$y = 5.2 \times 10^{-2}x + 0.02 \ ; \ R^2 = 0.9945 \qquad III.1$$

where y is the absorbance at 252 nm and x Ganciclovir concentration (µg.mL^{-1}).

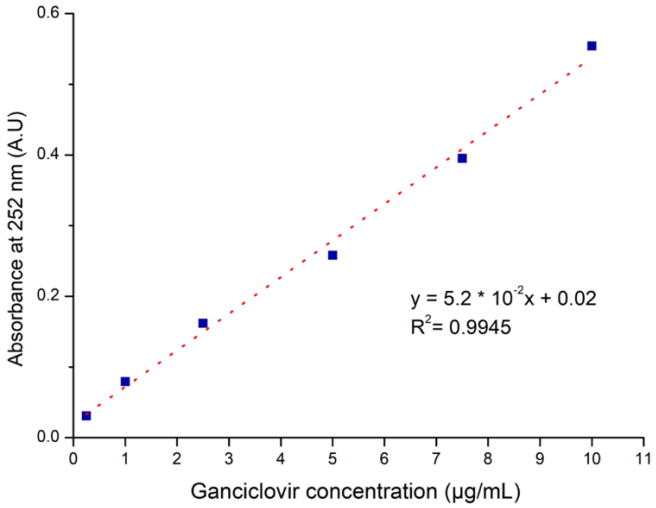

Figure 7: *Calibration curve of Ganciclovir absorbance at 252 nm in PBS as solvent.*

1.2.5.1.2. Destabilization of the polymersome membranes

To measure free ganciclovir in solution was a first step, releasing loaded drug from nanoparticle to quantify it is then necessary. Thus, as Ganciclovir cannot be measured in DMSO, we decided to add a detergent to disturb block copolymer polymersomes directly in PBS. Three typical surfactants were evaluated: Hellmanex™, Triton G100 and SDS. To measure surfactant efficiency on disturbing nanoparticle self-assembly, we decided to follow scattered light due to the suspension by DLS 90°. Intensity was measured first on the sample of vesicle and after surfactant addition. Assays were done on vesicles made as previously described: microfluidic assisted self-assembly of PEG_{22}-*b*-$PTMC_{51}$ at 10 $mg.mL^{-1}$ in DMSO, DMSO/PBS ratio of 20/80 %vol and a total flow rate of 1000 $\mu L.min^{-1}$ in micromixer chip. The smallest volume of surfactant solution needs to be used to avoid dilution of the sample. Several volumes of addition and concentration of surfactant were tested as well as time/temperature for surfactant to disturb self-assembly: no waiting time at 25°C or overnight at 60°C. Results are summarized in table 1.

Table 1 *: Effect of surfactant addition on PEG_{22}-b-$PTMC_{51}$ vesicles observed by measuring Derived Count Rate of the solution by DLS 90°. Hellmanex™ and Triton are presented in liquid form to be diluted while SDS is a powder to be dissolved. Surfactant solution composition is thus given in agreement with initial form of detergent.*

Sample volume (µL)	Added volume of surfactant solution (µL)	Surfactant solution composition	Conditions (Temperature and time)	Remaining intensity after dilution factor withdrawal (%)
Hellmanex™				
50	10	20 %vol	25 °C, no waiting time	100%
100	10	10 %vol	60°C overnight	0.40%

Triton X100				
100	50	10 %vol	25 °C, no waiting time	59%
100	50	10 %vol	60°C overnight	17%
Sodium Dodecyl Sulfate				
100	10	10 mg.mL^{-1}	25 °C, no waiting time	8%
100	10	45 mg.mL^{-1}	25 °C, no waiting time	2%
400	40	45 mg.mL^{-1}	60°C overnight	3%
400	40	115 mg.mL^{-1}	25 °C, no waiting time	0.05%

Hellmanex™ and Triton X100 give better results after being let for the night at 60°C (Thermomixer was used for this purpose), when SDS action is instantaneous. From all those tests, Triton X100 is giving the worst results, keeping at least 17% of the initial vesicle signal, leading to a potential uncomplete disturbance of vesicles. Increasing concentration of Triton in solution was hard because Triton X100 is a viscous liquid which forms a thick gel when mixed with 50 %vol of water. The Triton X100 was therefore not selected.

We then studied signal of Hellmanex™ and SDS in the best conditions: 1%vol solution of Hellmanex™ and 11.5 mg.mL^{-1} of SDS, both in PBS. Figure 8 gives absorbance spectra for 1%vol solution of Hellmanex™ and 11.5 mg.mL^{-1} of SDS, Ganciclovir at 10 µg/mL in a solution of Hellmanex™ 1%vol and Ganciclovir at 10 µg.mL^{-1} in a solution of SDS at 11.5 mg.mL^{-1}.

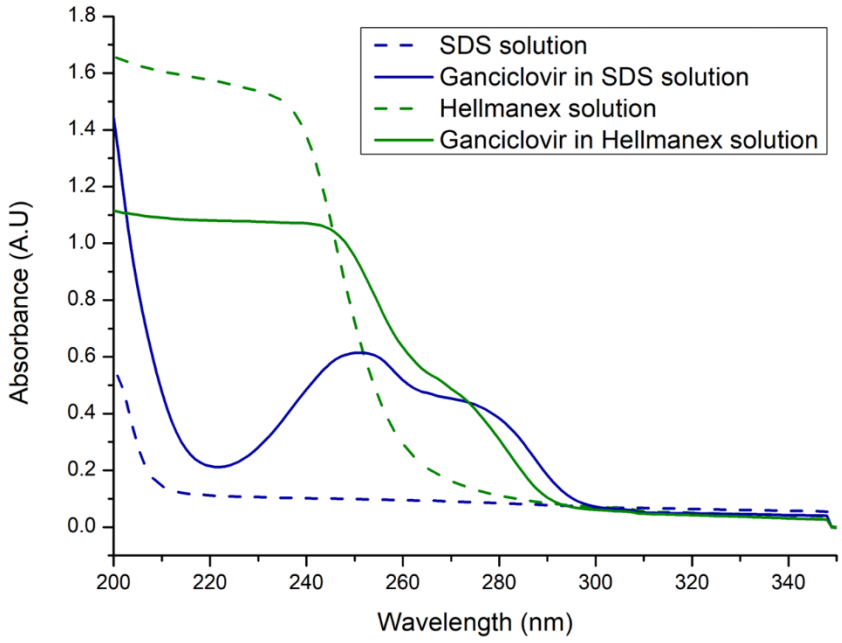

***Figure 8**: Absorbance spectra of SDS solution, Hellmanex ™ solution and Ganciclovir at 0.01 mg.mL^{-1} in SDS or in Hellmanex ™ solution.*

As depicted by Figure 8, Hellmanex™ shows a signal covering the one of Ganciclovir at 252 nm. Thus, SDS will be kept. To break PEG_{46}-*b*-$PTMC_{119}$ vesicle, 300 µL of sample needs to be diluted with 180 µL of a SDS solution at 115 mg.mL^{-1} of SDS. Thus, when comparing scattered intensity of initial

sample and diluted one, a residual signal of 3% is kept after withdrawing effect of dilution. These conditions are not giving any different signal by UV spectroscopy.

1.2.5.2. Doxorubicin

Doxorubicin Hydrochloride is known to have a good fluorescent signal.[24] We decided to build a calibration for Doxorubicin HCl quantification by fluorescence spectroscopy, in DMSO. We first determined excitation wavelength as the wavelength showing the maximum of absorbance. Excitation wavelength was measured at 481 nm, as shown in figure 9.

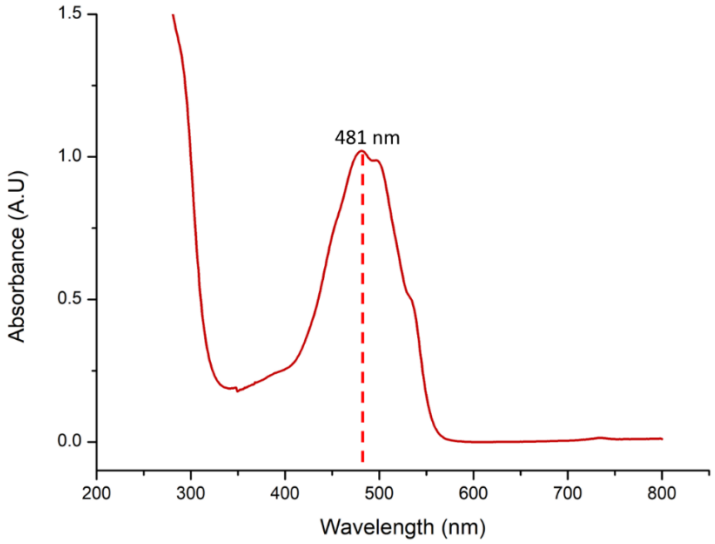

***Figure 9**: Doxorubicin HCl (0.05 mg.mL^{-1} in DMSO) absorbance signal measured by UV-Vis spectroscopy. Maximum absorbance is measured at 481 nm.*

We took advantage of absorbance measurement to determine Doxorubicin concentration allowing to reach an absorbance under 0.1 (A.U). We built a calibration curve of Doxorubicin absorbance depending on its concentration and obtained a linear calibration curve with the following equation after linear fitting (Equation III.2) :

$$y = 18.62\,x + 0.02 \;\; ; \;\; R^2 = 0.9976 \qquad III.2$$

y as the absorbance (A.U) and x as the Doxorubicin concentration (in mg.mL^{-1}). To build this curve, solvent and cuvette signal has been withdrawn.

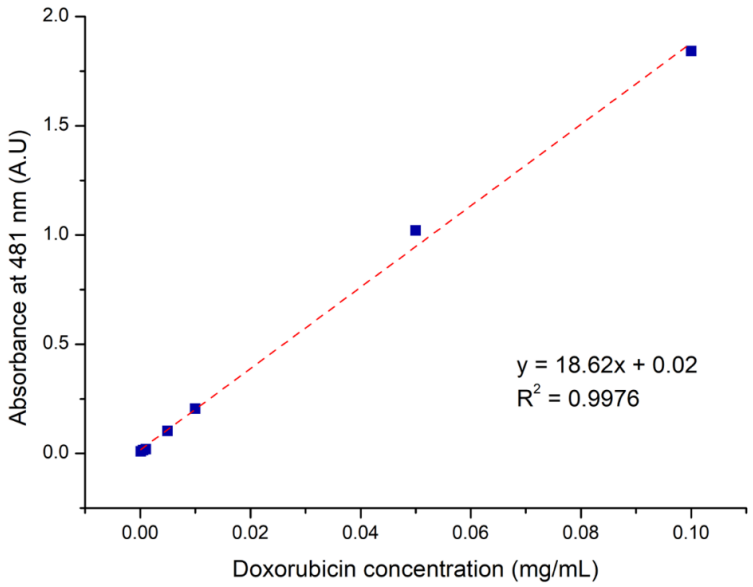

Figure 10: *UV calibration curve of Doxorubicin HCl, absorbance at 481 nm.*

Starting from 0.1 $mg.mL^{-1}$, which is the concentration having an absorbance of 0.1 A.U measured by UV spectrometer, we proceed in lowering this concentration from 1.10^{-3} to 5.10^{-5} $mg.mL^{-1}$ to obtain a calibration a curve by fluorescence. We first determined the maximum emission wavelength as being 592 nm using 481 nm as the wavelength of excitation, as previously determined. Figure 11 shows emission spectrum of Doxorubicin in DMSO, excited at 481 nm.

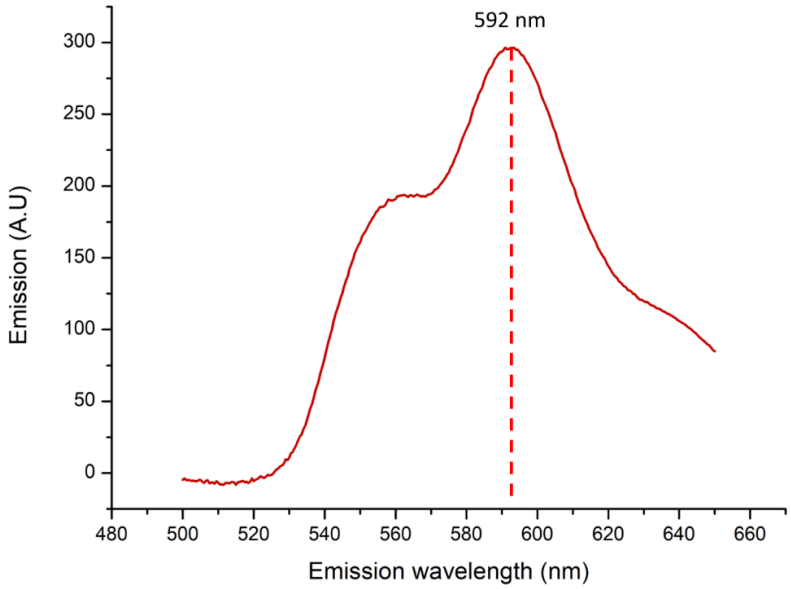

Figure 11: *Doxorubicine HCl (0.1 µg.mL^{-1} in DMSO) emission measured by fluorescent spectroscopy when excited at 481 nm. Maximum absorbance is measured at 481 nm. Maximum emission is measured at 592 nm.*

We used this emission wavelength to build the calibration curve of fluorescence intensity depending on Doxorubicin concentration and obtained a linear calibration curve following this equation (Equation III.3) :

$$y = 3.52\,x \times 10^{-3} - 92.9 \;;\; R^2 = 0.9974 \qquad III.3$$

y as fluorescence emission at 592 nm when excited at 481nm and x as Doxorubicin concentration (µg.mL^{-1}). To build this curve, solvent and cuvette signal has been withdrawn. Calibration curve is depicted by figure 12.

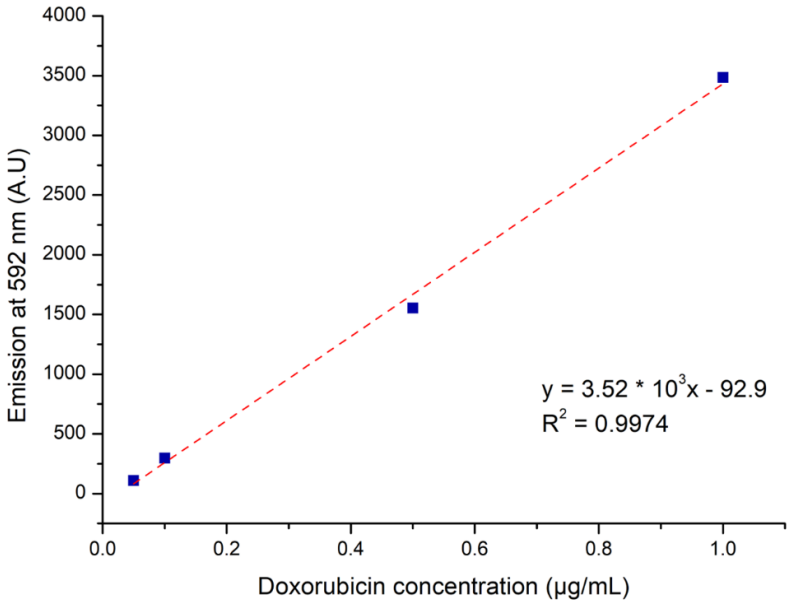

***Figure 12**: Fluorescence calibration curve of Doxorubicin HCl, fluorescence emission measured at 592 nm when excited at 481 nm.*

To release loaded Doxorubicin from vesicles, choice was made to freeze-dry vesicle solution after purification and to solubilize it again in DMSO. DMSO being a good solvent for both drug and copolymer, self-assembly would be reversed. In a typical experiment, 2 aliquots of 0.5 mL were taken from each sample to quantify, put in tared Eppendorf, and freeze-dried overnight. Same thing was done with pure PBS. Dry matter was then weighted to obtain polymer + drug mass (using PBS dry mass to be withdrawn from aliquots mass). 0.5 mL of DMSO was then added to each aliquot and let to solubilize 1h under magnetic stirring. Centrifugation (Fisher Scientific, Mini Centrifuge Zentrifuge) was then used to isolate insoluble PBS salts. Quantification was then made by fluorescent spectroscopy using the previously mentioned calibration curve.

1.2.5.3. Coumarin 6

Coumarin 6, as a fluorescent compound, will be quantified using the same protocol as Doxorubicin. First, UV spectrometer was used to determine excitation wavelength to be 468 nm (Figure 13). Advantage was taken from UV absorbance measurement to determine concentration of coumarin which undergo 0.1 A.U of absorbance at 468 nm.

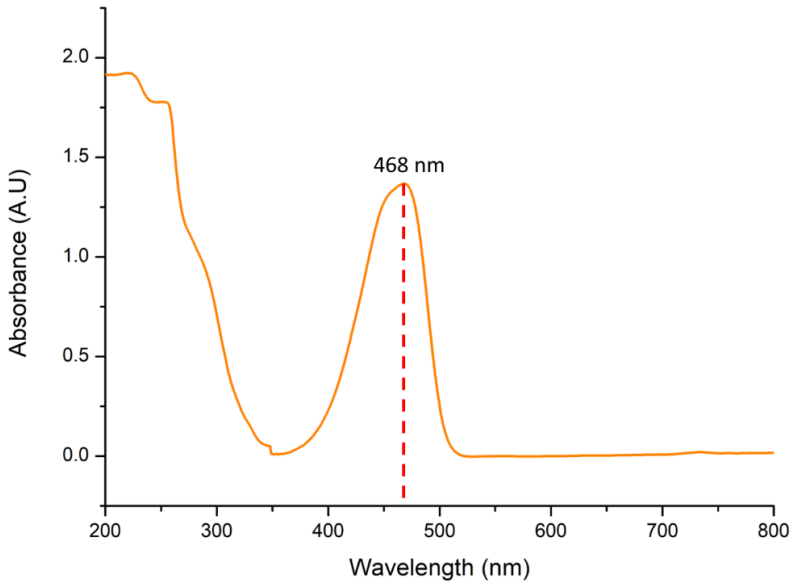

***Figure 13**: Coumarin 6 (10 µg.mL^{-1} in DMSO) absorbance signal measured by UV-Vis spectroscopy. Maximum absorbance is measured at 468 nm.*

Calibration curve of absorbance at 468 nm was thus realized, giving the following equation (equation III.4):

$$y = 1.36\,x \times 10^{-1} + 0.02 \;;\; R^2 = 0.9993 \qquad III.4$$

y as the absorbance at 468 nm and x as the coumarin concentration (in µg.mL^{-1}).

To build the calibration curve given by figure 14, solvent and cuvette signal has been withdrawn.

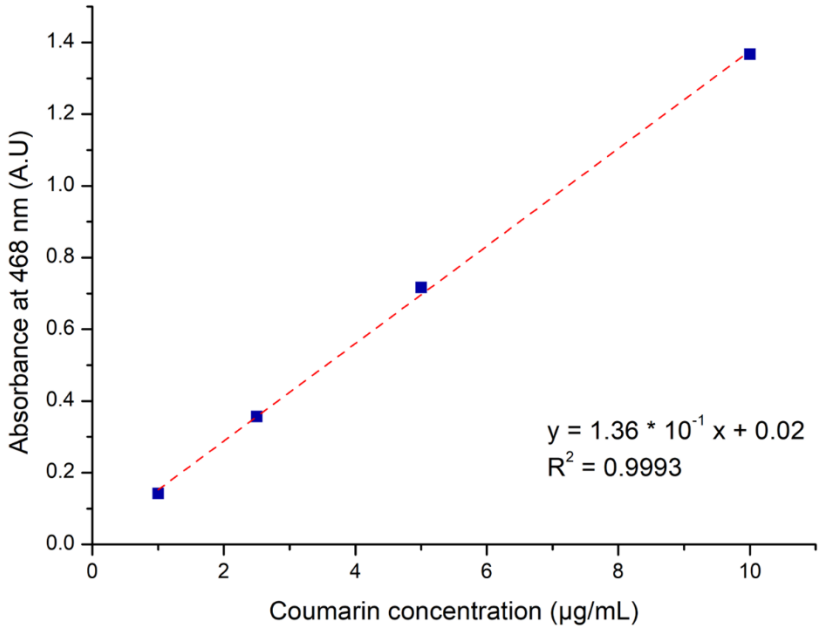

***Figure 14**: UV calibration curve of Coumarin 6 absorbance at 468 nm.*

We thus started from 0.5 µg.mL^{-1} and lowered concentration to obtained calibration curve by fluorescence spectroscopy. We started by looking for emission wavelength using 468 nm as excitation wavelength and obtained 514 nm as the emission wavelength, as shown by figure 15.

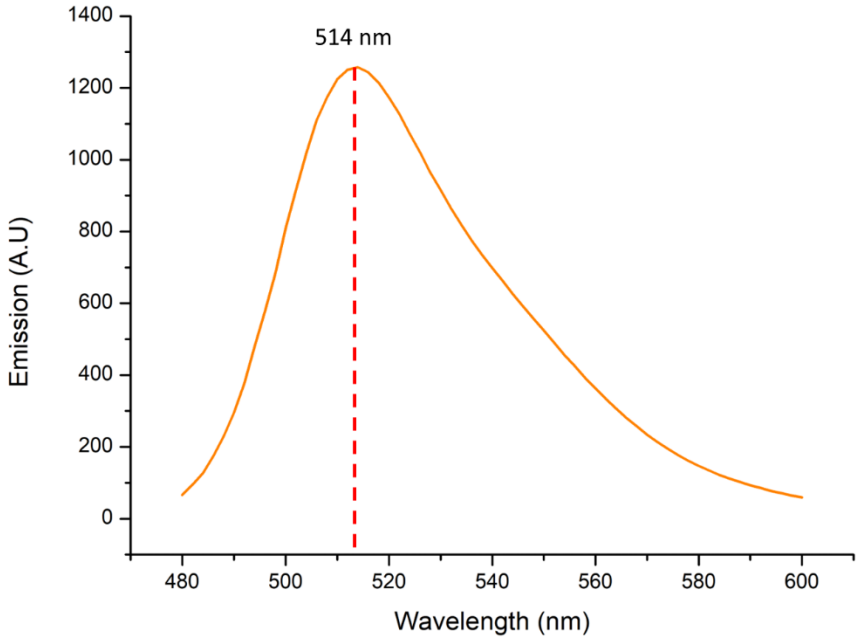

Figure 15: *Coumarin 6 (0.25 µg.mL^{-1} in DMSO) emission measured by fluorescent spectroscopy when excited at 468 nm. Maximum absorbance is measured at 481 nm. Maximum emission is measured at 514 nm.*

The calibration curve of coumarin emission depending on its concentration was obtained following this equation (equation III.5):

$$y = 5.22x \times 10^3 - 2.46 \; ; \; R^2 = 0.9996 \qquad III.5$$

y as the fluorescence emission at 514 nm when excited at 468nm and x as the coumarin concentration (in µg.mL^{-1}).

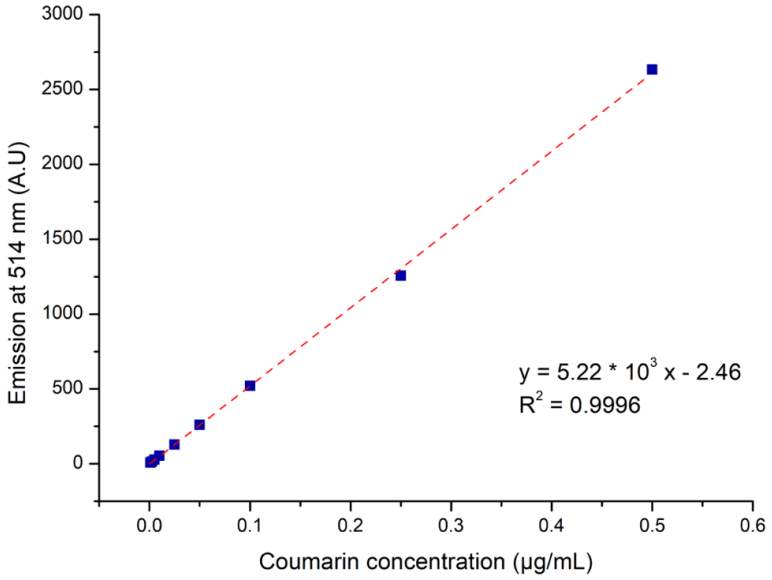

***Figure 16**: Fluorescence calibration curve of Coumarin 6 with fluorescence emission measured at 514 nm when excited at 468 nm.*

As for Doxorubicin, releasing coumarin from vesicle was done by freeze-drying vesicle solution and resolubilizing it in DMSO. Basically, 2 aliquots of 0.5 mL are taken from each sample to quantify, put in tared Eppendorf, and put overnight to freeze-dry. Same thing is done with pure PBS. Dry matter is then weighted to obtain polymer + drug mass (using PBS dry mass to be withdrawn from aliquots mass). 0.5 mL of DMSO is then added to each aliquot and let to solubilize 1h under magnetic stirring. Centrifugation is then used to pushed back to the bottom of the Eppendorf insoluble salts. Quantification is then made by fluorescent spectroscopy using the previously mentioned calibration curve.

1.2.6. Active loading

1.2.6.1. pH gradient

To create an active loading by pH gradient, we decided to self-assemble vesicles into an acidic aqueous solvent at pH = 3. Citric acid buffer was made at 10 mM with 150 mM of NaCl to reach an osmolarity of 300 mOsm.L^{-1} and a pH of 3. For 100 mL of acidic buffer, 936 mg of NaCl, 174 mg of citric acid and 28 mg of sodium citrate are solubilized in water. pH and osmolarity was adjusted using pH-meter and Osmometer.

This aqueous solvent was used in microfluidic-assisted self-assembly in micromixer chip as described in previous chapter with 10 mg.mL^{-1} of PEG-*b*-PTMC in DMSO, 20/80 %vol of organic/aqueous solvent at 1000 µL.min^{-1}. Samples of 2 mL were collected and analyzed by DLS 90°. Samples were then dialyzed using 25 kDa membrane to withdraw DMSO and exchange external aqueous solvent. 3 baths of 2L were done in 24h. First bath was made in same aqueous solvent used in self-assembly, two others were made in PBS, 300 mOsm.L^{-1}, pH = 7.4. After dialysis, Ganciclovir was added. A solution of 20 mg.mL^{-1} of Ganciclovir in DMSO is added to reach 20 % of DMSO or a solution

of 10 mg.mL^{-1} of Ganciclovir to reach 40 % of DMSO. Samples were let to agitate under magnetic stirring for 19 h, 38 h or 72 h.

1.2.6.2. Ionic gradient

To create active loading by ionic gradient, the same protocol was used with pH-gradient, with the exception that aqueous solvent was replaced by ammonium sulfate solution. To obtain 100 mL of ammonium sulfate solution, 1.887 g of ammonium sulfate was solubilized in water. Osmolarity was adjusted using an osmometer and pH is not adjusted, finally measured at pH = 5.3.

This aqueous solvent was used in microfluidic assisted self-assembly in micromixer chip as previously described with 10 mg.mL^{-1} of PEG-*b*-PTMC in DMSO, 20/80 %vol of organic/aqueous solvent at 1000 µL.min^{-1}. Samples of 2 mL were collected and analyzed by DLS 90°. Samples were purified by dialysis using 25 kDa membrane to withdraw DMSO and exchange external aqueous solvent. 3 baths of 2L were done in 24h. First bath was made in same aqueous solvent used in self-assembly, two others were made in PBS, 300 mOsm/L, pH = 7.4. After dialysis, ganciclovir solubilized was added. 20 mg.mL^{-1} of Ganciclovir in DMSO was added in samples to reach 20 % of DMSO or 10 mg.mL^{-1} of Ganciclovir was added to reach 40 % of DMSO. Samples were let to agitate under magnetic stirring for 19 h, 38 h or 72 h.

1.2.7. Characterization techniques

Characterization techniques used and described in the second chapter will be also used in this chapter and will not be described again. Mobile DLS, DLS 90°, Cryo-TEM will be used in addition to UV spectroscopy and Fluorescence spectroscopy, as previously described. Polarized optical Axioskop 40 Zeiss microscope equipped with a AxioCam 105 color camera connected to the computer will be used to observe optical birefringence characteristic to drug crystallinity.

2. Critical water content measurement for copolymer and drug compatibility

In the previous chapter, the critical water content (CWC) has been measured for the copolymer to ensure that optimal parameters are used for microfluidic-assisted self-assembly. As reminder, it has been proved that the CWC for PEG_{22}-*b*-$PTMC_{51}$ polymersomes were evaluated around 11-12% vol, with a weak dependency with the initial concentration of block polymers used during the self-assembly process. In addition, the CWC of the drugs has been measured to ensure that no precipitation of the drugs occurs at a lower water content and before the self-assembly of the block copolymer. By determining the CWC of both the copolymer and the drug, the optimal conditions for nanoprecipitation can potentially be identified to ensure efficient and effective encapsulation of the drug within the copolymer vesicles.

2.1. Evaluation of the critical water content of Ganciclovir

Human cytomegalovirus (HCMV) is a pathogen that causes severe disease and mortality in immunocompromised hosts. Although current treatments such as ganciclovir (GCV), foscarnet, and cidofovir are available, their limited efficacy, high frequency of relapse, and toxic side effects present major challenges. There is a need for new, more effective treatments to combat this virus and the GCV encapsulation inside polymersomes that can induce a local delivery of this drug close to the infection site could be a potential strategy. The therapeutic efficacy of Ganciclovir delivery was evaluated by measuring the viral load in tissues. To achieve the necessary active dose of Ganciclovir (80 $mg.kg^{-1}$ intravenously), the drug loading content of around 10 % in polymersomes will be targeted. The log P of GCV is around -1.66, which indicates a hydrophilic drug that will be more likely loaded in the lumen of a vesicle or other hydrophilic carriers.[25]

The critical water content (CWC) of GCV was first measured by using experimental methods described in the second chapter. 1 mL of GVC in different concentrations (from 10 to 40 $mg.mL^{-1}$) was solubilized in DMSO and water was added at 40 $\mu L.min^{-1}$ under magnetic stirring at 250 rpm and the intensity of light scattered was measured *in situ* during water addition by using mobile DLS.

We first tried to determine the CWC of a solution of 10 $mg.mL^{-1}$ of Ganciclovir. However, no discernible change in scattered light intensity could be observed upon the addition of water up to 70 %vol. Thus, we increased concentration to 20, 30 and 40 $mg.mL^{-1}$. The results indicated a decrease in CWC as the concentration increased, from 61 % vol of water at 20 $mg.mL^{-1}$ to 38 % vol of water at 40 $mg.mL^{-1}$ (Figure 17), which might be correlated to a linear behavior for CWC decrease when the concentration in GCV is increased. (Equation III.6)

$$y = -1.15\,x + 82.83\ , R^2 = 0.97 \qquad III.6$$

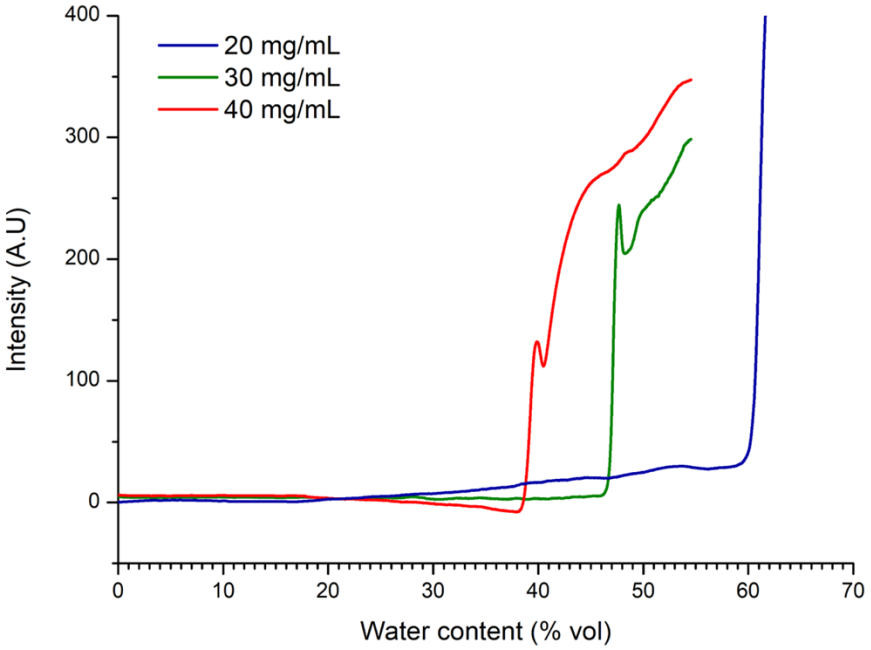

Figure 17: *Scattered light intensity measured in situ during water addition in DMSO solution with different concentrations of Ganciclovir (blue line = 20 mg.mL^{-1}, green line = 30 mg.mL^{-1} and red line = 40 mg.mL^{-1}). Each curves are the average results of experiment done twice, with solvent signal withdrawn and smoothed by Savitzky-Golay smoothing methods, as previously described.*

The CWC of Ganciclovir differs significantly from the CWC of PEG_{22}-*b*-$PTMC_{51}$ (around 11 %vol) indicating that it is unlikely to precipitate prior to copolymer self-assembly. However, as illustrated in Figure 18, "precipitation" is not the appropriate term for Ganciclovir as it tends to crystallize instead. The mechanism of crystallization of Ganciclovir in water is a result of the interplay between the hydrophilic and hydrophobic properties of the drug molecule and the water molecules, leading to the formation of a stable crystal lattice structure. In addition to polymorphism, GCV can also undergo other types of crystallization, such as pseudopolymorphism, which involves the formation of different crystal structures with the same chemical composition but different solubility properties.[26] The formation of different polymorphic forms of Ganciclovir can depend on factors such as the temperature, solvent, and rate of cooling during the crystallization process[27,28]. Polymorphism, which was once overlooked or undervalued for many years, has recently garnered the attention of numerous pharmaceutical industries. It is now a common practice to take in consideration the various polymorphic forms of a given active pharmaceutical ingredient (API) and the investigation, characterization, and control of polymorphism are crucial for the pharmaceutical formulation, as different polymorphic forms of a drug may exhibit distinct physical and chemical properties that can significantly affect the drug's stability, solubility, suspensibility, formulation, shelf life, and bioavailability. Additional experiments using X-ray diffraction would have been relevant to perform in order to assess the crystallinity of GCV obtained after precipitation.

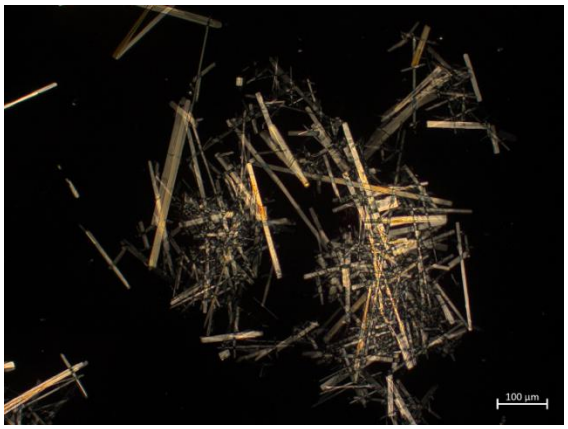

Figure 18: *Observation of Ganciclovir crystals by cross-polarized optical microsopy after slow addition of water in a solution of Ganciclovir solubilized at 20 mg.mL^{-1} in DMSO.*

2.2. Evaluation of the critical water content of Coumarin 6

Coumarin 6 is a hydrophobic molecule with a poor solubility in water. Coumarin 6 is often used as a fluorescent probe for hydrophobic environments, such as the interior of lipid bilayers or micelles. Coumarin derivatives have been studied as potential drug candidates due to their hydrophobicity and ability to interact with hydrophobic regions of enzymes or receptors.[29] In our case, Coumarin 6 was selected as a model molecule used to mimic a hydrophobic drug. Indeed, the log P of Coumarin 6 (Log P = 4.9) is representative of a hydrophobic molecule. Coumarin 6 will more likely be loaded in vesicle membrane due to their neglectable solubility in water.

The CWC of coumarin 6 was evaluated with the same protocol described for the evaluation of the CWC of Ganciclovir: 1 mL of Coumarin in DMSO in different concentrations (from 0.25 to 2 mg.mL^{-1}) was prepared and stirred at 250 rpm. Water was added slowly at 40 µL.min^{-1} and the intensity of scattered light was measured *in situ* during water addition. Figure 19 shows that CWC of Coumarin has the same behavior than the CWC of Ganciclovir, with a CWC that decreases when the Coumarin concentration is increased. Dependency observed is not linear.

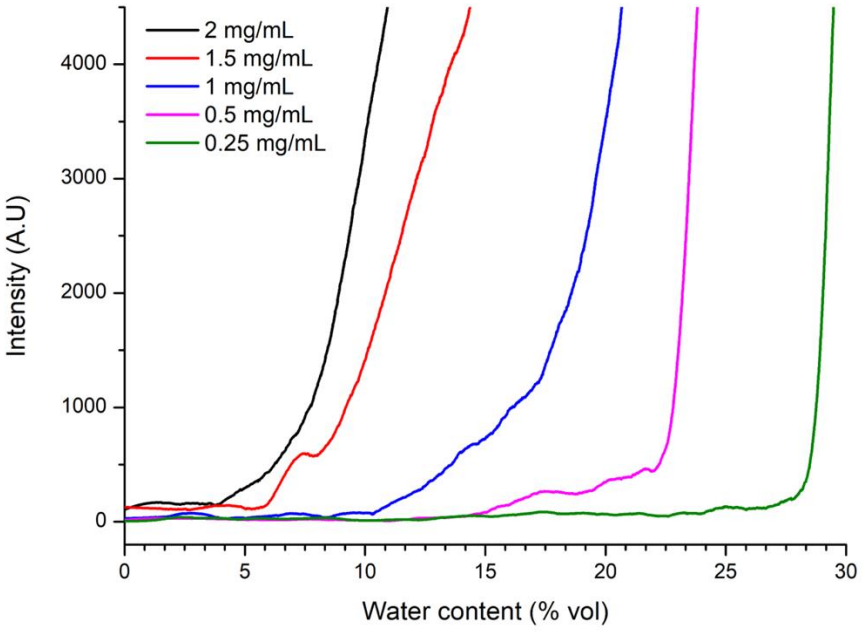

***Figure 19**: Scattered light intensity measured during water addition in organic solution, at different concentrations of Coumarin 6 in DMSO (black line = 2 mg.mL^{-1} , red line = 1.5 mg.mL^{-1}, blue line = 1 mg.mL^{-1}, pink line = 0.5 mg.mL^{-1} and green line = 0.25 mg.mL^{-1}). Curves are the average results of experiments done twice, solvent signal withdrawn and smoothed by Savitzky-Golay smoothing methods as previously described.*

As PEG_{22}-*b*-$PTMC_{51}$ has a CWC around 11 %vol, Coumarin 6 concentration will be kept lower than 1.5 mg.mL^{-1} during the drug loading assay, to avoid Coumarin precipitation before the copolymer self-assembly and ensure an efficient encapsulation. In addition, the behavior of Coumarin 6 after water addition is also not properly relied to a precipitation mechanism but more to a crystallization mechanism, as represented in Figure 20.

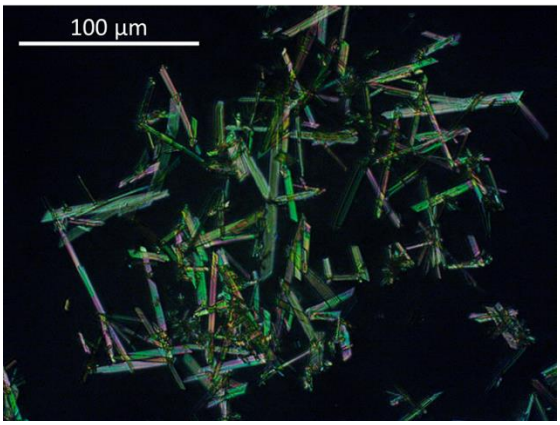

***Figure 20**: Observation of Coumarin 6 crystals" by cross-polarized optical microsopy after slow addition of water in a solution of coumarin 6 solubilized in DMSO.*

2.3. Evaluation of the critical water content of Doxorubicin

Doxorubicin is a well-known chemotherapy drug already used to treat a variety of cancers, including breast cancer, lymphoma, and leukemia. Its mechanism of action involves intercalating into DNA and inhibiting the replication of cancer cells, ultimately leading to cell death. Doxorubicin also generates reactive oxygen species (ROS) that cause cellular damage and ultimately lead to cell death.[30] However, Doxorubicin can also cause damage to healthy cells, which can result in side effects such as an increase of risk of infection. To minimize these side effects, Doxorubicin is typically administered in a controlled manner. For instance, Doxil™ or Caelyx™ commercial formulations are Doxorubicin encapsulated in liposomes made up of hydrogenated soy phosphatidylcholine (HSPC), cholesterol, and a polyethylene glycol (PEG) coating[31]. The log P of Doxorubicin is approximately 1.7, indicating that it is moderately hydrophobic. Doxorubicin is an amphiphilic drug due to its hydrophilic sugar moiety and its hydrophobic aromatic ring. This amphiphilic nature allows Doxorubicin to interact with both hydrophilic core and hydrophobic membrane of vesicles, enabling it to cross the membranes and be present inside the core of the vesicles. The specific location of Doxorubicin within a polymersome or a liposome can vary depending on the formulation and design of the polymersome, and can be tailored to optimize drug delivery and efficacy.[16,18]

The CWC of Doxorubicin was evaluated with the same protocol described earlier: 1 mL of Doxorubicin hydrochloride in DMSO was prepared with different concentrations (up to 40 $mg.mL^{-1}$) and stirred at 250 rpm. Water was added slowly at 40 $\mu L.min^{-1}$ and the intensity of scattered light was determined *in situ* during water addition. In the case of Doxorubicin hydrochloride, no signal change was measured when water was added. This phenomenon might be explained by its amphiphilic properties giving a high solubility of Doxorubicin in both DMSO (≥ 100 $mg.mL^{-1}$ measured) and water (around 50 $mg.mL^{-1}$). It is thus impossible to reach a bad solvent condition even with the highest Doxorubicin concentration.

In conclusion, it appears that no precipitation of Doxorubicin can occur during the polymersome nanoprecipitation, indicating that no caution needs to be exercised in the selection of Doxorubicin concentration during its passive encapsulation via PEG-*b*-PTMC self-assembly. Only the presence of the polymers, offering a better thermodynamic environment could drive the encapsulation. The same indication applies to Ganciclovir, whose CWC is always higher than that of PEG-*b*-PTMC, but care should be taken in the choice of coumarin 6 concentration, which should be kept below 1.5 $mg.mL^{-1}$.

3. Microfluidic assisted passive loading of drugs

3.1. Towards PEG_{22}-*b*-$PTMC_{51}$ loaded vesicles

Passive loading of the drugs was considered after evaluating the right concentration of the three drugs needed to avoid aggregation during water addition and before self-assembly. Microfluidic assisted self-assembly was performed with an organic solvent containing both PEG_{22}-*b*-$PTMC_{51}$ and drug. Copolymer concentration was kept at 10 $mg.mL^{-1}$ in DMSO. 10 $mg.mL^{-1}$ of Ganciclovir, 5 $mg.mL^{-1}$ of Doxorubicin hydrochloride or 1.25 $mg.mL^{-1}$ of Coumarin 6 was added to the copolymer solution. The feed weight ratio (drug concentration / copolymer concentration) was thus calculated as 100 % for GCV, 50% for Doxorubicin and 12.5 % for Coumarin 6. Microfluidic assisted self-assembly was performed using PBS at 300 $mOsm.L^{-1}$ and pH = 7.4 as an aqueous solvent. Organic/aqueous solvent ratio was kept at 20/80 %vol and total flow rate at 1000 $\mu L.min^{-1}$.

After polymersome formation, we verified that the presence of the drug and the purification method had no influence on the final size of the vesicles formed (Table 2). The first selected purification method involved dialysis, based on the diffusion of solutes through a semi-permeable membrane from an area of high concentration to an area of low concentration, driven by the gradient of concentration, was suspected to be able to let loaded drug to escape. Indeed, during the dialysis, the membrane of the polymersomes does not exhibit its final rigidity since organic solvent is still present and can plasticize it, possibly causing leakage of the encapsulated molecules during the early stages of dialysis. We thus decided to compare dialysis with another purification process involving the use of size exclusion column, called Sephadex™ column. This gel filtration matrix is composed of cross-linked dextran beads with controlled pore size, allowing a separation of molecules based on their size and shape that is less time-consuming than dialysis purification.

***Table 2** : Hydrodynamic Diameter D_H and polydispersity index PDI acquisitions obtained by DLS 90° after self-assembly of PEG_{22}-b-$PTMC_{51}$ vesicles. Purification was performed by dialysis or by the use of a size exclusion column. Samples were purified by dialysis with a membrane of 25 kDa, with 3 bath changes (of 2L each) in 24 h and by exclusion size column using a Sephadex™ G100 column. The indicated values are the average of six assays with the calculated standard deviations.*

Drug	Purification technique	Hydrodynamic Diameter D_H (nm)	PDI
Ganciclovir	Dialysis	132 ± 5	0.122 ± 0.015
	Exclusion size column	144 ± 5	0.128 ± 0.004
Doxorubicin HCl	Dialysis	148 ± 6	0.129 ± 0.016
	Exclusion size column	149 ± 2	0.115 ± 0.021
Coumarin 6	Dialysis	146 ± 3	0.116 ± 0.013
	Exclusion size column	144 ± 5	0.117 ± 0.018
Unloaded	Dialysis	161 ± 4	0.138 ± 0.06

Regarding the morphology of polymersomes after passive encapsulation, a decrease in size is observed in presence of drugs, with a size decrease of about 10 to 20 %, but a homogeneous population of formed polymersomes is still obtained (PDI in the same range). Drug might be changing solvent properties leading to a change in solvent interdiffusion speed, that may induce change in

vesicle size.[32] Also, neither purification process seems to influence the final morphology of the obtained nanoparticles.

The quantification of loaded drug was then performed by spectroscopy after the establishment of calibration curves by UV and fluorescence spectroscopy and the disruption of vesicles for releasing drug. For Ganciclovir, SDS surfactant was added for the disruption of polymersome membrane and absorbance at 252 nm was measured. For Doxorubicin and Coumarin 6, samples were freeze-dried and solubilized in DMSO before the measurement of the fluorescent signal emitted by the drug ($\lambda_{exc}/\lambda_{em}$ of Doxorubicin = 481/592 nm and $\lambda_{exc}/\lambda_{em}$ of Coumarin 6 = 468/514 nm).

Drug Loading Content (DLC) and Drug Loading Efficiency (DLE) were calculated using the following equations (Equations III.6 and III.7). Table 3 gathers results of DLC and DLE according to the encapsulated drug and the purification process that was used.

$$DLC = \frac{loaded\ drug\ mass}{loaded\ vesicles\ mass} \times 100 \qquad III.6$$

$$DLE = \frac{loaded\ drug\ mass}{initial\ drug\ mass} \times 100 \qquad III.7$$

***Table 3** : Drug Loading Content (DLC) and Drug Loading Efficiency (DLE) of Ganciclovir, Doxorubicin and Coumarin 6 loaded in PEG_{22}-b-$PTMC_{51}$ vesicles depending on purification process used. Grey square are estimations and not measured data.*

Drug	Purification	DLC (%)	DLE (%)
Ganciclovir	Dialysis	< 0.025	< 0.019
	Exclusion size column	< 0.024	< 0.017
Doxorubicin HCl	Dialysis	0.053 ± 0.008	0.089 ± 0.022
	Exclusion size column	0.004 ± 0.0002	0.008 ± 0.0004
Coumarin 6	Dialysis	0.087 ± 0.033	0.486 ± 0.134
	Exclusion size column	0.087 ± 0.009	0.563 ± 0.083

For all three drugs, loading content and loading efficiency values are extremely low, especially compared to typical values obtained for other polymersomes (around 5-10 %)[33]. For ganciclovir, after solvent and copolymer signal withdrawal, the remaining absorbance signal was negligible. Thus, loaded amount of ganciclovir might be under the detection limit and only an estimation of DLC could be determined. For the other two molecules, the hydrophobic Coumarin 6 seems to have better loading capacity than the amphiphilic Doxorubicin. Moreover, when comparing purification processes, no difference was observed between dialysis and size exclusion column process for the hydrophobic drug. For Doxorubicin, a higher loading content and efficiency was quantified after dialysis purification. This might be the sign of adsorbed drugs present at the surface of vesicles that could be removed only by size exclusion purification process. This phenomenon wouldn't be possible with hydrophobic molecules as they tend to be located in the membrane. To improve the passive loading of drugs, two routes are considered: (i) fusing the CWC of the drug and copolymer to "force" them to assemble

concomitantly, or (ii) increasing the membrane thickness of the formed polymersomes to limit diffusion through the membrane.

3.2. Improving Ganciclovir passive loading by tuning the CWC of PEG_{22}-b-$PTMC_{51}$

Regarding low results obtained for DLC and DLE, we tried to improve passive loading drugs by merging the CWC of PEG_{22}-*b*-$PTMC_{51}$ and drug. Ganciclovir was selected as the model drug. By playing on organic solvent composition by combining Acetone with DMSO in a certain ratio, we were able to decrease the CWC of Ganciclovir and increase the CWC of the copolymer.

We first evaluated the variation of CWC for copolymer and drug separately according to the ratio of DMSO/Acetone. We measured light scattered intensity for a solution of 2.5 $mg.mL^{-1}$ of PEG_{22}-*b*-$PTMC_{51}$ block copolymer in a mixture of DMSO/Acetone of 100/0, 75/25, 50/50, 25/75 or 0/100 %vol, with an addition of water at 40 $\mu L.min^{-1}$, as previously performed. Same measurements were done for a solution of Ganciclovir at 20 $mg.mL^{-1}$ in a mixture of DMSO/Acetone, with different ratios than block copolymer, as ganciclovir is not soluble in acetone only : 100/0, 75/25, 50/50, 45/55 or 40/60 %vol. Figure 21 and Figure 22 represent the CWC obtained respectively for PEG_{22}-*b*-$PTMC_{51}$ and Ganciclovir at different organic solvent compositions.

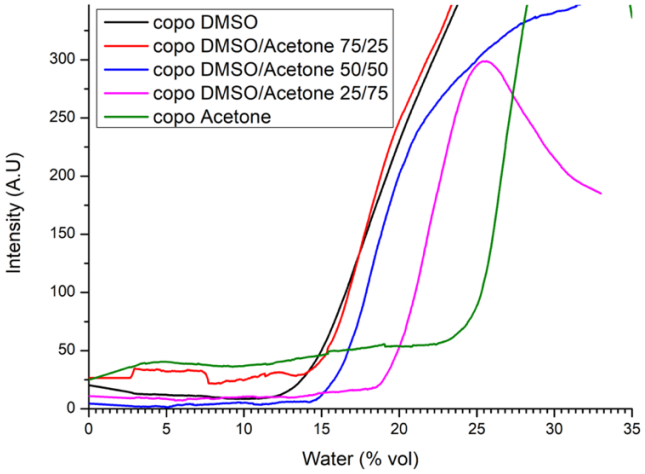

Figure 21: *Light scattered intensity by PEG_{22}-b-$PTMC_{51}$ in organic solution while water is added, depending on DMSO/Acetone composition of the organic solvent (black line = DMSO , red line = DMSO/Acetone 75/25, blue line = DMSO/Acetone 50/50, pink line = DMSO/Acetone 25/75 and green line Acetone). Curves are the average results of experiments done twice, solvent signal withdrawn and smoothed by Savitzky-Golay smoothing methods as previously described.*

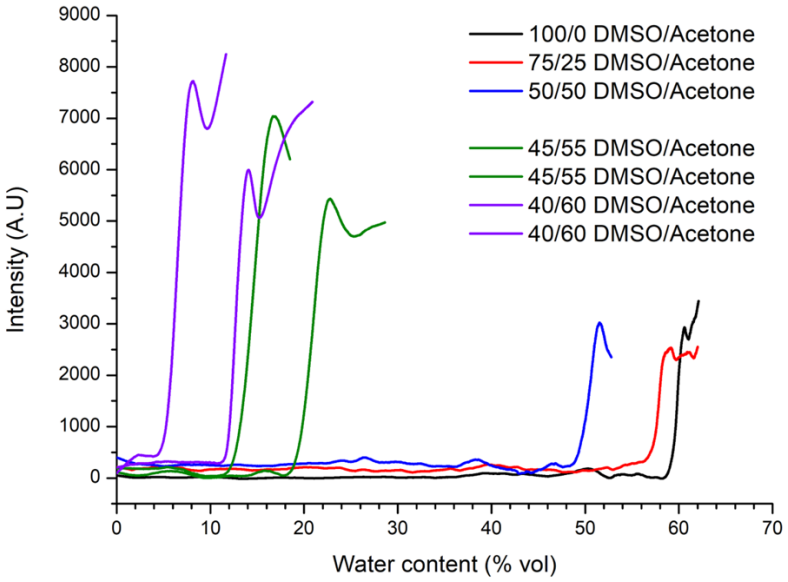

***Figure 22**: Light scattered intensity by Ganciclovir in organic solution while water is added, depending on DMSO/Acetone composition of the organic solvent (black line = DMSO, red line = DMSO/Acetone 75/25, blue line = DMSO/Acetone 50/50, green line = DMSO/Acetone 44/55 and violet line = DMSO/Acetone 40/60). Curves are the average results of experiments done twice, solvent signal withdrawn and smoothed by Savitzky-Golay smoothing methods as previously described.*

Concerning the variation of CWC of PEG_{22}-*b*-$PTMC_{51}$, using a mixture of DMSO/Acetone has proven to be efficient to increase CWC, with an increase of 11% in DMSO/Acetone 100/0 to 24% in DMSO/Acetone 0/100. Concerning the CWC of ganciclovir, the presence of acetone seems to decrease the value of the CWC, with a CWC of 5-10% with a solution of DMSO/Acetone at 40/60, instead of a CWC of 60% for DMSO/Acetone 100/0. Moreover, a change in Ganciclovir crystallization is observed according to the initial organic solvent, as depicted in Figure 23 by using polarized optical microscopy. Additional experiments using X-ray diffraction would have been relevant to perform in order to assess the crystallinity of GCV obtained after precipitation.

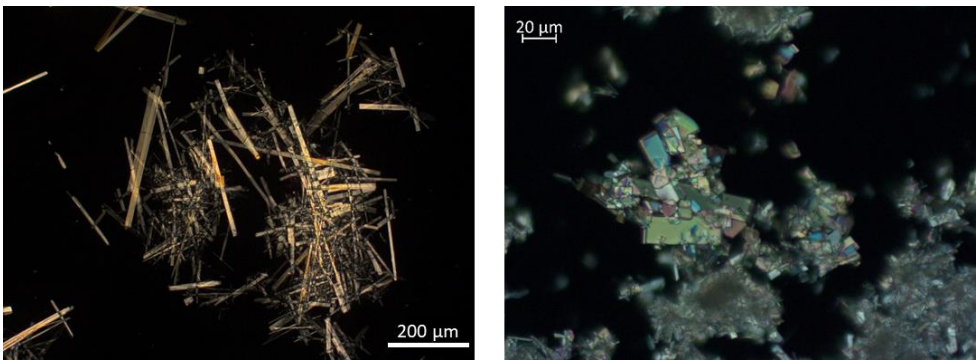

***Figure 23:** Observation of Ganciclovir "precipitate" by polarized optical microsope revealing the presence of crystals after adding water to a solution of Ganciclovir previously solubilized in DMSO only (left image) or in a solution of 40/60 %vol DMSO/Acetone (right image).*

By using an initial mixture of organic solvent of DMSO/Acetone 45/55 %vol, an organic/aqueous ratio of 20/80 %vol for self-assembly, we will be able to have drug crystallization and copolymer self-assembly at the same time, which could lead to loading of nuclei of drug crystals that

will theoretically allow a better drug loading inside our formed vesicles (figure 24). This hypothesis will nevertheless strongly depend on self-assembly pathway (swelling micelles or elongated micelles fold to vesicles, as explained in the first chapter) and complementary studies of self-assembly pathway seems to be necessary to provide answers to our loading issues.

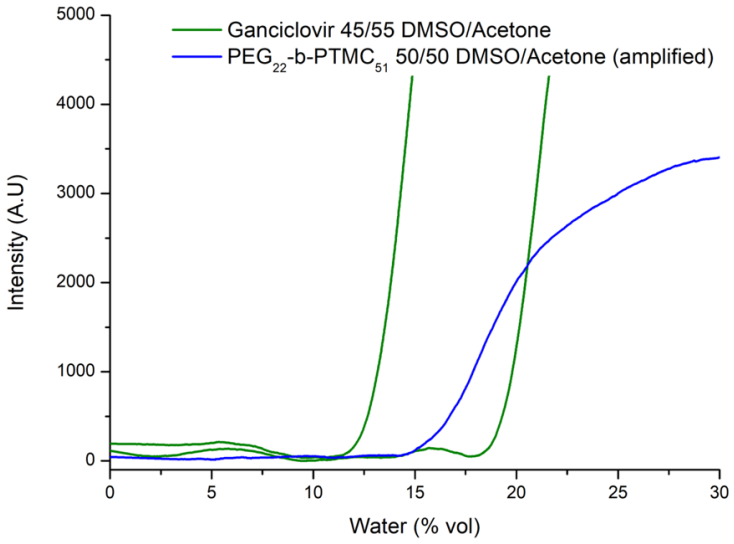

Figure 24: *Light scattered intensity by Ganciclovir (green) and PEG_{22}-b-$PTMC_{51}$ (blue) in organic solution while water is added, depending on DMSO/Acetone composition of the organic. Solvent signal withdrawn and smoothed by Savitzky-Golay smoothing methods as previously described.*

Before starting self-assembly assays with a co-precipitation of drug and block copolymers, the reproducibility of the process was tested for condition of DMSO/Acetone of 40/60 or 44/55 % vol during CWC assays. Indeed, as mentioned earlier, crystallization strongly depends on thermodynamic parameter variations, especially temperature. The CWC experiments with DMSO/acetone 40/60 %vol were then repeated. Figure 24 and 25 give an example of the difference observed between two duplicates of an experiment and the temperature measured in the room. A lower temperature (21.5 °C) tends to lead to premature crystallization (CWC of 10%) when increasing temperature (24 °C) leads to postponing crystallization (CWC of 50%). This phenomenon that happens in a small interval of temperature variation highlights the complexity of Ganciclovir crystallization. We measured the increase in temperature during CWC measurement and compared it with the increase of temperature in microfluidic chip during self-assembly by using a thermal camera (Figure 25). Solutions seemed to never exceed 24 °C during CWC measurement when microfluidic chip heat up to 27 °C during self-assembly of PEG_{22}-*b*-$PTMC_{51}$ block copolymers (Figure in appendix).

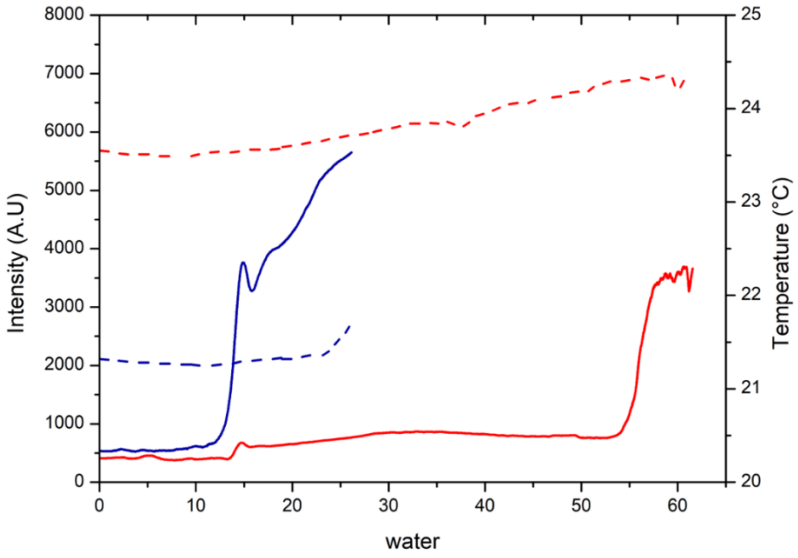

Figure 25: *Light scattered intensity by Ganciclovir in organic solution while water is added starting in an organic solvent composed of 40/60 %vol of DMSO/Acetone. Influence of temperature (represented with dotted lines)*

We found that the temperature in the microfluidic chip was not sufficiently well controlled by the temperature control unit present on the bottom of the microfluidic chip and provided by our supplier Dolomite™. An aluminum piece that will better conduct thermal flows from glass chip to cooling system was fabricated and focused air flow was used to dissipate heat from the top of the chip, as shown in Figure 26. By using thermal camera Optris PI 230, we evidenced that we were able to maintain a temperature of 24 °C in the microfluidic chip during self-assembly experiment. Unfortunately, due to a lack of time and the non-availability of all the necessary equipment to perform temperature-controlled microfluidic self-assembly, we were not able to perform co-precipitation of PEG_{22}-*b*-$PTMC_{51}$ block copolymers and Ganciclovir in these better controlled conditions.

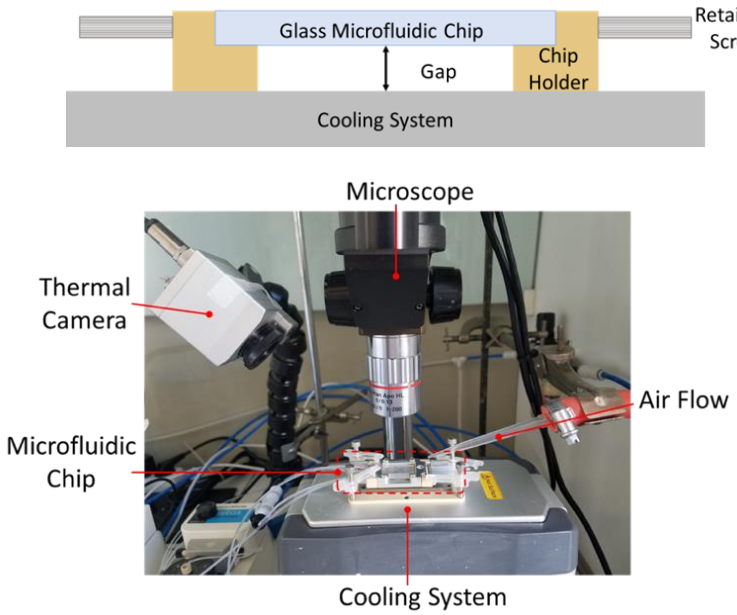

***Figure 26**: (Top) Schematic representation of chip holder highlighting gap between the chip and the cooling system, resulting in poor heat dissipation from the chip. (Bottom) Final microfluidic set-up allowing to control temperature in microfluidic chip during self-assembly.*

3.3. Towards PEG_{46}-*b*-$PTMC_{119}$ loaded vesicles

We also thought that the low DLC and DLE values obtained for all drug models were due to vesicle leakage from a too high permeability of their membrane. As a reminder, the membrane permeability is primarily controlled by the polymer forming the hydrophobic block which affects the fluidity and thickness of the polymersome membrane and the diffusion of molecule inside this membrane primarily depends on the membrane thickness according to Fick's first law. The diffusion coefficient of polymersome's membrane was found to decrease with increasing molecular weight of the copolymer.[34] Coralie Lebleu reported a scaling law between PEG-*b*-PTMC molar mass and membrane thickness[22]. She experimentally determined by Cryo-TEM and SANS experiments a relation between the hydrophobic membrane thickness (δ) and the hydrophobic block molar mass (M_H) that is consistent with theoretical predictions and slightly differs according to the experimental methods that was used (Equations III.8 and III.9):

$$\delta_{PTMC}(cryo-TEM) = 0{,}35 \times {M_H}^{0.42} \qquad III.8$$

$$\delta_{PTMC}\,(SANS) = 0{,}21 \times {M_H}^{0.46} \qquad III.9$$

Therefore, the molar mass of the hydrophobic blocks was shown to play a critical role in vesicle permeability.[35–37] To overcome the issue of low drug loading, we intended to use a high molar mass copolymer with similar hydrophilic ratio by replacing PEG_{22}-*b*-$PTMC_{51}$ by PEG_{46}-*b*-$PTMC_{119}$.

3.3.1. Optimization of PEG_{46}-*b*-$PTMC_m$ copolymer composition to favor vesicle self-assembly

We started the synthesis of longer PEG-*b*-PTMC by using a larger PEG initiator (PEG_{46}-OH compared to PEG_{22}-OH used before) for the ring opening polymerization (ROP) of trimethylene carbonate monomer. We then proceeded in synthetizing by ROP a series of PEG_{46}-*b*-$PTMC_m$ copolymers presenting hydrophilic weight fraction in the same range than PEG_{22}-*b*-$PTMC_{51}$ (f_{PEG} = 16%). We first obtained the block copolymer PEG_{46}-*b*-$PTMC_{94}$ (f_{PEG} = 17%). The self-assembly of this longer block copolymer was performed in microfluidic (DMSO/PBS 30/70 %vol, 1000 µL.min^{-1} of total flow rate) and nanoparticles that are formed were analyzed by DLS (Appendix Table A1) and observed by Cryo-TEM. As presented in Figure 27, PEG_{46}-*b*-$PTMC_{94}$ nanoparticles tend to form more wormlike structures instead of vesicles, compared to PEG_{22}-*b*-$PTMC_{51}$ nanoparticles formulated by microfluidic.

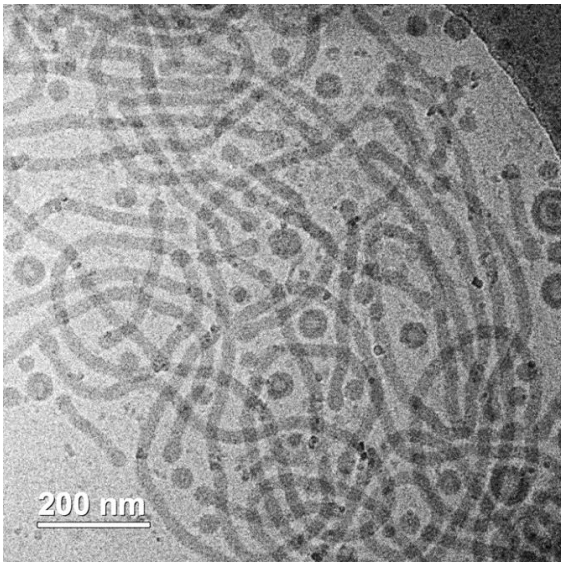

Figure 27: *Cryo-TEM representation of PEG_{46}-b-$PTMC_{94}$ worm-like structures after microfluidic assisted self-assembly and purification by dialysis.*

As reported by Jain *et al.*[38], when the overall molar mass of a copolymer is increased, keeping a same PEG fraction than a shorter one might lead to a variation in the shape of self-assembled nanoparticles. In order to maintain the same nanoparticle structure, decreasing the hydrophilic PEG fraction could be a potential solution. We thus synthesized PEG_{46}-*b*-$PTMC_{121}$ with a slightly lower hydrophilic fraction (f_{PEG}=14%). After self-assembly in microfluidic (50/50 %vol DMSO/PBS, 1000 µL.min^{-1} of total flow rate), it was observed by cryo-TEM that this copolymer forms well-defined vesicular structures (Figure 28). Another copolymer (larger batch) was synthesized with a slight change in the hydrophobic block (namely PEG_{46}-*b*-$PTMC_{119}$) that forms same vesicular structures and was used for the optimizing self-assembly experiments.

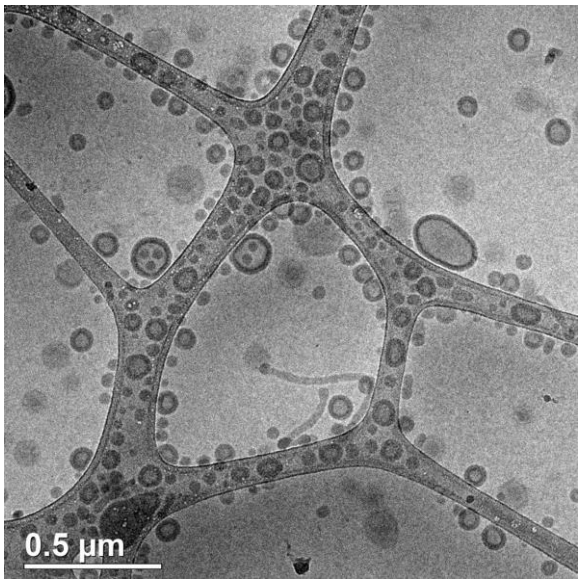

Figure 28: *Representation of PEG_{46}-b-$PTMC_{121}$ vesicles by Cryo-TEM after microfluidic assisted self-assembly and dialysis purification.*

Membrane thickness of self-assembled vesicles of PEG_{22}-*b*-$PTMC_{51}$ and PEG_{46}-*b*-$PTMC_{119}$ were measured on Cryo-TEM images. Measured on 30 vesicles for each copolymer, vesicles present an average membrane thickness of 11.5 ± 1.3 nm and 21.0 ± 2.6 nm respectively for vesicle of PEG_{22}-*b*-$PTMC_{51}$ and PEG_{46}-*b*-$PTMC_{119}$. These results confirm the increase in membrane thickness while using PEG_{46}-*b*-$PTMC_{119}$ compared to PEG_{22}-*b*-$PTMC_{51}$ and are almost fitting scaling law proposed by Coralie Lebleu (Equation III. 8), which was predicting thickness of 12.7 and 18.1 nm respectively for vesicle of PEG_{22}-*b*-$PTMC_{51}$ and PEG_{46}-*b*-$PTMC_{119}$.

3.3.2. Microfluidic parameters for a monodispersed and reproductible self-assembly

3.3.2.1. Critical Water Content measurement to induce self-assembly

As previously reported for PEG_{22}-*b*-$PTMC_{51}$ in the second chapter, the CWC of PEG_{46}-*b*-$PTMC_{119}$ was measured *in situ* by dynamic light scattering when water was added to a copolymer solubilized in DMSO. Copolymer solution of 1, 5 and 10 $mg.mL^{-1}$ in DMSO was stirred at 250 rpm while water was added at 40 $\mu L.min^{-1}$. Scattered light intensities according to block copolymer concentration are represented in Figure 29. The same behavior was observed for PEG_{22}-*b*-$PTMC_{51}$ and PEG_{46}-*b*-$PTMC_{119}$, with a CWC measured around 12 %vol. A slight reduction of the CWC with increasing copolymer concentration was then observed for all overall molar masses of PEG-*b*-PTMC block copolymers, from 12.5 % v/v CWC for 1 $mg.mL^{-1}$ of copolymer to 10.5 % for 10 $mg.mL^{-1}$, in agreement with results previously reported in the second chapter.

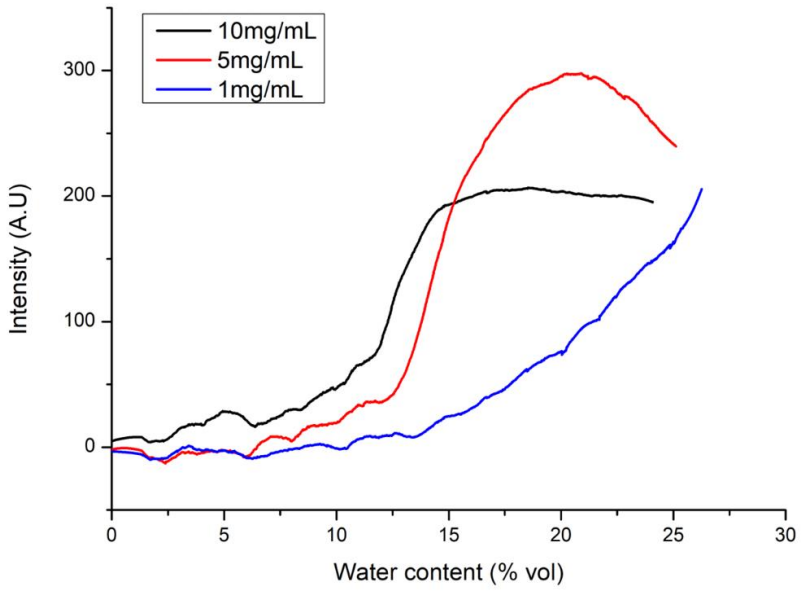

Figure 29: *Scattered intensity measured during water addition in organic solution, at different concentrations of PEG_{46}-b-$PTMC_{119}$ in DMSO. Represented curves are the average result of experiments carried out in duplicate and are smoothed by Savitzky-Golay method.*

3.3.2.2. Optimizing microfluidic assisted self-assembly of PEG_{46}-b-$PTMC_{119}$

As previously reported, a solution of PEG_{46}-*b*-$PTMC_{119}$ of 10 $mg.mL^{-1}$ in DMSO was used in microfluidic assisted self-assembly, with a total flow rate set at 1000 $\mu L.min^{-1}$. Aqueous solvent used was PBS at 300 $mOsm.L^{-1}$ and pH = 7.4. Organic/aqueous solvent ratio was varied from 50/50 %vol to 20/80 %vol. Aliquots were collected for each ratio and analyzed by DLS 90° before purification. Table 4 gives PDI for each ratio.

Table 4 : *polydispersity index measured by DLS 90° of PEG_{46}-b-$PTMC_{119}$ nanoparticles formed on microfluidic assisted self-assembled, depending on organic/aqueous solvent ratio used.*

Ratio organic/aqueous solvent (%vol)	**D_H (nm)**	**PDI**
20/80	191 ± 5	0.20 ± 0.02
30/70	210 ± 49	0.33 ± 0.05
40/60	197 ± 17	0.24 ± 0.02
50/50	183 ± 13	0.15 ± 0.04

According to table 4, the organic/aqueous solvent ratio of 20/80 %vol and 50/50 %vol tend to form a homogeneous population of vesicles, according to low PDI values obtained, close to 0.1. Table 5 gives results obtained for an organic/aqueous solvent ratio of 20/80 %vol and 50/50 %vol before and after purification process.

Table 5: *Diameter and dispersity of vesicles made by microfluidic assisted self-assembly with PEG_{46}-b-$PTMC_{119}$, before and after purification and filtration with a filter of 0.45 µm. Three samples of 2 mL per ratio were made and purified by dialysis before analyze by DLS 90°.*

Organic/Aqueous solvent ratio (%vol)	Before purification		After purification	
	Hydrodynamic Diameter D_H (nm)	PDI	Hydrodynamic Diameter D_H (nm)	PDI
20/80	183 ± 2	0.11 ± 0.03	153 ± 9	0.14 ± 0.01
50/50	185 ± 29	0.22 ± 0.04	141 ± 1	0.12 ± 0.01

In conclusion, the ratio of 50/50 %vol was preferred as providing vesicles of rather similar size with a smaller PDI. However, the 20/80 %vol conditions will be used if needed, as results obtained are acceptable (but final concentration is lower).

3.3.3. Improving passive drug loading with PEG_{46}-*b*-$PTMC_{119}$

As for PEG_{22}-*b*-$PTMC_{51}$, we tried to load our three molecules in vesicles formed with PEG_{46}-*b*-$PTMC_{119}$ by using passive loading. A solution of PEG_{46}-*b*-$PTMC_{119}$ at 10 mg.mL^{-1} in DMSO was made in which either 10 mg.mL^{-1} of Ganciclovir, 5 mg.mL^{-1} of Doxorubicin HCl or 1.25 mg.mL^{-1} of Coumarin 6 was added. The feed weight ratio (drug concentration / copolymer concentration) was thus calculated as 100 % for GCV, 50% for Doxorubicin and 12,5 % for Coumarin 6. Aqueous solvent used was PBS at 300 mOsm.L^{-1} and pH = 7.4. Microfluidic assisted self-assembly was performed in the ideal condition (1000 µL.min^{-1} for the total flow rate), with the organic/aqueous ratio of 50/50 %vol for Ganciclovir of Doxorubicin loading assays. Unfortunately, for Coumarin 6, aggregation and obstruction of the chip occurred at this ratio and 20/80 %vol was used for Coumarin 6 experiments. After purification either with dialysis or with the use of exclusion size column, dynamic light scattering was performed. Obtained results are summarized in Table 6.

Table 6*: Hydrodynamic Diameter D_H and polydispersity index PDI acquisitions obtained by DLS 90° after self-assembly of PEG_{46}-b-$PTMC_{119}$ vesicles. Purification was done by dialysis or by the use of exclusion size column. Samples were purified by dialysis with a membrane of 25 kDa, with 3 bath changes (of 2L each) in 24 h and by exclusion size column using a Sephadex™ G100 column. The indicated values are the average of three assays with the calculated standard deviations.*

Drug	Purification	Hydrodynamic Diameter D_H (nm)	PDI
Ganciclovir	Dialysis	140 ± 6	0.129 ± 0.009
	Exclusion size column	126 ± 8	0.092 ± 0.011
Doxorubicin HCl	Dialysis	139 ± 2	0.111 ± 0.010
	Exclusion size column	139 ± 4	0.094 ± 0.014
Coumarin 6	Dialysis	127 ± 3	0.131 ± 0.007
	Exclusion size column	128 ± 3	0.110 ± 0.011
Unloaded	Dialysis	141 ± 1	0.14 ± 0.01

As previously observed, a small reduction in size is also observed for PEG_{46}-*b*-$PTMC_{119}$ vesicles probably due to the change of solvent properties in presence of added molecules, leading to a change in interdiffusion speed and thus an impact on vesicle size.[32]

Quantification of loaded drug was done as previously reported. For Doxorubicin HCl and Coumarin 6, purified samples were freeze-dried and solubilized again in DMSO. For Ganciclovir, SDS was added to destabilize and break the membrane of polymersome. Doxorubicin and Coumarin in DMSO was quantified using calibration curve by fluorescence spectroscopy (Doxorubicin: $\lambda_{Ex}/\lambda_{Em}$ = 481 / 592 nm; Coumarin 6 $\lambda_{Ex}/\lambda_{Em}$ = 468/514 nm). Ganciclovir was quantified using calibration curve of UV absorbance at 252 nm. Drug Loading Content (DLC) and Drug Loading Efficiency (DLE) were calculated for PEG_{46}-*b*-$PTMC_{119}$ vesicles and a comparison between PEG_{22}-*b*-$PTMC_{51}$ and PEG_{46}-*b*-$PTMC_{119}$ vesicles is established in Table 7.

Table 7: *Drug Loading Content (DLC) and Drug Loading Efficiency (DLE) of Ganciclovir, Doxorubicin and Coumarin 6 loaded in PEG_{22}-b-$PTMC_{51}$ and PEG_{46}-b-$PTMC_{119}$ vesicles depending on purification processes. Grey square are estimations and not measured data. The indicated values are the average of three assays with the calculated standard deviations.*

Drug	**Purification**	**PEG_{22}-*b*-$PTMC_{51}$**		**PEG_{46}-*b*-$PTMC_{119}$**	
		DLC (%)	**DLE (%)**	**DLC (%)**	**DLE (%)**
Ganciclovir	Dialysis	< 0.025	< 0.019	**0.325** ± 0.165	**0.595** ± 0.286
	Exclusion size column	< 0.024	< 0.017	**0.245** ± 0.119	**0.462** ± 0.210
Doxorubicin HCl	Dialysis	**0.053** ± 0.008	**0.089** ± 0.022	**0.072** ± 0.017	**0.110** ± 0.032
	Exclusion size column	**0.004** ± 0.0002	**0.008** ± 0.0004	**0.016** ± 0.001	**0.030** ± 0.003
Coumarin 6	Dialysis	**0.087** ± 0.033	**0.486** ± 0.134	**0.118** ± 0.019	**0.557** ± 0.093
	Exclusion size column	**0.087** ± 0.009	**0.563** ± 0.083	**0.075** ± 0.003	**0.368** ± 0.023

Concerning results obtained with ganciclovir, loaded drug in PEG_{46}-*b*-$PTMC_{119}$ vesicles was measurable by UV spectroscopy. However, drug loading content remain far from the target of 10 % that should be necessary for improving therapeutic activity of GCV in the organism.

For hydrophobic molecules, such as Coumarin 6, we thought that increasing membrane thickness was going to increase hydrophobic molecules loading as they tend to be located in the thicker membrane. With the example of Coumarin 6, we observed no drastic change in loading content or efficiency. It appears that we have reached the maximum amount of hydrophobic drug that can be loaded into our objects, or that passive loading from microfluidic assisted self-assembly is not the appropriate method to load an important amount of drug. Concerning Doxorubicin, despite the low amount of drug loaded similar to coumarin 6 and ganciclovir for both copolymers, it could be interesting to underline that a lower drug content is obtained when samples are purified by exclusion size column instead of dialysis for PEG_{46}-*b*-$PTMC_{119}$ vesicles, which seems to be in agreement with adsorbed molecules removed by purification with size exclusion, as already observed for PEG_{22}-*b*-$PTMC_{51}$ vesicles. Ganciclovir is following the same behavior.

We tried to understand why drug loading is not efficient for all three evaluated drugs, independently of their hydrophobic or hydrophilic behavior. We explored the self-assembly pathway hypothesis as an explanation for such a low loading rate. Indeed, two self-assembly ways are reported in literature, one being less favorable to hydrophilic drug loading as represented on Figure 17 in the first chapter. Indeed, when pathway implies swelling micelles, hydrophilic drug has to cross a hydrophobic membrane to reach the aqueous core of the vesicle, which might be unfavorable. Chapter 4 will be dedicated to a better understanding of the self-assembly mechanism of PEG-*b*-PTMC.

In an attempt to solve the problem of this low Ganciclovir loading by passive loading, active loading was evaluated on PEG_{22}-*b*-$PTMC_{51}$ vesicles by using two mechanisms: by the creation of a pH gradient or an ionic gradient.

4. Active loading using PEG_{22}-*b*-$PTMC_{51}$

Active loading is a method used for encapsulating drugs inside vesicles after their formation. It consists in active transport of the drugs into the vesicles by exploiting a concentration gradient or electrochemical potential difference across the membrane. This method allows for a higher drug loading capacity compared to passive encapsulation methods. One common mechanism used for active loading is the pH gradient method. In this method, the drug is protonated, deprotonated or uncharged to make it more hydrophilic or hydrophobic, respectively, depending on the pH of the medium. The pH gradient across the membrane can be created by adjusting the pH of the external medium or by adding an acid or a base inside the polymersome. Another mechanism for active loading is the ion gradient method. In this method, the drug is charged and transported into the polymersome by exploiting the electrochemical potential difference across the membrane. The ion gradient can be created by adjusting the ion concentration of the external medium. For both cases, the polymersome membrane is designed to a certain permeability, which allows the protonated or deprotonated drug to enter the polymersome and being trapped inside the core.

4.1. Active loading through the use of pH gradient

Active loading through the use of pH gradient is well explored for Doxorubin encapsulation. In this case, the aqueous core is adjusted at acidic pH (less than 5) resulting in protonation and positive charge of Doxorubicin, and the external phase is adjusted to a pH close to 7, which makes Doxorubicin more neutral and allows it to easily cross the hydrophobic membrane of the polymersome. Because of the pH gradient, the neutral Doxorubicin diffuses through the membrane to reach the aqueous core of the vesicles. Indeed, the acidic environment of the vesicle core increases the solubility of Doxorubicin and thus offers a higher loading efficiency while at the same time the protonated form will remain trapped inside the vesicle[16,18].

Inspired from the contribution of Cheung *et al.* on Doxorubicin encapsulation by active loading, we created a pH gradient allowing to have neutral Ganciclovir molecules in the external media and able to cross vesicle membrane. To know which pH is necessary to create a concentration gradient and a transformation from neutral to charged form of Ganciclovir, we used MarvinSketch software to predict forms of the molecule depending on pH. Figure 30 shows the distribution of protonated, neutral and deprotonated species for ganciclovir as a function of pH according to predictions given by Marvin software. Positively charged forms of ganciclovir are predicted to appear around pH = 4.8, with an amount increasing prior to un-charged molecule when pH decreases. Thus, we aimed to create an acidic core for PEG_{22}-*b*-$PTMC_{51}$ vesicles with a pH = 3, corresponding theoretically to an amount of charged ganciclovir superior to the neutral form.

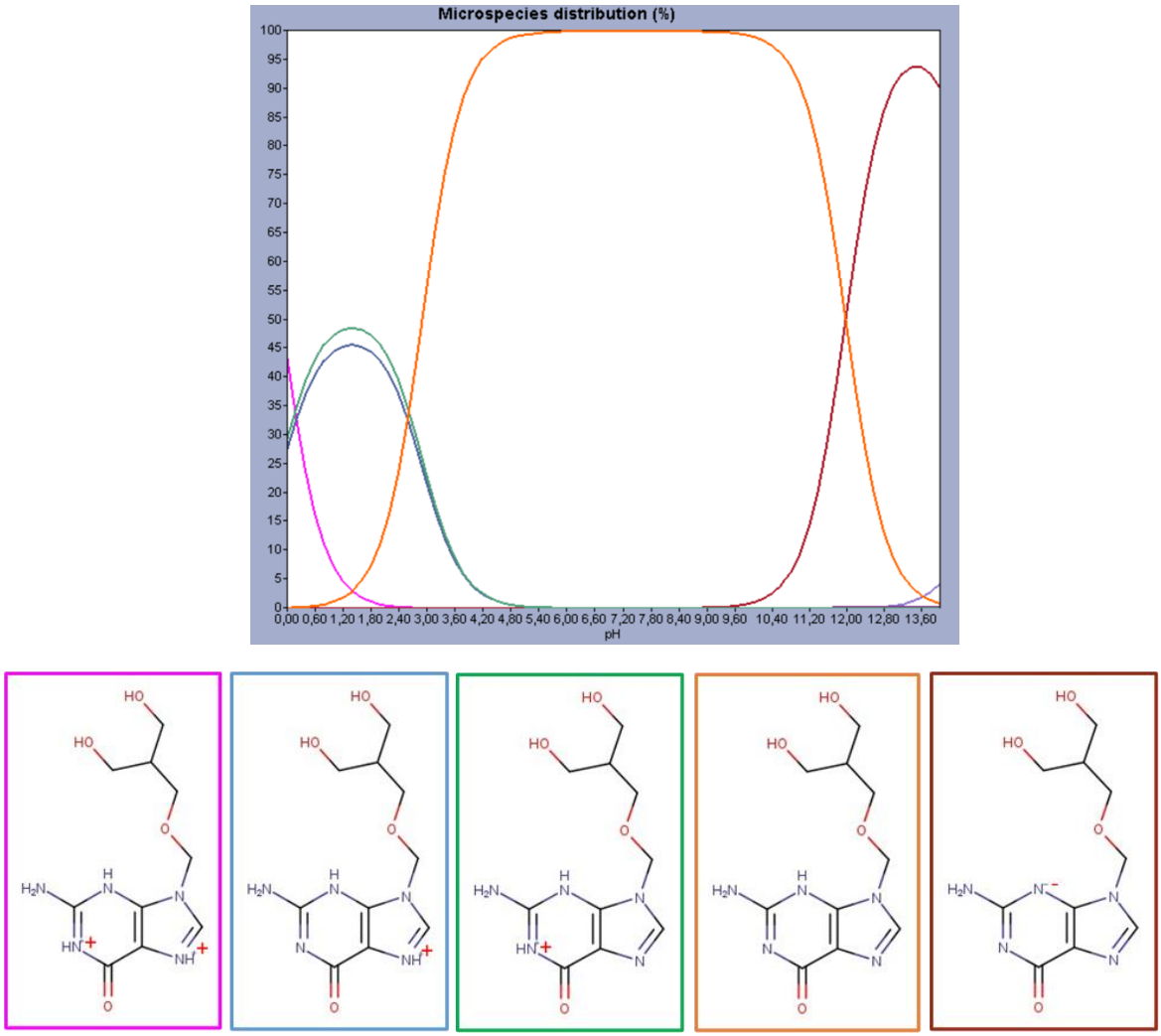

***Figure 30**: Ganciclovir forms distribution according to pH using the prediction given by MarvinSketch software. Each curve represents a percentage distribution of the protonated/neutral/deprotonated forms framed in the same color as the curve.*

To proceed in active loading by pH gradient, aqueous solvent for microfluidic self-assembly was changed from PBS to citric acid buffer at pH=3. Ratio of organic/aqueous solvent was kept at 20/80 %vol and a total flow rate of 1000 µL.min^{-1} was set. Samples are then purified by using dialysis against citric acid buffer for the first bath, to withdraw DMSO and fix vesicular shape. Samples are then purified by dialysis against PBS with similar osmolarity to exchange external medium to a neutral pH.

During the addition of ganciclovir and inspired by Choucair *et al.*[39], we decided to add DMSO as a plasticizer to increase the fluidity of the membrane but also for increasing the solubility of Ganciclovir, the solubility of GCV in DMSO is reported to be approximately 50 mg.mL^{-1} and typically in the range around 1 mg.mL^{-1} in PBS, at room temperature. 20 % vol or 40 % vol of DMSO is added in two samples, in addition of a final concentration of Ganciclovir of 4 mg.mL^{-1} in solution. Solutions were let to stir at room temperature for 72 h. After 72 h of stirring, samples containing 40% vol of DMSO presented precipitates. Such a high DMSO content may have allowed copolymer to rearrange and precipitate. We thus decided to keep a 20 % vol DMSO content with a time of stirring lower (19 h or 38 h). Samples were then dialyzed against PBS to remove unloaded drug and DMSO. After each step of active loading process, the characterization of the size was evaluated by DLS and results obtained are given in Table 8.

Table 8: *DLS 90° analysis results along process of active loading of Ganciclovir by pH gradient: after microfluidic self-assembly, after external medium change, after stirring with drug (with 20% vol of DMSO) and after final purification. The indicated values are the average of four assays (with 2 mL of suspension collected for each result) with the corresponding standard deviations.*

Agitation time in the presence of Ganciclovir	After Microfluidic		After external medium change		After stirring with drug		After final purification	
	D_H (nm)	PDI	D_H (nm)	PDI	D_H (nm)	PDI	D_H (nm)	PDI
19 h	145 ± 2	0.143 ± 0.003	166 ± 4	0.150 ± 0.007	160 ± 7	0.179 ± 0.003	191 ± 18	0.255 ± 0.052
38 h	152 ± 4	0.139 ± 0.014	166 ± 0	0.154 ± 0.003	160 ± 19	0.260 ± 0.071	258 ± 60	0.442 ± 0.040
Without agitation time and no drug	147 ± 4	0.141 ± 0.007					161 ± 4	0.138 ± 0.06

Results obtained show an increase in hydrodynamic diameter and PDI during the experiment, especially after final purification. It seems that a destabilization occurs when vesicles are stirred with drug and DMSO, and dialysis increased this phenomenon. To better understand what happened, the sample let 38 h to stir in presence of GCV was analyzed by Cryo-TEM. Figure 31 confirms that the process of drug incorporation by active loading destabilizes the polymersome structure. DMSO may help objects to rearrange in larger nanoparticles and tend also to form worm-like structures. In addition, during the step of drug incorporation, the temperature of suspension has increased up to 30°C due to long-time magnetic stirring that would be a supplementary factor to enhance the mobility to polymer chain to new self-assembly. This experiment highlighted that active loading by pH gradient might disturb the thermodynamic equilibrium necessary to maintain the block copolymer self-assembly into vesicles. The presence of DMSO for improving active loading could be one of the main factors involved and further experiments should be performed to better elucidate this behavior, for instance by using other plasticizer solvent (such as Dioxane) or without adding other plasticizer solvent. The impact of the pH change of the aqueous medium before and after PEG_{22}-*b*-$PTMC_{51}$ self-assembly could also be assessed by light scattering and cryo-TEM analysis.

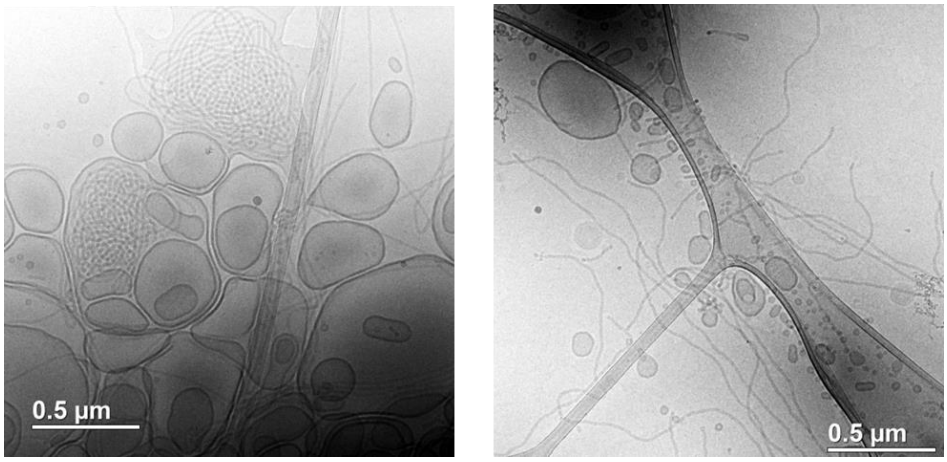

Figure 31: *Cryo-TEM images obtained from PEG_{22}-b-$PTMC_{51}$ vesicle after active loading by pH gradient of Ganciclovir with an agitation time in the presence of Ganciclovir of 38 h .*

4.2. Active loading through the use of ionic gradient

The general mechanism of active loading by ionic gradient involves the use of a solution containing a high concentration of the drug and a low concentration of salt ions (such as sodium chloride or ammonium sulfate) and placed at the exterior of the vesicles. This creates an ionic gradient across the membrane of vesicles previously formulated, with a high concentration of salt ions on the inside and a low concentration on the outside. After crossing the vesicle membrane, the high concentration of salt ions causes the drug to be trapped inside the vesicles. In the case of Doxorubicin, ammonium sulfate salts are used due to the formation of electrostatic complexes between the positively charged amino sugar moiety of Doxorubicin with the negatively charged sulfate anions of ammonium sulfate, according to Fritze *et al.* [16]. Overall, the active loading mechanism by ionic gradient provides a way to achieve high drug encapsulation efficiency.

In parallel to pH gradient, same protocol for active loading of Ganciclovir was followed with an ammonium gradient. We thus changed aqueous solvent for microfluidic assisted self-assembly of PEG_{22}-*b*-$PTMC_{51}$ from PBS to an ammonium sulfate solution at pH = 5.3, with an osmolarity of 300 $mOsm.L^{-1}$. Ratio of organic/aqueous solvent was kept at 20/80 %vol and a total flow rate at 1000 $\mu L.min^{-1}$. The obtained suspensions were purified by dialysis against ammonium sulfate solution for the first bath, and PBS for the two others. 20% vol of DMSO was added with Ganciclovir to reach a Ganciclovir final concentration in solution of 4 $mg.mL^{-1}$. Solutions were let to stir for 19 h and 39 h. After each step of active loading process, the characterization of the size and the PDI was evaluated by DLS and results obtained are given in Table 9.

Table 9: *DLS 90° analysis results along process of active loading of Ganciclovir by ionic gradient: after microfluidic self-assembly, after external medium change, after stirring with drug (with 20% vol of DMSO) and after final purification. The indicated values are the average of four assays (with 2 mL of suspension collected for each result) with the corresponding standard deviations.*

Agitation time in the presence of Ganciclovir	After Microfluidic		After external medium change		After stirring with drug		After final purification	
	D_H (nm)	PDI	D_H (nm)	PDI	D_H (nm)	PDI	D_H (nm)	PDI
19 h	**169** ± 4	**0.168** ± 0.007	**149** ± 4	**0.160** ± 0.030	**154** ± 15	**0.212** ± 0.086	**170** ± 18	**0.258** ± 0.070
38 h	**173** ± 4	**0.162** ± 0.009	**156** ± 6	**0.159** ± 0.027	**158** ± 13	**0.220** ± 0.013	**190** ± 28	**0.500** ± 0.061

Results obtained show the same tendency for active loading by pH gradient or ionic gradient, with an increase in hydrodynamic diameter and PDI along experiment, especially after final purification. The sample let 38 h to stir in presence of GCV was analyzed by Cryo-TEM. Figure 32 confirms that the process of incorporating drug by active loading with an ionic gradient also destabilizes the shape of the polymersomes with a tendency to form worm-like structures that might be due to the presence of DMSO and the slight heating of magnetic stirrer allowing PEG_{22}-*b*-$PTMC_{51}$ chains to rearrange. These preliminary results tend to show that the active loading protocols typically used for liposomes cannot be directly adapted to polymersomes, especially for those formed with the block copolymer PEG_{22}-*b*-$PTMC_{51}$. Due to nanoparticle instability and precipitation during purification, DLC quantification was not performed for both active loading methods.

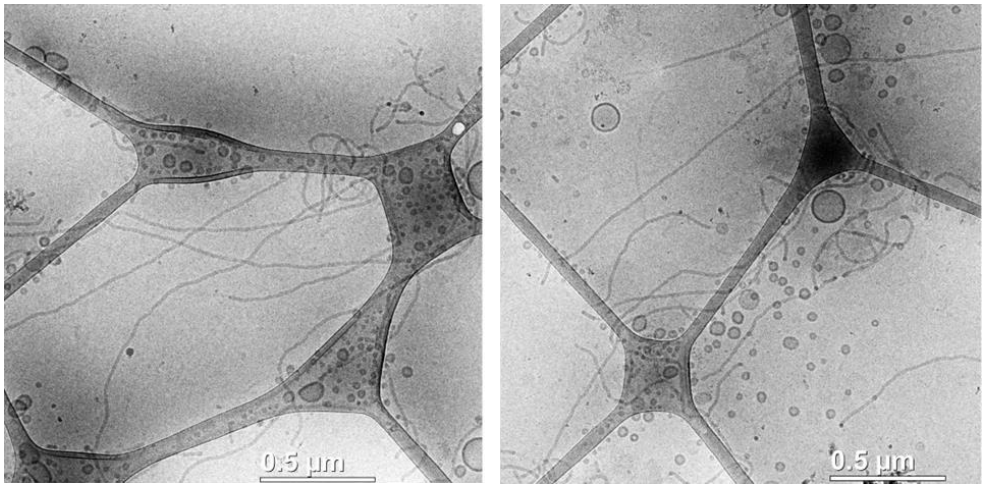

Figure 32: *Cryo-TEM images obtained from PEG_{22}-b-$PTMC_{51}$ vesicle after active loading by ionic gradient of Ganciclovir with an agitation time in the presence of Ganciclovir of 38 h.*

Consequently, following these observations, active loading protocols need to be improved. We should think about:

- optimizing formulations parameters for PEG_{22}-*b*-$PTMC_{51}$ polymersomes with a drug well known, used in active loading, such as Doxorubicin,
- trying both active loadings, using a smaller amount to none DMSO or another plasticizer agent such as dioxane,
- tuning the pH or the concentration or salts in order to avoid the destabilization of the membrane,
- using water bath to disperse heat produced by magnetic stirrer during the process.

Another last active loading that could be interesting to evaluate with our system is the use of an “osmotic shock”, well-known in the field of liposomes for active loading. Briefly, liposomes are subjected to a weak "osmotic shock," which involves exposing them to a hypotonic solution followed by a hypertonic solution contained the drug. This process helps to transiently destabilize the liposome membrane, allowing the drug and solute to diffuse across the membrane and become concentrated inside the liposomes. Finally, the liposomes are purified to remove any unencapsulated drug. The weak “osmotic shock” method has several advantages over other active loading methods. For instance, it can be used to encapsulate a wide range of drugs, including both hydrophilic and hydrophobic compounds. However, the osmotic shock step can be harsh on the liposome membrane, potentially leading to lower stability and increased leakage of the encapsulated drug. Besides, in the previous chapter, we demonstrated that a hypertonic variation of 300 $mOsm.L^{-1}$ led to an important decrease of the size of the PEG_{22}-*b*-$PTMC_{51}$ vesicles. Controlling the osmolarity variation during hypotonic or hypertonic shocks seems to be a key parameter to be evaluated to avoid any modification of the size of the polymersomes.

5. Conclusion

In this chapter we tried to take advantage of the specificity of polymersomes to be able to load hydrophobic and hydrophilic drugs to encapsulate Ganciclovir and Doxorubicin HCl, which are rather hydrophilic, and Coumarin 6 that is strongly hydrophobic.

After determining the critical water content for drug precipitation, avoiding anticipated drug precipitation prior to polymer self-assembly, we attempted to passively load each drug by adding them in the preestablished process of microfluidic self-assembly of PEG_{22}-*b*-$PTMC_{51}$.

After purification, drug was released from vesicle using either a surfactant to destabilize vesicle membrane, or an organic solvent to solubilize again copolymer. UV-vis spectroscopy and fluorescent spectroscopy were used to quantify free drug through the use of pre-made calibration curve. Thus, measuring Ganciclovir UV absorbance at 252 nm, Doxorubicin HCl fluorescent emission at 592 nm when excited at 481 nm, and Coumarin 6 fluorescent emission at 514 nm when excited at 468 nm, we realized that the passive loading of the three drugs systematically resulted in a low drug content, all inferior to 0.1 %. These drug content are unsatisfactory as literature reports that Ganciclovir has already been loaded up to a loading content of 16.3 % in liposomes[40] and Doxorubicin has been loaded up to 23% in polymersomes [41].

Facing this low loading, we first though that vesicle membrane was not thick enough to retain the loaded drugs. We thus decided to try passive loading, replacing the usual PEG_{22}-*b*-$PTMC_{51}$ (f_{PEG} = 16%) by a copolymer twice larger, namely PEG_{46}-*b*-$PTMC_{119}$ (f_{PEG} = 14%). After optimizing PEG_{46}-*b*-$PTMC_{119}$ microfluidic assisted self-assembly as previously performed with PEG_{22}-*b*-$PTMC_{51}$, we proceeded in passive loading of our three drug models.

We were considering an improved loading of the hydrophobic drug, as the membrane was thicker, but drug loading content remained the same. This might be due to self-assembly process itself being inefficient for passive loading, or a denser entanglement of hydrophobic drug in longer copolymer, not providing an increased reservoir for hydrophobic drug. If hydrophilic drug loading seems more important with longer copolymer, it remain insufficient for drug delivery, hardly reaching 0.5% of drug loading content.

Comparing purification methods, sephadex (size exclusion column) purified sample showed lower DLC than dialyzed one for hydrophilic drug. We suppose that adsorbed molecules were more efficiently eliminated by sephadex column compared to dialysis.

In order to improve DLC, active loading of Ganciclovir was tried using both pH gradient, with an inner core at pH = 3 and outer medium at pH = 7.4, and an ionic gradient, using ammonium sulfate. After microfluidic self-assembly and exchange of external medium to create the gradient, Ganciclovir in DMSO was added and let to stir for several hours. DMSO was supposed to play the role of plasticizer to allow drug to cross vesicle membrane, but it appears that 20% vol of DMSO was allowing PEG_{22}-*b*-$PTMC_{51}$ membrane to rearrange in what Cryo-TEM shows to be wormlike micelles.

To increase drug loading several experiments are still conceivable. Passive loading using microfluidic assisted self-assembly may not be relevant. We would like to tune microfluidic parameters such as organic solvent composition and temperature control, to allow drug precipitation and copolymer self-assembly at the same amount of water to allow loading of drug nuclei crystals.

The lack of drug loading during passive loading might also be due to self-assembly mechanism itself. Indeed, as described in Chapter I, vesicles are resulting either from membrane formation and closure or from swollen micelles transformation. If the last one is favored, it has been demonstrated that loading was quite inefficient as drugs hardly cross hydrophobic vesicle membrane.

Chapter IV will be consequently dedicated to the elucidation of the self-assembly mechanism during microfluidic formulation.

6. Appendix

6.1. Temperature measurement during solvent exchange processes

We observed that temperature is having an impact on Ganciclovir crystallization during it CWC measurement. We measured temperature reached during CWC of Ganciclovir in the organic solvent DMSO/acetone 45/55 and observe an increase in temperature that didn't exceed 24°C. For comparison, we measured temperature that can be reached during copolymer self-assembly in the microfluidic chip by running 20/80 DMSO/PBS in the micromixer chip. In this case, temperature increase up to 27°C, highlighting the need for a better control of temperature during microfluidic experiment to be able to maintain temperature at 24°C. Figure A1 shows pictures taken by thermal camera Optris PI 230 giving access to temperature during CWC and microfluidic experiments.

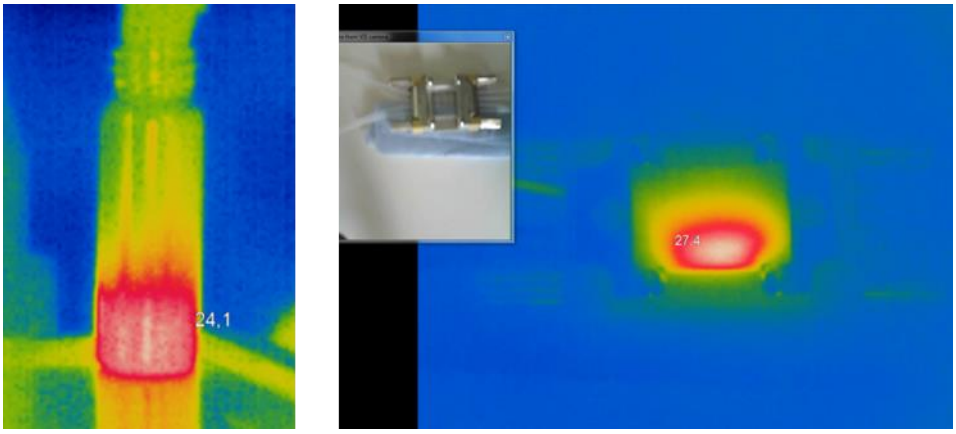

Figure A1: *Temperature measured by thermal camera Optris PI 230, during CWC measurement in vial (left) or in microfluidic chip. Highest temperature reached are 24.1 °C (left) and 27.4 °C (right)*

6.2. DLS measurement of PEG_{44}-b-$PTMC_m$ self-assemble nanoparticles

To improve vesicle impermeability, we intended to use a higher molar mass for copolymer by replacing PEG_{22}-*b*-$PTMC_{51}$ by PEG_{46}-*b*-$PTMC_{119}$. During the optimization of PEG_{46}-*b*-$PTMC_m$ composition to favor vesicle self-assembly, two block copolymers were synthetized: PEG_{46}-*b*-$PTMC_{94}$ and PEG_{46}-*b*-$PTMC_{121}$. Microfluidic assisted self-assembly of PEG_{46}-*b*-$PTMC_{94}$ was performed using 30/70 %vol DMSO/PBS at a set total flow rate of 1000 µL.min^{-1}. Microfluidic assisted self-assembly of PEG_{46}-*b*-$PTMC_{121}$ was performed using 50/50 %vol DMSO/PBS at a set total flow rate of 1000 µL.min^{-1}. Hydrodynamic diameter and polydispersity index were measured by DLS prior to be analyzed by Cryo-TEM (Table A1).

***Table A1**: DLS 90° analysis results of PEG_{46}-b-$PTMC_m$ microfluidic assisted self-assembled nanoparticles after final purification. The indicated values are the average of 2 assays (with 2 mL of suspension collected for each result) with the corresponding standard deviations. Nanoparticles observed by cryo-TEM are precised.*

Copolymer	Hydrodynamic diameter (nm)	PDI	Nanoparticle aspect (Cryo-TEM)
PEG_{46}-*b*-$PTMC_{94}$	183 ± 7	0.14 ± 0.006	Wormlike micelles
PEG_{46}-*b*-$PTMC_{121}$	141 ± 1	0.12 ± 0.01	Vesicles

7. References

(1) Peer, D.; Karp, J.; Hong, S.; Farokhzad, O.; Margalit, R.; Langer, R. Nanocarriers as an Emerging Platform for Cancer Therapy. *Nature nanotechnology* **2007**, *2*, 751–760. https://doi.org/10.1038/nnano.2007.387.

(2) Alexis, F.; Pridgen, E.; Molnar, L. K.; Farokhzad, O. C. Factors Affecting the Clearance and Biodistribution of Polymeric Nanoparticles. *Mol. Pharmaceutics* **2008**, *5* (4), 505–515. https://doi.org/10.1021/mp800051m.

(3) Ventola, C. L. Progress in Nanomedicine: Approved and Investigational Nanodrugs. *P T* **2017**, *42* (12), 742–755.

(4) Matoori, S.; Leroux, J.-C. Twenty-Five Years of Polymersomes: Lost in Translation? *Mater. Horiz.* **2020**, *7* (5), 1297–1309. https://doi.org/10.1039/C9MH01669D.

(5) Rideau, E.; Dimova, R.; Schwille, P.; Wurm, F. R.; Landfester, K. Liposomes and Polymersomes: A Comparative Review towards Cell Mimicking. *Chem. Soc. Rev.* **2018**, *47* (23), 8572–8610. https://doi.org/10.1039/C8CS00162F.

(6) Pallavi, P.; Harini, K.; Gowtham, P.; Girigoswami, K.; Girigoswami, A. Fabrication of Polymersomes: A Macromolecular Architecture in Nanotherapeutics. *Chemistry* **2022**, *4* (3), 1028–1043. https://doi.org/10.3390/chemistry4030070.

(7) Colley, H. E.; Hearnden, V.; Avila-Olias, M.; Cecchin, D.; Canton, I.; Madsen, J.; MacNeil, S.; Warren, N.; Hu, K.; McKeating, J. A.; Armes, S. P.; Murdoch, C.; Thornhill, M. H.; Battaglia, G. Polymersome-Mediated Delivery of Combination Anticancer Therapy to Head and Neck Cancer Cells: 2D and 3D *in Vitro* Evaluation. *Mol. Pharmaceutics* **2014**, *11* (4), 1176–1188. https://doi.org/10.1021/mp400610b.

(8) Bannan, C. C.; Calabró, G.; Kyu, D. Y.; Mobley, D. L. Calculating Partition Coefficients of Small Molecules in Octanol/Water and Cyclohexane/Water. *J. Chem. Theory Comput.* **2016**, *12* (8), 4015–4024. https://doi.org/10.1021/acs.jctc.6b00449.

(9) Cumming, H.; Rücker, C. Octanol–Water Partition Coefficient Measurement by a Simple 1H NMR Method. *ACS Omega* **2017**, *2* (9), 6244–6249. https://doi.org/10.1021/acsomega.7b01102.

(10) Faulds, D.; Heel, R. C. Ganciclovir. A Review of Its Antiviral Activity, Pharmacokinetic Properties and Therapeutic Efficacy in Cytomegalovirus Infections. *Drugs* **1990**, *39* (4), 597–638. https://doi.org/10.2165/00003495-199039040-00008.

(11) Markham, A.; Faulds, D. Ganciclovir. An Update of Its Therapeutic Use in Cytomegalovirus Infection. *Drugs* **1994**, *48* (3), 455–484. https://doi.org/10.2165/00003495-199448030-00009.

(12) Abraham, S.; McKenzie, C.; Masin, D.; Ng, R.; Harasym, T.; Mayer, L.; Bally, M. In Vitro and in Vivo Characterization of Doxorubicin and Vincristine Coencapsulated within Liposomes through Use of Transition Metal Ion Complexation and PH Gradient Loading. *Clinical cancer research : an official journal of the American Association for Cancer Research* **2004**, *10*, 728–738. https://doi.org/10.1158/1078-0432.CCR-1131-03.

(13) Andriyanov, A.; Koren, E.; Barenholz, Y.; Goldberg, S. Therapeutic Efficacy of Combining PEGylated Liposomal Doxorubicin and Radiofrequency (RF) Ablation: Comparison between Slow-Drug-Releasing, Non-Thermosensitive and Fast-Drug-Releasing, Thermosensitive Nano-Liposomes. *PloS one* **2014**, *9*, e92555. https://doi.org/10.1371/journal.pone.0092555.

(14) Tian, M.; Liu, X.; Song, L.; Qi, X. Preparation and Properties of Fluorescent Labels Coumarin-6/HP-β-CD Complex by Nasal Drug Delivery. *IOP Conference Series: Earth and Environmental Science* **2019**, *252*, 022049. https://doi.org/10.1088/1755-1315/252/2/022049.

(15) Goddard, A.; Apebende, E.; Lentz, J. C.; Carmichael, K.; Taresco, V.; Irvine, D.; Howdle, S. Synthesis of Water-Soluble Surfactants Using Catalysed Condensation Polymerisation in Green Reaction Media. *Polymer Chemistry* **2021**, *12*. https://doi.org/10.1039/D1PY00415H.

(16) Fritze, A.; Hens, F.; Kimpfler, A.; Schubert, R.; Peschka-Süss, R. Remote Loading of Doxorubicin into Liposomes Driven by a Transmembrane Phosphate Gradient. *Biochimica et Biophysica Acta (BBA) - Biomembranes* **2006**, *1758* (10), 1633–1640. https://doi.org/10.1016/j.bbamem.2006.05.028.
(17) Haran, G.; Cohen, R.; Bar, L. K.; Barenholz, Y. Transmembrane Ammonium Sulfate Gradients in Liposomes Produce Efficient and Stable Entrapment of Amphipathic Weak Bases. *Biochim Biophys Acta* **1993**, *1151* (2), 201–215. https://doi.org/10.1016/0005-2736(93)90105-9.
(18) Cheung, B. C.; Sun, T. H.; Leenhouts, J. M.; Cullis, P. R. Loading of Doxorubicin into Liposomes by Forming Mn2+-Drug Complexes. *Biochim Biophys Acta* **1998**, *1414* (1–2), 205–216. https://doi.org/10.1016/s0005-2736(98)00168-0.
(19) Mayer, L. D.; Bally, M. B.; Cullis, P. R. Uptake of Adriamycin into Large Unilamellar Vesicles in Response to a PH Gradient. *Biochimica et Biophysica Acta (BBA) - Biomembranes* **1986**, *857* (1), 123–126. https://doi.org/10.1016/0005-2736(86)90105-7.
(20) Nichols, J. W.; Deamer, D. W. Catecholamine Uptake and Concentration by Liposomes Maintaining p/ Gradients. *Biochim Biophys Acta* **1976**, *455* (1), 269–271. https://doi.org/10.1016/0005-2736(76)90169-3.
(21) Mayer, L. D.; Tai, L. C.; Bally, M. B.; Mitilenes, G. N.; Ginsberg, R. S.; Cullis, P. R. Characterization of Liposomal Systems Containing Doxorubicin Entrapped in Response to PH Gradients. *Biochim Biophys Acta* **1990**, *1025* (2), 143–151. https://doi.org/10.1016/0005-2736(90)90091-2.
(22) Lebleu, C. Polymersomes Based on PEG-b-PTMC towards Cell-Mediated Delivery of Nanomedicines. phdthesis, Université de Bordeaux, 2019. https://tel.archives-ouvertes.fr/tel-03463393 (accessed 2022-04-20).
(23) Page, T.; Sherwood, C.; Connor, J. D.; Tarnowski, T. Simple Reversed-Phase High-Performance Liquid Chromatography Quantitation of Ganciclovir in Human Serum and Urine. *J Chromatogr B Biomed Appl* **1996**, *675* (2), 342–346. https://doi.org/10.1016/0378-4347(95)00381-9.
(24) *Switchable Fluorescence of Doxorubicin for Label-Free Imaging of Bioorthogonal Drug Release - PMC*. https://www.ncbi.nlm.nih.gov/pmc/articles/PMC7397846/ (accessed 2023-04-03).
(25) Duan, J.; Paris, W.; Kibler, P.; Bousquet, C.; Liuzzi, M.; Cordingley, M. G. Dose and Duration-Dependence of Ganciclovir Treatment against Murine Cytomegalovirus Infection in Severe Combined Immunodeficient Mice. *Antiviral Res* **1998**, *39* (3), 189–197. https://doi.org/10.1016/s0166-3542(98)00038-2.
(26) Fernandes, J. A.; Galli, S.; Palmisano, G.; Volante, P.; Mendes, R. F.; Paz, F. A. A.; Masciocchi, N. Reviewing the Manifold Aspects of Ganciclovir Crystal Forms. *Crystal Growth & Design* **2016**, *16* (7), 4108–4118. https://doi.org/10.1021/acs.cgd.6b00617.
(27) Chadha, R.; Arora, P.; Saini, A.; Bhandari, S. Crystal Forms of Anti-HIV Drugs: Role of Recrystallization; 2012. https://doi.org/10.5772/33777.
(28) Park, S.; Yeo, S. Antisolvent Crystallization of Sulfa Drugs and the Effect of Process Parameters. *Separation Science and Technology* **2007**, *42* (12), 2645–2660. https://doi.org/10.1080/01496390701512976.
(29) Kaur, M.; Kohli, S.; Sandhu, S.; Bansal, Y.; Bansal, G. Coumarin: A Promising Scaffold for Anticancer Agents. *Anticancer Agents Med Chem* **2015**, *15* (8), 1032–1048. https://doi.org/10.2174/1871520615666150101125503.
(30) van der Zanden, S. Y.; Qiao, X.; Neefjes, J. New Insights into the Activities and Toxicities of the Old Anticancer Drug Doxorubicin. *FEBS J* **2021**, *288* (21), 6095–6111. https://doi.org/10.1111/febs.15583.
(31) Northfelt, D. W.; Dezube, B. J.; Thommes, J. A.; Miller, B. J.; Fischl, M. A.; Friedman-Kien, A.; Kaplan, L. D.; Du Mond, C.; Mamelok, R. D.; Henry, D. H. Pegylated-Liposomal Doxorubicin versus Doxorubicin, Bleomycin, and Vincristine in the Treatment of AIDS-Related Kaposi's Sarcoma: Results of a Randomized Phase III Clinical Trial. *Journal of Clinical Oncology* **1998**, *16* (7), 2445–2451. https://doi.org/10.1200/JCO.1998.16.7.2445.
(32) Sanson, C.; Schatz, C.; Le Meins, J.-F.; Brûlet, A.; Soum, A.; Lecommandoux, S. Biocompatible and Biodegradable Poly(Trimethylene Carbonate)-b-Poly(l-Glutamic Acid) Polymersomes: Size Control and Stability. *Langmuir* **2010**, *26* (4), 2751–2760. https://doi.org/10.1021/la902786t.

(33) Sharma, A. K.; Prasher, P.; Aljabali, A. A.; Mishra, V.; Gandhi, H.; Kumar, S.; Mutalik, S.; Chellappan, D. K.; Tambuwala, M. M.; Dua, K.; Kapoor, D. N. Emerging Era of "Somes": Polymersomes as Versatile Drug Delivery Carrier for Cancer Diagnostics and Therapy. *Drug Deliv. and Transl. Res.* **2020**, *10* (5), 1171–1190. https://doi.org/10.1007/s13346-020-00789-2.

(34) Miller, A. J.; Pearce, A. K.; Foster, J. C.; O'Reilly, R. K. Probing and Tuning the Permeability of Polymersomes. *ACS Cent Sci* **2021**, *7* (1), 30–38. https://doi.org/10.1021/acscentsci.0c01196.

(35) Discher, D. E.; Ahmed, F. Polymersomes. *Annu Rev Biomed Eng* **2006**, *8*, 323–341. https://doi.org/10.1146/annurev.bioeng.8.061505.095838.

(36) Bermudez, H.; Brannan, A. K.; Hammer, D. A.; Bates, F. S.; Discher, D. E. Molecular Weight Dependence of Polymersome Membrane Structure, Elasticity, and Stability. *Macromolecules* **2002**, *35* (21), 8203–8208. https://doi.org/10.1021/ma020669l.

(37) Le Meins, J.-F.; Sandre, O.; Lecommandoux, S. Recent Trends in the Tuning of Polymersomes' Membrane Properties. *Eur Phys J E Soft Matter* **2011**, *34* (2), 14. https://doi.org/10.1140/epje/i2011-11014-y.

(38) Jain, S.; Bates, F. S. On the Origins of Morphological Complexity in Block Copolymer Surfactants. *Science* **2003**, *300* (5618), 460–464. https://doi.org/10.1126/science.1082193.

(39) Choucair, A.; Lim Soo, P.; Eisenberg, A. Active Loading and Tunable Release of Doxorubicin from Block Copolymer Vesicles. *Langmuir* **2005**, *21* (20), 9308–9313. https://doi.org/10.1021/la050710o.

(40) Asasutjarit, R.; Managit, C.; Phanaksri, T.; Treesuppharat, W.; Fuongfuchat, A. Formulation Development and in Vitro Evaluation of Transferrin-Conjugated Liposomes as a Carrier of Ganciclovir Targeting the Retina. *Int J Pharm* **2020**, *577*, 119084. https://doi.org/10.1016/j.ijpharm.2020.119084.

(41) Sanson, C.; Schatz, C.; Le Meins, J.-F.; Soum, A.; Thévenot, J.; Garanger, E.; Lecommandoux, S. A Simple Method to Achieve High Doxorubicin Loading in Biodegradable Polymersomes. *J Control Release* **2010**, *147* (3), 428–435. https://doi.org/10.1016/j.jconrel.2010.07.123.

Chapter IV.

Elucidation of self-assembly mechanism

Table of contents

Introduction 193

1. Experimental Section 195

1.1. Materials 195

1.2. Methods 195

2. PEG-*b*-PTMC self-assembly study mechanism: step by step observation at the microscale 198

3. *In-operando* monitoring of PEG_{22}-*b*-$PTMC_{51}$ self-assembly by X-Ray measurement (SAXS) 203

3.1. Evaluation of PEG_{22}-b-$PTMC_{51}$ polymersome structure by laboratory SAXS acquisitions at rest within quartz capillaries. 203

3.2. Optimization of microfluidic device for Synchrotron SAXS acquisitions 206

3.3. Synchrotron SAXS measurements and data analysis 212

4. Conclusion 229

5. Appendix 231

5.1. Vesicle fitting model from SasView software 231

5.2. Elongated micelle fitting model 232

6. References 235

Introduction

In this last chapter, the focus will be on elucidating the self-assembly mechanism of PEG_{22}-*b*-$PTMC_{51}$ polymersomes. Two main mechanisms for vesicle formation were proposed in the literature, as described in Figure 1.[1,2] The first mechanism (Mechanism I) proposes that spherical micelles are first formed evolving into worm-like micelles. These elongated micelles flatten to form disk-like micelles (bilayer sheets) which close up to form vesicles. Intermediates has been predicted by simulation[3] and verified experimentally[4]. Chen *et al.* studied the rod-to-vesicle transition mechanism of PS_{310}-*b*-PAA_{52} (poly(styrene)-*block*-poly(acrylic acid)) by trapping intermediate morphologies with quenching the samples to liquid nitrogen temperature, isolating the aggregates by freeze-drying, and then observing them with TEM. In a drug loading context, such pathway necessarily involves loading of the surrounding environment within aqueous lumen of the vesicle upon closure of the 2D sheet into vesicles. In this case, good levels of encapsulation of hydrophilic molecules are anticipated.

The second mechanism (Mechanism II, Figure 1) involves the initial formation of spherical micelles that grow to large and energetically unfavorable spherical micelles. These micelles restructure into vesicles. This mechanism has been proposed on the basis of dynamic simulations[5] and highlighted by experiment.[6] *Adams et al.* achieved to observe by cryo-TEM, intermediates from PEG-*b*-PDEAMA self-assembly into vesicles, by a pH switch self-assembly process. Such process would prevent loading of high levels of hydrophilic molecules. Restructuring of the swollen micelles into vesicles should allow water to enter the interior and thus pass through the polymer pre-membrane, plasticized by the organic solvent. Such constraints lead to a lack of efficiency of the encapsulation by following the mechanism II.

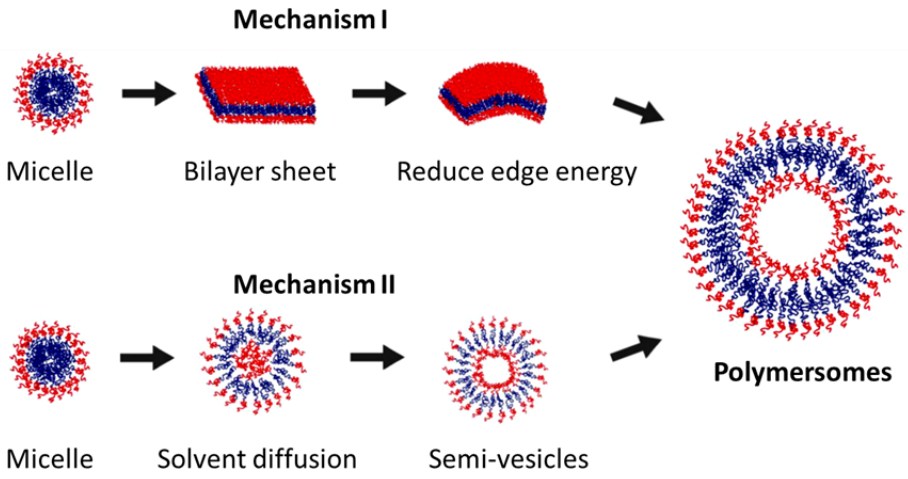

Figure 1: *Schematic representation of supposed mechanisms of vesicle formation. Adapted from Iqbal et al.* [2]

As demonstrated in Chapter 3, passive loading of drugs during microfluidic assisted self-assembly of PEG-*b*-PTMC copolymers leads to very low drug loading content and efficiency. One can thus anticipate a type II mechanism for the formation of PEG-*b*-PTMC vesicles, which we aim at demonstrating experimentally.

One could consider different experimental methods to analyze and characterize the formation of self-assembled nano-objects.[7,8] First, dynamic light scattering (DLS) can provide nanoparticles size through the determination of their hydrodynamic radius R_H. Coupled with static light scattering (SLS) that allows the determination of the radius of gyration of nanoparticles R_G, the shape factor $\rho=R_G/R_H$ can provide an indication on nanoparticle's morphology[9,10]. Small angle X-ray scattering (SAXS) can also provide quantitative information from the form factor analysis, including the shape and size of the nanoparticles, as well as their internal structure. Direct observations are also used with optical and fluorescent microscopies or transmission electron microscopy (TEM), allowing for direct observation of the nanoparticles and confirming scattering experiments.[7,11] However, only limited contributions are reported on the *in-operando* study of self-assembly of block copolymers. [12–14] X-Ray scattering is often referred as a suitable technic for this type of study.

In this chapter, we proposed two ways to elucidate PEG-*b*-PTMC self-assembly mechanism. The first one involves fluorescent confocal microscopy observation of copolymer self-assembly into giant vesicles. In a second time, we propose to proceed in small angle X-Ray scattering (SAXS) experiment at synchrotron SOLEIL on an *in operando* microfluidic co-flow set-up to elucidate small vesicle self-assembly.

1. Experimental Section

1.1. Materials

Solvents: Dimethylsulfoxide (DMSO) was purchased from Sigma-Aldrich, Acetone from Acros Organics, PBS 10x was purchased from Euromedex and diluted to obtain PBS 1x.
pH and osmolarity of aqueous solutions were adjusted using a pH meter *inoLab® pH 730 WTW* and an osmometer *Löser automatic TypM 10-25µL*, to reach pH=7.4 ± 0.1 and an osmolarity of 300 ± 4 mOsm/L.
PEG_{22}-*b*-$PTMC_{51}$ was synthetized by ring-opening polymerization of TMC using MeO-PEG_n-OH as macroinitiator. This synthesis was already reported by Coralie Lebleu and was performed by Pierre Lalanne following similar procedure.[15] PEG_{22}-*b*-$PTMC_{51}$-Cy5.5 was obtained from functionalization of PEG_{22}-*b*-$PTMC_{51}$-COOH with Cyanine 5.5.
Calcein was purchased from Sigma Aldrich.

1.2. Methods

Nanoprecipitation: PEG_{22}-*b*-$PTMC_{51}$ self-assembly by nanoprecipitation was performed on 1 mL of copolymer solution at a desired concentration in either DMSO or Acetone, by adding water using a Harvard Apparatus syringe driver, at 40µL.min^{-1}. Solution was agitated at 250 rpm at room temperature.

Co-Flow set-up manufacturing: Co-flow set up was home-made as follows and schematically represented on Figure 2. PLA (poly(lactic acid)) plates were 3D-printed by MINT laboratory *(Micro et Nanomédecines translationnelles).* Square Borosilicate capillary (ID : 2 mm, OD : 2.8 mm, length : 30 cm, ref : S102), cut at 10cm, and Round Borosilicate capillary (ID : 1.5 mm , OD : 1.8 mm, length : 10 cm, ref : CV1518) were purchased from CM Scientific. Using Loctite Power Epoxy resin, square capillary was first glued to PLA plate for its extremity to go 2 cm on the plate, centered. Round capillary was then glued to the plate after being inserted in square capillary until going 2 mm out of plate, in the square capillary. Syringe needle (ID : 0.84 mm, OD : 1.27 mm , length : 12.7 mm, ref : Z112118) was purchased from Poly Dispensing Systems and dug to fit square and round capillary, using a soldering iron. Dug needle was then glued at the junction of square and round capillary. Thus, round capillary outlet being inner flow entry, and needle being outer flow entry. Glue was added all around needle to ensure sealing and let to cure for 24h.

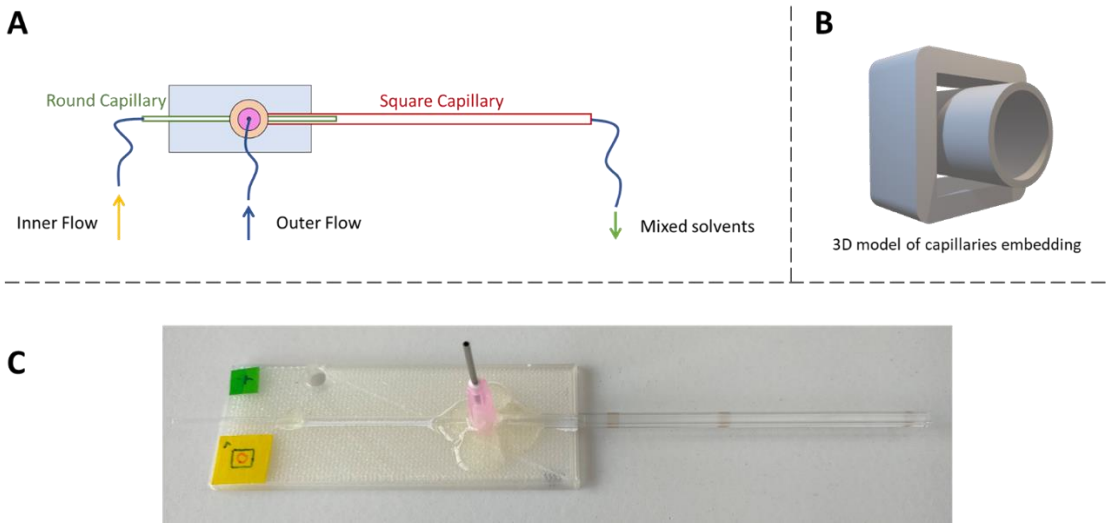

***Figure 2**: A) Schematic representation of home-made Co-flow set-up, B) 3D model of capillaries embedding, C) Picture of co-flow set-up.*

Synchrotron Set-up: Co-flow set-up above mentioned was maintained vertically through the help of 3D printed PLA piece, provided by MINT laboratory. PLA co-flow set-up plate had dovetail hedges that allowed it to fit into set-up holder and slide to adjust vertical position. Screw was used to fix co-flow set-up position. Clamp was intended to slightly pinch final capillary. Clamp could slide on set-up holder to be aligned with co-flow set-up, allowing to fix co-flow outlet without exerting tension on capillary. Co-flow holder was hollowed out to allow X-Ray measurement along square capillary. Receptacle for vial was also 3D printed and used to collect final solution (Figure 3). Syringe pump used to control flow rates was a Cetoni "Low Pressure Syringe Pump neMESYS 290N" apparatus, controlled by Nemesys UserInterface software. It was equipped with Cetoni contiflow electro-valve allowing to refill syringe without withdrawing it from syringe driver. Set-up and syringe pump were connected with fluorinated ethylene propylene tubing (1/16" x 0.25 mm). Connection between tubing and capillaries were done using a small piece of flexible silicone tubing.

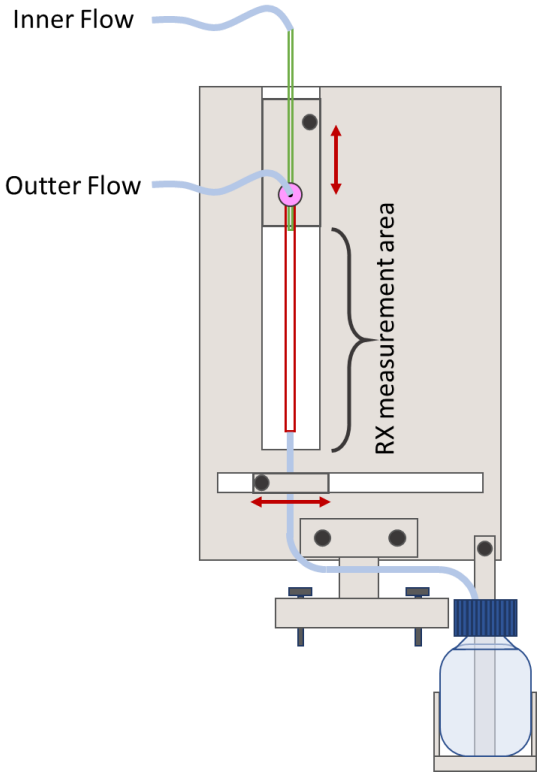

***Figure 3**: Schematic representation of the co-flow set-up and set-up holder used to maintain co-flow set-up vertically during X-Ray measurement.*

Confocal microscopy observation: Laser Scanning Confocal Microscopy Images were acquired on an inverted Leica TCS SP5 microscope equipped with an HCX PL APO 63x, NA 1.4 oil immersion objective in fluorescence mode. Samples (≈20 µL) were injected in µ-slide (chambered coverslip) with uncoated 8 wells from Ibidi GmbH. The laser outputs were controlled via the Acousto-Optical Tunable Filter (AOTF) and the two collection windows using the Acousto-Optical Beam Splitter (AOBS) and photomultiplicators (PMT) as follows: Cyanine5.5 was excited with a Helium-Neon laser at 633 nm (20%) and measured with emission setting at 650-750 nm. Images were collected using the microscope in simultaneous mode with a format of 512x512 pixels.

2. PEG-*b*-PTMC self-assembly study mechanism: step by step observation at the microscale

To better understand PEG_{22}-*b*-$PTMC_{51}$ self-assembly mechanism, a way to observe intermediates between free chains in solution and polymersomes was developed. The self-assembly process was first analyzed by measuring the change in scattered intensity when adding water into copolymer solution in organic solvent using a mobile DLS set-up (from Cordouan). Water was added punctually, and light scattered intensity was measured during and between water addition. The effect of water addition was measured to determine whether, once a critical water content (CWC) was reached and water addition was stopped, the intensity continued to increase or stabilized. One can indeed anticipate two possible scenarios, as described in Figure 4. First, the objects spontaneously grow and all free chains are transformed into nanoparticles after reaching the CWC (blue curve). Alternatively, self-assembly can occur in a progressive manner, with a gradual increase upon addition of water. In this case, we will assume that meta-stable objects are obtained between each addition of water, which allows us to follow the self-assembly process step by step.

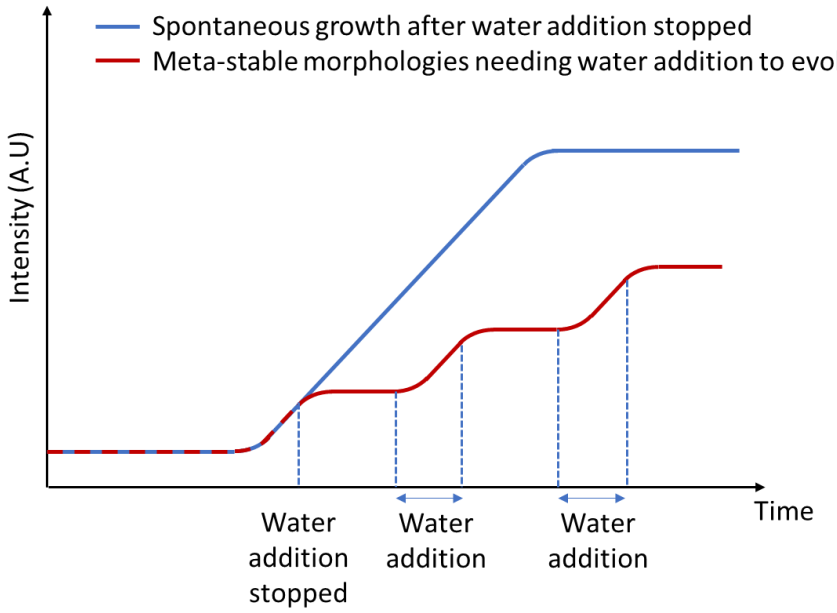

Figure 4: *Schematic representation of the evolution of scattered light from a copolymer solution during water addition, illustrating the hypothesis of spontaneous growth of polymersome. Blue curve represents an absence of water addition after reaching the CWC value and red curve represents a stepwise addition of water after reaching the CWC value. Experiments were performed twice for each condition.*

1 mL sample of a solution of 2.5 $mg.mL^{-1}$ of PEG_{22}-*b*-$PTMC_{51}$ in DMSO was studied during water addition under magnetic stirring at 250 rpm, using 70 % of NanoKin laser power. Water was added at 40 $\mu L.min^{-1}$ until reaching 10 %vol of water by steps of 5 %vol. To ensure consistency with the CWC measurements presented in the second chapter, the volume of water added to the PEG_{22}-b-$PTMC_{51}$ solution was stopped after the CWC value, which was determined to be 12%. Then, water solution was added with a step of 1% vol until the water content reached 16%, after which the volume added was increased to 5% until it reached 20%. A waiting period of 30 minutes was observed between each water addition to allow the sample to equilibrate. Figure 5 presents results obtained during this second

process. The observed steps during the stepwise water addition are in clear agreement with a progressive evolution of the self-assembly process. Consequently, a higher amount of water than CWC is needed to reach complete self-assembly, from free chains to polymersomes. Thus, meta-stable intermediate morphologies seem to be observable during such gradual water addition process.

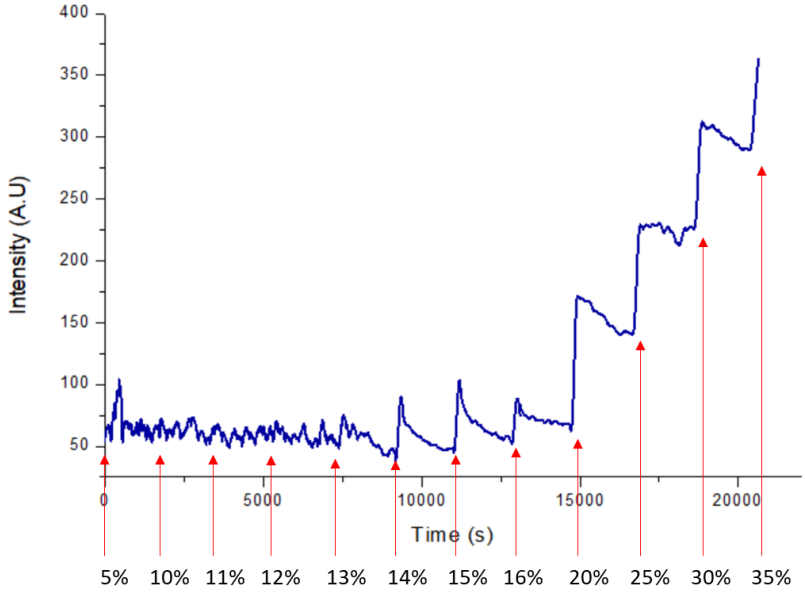

Figure 5: *Dynamic light scattering intensity measured continuously on a sample of PEG_{22}-b-$PTMC_{51}$ in DMSO, undergoing gradual addition of water. A waiting time of 30 min between two water additions are represented by red arrows.*

Figure 5 shows that in these conditions the self-assembly process starts at around 13% of water. Between 13% and 15%, equilibration time allowed system to relax, probably because the nuclei formed are not stable enough and progressively disassemble over time. By adding water at the initial stages, self-assembly can start upon contact with a sufficient quantity of water, but this process can be reversed by organic and aqueous solvent homogenization. When the amount of water added reaches a certain level, it creates an overall bad solvent state for both copolymer blocks, facilitating block copolymer self-assembly and leading to the transition from intermediate morphologies to the final formation of vesicles.

To observe these intermediate morphologies under microscope, similar experiments were reproduced with the addition of a fluorescently labelled polymers: 1 mL of PEG_{22}-*b*-$PTMC_{51}$ in DMSO at 10 $mg.mL^{-1}$ with 1% wt of PEG_{22}-*b*-$PTMC_{51}$-Cy5.5 was used to allow confocal microscopy observations. Cyanine 5.5 is a fluorescent probe (λ_{Ex} /λ_{Em} = 683/703 nm) that was functionalized on PEG-*b*-PTMC chains. Water was added to the DMSO solution using a syringe driver at 40 $\mu L.min^{-1}$ and the resulting morphologies were observed by fluorescent confocal microscopy after the addition of 16, 26, 45, 63 and 80 %vol of water (Figure 6). A first step of "droplet" formation can be observed at 16 %vol of water addition (Figure 6a). Then, these droplets are growing continuously with water addition from 16 %vol to 45 %vol (Figure 6 b,c). This mechanism strongly resembles a liquid-liquid phase separation mechanism, where the polymer concentrates into these droplets. After 63 %vol of water added in solution, droplet surface texture changed from "smooth to blurry" as illustrated in Figure 6f. Droplets seemed to be coated with a layer that appeared less dense than the core of the droplets.

After 80 %vol of water added, the droplets surface continued to swell and clear membrane formation could be observed, as the budding occurred on the polymersome membranes (Figure 7a). When performing a Z-stack acquisition from confocal microscopy to produce a 3D structure of the polymersomes, all the droplets seemed to be formed of membranes that are denser in the core (Figure 7a) and tend to be more swollen at the interface (Figure 7b).

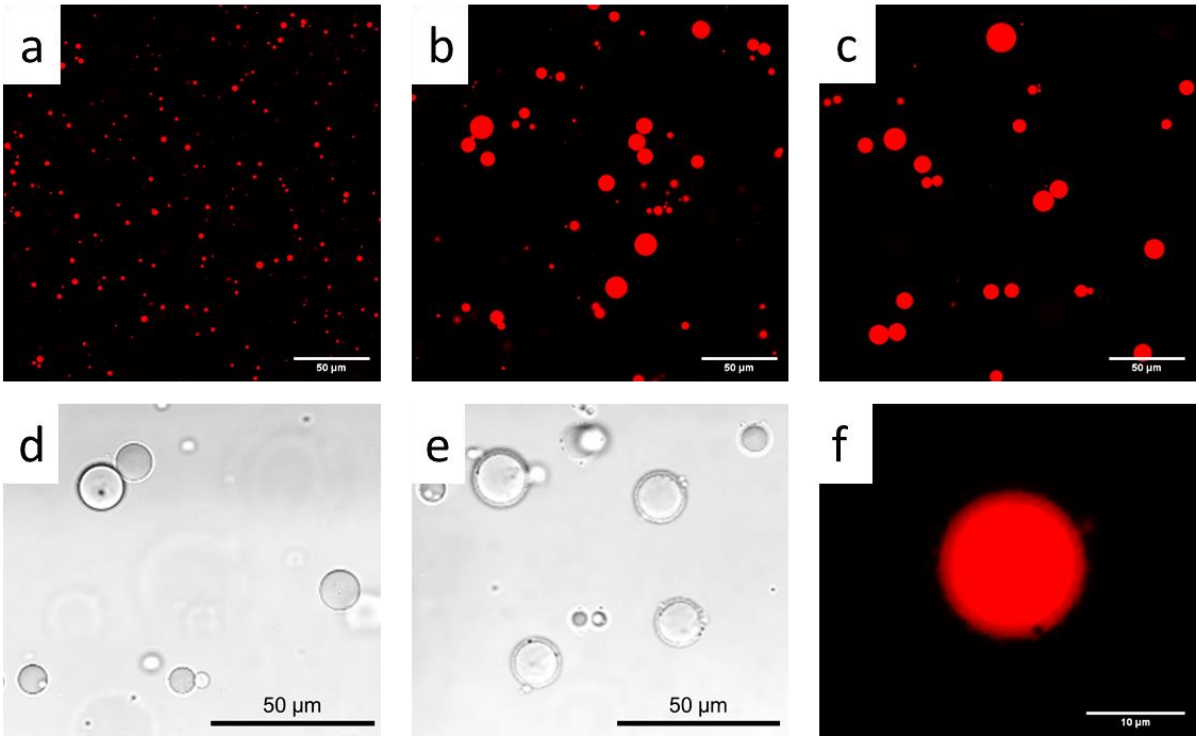

Figure 6: *Confocal microscopy observations in the red channel or in brightfield channel of PEG_{22}-b-$PTMC_{51}$ and PEG_{22}-b-$PTMC_{51}$-Cy5.5 in DMSO after water addition at (a)16, (b) 26, (c) 45 % (red), (d) 45% (brightfield), (e) 63 % (brightfield) and (f) 63% (red) of water content. Images shows copolymer coacervates that are growing with water content.*

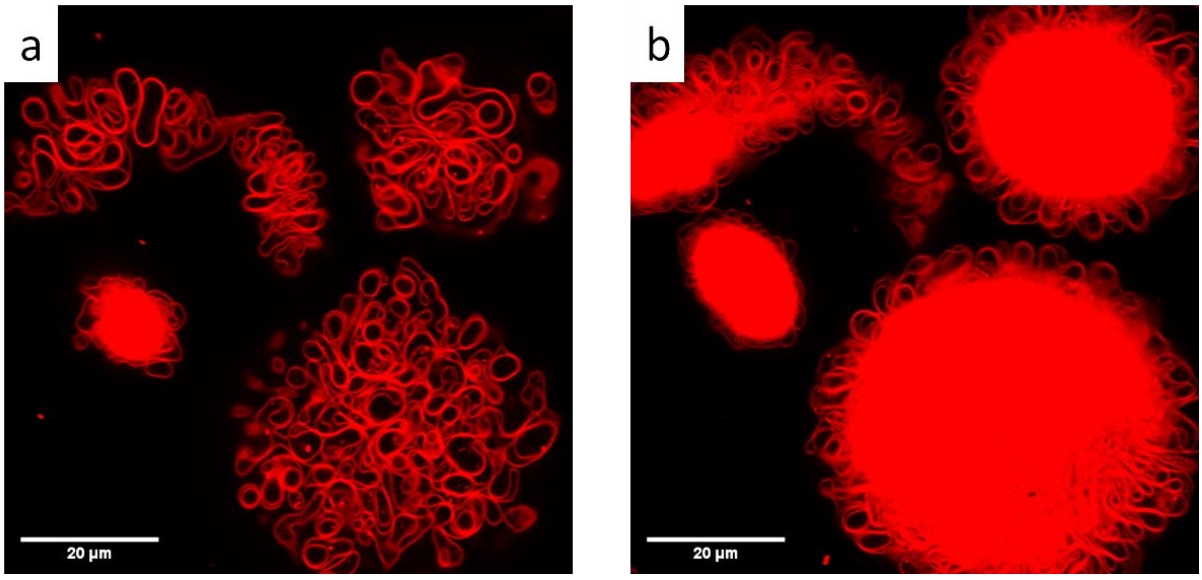

Figure 7: *Confocal microscopy observations in the red channel of PEG_{22}-b-$PTMC_{51}$ and PEG_{22}-b-$PTMC_{51}$-Cy5.5 in DMSO after 80%vol of water addition. b : Surface of the object, a: center of object revealing compacted membrane loops.*

Unfortunately, the membrane loops did not detach from each other, even after extensive dialysis, vortex and ultrasonication. It is likely that when the water content is too high, the membranes are strongly entangled into the coacervate droplet and do not have enough mobility to detach.

The morphologies observed during the self-assembly evaluation were dependent on volume of water added between each observation. To be able to observe the morphology evolution in a more continuous manner, we decided to change DMSO for acetone and let acetone evaporate continuously. After the addition of 30% vol of water in 1 mL of PEG_{22}-*b*-$PTMC_{51}$ in acetone at 2 $mg.mL^{-1}$ with 1 %wt of PEG_{22}-*b*-$PTMC_{51}$-Cy5.5, we injected sample in µ-slide (chambered coverslip) with uncoated 8 wells from Ibidi GmbH uncovered to allow acetone evaporation. In this situation, the water content will increase continuously during acetone evaporation. Then, the evolution of the observed morphologies during acetone evaporation was followed over time. Figure 8a shows first moments of assembly, showing copolymer coacervate droplets in the acetone/water mixture. Droplets continued to coalesce until reaching a water content that prevent them from fusing anymore. Similar buddings appeared at the surface of droplets at the end of the self-assembly process as observed with DMSO and as can be seen in Figure 8e. Process is perfectly reproductible. Figure 9 is a focus of the above-mentioned experiment to observe more precisely the vesicle formation phenomenon. The growth of polymersomes is observed at the surface of the droplets for both organic solvents (DMSO and Acetone). However, vesicles can detach from the cluster during acetone evaporation, unlike DMSO, for which no detachment of vesicles is observed.

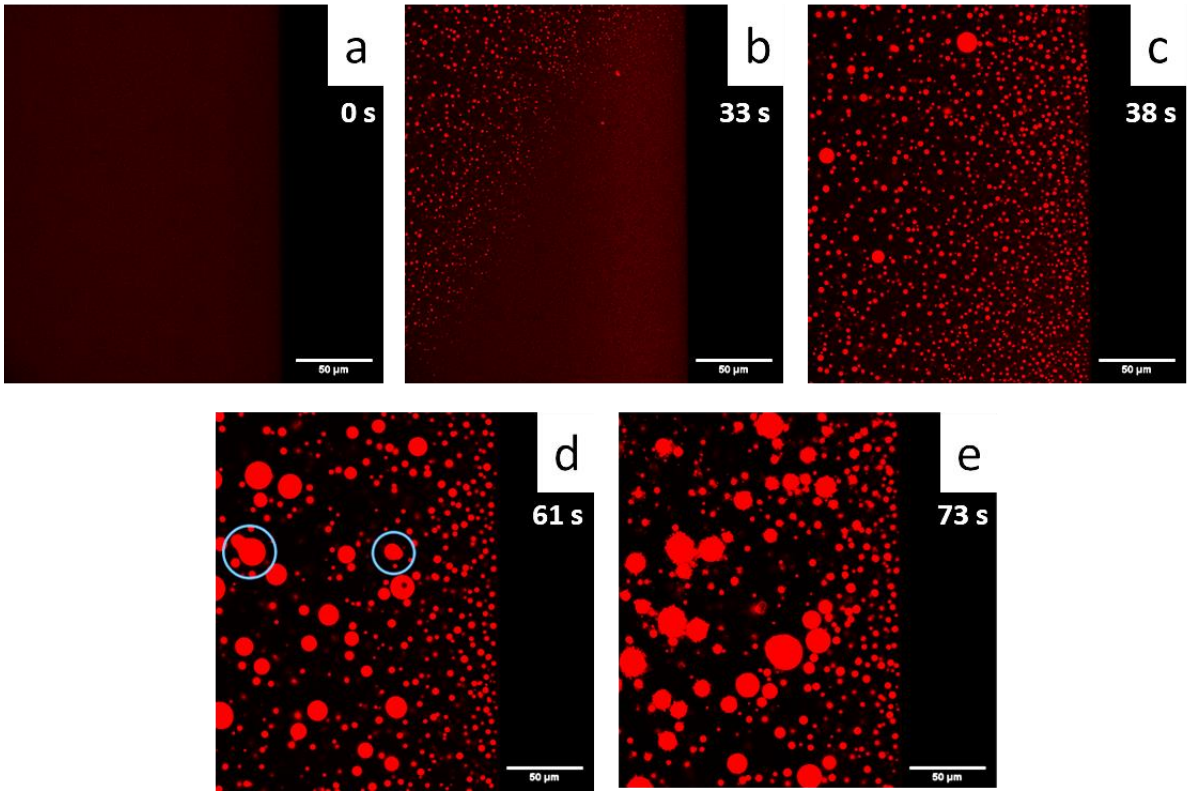

Figure 8: *Confocal microscopy observations in the red channel of PEG_{22}-b-$PTMC_{51}$ and PEG_{22}-b-$PTMC_{51}$-Cy5.5 in Acetone after 30 %vol of water addition. a to e : increase of water content through acetone evaporation. Blue circles represented in (d) enhance liquid-liquid phase separation and droplets coalescence and (e) image present buddings on the surface of droplets. Time from t = 0 s first picture to t = 73 s last picture are given as an indication.*

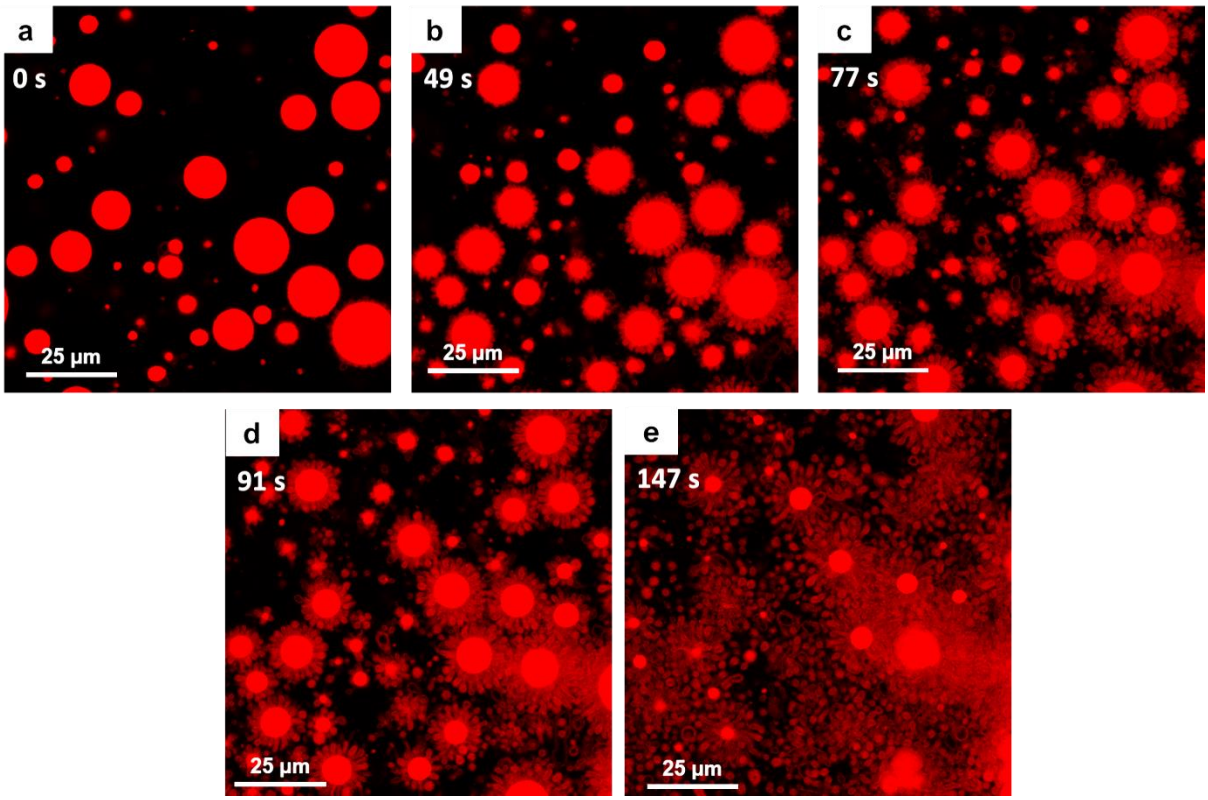

Figure 9: *Confocal microscopy observations in the red channel of PEG_{22}-b-$PTMC_{51}$ and PEG_{22}-b-$PTMC_{51}$-Cy5.5 in Acetone after 30%vol of water addition. a to e : increase of water content through acetone evaporation. A growth then a detachment of vesicles from reservoir droplets are observed. Time from t = 0 s first picture to t = 147 s last picture are given as an indication.*

Both experiments performed from DMSO and acetone as an organic solvent are consistent and highlighted similar mechanism when the water content was increased. The first step was the appearance of a liquid-liquid phase separation step where the copolymers were concentrated in coacervate droplets. These droplets coalesced up to a certain water content. The optical resolution of the confocal did not allow to observe the internal structure of the coacervates at this stage. Once water content reached a sufficient ratio to prevent droplets from coalescing, budding starts to appear from the droplet surface. In the case of DMSO as organic solvent, the system seems to be kinetically trapped at this stage. However, in the case of acetone, these buddings are giving rise to vesicles that are spontaneously detached from the coacervate surface. These coacervates being fully composed of entangled membranes.

Interestingly, the observed phenomenon does not exactly correspond to one of the two mechanisms of vesicle formation proposed by literature[2]. However, the observed vesicle growth from droplets is closer to vesicle forming through swelling micelles (mechanism II) than lamellar membranes fold inward, forming vesicular structures (mechanism I). Consequently, such mechanism does not favor drug encapsulation, as already mentioned.

As Bleul *et al.*[1] mentioned, the mechanism of vesicle formation strongly dependents on the exact conditions of the experiment, including process used to induce self-assembly. This first experiment allowed us to illustrate the formation mechanism of vesicles in a solvent exchange process. However, such microscopic observations did not allow us to evidence the very first steps of the self-

assembly process, close to the CWC. Also, in such experiments, we are also far from the characteristic solvent exchange diffusion times encountered in a microfluidic system. As such, with the aim of better understanding this vesicle formation mechanism in microfluidic assisted self-assembly, we decided to study the evolution of microstructures with an *in-operando* monitoring by X-Ray measurements.

3. *In-operando* monitoring of PEG_{22}-*b*-$PTMC_{51}$ self-assembly by X-Ray measurement (SAXS)

Small-angle X-ray scattering (SAXS) is a powerful technique for the characterization of the morphology and structural features of vesicles, and it provides information on the size, shape, and internal structure of vesicles, which are critical parameters for understanding their properties and behavior. Small-angle X-ray scattering (SAXS) is a non-destructive technique that is commonly used to study the structure and morphology of biological molecules or nanoparticles, including vesicles and polymersomes. The basic principle of SAXS is that a beam of X-rays is directed at the sample, and the scattered X-rays are collected on a detector. The scattered X-rays are diffracted at small angles (usually less than 10 degrees), and the scattering pattern is analyzed to obtain information on the sample's structure and morphology. In the case of vesicles, the X-rays will interact with the electrons within the vesicles and solvent, and their electron contrast is the main source of scattering. The SAXS intensity pattern thus provides information on the size, shape and membrane thickness of the vesicles.

Previously, SAXS acquisition was performed on nanoparticles obtained at the end of the formulation process but nowadays, there is an interest on evaluating the shape and structure of intermediate structures for a better understanding of self-assembly or nanoprecipitation mechanism for improving drug loading. That was one of the goals of the GALECHIP concept[16], which is a homemade designed microfluidic chip that formulates nanomedicines, specifically lipid nanocapsules (LNCs), under controlled process conditions. LNCs were successfully produced using chips manufactured by 3D printing and deep reactive ion etching technologies, with highly monodispersed sizes ranging from 25 nm to 100 nm. The transparent Si/Glass chip was also used for the small angle X-ray scattering (SAXS) analysis of the LNC formulation *in operando*. SAXS study of PEG_{22}-*b*-$PTMC_{51}$ microfluidic self-assembly *in-operando* was inspired by the GALECHIP concept on *in-operando* SAXS mapping for the study of phase inversion composition of lipid nanocapsules in Si/Glass microfluidic chips[14]. A session of experiment was obtained on SWING line of the SOLEIL synchrotron (Paris) in November 2022 in collaboration with MINT laboratory (*Micro et Nanomedecines Translationelles*; Angers, France), more particularly Brice Calvignac, and Guillaume Brotons (University of Le Mans, France) and Jacques Leng and Jean-Baptiste Salmon from Laboratory of Futur (Solvay).

3.1. Evaluation of PEG_{22}-b-$PTMC_{51}$ polymersome structure by laboratory SAXS acquisitions at rest within quartz capillaries.

Before the evaluation of self-assembly of block copolymers in situ with SAXS at synchrotron SOLEIL, preliminary data were obtained by using laboratory X-ray source to ensure the ability to obtain a good contrast between solvent and copolymer and to measure significant signal of PEG-*b*-PTMC vesicles and their intermediate morphologies. A sample of microfluidic assisted self-assembled vesicles

made using a solvent ratio of 20/80 %vol DMSO/water and a total flow rate of 1000 µL.min^{-1} was analyzed using a laboratory X-ray source. DMSO wasn't withdrawn from final solution. Ultrafiltration was used to increase final copolymer concentration up to 7.3 mg.mL^{-1}.

The SAXS measurements of our samples were made on the Xeuss 2.0 SAXS spectrometer (Xenocs, France) couple with FOX3D (Xenocs, France), single reflection optical mirror, available at the Transform platform on the campus of Bordeaux University, with the acknowledged help of Ahmed Bentaleb. The X-ray source is a standard copper cathode, therefore λ = 1.54189 Å, the detector is a highly sensitive CCD camera (Pilatus, Swiss Light Source) centered on Kα ray (λ= 1.54 Å) of copper. The samples were put in Lindeman glass capillaries (transparent to X-rays) with diameter < 0.5 mm at the tip (WJM Glas, Glastechnik und Konstruktion), which are sealed with a flame. The system delivered a collimated beam of 8 KeV under vacuum defined by two motorized anti-diffusing slots. Sample was exposed two times 3 hours and the data are collected in absolute intensity. Distance between sample and detector was varied as follow: 2.48, 1.828, 1.186 and 0.542 m to enlarge the scattering vector q-range from q_{min}= 4.5.10^{-3} Å^{-1} to q_{max}= 0.73 Å^{-1}. Curves obtained from the different sample-to-detector distances are given in Figure 10.

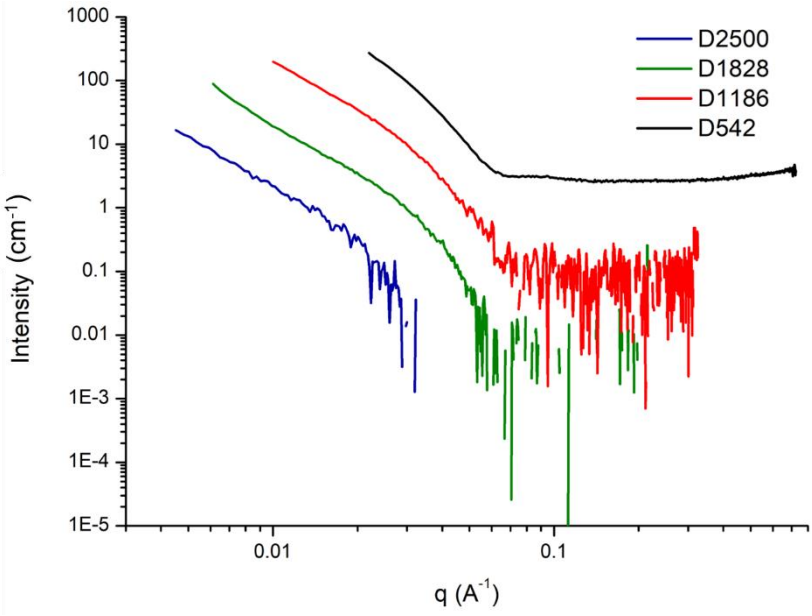

***Figure 10**: Diffracted X-ray intensity of microfluidic assisted self-assembled vesicles as a function of q from different sample-to-detector distances: 2.48 m (blue line), 1.828 m (green line), 1.186 m (red line) and 0.542 m (black line). The diffractograms of the diffracted intensity as a function of q were obtained by treating data with Foxtrot software (Collaboration between Xenocs and Soleil synchrotron).*

A combination of those curve allows to obtain a continuous curve covering a large range of q (Figure 11), from which solvent has been withdrawn by parts. SasView software was then used to fit the obtained curve (Figure 11, black curve). As objects were known to be vesicle from previous MALS and Cryo-TEM analysis (Chapter II), we decided to use a fit model of vesicle (detailed in Appendix).

Best fit parameters are given in Table 1. Fits of the SAXS data correspond unambiguously to a polymersome solution with parameters in agreement with calculated values (details on how expected values where determined are available in Appendix). This result proves that signal of our polymersomes can be obtained from laboratory size SAXS spectrometer which is encouraging for future measurements at Synchrotron.

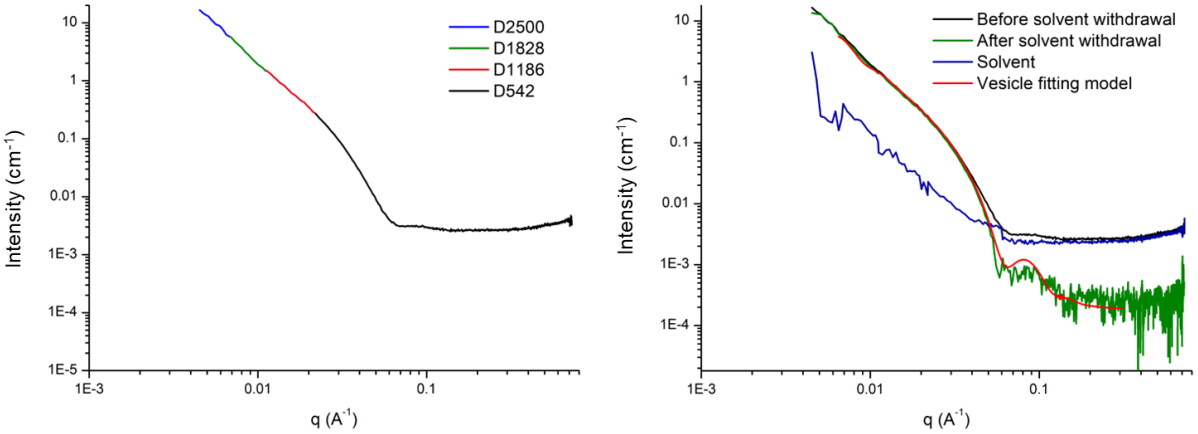

***Figure 11**: (left) Combination of diffracted X-ray intensity of microfluidic assisted self-assembled vesicles as a function of q from different sample-to-detector distances: 2.48 m, 1.828 m, 1.186 m and 0.542 m. (right) solvent signal (blue line) and solvent withdrawal leading to ready-to-fit curve (green line), vesicle fitting model (red line).*

***Table 1**: Parameters obtained from SasView software fitting of the combination of diffracted X-ray intensity of microfluidic assisted self-assembled vesicles as a function of q from different sample-to-detector distances: 2.48 m, 1.828 m, 1.186 m and 0.542 m, fitted with a polymersome model. φ is the volume fraction of the shell materiel, $R_{vesicle,inner}$ is the radius of inner core of the vesicle, $\rho_{solvent}$ is the scattering length density of the solvent (which is the same as for the core in vesicle case), $\rho_{membrane}$ is the scattering length density of the shell, background is a flat level.*

Parameters	**Best fit parameters (Sample 20/80 DMSO/PBS)**	**Expected calculated values**
Background (cm^{-1})	0.19×10^{-3}	-
$\rho b_{membrane}$ ($Å^{-2}$)	8.9×10^{-6}	9×10^{-6}
$\rho b_{solvent}$ ($Å^{-2}$)	9.57×10^{-6} (fixed)	9.57×10^{-6}
$\lvert\Delta\rho b\rvert$ ($Å^{-2}$) with $\Delta\rho b = \rho b_{membrane} - \rho b_{solvent}$	0.67×10^{-6}	0.57×10^{-6}
φ (Membrane volume fraction)	0.0070	0.0073
$R_{vesicle,inner}$ (Å)	594.46	490 if monodisperse
d, membrane thickness (Å)	99	115 ± 13
Radius distribution (σ_R, normalized Log-Normal distribution function)	0.1965	0.16
Membrane thickness distribution (σ_d, normalized Gaussian distribution function)	0.134	-
χ^2 (fitting error)	1.515	-

3.2. Optimization of microfluidic device for Synchrotron SAXS acquisitions

3.2.1. Evaluation of the Galenic-on-a-chip microfluidic device

We first considered using the microfluidic chip used during the PhD project of Nicolas Rolley for *in operando* SAXS study[14]. The chip we used was a meander chip, which consisted of a 50 cm long channel with several meanders onto a 2.6 × 4 cm glass chip with two inputs and one output. The channel was 1.5 mm deep and 0.15 mm wide, and the microfluidic chip is depicted in Figure 12.

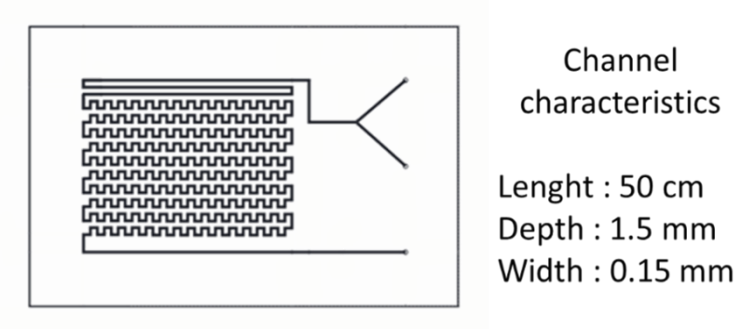

Figure 12: *Microfluidic Meander Chip imagined, drawn and produced by MINT laboratory.*

This chip operates on pure diffusion for solvent mixing purposes. By considering the chip dimension and a laminar flow regime for both solvents, we estimated the flow rate necessary for interdiffusion to be complete at the output of the channel by using the Stokes-Einstein diffusion law (Equation IV. 1) :

$$t = \frac{\Delta^2}{D} \qquad IV.1$$

with Δ (m) the distance through which diffusion is occurring and D (m^2/s) the coefficient diffusion.

By taking D ≈ 10^{-9} m^2/s, considering small molecules of solvent[17], to diffuse over the width of the channel, we obtain a complete interdiffusion of solvent after 22.5 s.

Considering chip characteristics and previous hypotheses, the total flow rate should not exceed 300 $\mu L.min^{-1}$ to allow complete diffusion over channel width. A test experiment was performed to ensure the formation of vesicle with this specific configuration of chip. A solution of PEG_{22}-*b*-$PTMC_{51}$ at 10 $mg.mL^{-1}$ in DMSO was used, solvent ratio of 20/80 %vol organic/aqueous solvent and a total flow rate of 100 $\mu L.min^{-1}$ were kept. Microfluidic assisted self-assembly was performed in the meander chip. Aqueous solvent used in this case was ultrapure water. On a sample of 2 mL done in duplicate, DLS analysis gave a mean diameter of 175 nm and a low PDI of 0.096. As confirmed by Cryo-TEM observations (Figure 13), the formation of vesicles can be obtained with a simple co-flow microfluidic system, where mixing is purely based on diffusion along the channel.

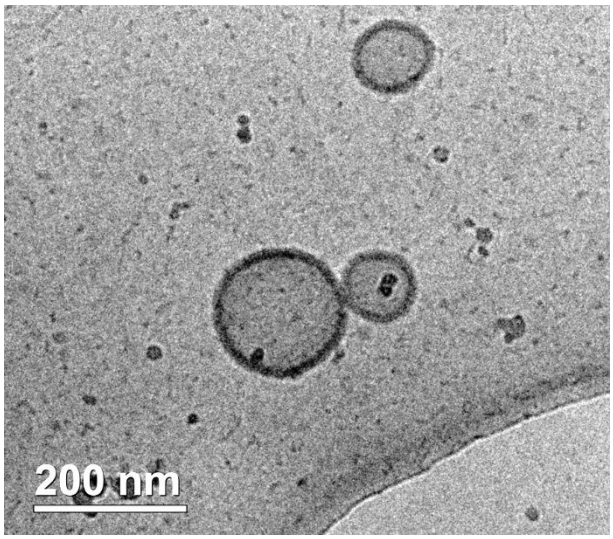

Figure 13: *Cryo-TEM images of PEG_{22}-b-$PTMC_{51}$ vesicles obtained with meander microfluidic chip.*

In the meander microfluidic chip, polymer solution in organic solvent was in contact with the walls of the channel. According to axial velocity profile described by Poiseuille law for a fluid in a tube, flow velocity at the walls of the tube is close to zero. Thus, if the copolymers stick to channel walls, it may nucleate aggregation of copolymer chains that will grow without being able to detach from the wall, due to the low-speed flow. The aggregate will grow until it is large enough to be detached by the flow. We have already observed this phenomenon in micromixer chip during the experiment for which copolymer concentration is high in Ch2.IV.1. Detachment of aggregate during X-Ray measurement may disturb the analysis. Consequently, another chip geometry was investigated to avoid such potential problem.

3.2.2. Co-flow home-made set-up

To avoid edge phenomenon that may potentially disturb our understanding from X-Ray measurements, we opted for a co-flow set up. With such microfluidic system, copolymer in organic solvent solution will come out of the inner capillary in the middle of outer capillary in which aqueous solvent is flowing, thus avoiding edge effect on the walls of the capillary. These embedded capillaries system was composed of a square outer capillary and a round inner capillary. Internal diameter of outer capillary had a dimension close to external diameter of inner capillary, allowing to easily center them. Set-up were home-made as described previously in this chapter.

To confirm the centered position of the inner jet of organic solvent in the outer capillary, a solution of fluoresceine in water was injected in the inner capillary while water was added in the outer one. We discovered that outer capillary dimension was large enough for the inner jet to be sensitive to earth's gravity. Indeed, set-up was first thought to be used horizontally, but as shown in figure 14, inner jet of fluoresceine solution ends up reaching the lower wall capillary. Keeping the jet centered in a horizontal position would require large flow rates that would be problematic for synchrotron experiments as experiment duration is limited by the syringe volume of external solvent (20 mL). We had then to orient the set-up vertically to correct this.

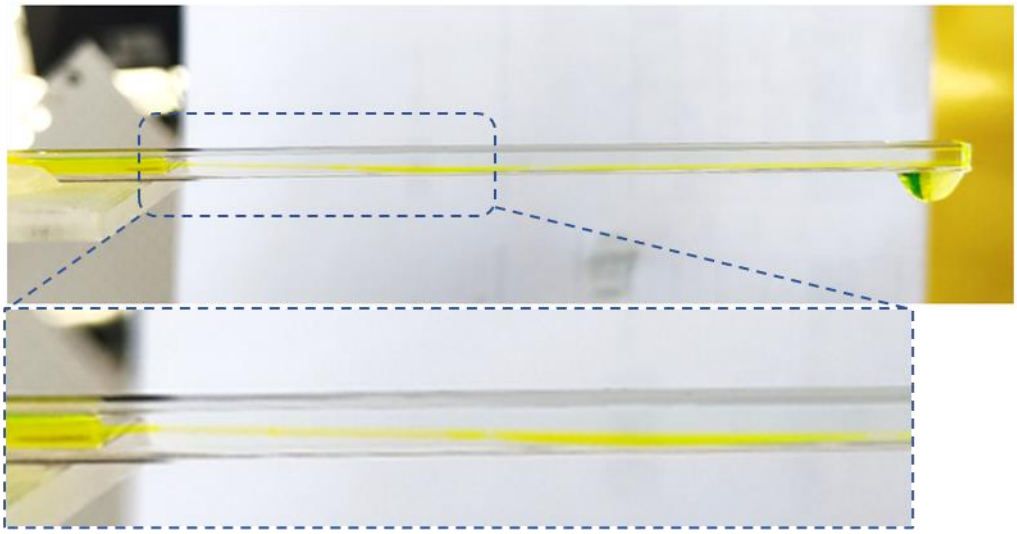

Figure 14: *Images of fluoresceine solution (inner capillary: 50 µL.min^{-1}) in water (outer capillary: 500 µL.min^{-1}) on which we can see colored trickle being centered when coming out of the capillary but reaching bottom wall of outer capillary after few centimeters.*

Such a round-square capillary set-up was then used for *in operando* study of PEG_{22}-*b*-$PTMC_{51}$ self-assembly by X-Ray measurement, positioned vertically. Due to this vertical position, Plateau-Rayleigh instability was observed when a jet of pure DMSO was injected in pure water as shown in Figure 15[18–20]. The instability causes the fluid to break up into smaller droplets or segments due to the balance between the surface tension of the fluid and the hydrodynamic pressure. The surface of the fluid column forms a series of bulges, called "Plateau borders," that act as centers of curvature, causing the surface to break up into smaller droplets or segments of equal size. To avoid such phenomenon, surface tension between solvents was reduced by adding 20 %vol of DMSO to the aqueous solvent, leading to DMSO injected in 20/80 % DMSO/Water. This allowed us to obtain a more stable flow as shown in Figure 15. Same strategy was applied when acetone was used as the organic solvent, aqueous solvent being thus 20/80 % v/v acetone/water.

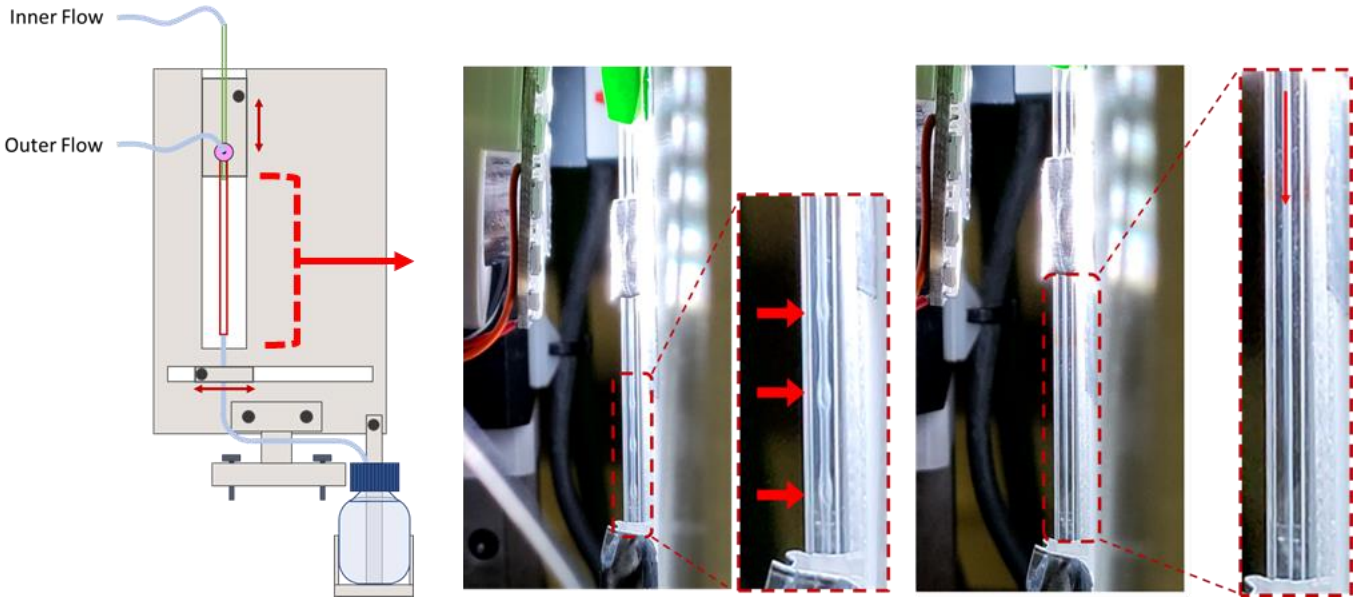

Figure 15: *(left) Schematic representation of set-up. (middle) Plateau-Rayleigh instabilities observed with DMSO as inner solvent and pure water as outer solvent. (right) Avoidance of Plateau-Rayleigh instabilities by using DMSO as inner solvent and 20/80 %vol DMSO/water outer solvent.*

3.2.3. Microfluidic experimental plan to study self-assembly process

One of the advantages of our proposed co-flow system is the ability to scan both directions (longitudinal and transverse) of the capillary by small angle X-Ray scattering (Synchrotron Soleil). Interdiffusion of solvent occurs perpendicularly to the flow direction. By scanning width of the capillary, different water contents can be observed, as shown in Figure 16. Moreover, scanning the width at different heights along the capillary enables the study of various stages/gradients of diffusion. Consequently, we conducted a scanning of the capillary width at three different heights.

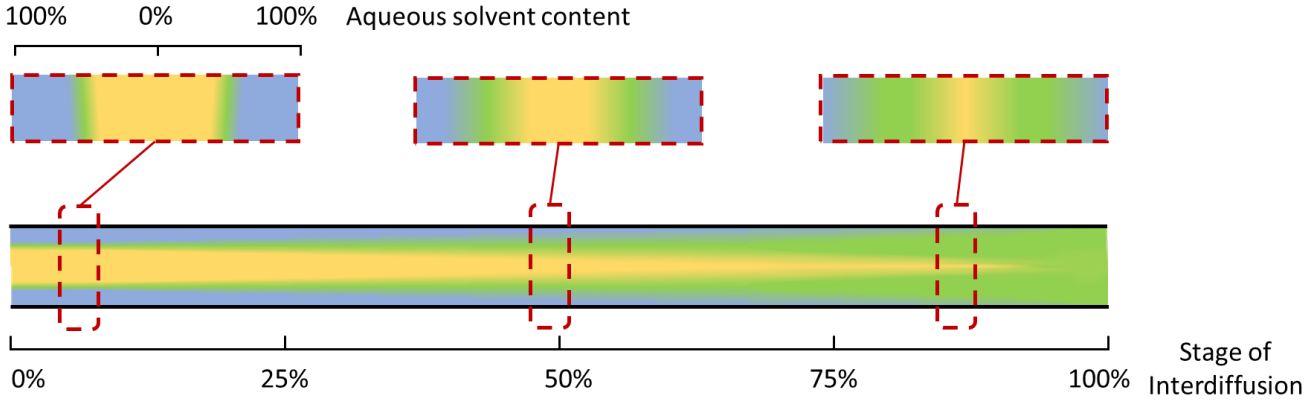

Figure 16: *Schematic representation of longitudinal and transverse solvent interdiffusion.*

Another interest of this set-up is the ability to change diffusion stage by varying flow rates, without moving along capillary. Thus, inspired by Oriane Bonhomme PhD work[21], we have developed parameters allowing to observe the different steps of the diffusion and thus of the self-assembly, by

modifying the flow rates. We considered two Newtonians fluids, with respective viscosity and flow rates η_i, η_e, Q_i and Q_e, as shown in Figure 17.

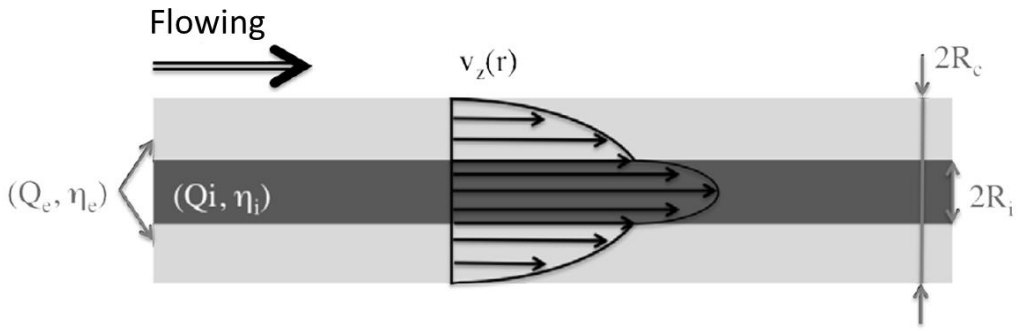

Figure 17: *Schematic representation of a co-flow system. Inner jet is represented in dark grey and outer flow in light gray. A velocity field is plotted in black. From Oriane Bonhomme PhD[20].*

The Stokes equations are solved for the internal fluid and external fluid separately. Considering boundary conditions and Poiseuille profile defined by pieces with a discontinuity of slope at the interface due to the difference in viscosity between the two phases, the velocity field can be linked to the flows imposed on each phase by integration. The inner jet being centered and of constant curvature in the direction of the flow, the pressure gradient is identical at all point of the flow and is denote $\partial_z P$.

The flow rate can be defined by equation IV.2 and IV.3:

$$Q_i = \frac{\pi \partial_z P R_i^2}{4}\left(\frac{R_i^2}{2\eta_i} + \frac{R_c^2 - R_i^2}{\eta_e}\right) \qquad IV.2$$

$$Q_e = \frac{\pi \partial_z P}{8\eta_e}\left(R_c^2 - R_i^2\right)^2 \qquad IV.3$$

By defining $\alpha = \sqrt{1 + m\frac{Q_i}{Q_e}}$, $m = \eta_e/\eta_i$ ratio of viscosities and $x = R_i/R_c$ radius of inner jet normalized to the size of the outer channel, the radius of inner jet and the pressure gradient are expressed as a function of the flow rates (equations IV.4 and IV.5) :

$$\partial_z P = \frac{8\eta_e Q_e}{\pi R_c^4 (1 - x^2)} \qquad IV.4$$

where

$$x = \sqrt{\frac{\alpha - 1}{\alpha - 1 + m}}$$

By Using Stokes-Einstein diffusion law (Equation IV.1) and by taking D = 10^{-9} $m^2.s^{-1}$, considering small molecules of solvent,[17,22] we can predict diffusion time depending on Q_i and Q_e.

By changing inner and outer flow rates, we ensure that the diffusion phenomenon takes place either on a short length of capillary or on a long length of capillary. For example, with an inner flow rate of **5 µL.min^{-1}** and an outer flow rate **of 50 µL.min^{-1}**, we obtained a radius of inner jet normalized to the size of the outer channel of x = 22%, meaning that inner jet represents 22% of outer capillary. Thus, total inter-diffusion will take 48.4 s to occur. But as the total flow rate is low, 48.4 s is the time needed to fill 1.1 cm of the capillary (2 mm side square for the capillary). Consequently, with such flow rate, we were able to study phenomenon happening mostly after diffusion (Figure 18a). In addition, with an inner flow rate of **50 µL.min^{-1}** with an outer flow rate of **480 µL.min^{-1}** , we obtained the same radius of inner jet normalized to the size of the outer channel of x = 22%, meaning that total inter-diffusion still occurs in 48.4 s but as flow rate is faster, 48.4 s is the time needed to fill 10.7 cm of the capillary. Since the capillary is 8 cm long, interdiffusion is not complete at the exit of the capillary, but these conditions allow us to study the phenomena that occur during interdiffusion. (Figure 18b) Based on these considerations, several flow rate combinations were used for *in operando* SAXS measurement to allow the access to phenomena happening during and after total inter-diffusion of solvent.

Table 2 gathers experiments and measurement parameters of *in operando* SAXS study of PEG_{22}-*b*-$PTMC_{51}$ self-assembly. This experimental design was built to cover two possibilities linked to copolymer self-assembly. If copolymer self-assembly time is slower than interdiffusion time, we thus needed a shorter distance necessary to reach full diffusion (Q_i = 5 µL.min^{-1}, Q_e = 50 µL.min^{-1}) to be able to study phenomena after diffusion in the capillary. The second option supposes that copolymer self-assembly occurs during interdiffusion of solvent: we thus need a longer distance to reach full diffusion to spread it along capillary (Q_i = 50 µL.min^{-1}, Q_e = 480 µL.min^{-1}).

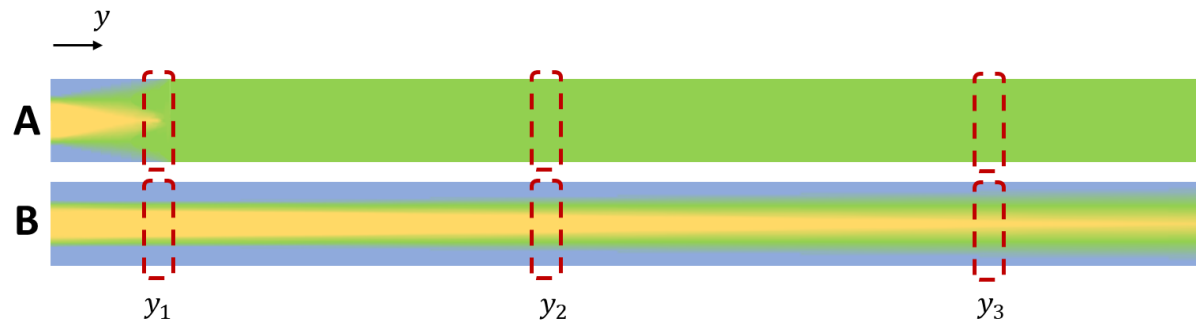

***Figure 18**: Schematic representation of the effect of changing flow rate on interdiffusion of solvent. Q_i is the flow rate of inner solvent jet (yellow) and Q_e the flow rate of outer solvent (blue). a) Q_i = 5 µL.min^{-1} and Q_e = 50 µL.min^{-1} b) Q_i = 50 µL.min^{-1} and Q_e = 480 µL.min^{-1}*

Table 2: *Parameters used to proceed in PEG_{22}-b-$PTMC_{51}$ self-assembly study by X-Ray measurements in operando. T_{diff} is the time necessary for interdiffusion to be completed, Y_{diff} corresponding location of completed interdiffusion in capillary, 0 cm being the output of inner capillary. Y_{mes} are the heights to which measurement have been performed. 9 mm being the output of inner capillary in the square capillary.*

Inner solvent	η_i (cP)	Outer solvent	η_e (cP)	Q_i ($\mu L.min^{-1}$)	Q_e ($\mu L.min^{-1}$)	x (%)	T_{diff} (s)	Y_{diff} (cm)	Y_{mes} (mm)
DMSO	2	20/80 %vol DMSO/ Water	1.34	5	50	22	48.4	1.1	10.3 35.4 76.7
				10	500	9.9	10	2.1	10.7 35.7 76.9
				25	1000	11.24	12.6	5.4	10.6 35.6 76.8
				50	1500	12.75	16.25	10.5	10.8 35.7 76.9
Acetone	0.34	20/80 %vol Acetone/ Water	1.6	25	1000	11.1	12.3	5.3	9.8 34.4 77.2

3.3. Synchrotron SAXS measurements and data analysis

In this section, we present the results of our experiments at synchrotron SOLEIL, on the SWING beamline, using a non-classical synchrotron beam for SAXS. Indeed, the beam was focused on the sample (and not the beamstop placed in front of the detector at a distance of 4 m from the sample), using Kirkpatrick-Baez type X-Ray mirrors placed upstream, and compound refractive lenses (CRL). The line was equipped with an undulator under vacuum U20. The 12 keV monochromatic beam (wavelength of X-Ray was fixed at 1.03 Å) was measured to be 25 µm wide (horizontal dimension) and 25 µm thick (vertical dimension), in order to perform fly-scan (for *in-operando* measurements). Gain of the EIGER X 4M detector was set to 4 for measurements in the co-flow set-up, and one for the measurements using standard quartz capillaries (detector at 2.5 m from the sample).

2D SAXS data are treated with Foxtrot software (version 3.5.10) developed on SWING beamline at synchrotron SOLEIL, in order to obtain 1D SAXS curves after radial averaging of 2D scattering images obtained on the Dectris detector. Before radial clustering, a mask is used to exclude the measured intensity behind the beamstop, which blocks the transmitter central beam and the dead pixels of the detector. Software masks were used to exclude the scattered intensity resulting from the reflection of the beam on capillary walls or scattering from instrument windows set in the beam path. An example of a mask is given in Figure 19. A correction was used to smooth out differences in pixel efficiencies. Intensity 1D SAXS curves, plotted as function of the wave vector q (in $Å^{-1}$) were obtained by applying usual corrections to reach an absolute intensity scale expressed in cm^{-1}. It is based on the measurement of the intensity scattered at small angles for pure water (SAXS reference signal at 0.01633 cm^{-1}).

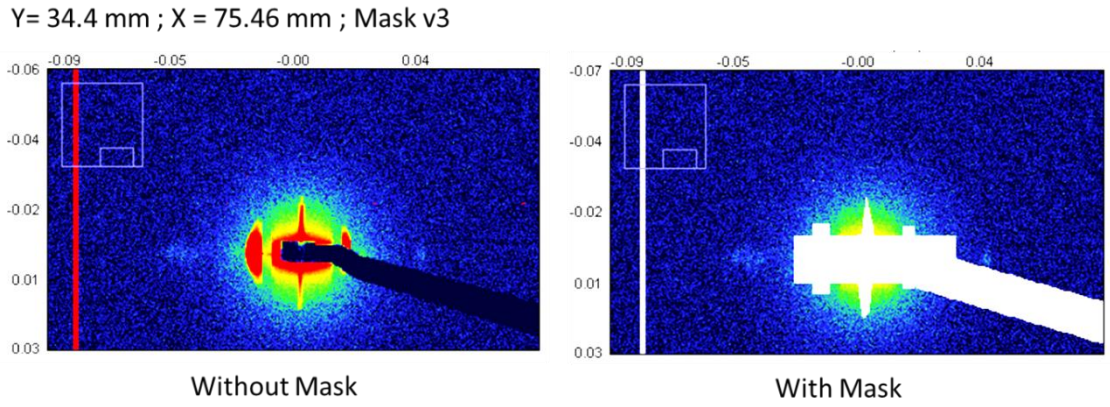

Figure 19: *2D scattering images obtained in operando: Sample 25 µL.min^{-1} of PEG$_{22}$-b-PTMC$_{51}$ 30 mg.mL^{-1} in acetone (inner jet), 1000 µL.min^{-1} acetone/water 20/80 %vol (outer solvent), Position in capillary : Y= 34.4 mm ; X = 75.46 mm (corresponding to centered positions in height and width. Without mask, and with mask.*

Figure 20 represent the curves obtained from the measurement of an empty capillary, full of air (blue), and shows scattering contribution coming mainly from scattering of the air in addition with contributions from capillary walls (400 µm thick, borosilicate) and instrument windows. Green curve was obtained from the measurement of water in the same capillary, red curve represents subtraction of empty capillary signal from water signal, showing an intensity of scattering at small angle of pure water around 0.01633 cm^{-1}.

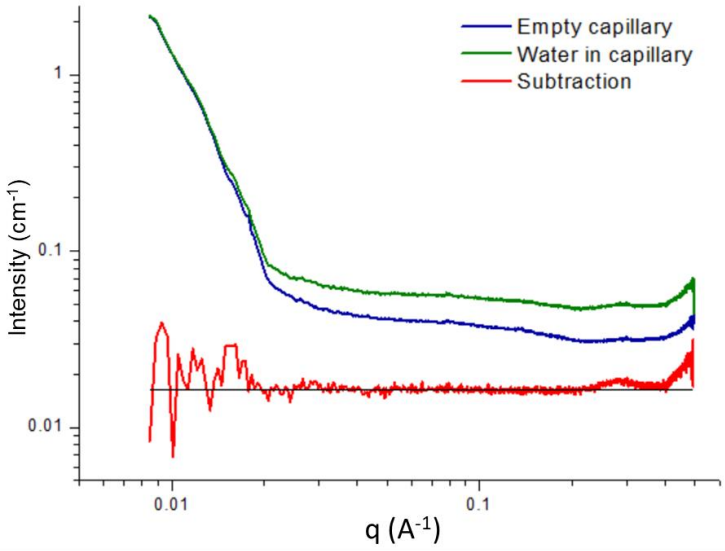

Figure 20: *SAXS Curves as raw signal (the intensity corresponding to a differential scattering cross section per scattering unit volume, in 1/cm) and SAXS intensity (cm^{-1}) plotted as function of wave vector q in log-log representation in a typical measurement in co-flow capillary. Blue and green curves correspond respectively to the raw signal collected with air and pure water. Signal for pure water is plotted in red with a black guide at 0.01633cm^{-1}.*

3.3.1. Reference SAXS measurements at rest in thin wall quartz capillaries

Well-characterized vesicle preparations performed in our "classical Dolomite" system were used to measure the SAXS signal (I(q) versus q curve, expressed in cm^{-1}) in conventional quartz capillaries with an internal diameter of 1.5 mm and a wall thickness of 10 µm. These measurements will be used as a reference and will be compared to measurement performed *in operando* in the co-flow set-up. Signal from solvent, measured in the same conditions (same capillary) was subtracted from sample signal. Samples used as reference are:

- Vesicles made at the laboratory, by microfluidic self-assembly using a 10 $mg.mL^{-1}$ PEG-*b*-PTMC solution in **DMSO**. Microfluidic process was performed using 20/80 % v/v ratio of DMSO/PBS solvent, total flow rate kept at 1000 $\mu L.min^{-1}$. Purification was done by dialysis.
- Vesicle made at the laboratory, by microfluidic assisted self-assembly using a 10 $mg.mL^{-1}$ PEG-*b*-PTMC solution in **Acetone**. Ratio of Acetone/Glucose was kept at 60/40 % v/v and total flow rate kept at 1000 $\mu L.min^{-1}$. Purification was done by evaporation.
- Vesicle made at Synchrotron in co-flow set-up using a 30 $mg.mL^{-1}$ solution of PEG-*b*-PTMC in **DMSO** at 25 $\mu L.min^{-1}$ (inner flow) and a solution of 20/80 %vol DMSO/water at 1000 $\mu L.min^{-1}$ (outer flow).
- Vesicle made at Synchrotron in co-flow set-up using a 30 $mg.mL^{-1}$ solution of PEG-b-PTMC in **Acetone** at 25 $\mu L.min^{-1}$ (inner flow) and a solution of 20/80 %vol Acetone/water at 1000 $\mu L.min^{-1}$ (outer flow).

Samples made at the laboratory have been proven to contain vesicle in Ch 2.III.2.

Fits of the data using a vesicle form factor for the calculated SAXS intensity in absolute scale, was used on the measurement of the above-mentioned sample, using the SasView software (vesicle model in appendix) (Figure 21 and 22). Best fit parameters used to build the fitted curve are given in Table 3 for samples involving DMSO as an organic solvent and in Table 4 for experiments involving Acetone. All parameters were free during the fitting except for the scattering length density of the solvent which was fixed here to known values.

Two models of vesicles were compared for vesicles made at synchrotron in co-flow using acetone as organic solvent. The first one picture a vesicle as composed of a core with same composition as external solvent, and a membrane composed of a unique component. The second model allow us to decompose the membrane in three layers: two layers of PEG surrounding a layer of PTMC (see appendix for more details). By observing fit parameters of this second model, we can see that scattering light density (SLD) of PEG layer is equal to the that of the solvent. This indicates that PEG is hydrated and its contribution to SLD membrane is neglectable. In addition, the SLD of the overall membrane for the first model is comparable to the SLD found for PTMC layer in the second model, enforcing the negligibility of PEG contribution. Thereafter, the simplified core-membrane model was utilized for subsequent analysis.

For the samples used as references, fit parameters are in agreement with the obtention of vesicle. The observed increase in fitting error for the suspensions formulated with the dolomite system could potentially be attributed to sample aging.

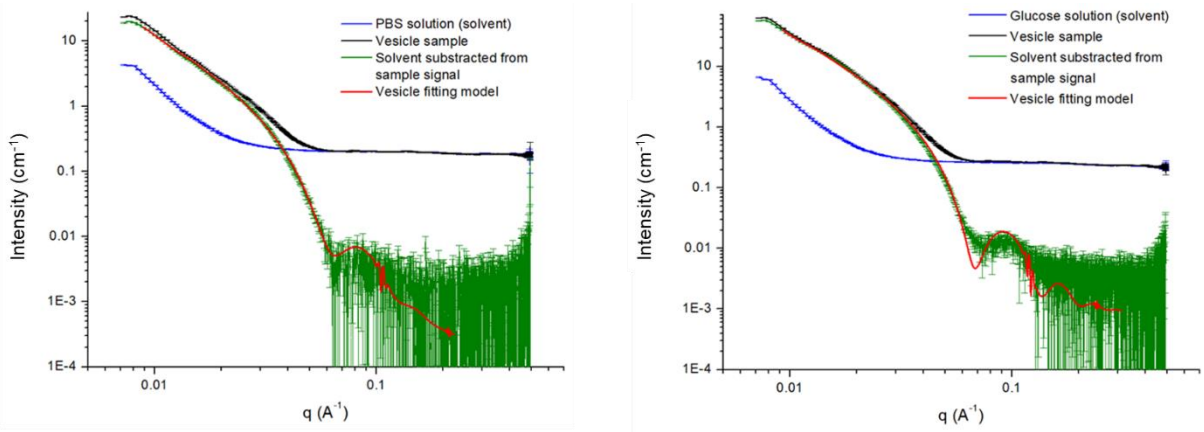

Figure 21: *X-ray intensity measured at rest for microfluidic assisted self-assembly of PEG-b-PTMC in Acetone (left) or DMSO (right) (black). Solvent (PBS or Glucose) (blue), subtraction of solvent from sample (green) and result given from SasView fit optimization (vesicle model) (red).*

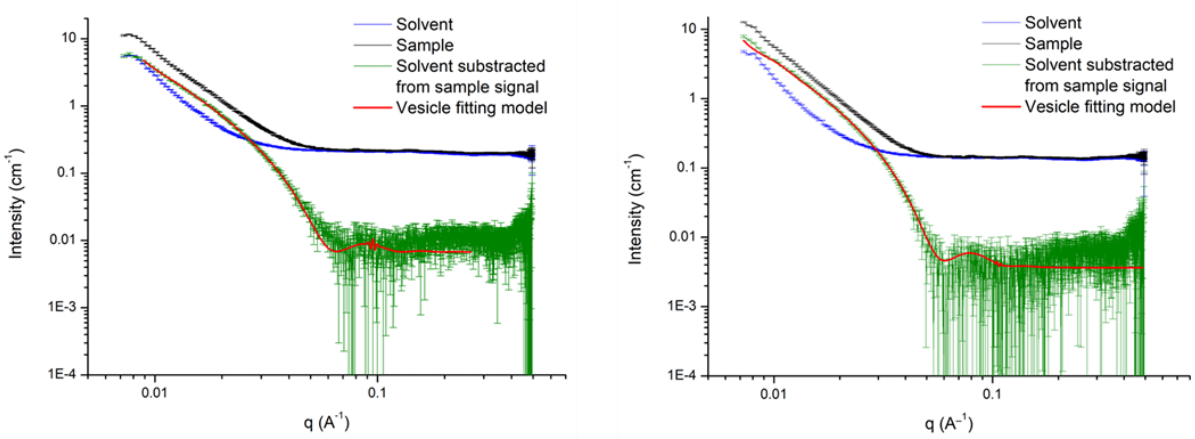

Figure 22: *X-ray intensity measured at rest of sample collected from co-flow set up, (**left**) inner flow: PEG-b-PTMC 30 mg.mL^{-1} at 25 µL.min^{-1} in acetone, outer flow: 20/80 %vol **Acetone**/Water at 1000 µL.min^{-1} (black). Solvent (20/80 %vol Acetone/Water) (blue), subtraction of solvent from sample (green) and result given from SasView fit optimization (vesicle model) (red). (**right**) inner flow: PEB-b-PTMC 30 mg/mL at 25µL/min in DMSO, outer flow: 20/80 %vol **DMSO**/Water at 1000 µL/min (black). Solvent (20/80 %vol DMSO/Water) (blue), subtraction of solvent from sample (green) and result given from SasView fit optimization (vesicle model) (red).*

Table 3: *Parameters obtained from vesicle fitting of samples made by microfluidic assisted self-assembly in* ***DMSO****. φ is the volume fraction of the shell materiel, $R_{vesicle,inner}$ is the radius of inner core of vesicle, $\rho_{solvent}$ is the scattering length density of the solvent (which is the same as for the core in vesicle case), $\rho_{membrane}$ is the scattering length density of the shell, background is a flat level.*

Parameters	**Best fit parameters (Microfluidic Micromixer chip DMSO/PBS in laboratory)**	**Best fit parameters (Synchrotron Co-flow DMSO/Water)**
Solvent of sample	SAXS in pure PBS	SAXS in DMSO/water 20/80 %vol
Background (cm^{-1})	0.211×10^{-3}	3.637×10^{-3}
$\rho b_{membrane}$ ($Å^{-2}$)	8.71×10^{-6}	8.99×10^{-6}
$\rho b_{solvent}$ ($Å^{-2}$)	9.44×10^{-6} (fixed)	9.57×10^{-6} (fixed)
$\lvert\Delta\rho b\rvert$ ($Å^{-2}$) with $\Delta\rho b = \rho b_{membrane} - \rho b_{solvent}$	0.73×10^{-6}	0.58×10^{-6}
φ (Membrane volume fraction)	0.0388	0.017
$R_{vesicle,inner}$ (Å)	507.12	699.94
d, membrane thickness (Å)	98.84	105
Radius distribution (σ_R, normalized Log-Normal distribution function)	0.288	0.2065
Membrane thickness distribution (σ_d, normalized Gaussian distribution function)	0.137	0.0997
χ^2 (fitting error)	210.22	33.69

Table 4: *Parameters obtained from vesicle fitting of samples made by microfluidic assisted self-assembly in* ***Acetone****. φ is the volume fraction of the shell materiel, $R_{vesicle,inner}$ is the radius of inner core of vesicle, $\rho_{solvent}$ is the scattering length density of the solvent (which is the same as for the core in vesicle case), $\rho_{membrane}$ is the scattering length density of the shell, background is a flat level.*

Parameters	**Best fit parameters (Microfluidic Micromixer chip Acetone/ glucose in laboratory)**	**Best fit parameters (Synchrotron Co-flow Acetone/Water)**	**Best fit parameters (Synchrotron Co-flow Acetone/Water)**
Fitting model	Vesicle	Vesicle	Refined-vesicle
Solvent of sample	SAXS in Glucose aqueous solution	SAXS in Acetone/water 20/80 %vol	
Background (cm^{-1})	0.835×10^{-3}	6.74×10^{-3}	8.57×10^{-3}
$\rho b_{membrane,PTMC+PEG}$ ($Å^{-2}$)	7.11×10^{-6}	8.45×10^{-6}	-
ρb_{PTMC_core} ($Å^{-2}$)	-	-	8.68×10^{-6}
ρb_{PEG_shell} ($Å^{-2}$)	-	-	9.02×10^{-6}
$\rho b_{solvent}$ ($Å^{-2}$)	9.44×10^{-6} (fixed)	9.02×10^{-6} (fixed)	9.02×10^{-6} (fixed)
$\lvert\Delta\rho b\rvert$ ($Å^{-2}$) with $\Delta\rho b = \rho b_{membrane} - \rho b_{solvent}$	2.33×10^{-6}	0.57×10^{-6}	0.34×10^{-6}
φ (Membrane volume fraction)	0.0116	0.0197	0.0102
$R_{vesicle,inner}$ (Å)	560.53	577.73	590.58
d, membrane thickness (Å)	92.42	96.21	-
d_{PTMC}	-	-	90.8
d_{PEG}	-	-	8.5
Radius distribution (σ_R, normalized Log-Normal distribution function)	0.229	0.280	0.2281
Membrane thickness distribution (σ_d, normalized Gaussian distribution function)	0.068	0.028	-
χ^2 (fitting error)	726.71	18.098	2.025

3.3.2. *In operando* measurements

As described previously, *in operando* measurement were recorded with a fly-scan of our co-flow sample mixing system. The capillary width (X axis, 2 mm ID) was scanned line by line with a step of 25 µm between acquisitions of typically 500 ms, at three different heights of the capillary (Y axis). Figure 23 illustrates typical two-dimensional (2D) scattering images acquired from a fly-scan along the X direction at a fixed Y position of a water-filled capillary. To avoid the interference caused by diffraction from the surface of the capillary walls, measurements of interest were conducted at positions farther away from the glass walls. These positions were selected to ensure that the 2D scattering images did not exhibit a red horizontal intensity line, as depicted in Figure 23 (B, D, and F).

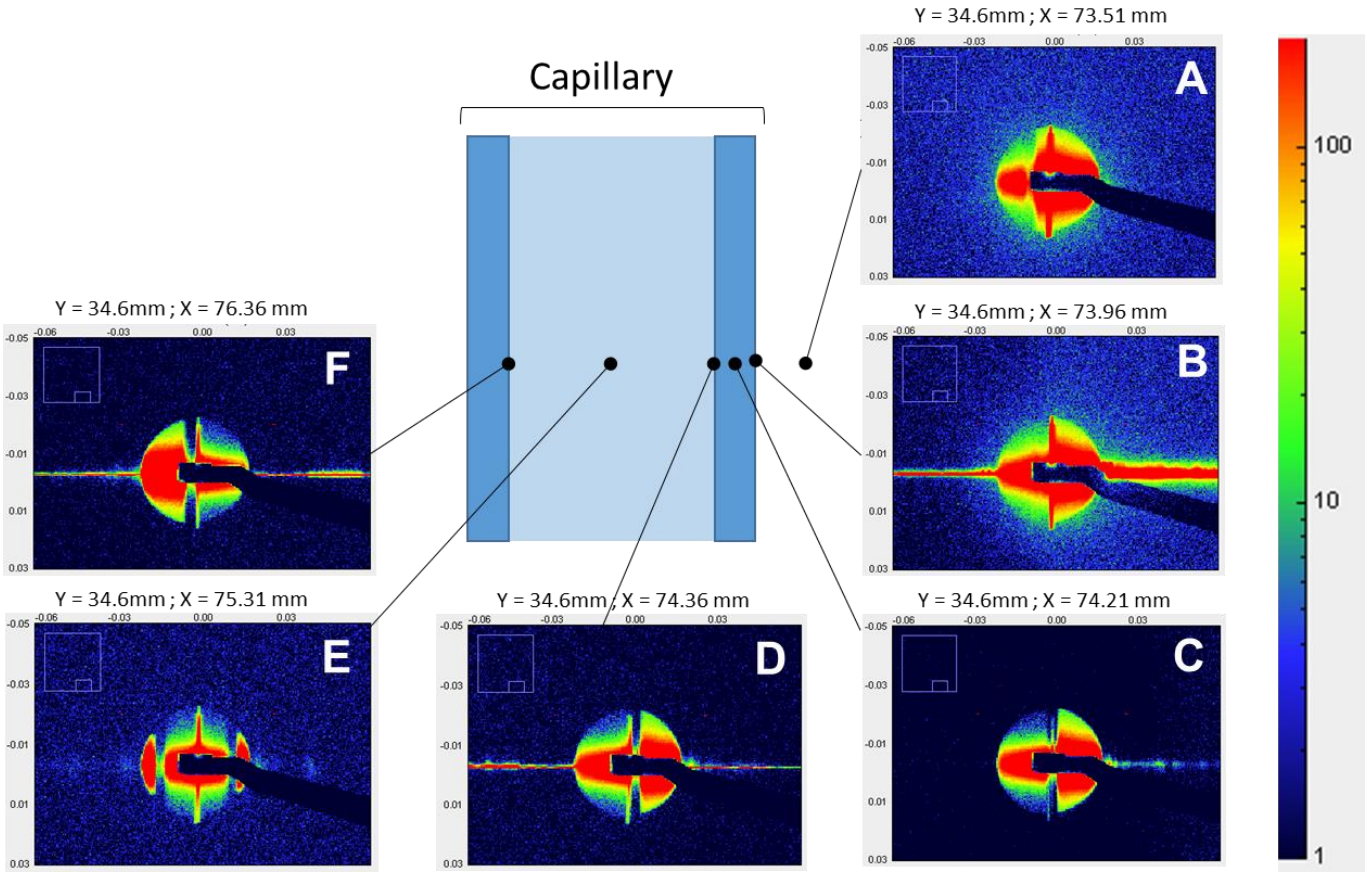

Figure 23: *2D scattering images obtained on capillary full of water, stop flow, along capillary width, height: Y = 34.6 mm. A to F, the beam is: A : outside of the capillary, B : external surface of capillary first wall, C : capillary wall, D: internal surface of capillary first wall, E : center of capillary and F : internal surface of capillary second wall.*

3.3.3. Analysis X-ray measurement on experiment performed with Acetone

During the *in-operando* experiment, the fly-scan conducted at a fixed height (Y position) revealed an axial symmetry in the signal. This symmetry originated from the center of the inner jet, as illustrated in Figure 24. Consequently, for the purpose of analysis, the curves selected were situated between the right wall and the inner jet, which is characterized by a maximum intensity (panel D in Figure 24).

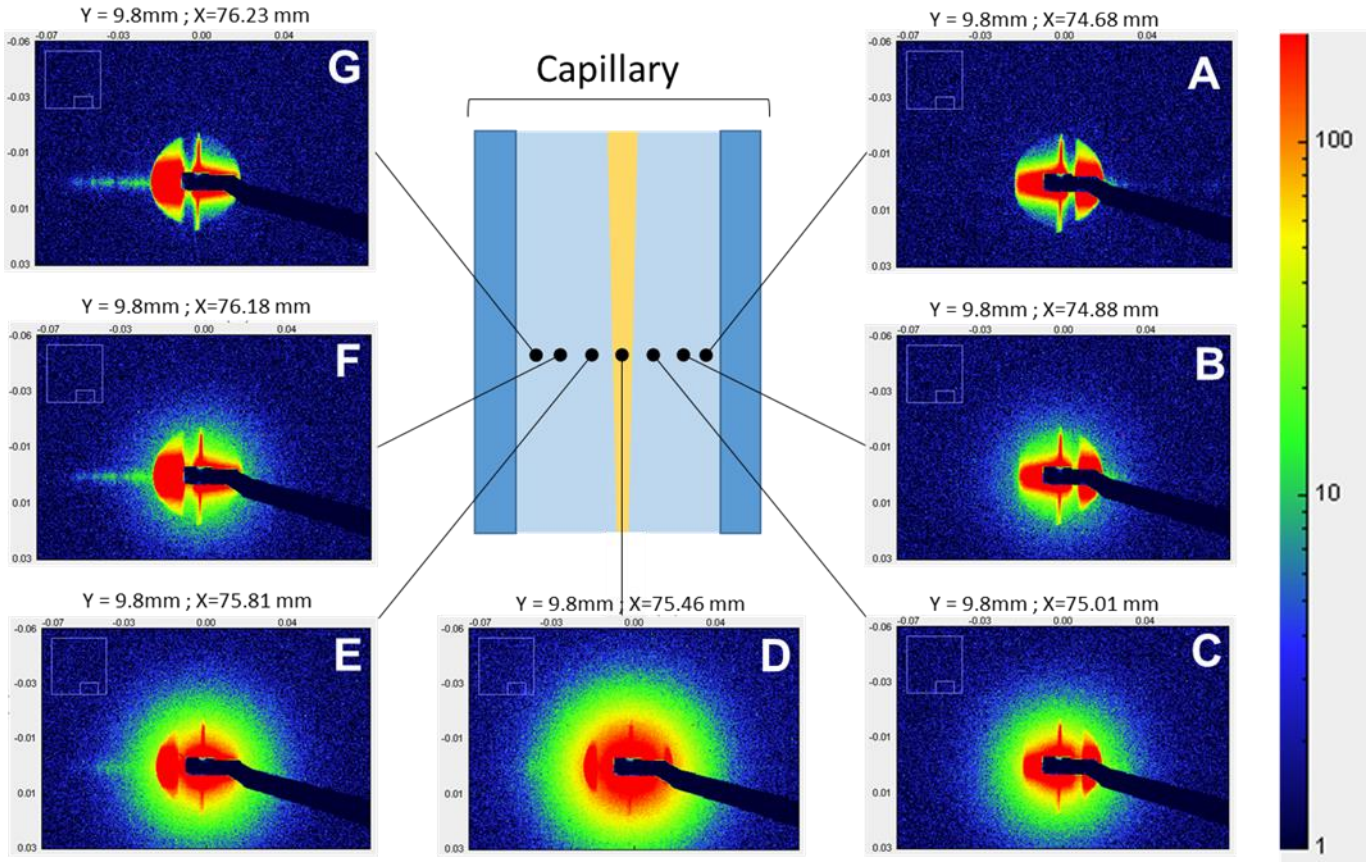

Figure 24: *2D scattering images obtained on capillary in operando, inner flow : 30 mg.mL^{-1} PEG$_{22}$-b-PTMC$_{51}$ in Acetone, outer flow : 20/80 %vol Acetone/water, along capillary width, height : Y = 9.8 mm. A to G, the beam is: A and G : close to capillary wall, B and F : further from capillary wall, closer to inner jet, C and E : closer / at the edge of the inner flow, D : maximum intensity, inner flow.*

Along the scan of the capillary width, five curves were extracted from five representative area of observed 2D scattering images. This selection was done for the three heights of measurement: Y = 9.8, 34.4 and 72.2 mm. Intensity curves SAXS, plotted as function of the wave vector q (in Å^{-1}) were obtained by applying usual corrections and solvent signal subtraction. Figure 25 shows 2D scattering images of the five areas selected on height Y = 9.8. Figures 27 and 29 are similar to Figure 25 with Y = 34.3 mm and Y = 77.2 mm, respectively. The intensity curves obtained after solvent withdrawal are compared to the corresponding signals obtained from the collected sample when it is analyzed at rest in a thin-wall quartz container.

For each height, we only fit the data with significant signal to noise ratio. SAXS 1D curves were fitted using the vesicle form factor model (Appendix Figure A1), and best fit parameters obtained from SasView are gathered in table 5, 6 and 7 for Y = 9.8, 34.3 and 77.2 mm, respectively. Figures 26 and 28 represent fitting models compared to experimental data for Y = 9.8 and 34.4 mm.

On Figure 26 and Table 5 (**Y = 9.8 mm**), we observed signals that correspond to large copolymer assemblies (polymersomes) with a radius around 500 Å and a clear slope close to q^{-2} at small angles. We can also see an oscillation corresponding to membrane thickness.

Signals at Y = 9.8 mm, X = 73.23 mm presents the most scattered intensity (Figure 25). The signal mentioned seems to be measured at the broad interface where the impinging jet of Acetone + copolymer interacts with water and undergoes mixing. This is where copolymer assemblies are formed

(highest concentration of scatters) and thus consequently the SAXS signal is stronger. Increasing proximity to this zone along the capillary width correlates with a higher volume fraction of the membrane observed. The volume fraction gradually decreases from 0.0258 at the nearest point (X = 75.23 mm) to 0.0051 at the farthest point (X = 74.86 mm), eventually leading to the pure water signal. Subsequently, the region where the capillary lateral glass borders scatter becomes apparent. In addition, the membrane thickness increases when we move away from the jet, going from 74.49 to 95.36 Å, corresponding to the membrane thickness observed on collected sample analyzed as reference (96.21 Å). This phenomenon is characteristic of PEG reorganization aiming to reduce contact surface between PEG + water and PTMC + traces of acetone.

Concerning the evolution of contrast, we can observe a general tendency for $\Delta\rho b$ to decrease from 1.12 to 0.679 Å^{-2} when we move away from the inner jet. This was expected as solvent composition changes from "close to pure" acetone in the inner jet ($\rho b_{Acetone} = 7.34$ Å^{-2}) to a mixture of acetone/water 20/80 %vol at outer capillary wall ($\rho b_{Acetone/water\ 20/80} = 9.02$ Å^{-2}). If we make the hypothesis that $\rho b_{membrane}$ do not change along scan, then $\Delta\rho b$ is expected to decrease when we move away from inner jet. For these fits, both $\rho b_{Acetone}$ and $\rho b_{membrane}$ weren't fixed. When looking at form factor equation (Appendix A.I) we can see that ρb of solvent and membrane aren't used independently and that only $\Delta\rho b$ is used. As we cannot affirm that membrane is free from acetone and because experiment itself make it hard to determine solvent composition for each position, it is impossible to fix one of those parameters to confirm the other one. But if we consider that the membrane remains pure PTMC along fly scan, we can fix $\rho b_{membrane} = 9$ Å^{-2} and estimate solvent composition for analyzed area using solvent fraction and $\rho b_{Acetone} = 7.34$ Å^{-2}, $\rho b_{Water} = 9.44$ Å^{-2}. In these conditions, at X = 75.23 mm (close to inner acetone jet) and considering $\Delta\rho b = 1.122$ Å^{-2}, we obtain a solvent composition of acetone/water of 74/26 %vol. For X = 74.86 mm (far from inner acetone jet), considering $\Delta\rho b = 0.679$ Å^{-2}, we obtain a solvent composition of acetone/water of 53/47 %vol. Those results are in agreement with progressive interdiffusion of solvents. For X = 74.86 and 75.01 mm which are the noisiest, we can in this case obtain fits with higher $\Delta\rho b$ (around 1.2 Å^{-2}), higher radius (higher of 50 Å approximately) and thinner membrane (around 88 Å).

One Figure 28, Table 6 (**Y = 34.4 mm**), we find signal corresponding to vesicle model again. Same behavior is observed for $\Delta\rho b$ which decreases when going away from center of capillary, with values from 0.6 Å^{-2} in the center of capillary (Solvent composition: acetone/water 48/52 %vol considering the membrane composed of pure PTMC) to 0.37 Å^{-2} (Solvent composition: acetone/water 38/62 %vol with same hypothesis). Solvent interdiffusion continues, resulting in this evolution of $\Delta\rho b$. Identic behavior is also observed for the volume fraction of the membrane that decrease when we measure further away from center of capillary.

The signals obtained at Y = 77.2 mm posed challenges when fitting them with a vesicle model, as the signals no longer exhibited a slope close to q^{-2} at small angles.. Signals are in favor of smaller objects with the emergence of a Gaussian plateau and a steeper slope. Other models were tested including the one for elongated micelle (Appendix for more details) (Table7). To our knowledge, the evolution of objects from vesicles to elongated micelles is hard to explain. Multiples hypothesis can be formulated from the unfortunate emergence of a measurement artifact, to a real change of morphology due to vesicle rupture. As sample collected does fit vesicle model, it remains hard to conclude without further information. Experiment should be done again, with fly scan at other heights of the capillary.

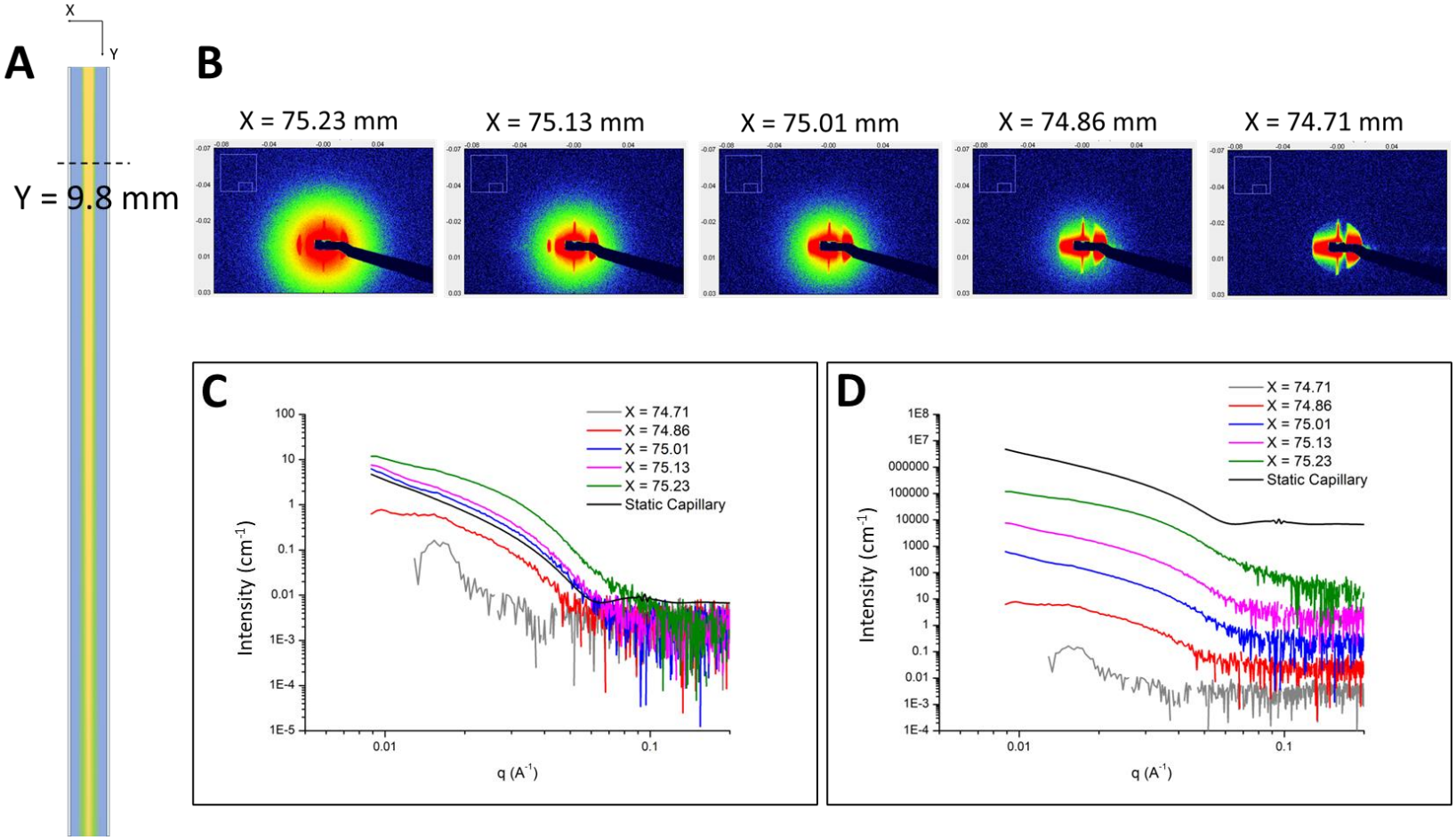

***Figure 25**: a) Schematic representation of in-operando capillary with Y = 9.8 mm represented by dotting line , b) 2D scattering images obtained on capillary in operando, inner flow : 30 mg.mL^{-1} PEG_{22}-b-$PTMC_{51}$ in Acetone, outer flow : 20/80 %vol Acetone/water, along capillary width, height : **Y = 9.8 mm** : X = 74.71, 74.86, 75.01, 75.13 and 75.23 mm, c) Associated intensity curves obtained after solvent withdrawal compared to vesicle fitting model for polymersomes obtained from static SAXS measurement of associated collected sample, d) Separation of intensity curve obtained by applying multiplicative factor : X = 74.72 (identical), X = 74.86 (factor 10), X = 75.01 (factor 100), X = 75.13 (factor 1 000), X = 75.23 (factor 10 000), Static Capillary vesicle fitting model (factor 1 000 000).*

Table 5: *Parameters obtained from vesicle fitting of signal recorded at* ***Y = 9.8 mm*** *in-operando co-flow set up, inner flow: PEG_{22}-b-$PTMC_{51}$ 30 mg.mL^{-1} at 25 µL.min^{-1}, outer flow: 20/80 %vol Acetone/Water at 1000 µL.min^{-1}. φ is the volume fraction of the shell materiel, $R_{vesicle,inner}$ is the radius of inner core of vesicle, $\rho_{solvent}$ is the scattering length density of the solvent $\rho_{membrane}$ is the scattering length density of the shell, background is a flat level.*

Parameters	X = 74.86	X = 75.01	X = 75.13	X = 75.23
Background (cm^{-1})	2.25 × 10^{-3}	1.65 × 10^{-3}	2.39 × 10^{-3}	0.11 × 10^{-3}
$\lvert\Delta\rho b\rvert$ (Å^{-2}) with $\Delta\rho b = \rho b_{membrane} - \rho b_{solvent}$	0.679 × 10^{-6}	0.8476 × 10^{-6}	1.0456 × 10^{-6}	1.1221 × 10^{-6}
φ (Membrane volume fraction)	0.00541	0.0118	0.0104	0.0258
$R_{vesicle,inner}$ (Å)	440.69	454.86	487.04	549.28
d, membrane thickness (Å)	95.36	90.43	86.36	74.731
Radius distribution (σ_R, normalized Log-Normal distribution function)	0.1361	0.1984	0.1882	0.1639
Membrane thickness distribution (σ_d, normalized Gaussian distribution function)	0.0228	0.114	0.0972	0.1
χ^2 (fitting error)	9.4	15.3	4	47.38

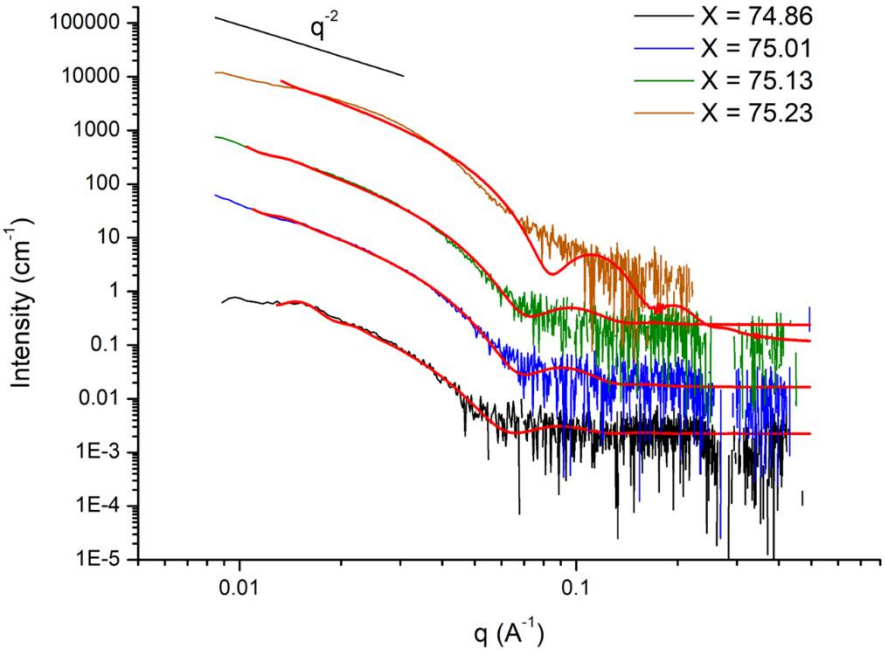

Figure 26: *X-ray intensity measured in flow from co-flow set up, inner flow: PEG-b-PTMC 30 mg.mL^{-1} at 25 µL.min^{-1} in acetone, outer flow: 20/80 %vol Acetone/Water at 1000 µL.min^{-1}. Signals are measured in the top height of the capillary (****Y = 9.8 mm****) for several positions in capillary width (X = 74.86, 75.01, 75.13 and 75.23 mm). Results given from SasView fit optimization (vesicle model) are represented for each curve in red.*

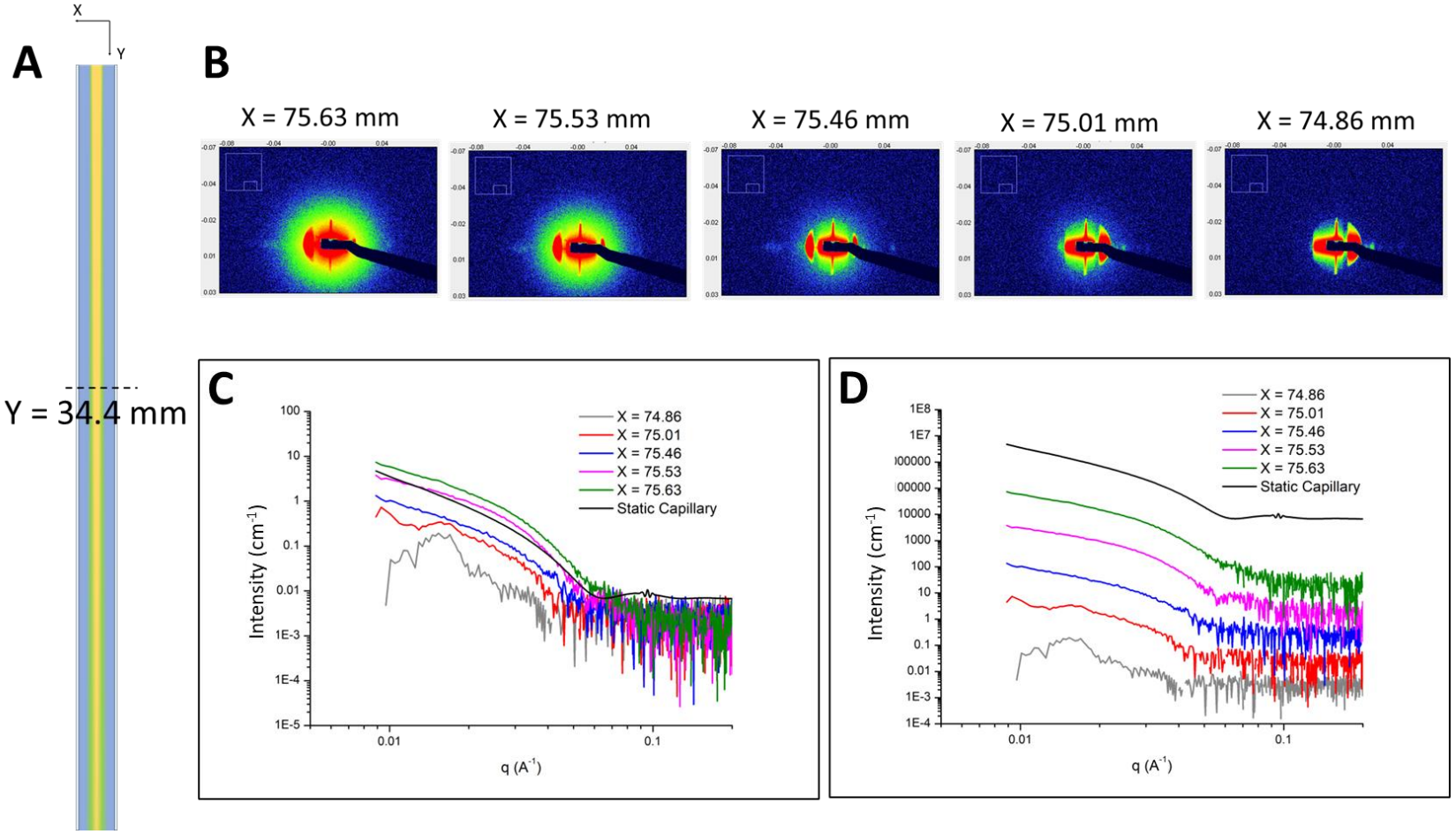

***Figure 27**: a) Schematic representation of in-operando capillary with Y = 34.4 mm represented by dotting line , b) 2D scattering images obtained on capillary in operando, inner flow : 30 mg.mL^{-1} of PEG$_{22}$-b-PTMC$_{51}$ in Acetone, outer flow : 20/80 %vol Acetone/water, along capillary width, height **: Y = 34.4 mm** : X = 74.86, 75.01, 75.46, 75.53, 75.63 mm, c) Associated intensity curves obtained after solvent withdrawal compared to vesicle fitting model for polymersomes obtained from static SAXS measurement of associated collected sample, d) Separation of intensity curve obtained by applying multiplicative factor : X = 74.86 (identical), X = 75.01 (factor 10), X = 75.46 (factor 100), X = 75.53 (factor 1 000), X = 75.63 (factor 10 000), Static Capillary vesicle fitting model (factor 1 000 000).*

Table 6 : *Parameters obtained from vesicle fitting of signal recorded at **Y = 34.4 mm** in-operando co-flow set up, inner flow: PEG_{22}-b-$PTMC_{51}$ 30 mg.mL^{-1} at 25 µL.min^{-1}, outer flow : 20/80 %vol Acetone/Water at 1000 µL/min. φ is the volume fraction of the shell materiel, $R_{vesicle,inner}$ is the radius of inner core of vesicle, $\rho_{solvent}$ is the scattering length density of the solvent, $\rho_{membrane}$ is the scattering length density of the shell, background is a flat level.*

Parameters	X = 75.01	X = 75.46	X = 75.53	X = 75.63
Background (cm^{-1})	2.05 × 10^{-3}	2.46 × 10^{-3}	1.12 × 10^{-3}	1.69 × 10^{-3}
$\lvert\Delta\rho b\rvert$ (Å^{-2}) with $\Delta\rho b = \rho b_{membrane} - \rho b_{solvent}$	0.373 × 10^{-6}	0.329 × 10^{-6}	0.706 × 10^{-6}	0.56 × 10^{-6}
φ (Membrane volume fraction)	0.00963	0.0209	0.0157	0.0389
$R_{vesicle,inner}$ (Å)	446.9	464.36	460.71	647.67
d, membrane thickness (Å)	97.83	88.02	92.147	85.266
Radius distribution (σ_R, normalized Log-Normal distribution function)	0.15	0.1889	0.1663	0.1768
Membrane thickness distribution (σ_d, normalized Gaussian distribution function)	0.0514	0.0638	0.0516	0.094
χ^2 (fitting error)	6.67	1.37	6.09	7.28

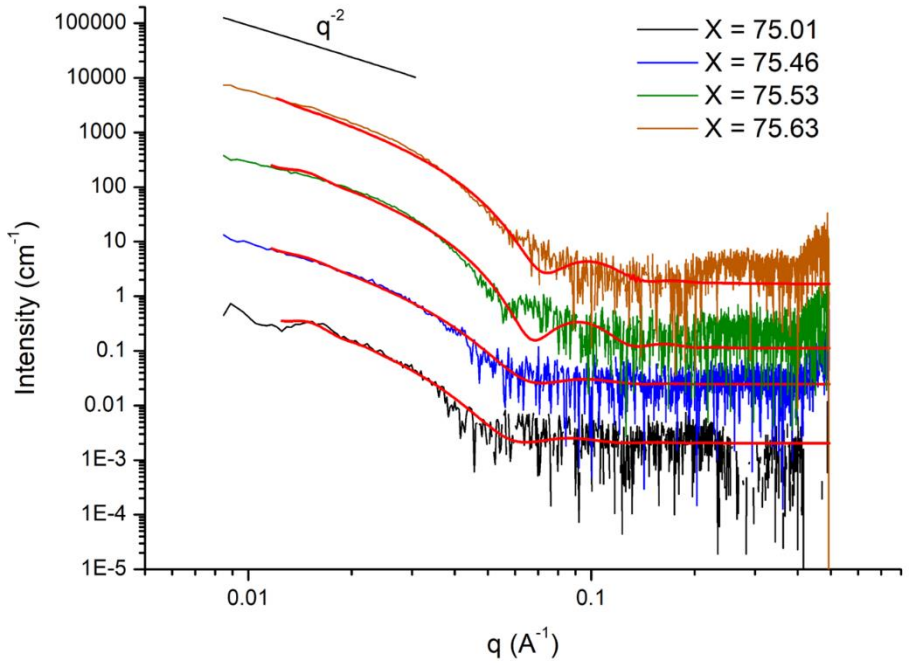

Figure 28: *X-ray intensity measured in flow from co-flow set up, inner flow: PEG-b-PTMC 30 mg.mL^{-1} at 25 µL.min^{-1} in acetone, outer flow: 20/80 %vol Acetone/Water at 1000 µL/min. Signal are measured in the middle height of the capillary (**Y = 34.4 mm**) for several positions in capillary width (X = 75.01, 75.46, 75.53 and 75.63mm). Results given from SasView fit optimization (vesicle model) are represented for each curve in red.*

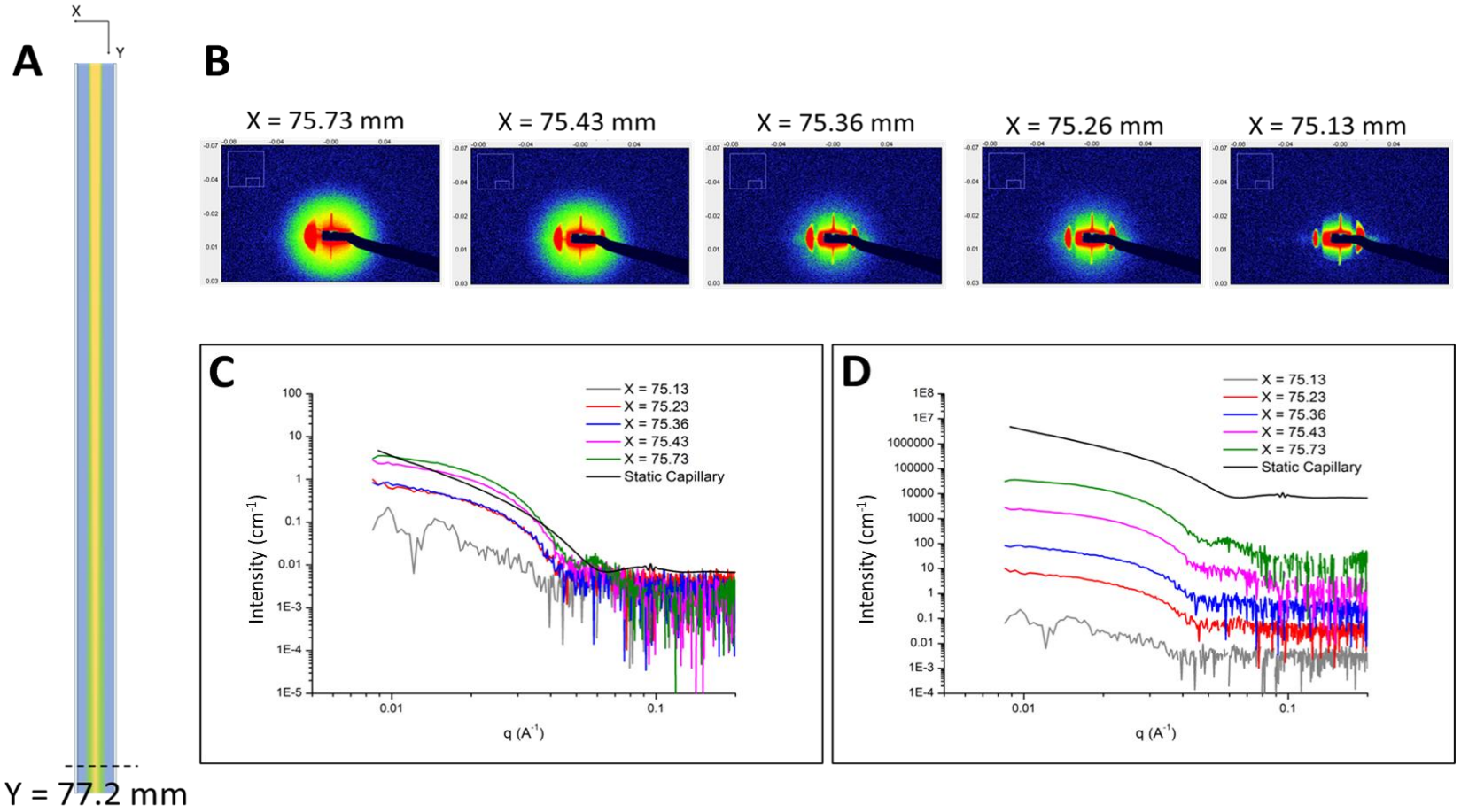

Figure 29: *a) Schematic representation of in-operando capillary with Y = 77.2 mm represented by dotting line , b) 2D scattering images obtained on capillary in operando, inner flow : 30mg.mL^{-1} PEG$_{22}$-b-PTMC$_{51}$ in Acetone, outer flow : 20/80 %vol Acetone/water, along capillary width, height :* ***Y = 77.2 mm*** *: X = 75.13, 75.26, 75.36, 75.43, 75.73 mm, c) Associated intensity curves obtained after solvent withdrawal compared to vesicle fitting model for polymersomes obtained from static SAXS measurement of associated collected sample, d) Separation of intensity curve obtained by applying multiplicative factor : X = 75.13 (identical), X = 75.26 (factor 10), X = 75.36 (factor 100), X = 75.43 (factor 1 000), X = 75.73 (factor 10 000), Static Capillary vesicle fitting model (factor 1 000 000).*

***Table 7**: Parameters obtained from elongated micelle fitting of signal recorded at **Y = 74.7 mm** in-operando co-flow set up, inner flow: PEG_{22}-b-$PTMC_{51}$ 30 mg.mL^{-1} at 25µL.min^{-1}, outer flow : 20/80 %vol Acetone/Water at 1000 µL.min^{-1}. N_{agg} is the number of copolymer chains, $\rho b_{membrane\_core}$ is the scattering length density of PTMC , $\rho b_{membrane\_brush}$ is the scattering length density of PEG , $\rho b_{solvent}$ is the scattering length density of the solvent, $\phi_{Solvent}$ is the fraction of solvent in core, R_G is the radius of gyration of brush chains, ε is the stretching factor for ellipsoidal micelle, S(q) is a structure factor added, background is a flat level and $\chi^2$is a fitting error.*

Parameters	**X = 75.73**
Background (cm^{-1})	0.90 × 10^{-3}
N_{agg}	1000
$\rho b_{membrane\_core}$ (Å^{-2})	8.99 × 10^{-6} (fixed)
$\rho b_{membrane\_brush}$ (Å^{-2})	8.826 × 10^{-6}
$\rho b_{solvent}$ (Å^{-2})	9.342 × 10^{-6}
$\phi_{Solvent}$ in core	0 (fixed)
R_G brush chains (Å)	11.89
d. For penetration of core/shell chains (if R_{core}<<R_g).	1 (fixed)
ε (stretching factor for ellipsoidal micelle)	5.12
S(q), type PY R_{HS} (Å)	115.6
S(q), ϕ_{HS}	0.0698
χ^2 (fitting error)	1.106

3.3.4. Analysis X-ray measurement on experiments performed with DMSO

Unfortunately, all fly-scans on experiments performed with DMSO were presenting the same kind of SAXS signal. For none of the experiment an evolution along capillary width was visible. For the three heights of the 4 experiments, 2D scattering images obtained on capillary *in operando* shows a characteristic SAXS ring as presented in figure 30.

This ring might be characteristic of a structure factor ring representative of a high concentration of small objects. But it can also be explained as a structure factor ring corresponding to correlation distance “membrane to membrane” if we imagine an object composed of dense membrane aggregates. Dense membrane aggregates were observed by confocal microscopy (Ch IV. Figure 7). This hypothesis is thus favored. Structural pic is measured at q = 0.02704 Å^{-1} (Figure 31) and is representative of a membrane center to membrane center distance of $\frac{\pi}{q} = 116$ Å, which is not far from membrane thickness previously found (around 96 Å without PEG layer contribution).

Indeed, experiments were reproduced back to the laboratory, highlighting a tendency for water from the outer capillary to climb up in inner capillary. This phenomenon might be due to vertical position of set up and difference of density between the two solvents. Copolymer thus meet water prior to area observable by X-Ray measurement. Self-assembly might even be completed before reaching the observable capillary.

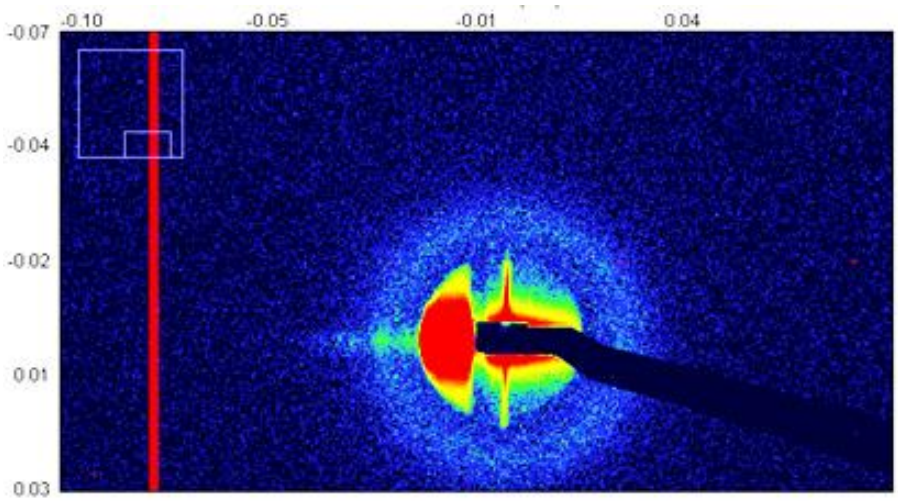

***Figure 30**: 2D scattering images obtained on capillary in operando, inner flow: 25µL.min^{-1} of 30mg.mL^{-1} PEG$_{22}$-b-PTMC$_{51}$ in DMSO, outer flow : 1000µL.min^{-1} 20/80 %vol DMSO/water. Y = 76.8 mm, X = 75.23 mm.*

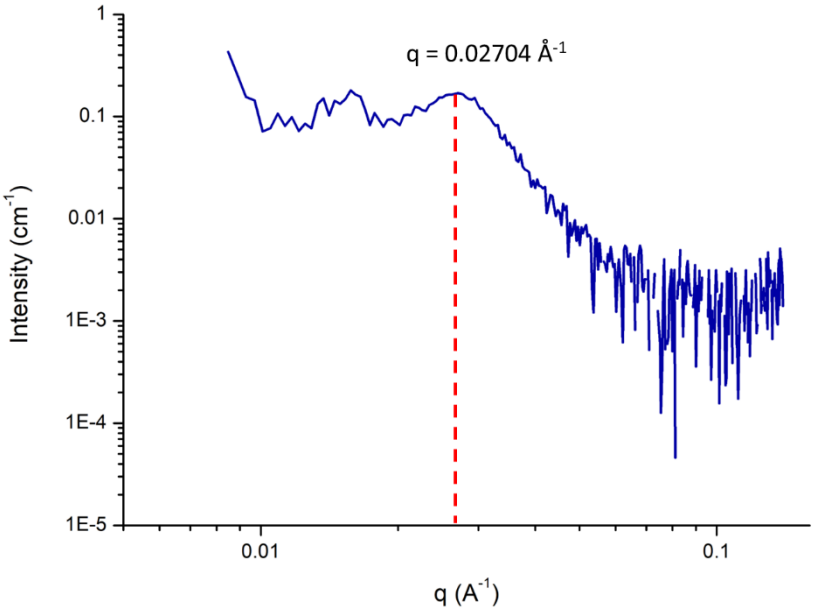

***Figure 31**: X-ray intensity measured in flow from co-flow set up, inner flow: PEG-b-PTMC 30 mg.mL^{-1} at 25 µL.min^{-1} in DMSO, outer flow: 20/80 %vol DMSO/Water at 1000 µL.min^{-1}. Signal are measured in the bottom height of the capillary (**Y = 76.8 mm**) for X = 75.23 mm.*

4. Conclusion

In this chapter, we tried to elucidate self-assembly mechanism of PEG_{22}-*b*-$PTMC_{51}$ to explain low loading results highlighted in Chapter III. Literature reports two main self-assembly mechanisms.

The first mechanism implies that the first step of free chain self-assembly is a micellar structure. It evolves into worm-like micelles that flatten and close up to from vesicles. This mechanism involves loading of surrounding medium, thus, reasonable levels of encapsulation of hydrophilic molecules is expected. The second mechanism proposes that first step micelles evolve into swollen micelles that restructure into vesicle. This mechanism is expected to prevent loading of high levels of hydrophilic molecules. We intended to prove that PEG_{22}-*b*-$PTMC_{51}$ was following second mechanism during it self-assembly.

We first proved that it was possible to kinetically trap intermediate morphologies by stopping the increase of water content. We used confocal microscopy to observe these intermediate morphologies with both organic solvents: DMSO and Acetone. Both organic solvents show similar behavior. We first observed a liquid-liquid phase separation in which copolymer forms coacervate droplets with organic solvent. Droplets coalesce up to a water content that prevent further coalescence. Budding is then observed at the surface of the droplets. System involving DMSO as an organic solvent seems to remain kinetically trapped at this stage, preventing vesicle to detach from droplets. On the other hand, experiment involving Acetone give rise to vesicle that spontaneously detached from the coacervate surface.

After proving the observability of PEG_{22}-*b*-$PTMC_{51}$ vesicles by X-Ray measurement on laboratory source of X-Ray, study was carried on microfluidic assisted self-assembly, forming vesicle that cannot be observed by confocal microscopy due to their size (< 200 nm), with *in operando* monitoring of X-Ray measurements in a microfluidic assisted self-assembly system. A co-flow set up was home made to allow X-Ray measurement during flow running. Several flow rate parameters were used to enable us to observe phenomena occurring during interdiffusion of solvents or after interdiffusion of solvents, depending on if copolymer self-assembly is faster than solvent interdiffusion.

Experiment using acetone as an organic solvent showed the fast formation of vesicular object, observable from the first measurement. In addition, signals obtained remain hard to explain due to an unusual mechanism that would imply formation of vesicle prior to elongated micelles. Experiment should be reproduced for better understanding. The co-flow set-up is suspected not to be the appropriate design to observe very first steps of self-assembly. Another chip design might be considered as well as other flow parameters. The experiments conducted using DMSO consistently yielded identical results across all flow rates tested, which indicated a problem of water rising in the inner capillary. This caused the copolymer and water to meet prematurely before reaching the observable area with X-Ray.

Regarding results detailed in this chapter, it remains difficult to confirm any self-assembly mechanism. Confocal microscopy isn't in favor of a self-assembly mechanism implying the close up of elongated micelles (mechanism I), which is in favor of giving an explanation for the low encapsulation efficiency of our vesicle, but this hypothesis couldn't be confirmed by SAXS measurements.

5. Appendix

5.1. Vesicle fitting model from SasView software

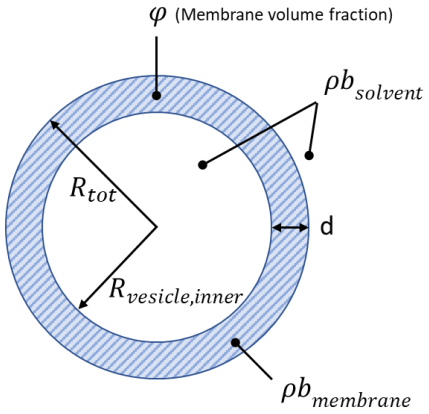

$$V_{tot} = \frac{4}{3}\pi \times R_{tot}^3$$

$$V_{vesicle,inner} = \frac{4}{3}\pi \times R_{vesicle,inner}^3$$

***Figure A1**: Schematic representation of vesicle model used for fittings of X-Ray measurements.*

Fittings of X-Ray measurements were using vesicle model to provide the form factor P(q) for a unilamellar vesicle. Vesicle model is identical to hollow sphere and form factor is expressed as follow (Equation A.1) :

$$P(q) = \frac{\varphi}{V_{shell}}\left[\frac{3\,V_{vesicle,inner}(\rho b_{solvent} - \rho b_{membrane})j_1(qR_{vesicle,inner})}{qR_{vesicle,inner}} + \frac{3\,V_{tot}(\rho b_{membrane} - \rho b_{solvent})j_1(qR_{tot})}{qR_{tot}}\right]^2 + B$$

Where φ is the volume fraction of the shell materiel, $V_{membrane}$ is the volume of shell, $V_{vesicle,inner}$ is the volume of the core, V_{tot} is the total volume, $R_{vesicle,inner}$ is the radius of core, R_{tot} is the outer radius of the shell, $\rho b_{solvent}$ is the scattering length density of the solvent (which is the same as for the core in vesicle case), $\rho b_{membrane}$ is the scattering length density of the shell (membrane), B refers to background, a flat level, and j_1 is the spherical Bessel function $j_1 = (\sin(x) - x\cos(x))/x^2$.

Expected values have been measured or calculated as follow:

- $\rho b_{membrane}$: We can either consider that PEG chains are hydrated and are not contrasted compared to pure solvent, in this case only PTMC is considered. Electronic density has been calculated around 0.32 electon. Å^{-3} considering 54 electrons per PTMC motif and an estimated volumic mass of 1 g.cm^{-3} (estimation). Scattering length density is obtained by multiplying electronic density by classical electron radius 2.818 10^{-5} Å. Thus $\rho_{membrane} = 8.99 \times 10^{-6}$ Å^{-2}. But we can consider that in presence of a mixture of solvent, PEG cannot be neglected. In this case, scattering length density is taking into account both polymer contribution, weighted by their respective molecular volume. ($V_{molecular,\ PEG22}$=1339.8 Å^3 and $V_{molecular,\ PTMC51}$= 8636.85 Å^3). In this case, $\rho b_{membrane} = 9.27 \times 10^{-6}$ Å^{-2}.
- $\rho b_{solvent}$ is calculated for solvent mixtures as the addition of SLD of each solvent, weighted by their respective volume fraction. ρb_{DMSO} : 1.01×10^{-5} Å^{-2}, ρb_{Water} : 9.44×10^{-6} Å^{-2}, $\rho b_{Acetone}$: 7.34×10^{-6} Å^{-2}, given by SLD calculator of SasView software.

- Note that for this form factor model (so-called spherical core-shell), only the SLD contrast matters, thus we fit $|\Delta\rho b|$ and not the absolute SLD values. Only the difference between $\rho b_{solvent}$ and $\rho b_{membrane}$ is determined if none of the p
- V_{tot} can be estimated by calculating sphere volume from a measured radius of the vesicle from DLS measurement.
- Membrane thickness has been estimated by Cryo-TEM (Ch III) for PEG_{22}-b-$PTMC_{51}$ vesicle around 11.5 nm.
- Radius distribution can be estimated as close to the polydispersity index of DLS measurement.
- φ can be estimated from V_{tot}, membrane thickness and copolymer concentration measured by dry extract.

A more refined model in which vesicle membrane is composed of three layers: a PTMC layer surrounded by two PEG layers, has been used to study the relevance of considering that hydrated PEG layer do not participate in overall membrane contrast. This model considers the vesicle as depicted by Figure A.2.

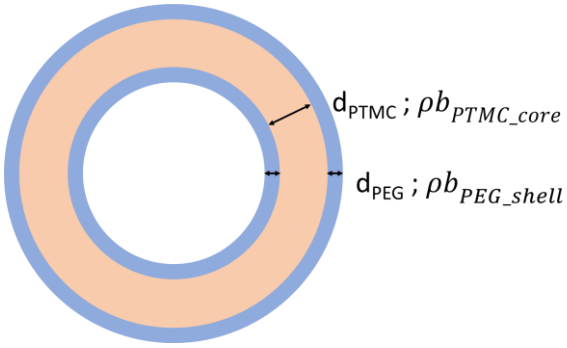

Figure A2: *Schematic representation of refined vesicle model used for fittings of X-Ray measurements where membrane is decomposed in 3 layers, the external ones being PEG layers with a PTMC layer in between.*

5.2. Elongated micelle fitting model

The form factor is based on a diblock copolymer ellipsoidal micelle (that can be oblate, prolate or spherical for ε=1 and $R_{core,x} = R_{core,y} \equiv R_{core,\rho}$, $R_{core,z} = \varepsilon R_{core,\rho}$) composed of N_{agg} copolymer chains.The core is represented by a homogeneous medium (ρb_{core}) that can be composed of a mixture of PTMC blocs and solvent. For the first set of fits, a constant $\rho b_{core} = 8.99\ 10^{-6}$ Å^{-2} corresponding to pure PTMC, was imposed , and we obtained for one polymer $V_{molecular,core\ chain} = 8636.85$ Å^3. The micelle core SLD can be fitted in the form of a solvent volume fraction in core parameter if needed ($\phi_{Solvent\ in\ core}$, up to now = 0). We assumed here that the core block is quite insoluble and forms a polymer melt core domain.

For the surrounding shell, we adopted a soluble block diffuse corona with Gaussian chains in good solvent, composed of a PEG block for which we obtain $V_{molecular,\ bruch\ chain} = 1339.8$ Å^3.

In the model we finally fit the aggregation number, so that each copolymer chain brings its own volume to the core and the brush (PEG corona) domains. In other words, the excess scattering coming from the electron density contrast with the surrounding solvent is consistent with the copolymer molecular

composition and densities of each block, for the calculated core domain and for the calculated corona domain.

$$I_{copo-micelle} = I_{core,self-correlation} + I_{shell,self-correlation} + I_{core-brush,cross-correlation} + I_{brush-brush,cross-correlation} \quad A.2$$

with the four contributions to intensity[23]:

The core form factor:

$$I_{core,self-correlation} = N_{agg}^2 \cdot (\Delta b_{core})^2 \cdot P_{core}(q) \quad A.3$$

where the excess scattering length of a core block chain is: $\Delta b_{core} = V_{core} \cdot (\rho b_{core} - \rho b_{solvent})$ and the form factor corresponds to a homogeneous ellipsoid scattering function. For the simplest case of a sphere (ε=1) it corresponds to:

$$P_{core}(q) = \left|F_{sphere}(q \cdot R_{core})\right|^2 \quad and \quad F_{sphere}(q \cdot R) = 3\frac{sin(q \cdot R) - q \cdot R \cdot cos(q \cdot R)}{(q \cdot R)^3} \quad A.4$$

since we fit the aggregation number, we must determine several quantities from it:

$$\mathrm{R}_{core} = \left(\frac{3}{4\pi} \cdot \frac{N_{agg} \cdot V_{core}}{1 - \phi_{\text{Solvent in core}}}\right)^{1/3} \quad A.5$$

The self-correlation term of the corona:

$$I_{shell,self-correlation} = N_{agg} \cdot (\Delta b_{brush})^2 \cdot P_{brush}(q) \quad A.6$$

where the excess scattering length of a core block chain is: $\Delta b_{brush} = V_{brush} \cdot (\rho b_{brush} - \rho b_{solvent})$ and the form factor is:

$$P_{brush}(q) = 2\frac{exp\left(-R_g^2 q^2\right) - 1 + R_g^2 q^2}{\left(R_g^2 q^2\right)^2} \quad A.7$$

Both form factors (P(q)) being normalized to one when q→0.

The cross-correlation term between core domain and chains in the brush shell:

$$I_{core-brush,cross-correlation} = 2N_{agg}^2 \cdot (\Delta b_{core} \cdot \Delta b_{brush}) \cdot S_{core-brush}(q) \quad A.8$$

where the cross-correlation term is:

$$S_{core-brush}(q) = F_{sphere}(q \cdot R_{core}) \cdot F_{Gauss\ chains}\left(q \cdot R_g\right) \cdot \frac{sin\left(q \cdot \left(R_{core} + d \cdot R_g\right)\right)}{\left(q \cdot \left(R_{core} + d \cdot R_g\right)\right)} \quad A.9$$

and $F_{Gauss\ chains}\left(q \cdot R_g\right) = \frac{1-exp\left(-R_g^2 q^2\right)}{\left(R_g^2 q^2\right)}$ the chains amplitude form factor.

The cross-correlation term between different brush chains in the diffuse shell is:

$$I_{brush-brush,cross-correlation} = N_{agg} \cdot \left(N_{agg} - 1\right) \cdot (\Delta b_{brush})^2 \cdot S_{brush-brush}(q) \qquad A.10$$

where

$$S_{brush-brush}(q) = \left[F_{Gauss\ chains}\left(q \cdot R_g\right) \cdot \frac{sin\left(q \cdot \left(R_{core} + d \cdot R_g\right)\right)}{\left(q \cdot \left(R_{core} + d \cdot R_g\right)\right)}\right]^2$$

and d=1 since the core radius R_{core} is much larger than the gyration radius of brush chains R_g.

A structure factor S(q) was added for more concentrated micelles using the Ornstein-Zernike equations for a Hard Sphere potential and an analytical solution from the Percus–Yevick equation (hard sphere type if enough with a potential giving a strong repulsive behaviour but short ranged: hard-sphere fluid approximation).

Parameters used involve hard sphere radius (R_{HS}) and volume fraction of hard sphere like interacting particles (ϕ_{HS}).Since we don't know the composition of solvent in the mixture exactly (should be between pure acetone $\rho b_{Acetone}$= 7.34 × 10^{-6} $Å^{-2}$ and a mixture of acetone/water 20/80 %vol $\rho b_{Acetone/water}$= 9.02 × 10^{-6} $Å^{-2}$), solvent SLD wasn't fixed. Solvent volume fraction in core: $\phi_{Solvent\ in\ core}$= 0 assuming pure polymer.

6. References

(1) Bleul, R.; Thiermann, R.; Maskos, M. Techniques To Control Polymersome Size. *Macromolecules* **2015**, *48* (20), 7396–7409. https://doi.org/10.1021/acs.macromol.5b01500.

(2) Iqbal, S.; Blenner, M.; Alexander-Bryant, A.; Larsen, J. Polymersomes for Therapeutic Delivery of Protein and Nucleic Acid Macromolecules: From Design to Therapeutic Applications. *Biomacromolecules* **2020**, *21* (4), 1327–1350. https://doi.org/10.1021/acs.biomac.9b01754.

(3) Uneyama, T. Density Functional Simulation of Spontaneous Formation of Vesicle in Block Copolymer Solutions. *J. Chem. Phys.* **2007**, *126* (11), 114902. https://doi.org/10.1063/1.2463426.

(4) Chen, L.; Shen, H.; Eisenberg, A. Kinetics and Mechanism of the Rod-to-Vesicle Transition of Block Copolymer Aggregates in Dilute Solution. *J. Phys. Chem. B* **1999**, *103* (44), 9488–9497. https://doi.org/10.1021/jp9913665.

(5) He, X.; Schmid, F. Dynamics of Spontaneous Vesicle Formation in Dilute Solutions of Amphiphilic Diblock Copolymers. *Macromolecules* **2006**, *39* (7), 2654–2662. https://doi.org/10.1021/ma052536g.

(6) Adams, D. J.; Adams, S.; Atkins, D.; Butler, M. F.; Furzeland, S. Impact of Mechanism of Formation on Encapsulation in Block Copolymer Vesicles. *Journal of Controlled Release* **2008**, *128* (2), 165–170. https://doi.org/10.1016/j.jconrel.2008.03.006.

(7) Pitman, M.; Larsen, J. The Characterization of Self-Assembled Nanostructures in Whole Blood. *Anal. Methods* **2020**, *12* (16), 2068–2081. https://doi.org/10.1039/D0AY00170H.

(8) Mourdikoudis, S.; M. Pallares, R.; K. Thanh, N. T. Characterization Techniques for Nanoparticles: Comparison and Complementarity upon Studying Nanoparticle Properties. *Nanoscale* **2018**, *10* (27), 12871–12934. https://doi.org/10.1039/C8NR02278J.

(9) Dautzenberg, H. Advances in Polymer Science. Vol. 48. Light Scattering from Polymers. Hg. von H.-J. CANTOW u. a. ; Berlin/Heidelberg/New York: Springer-Verlag 1982, 167 S., Lwd., DM 98,–. *Acta Polymerica* **1984**, *35* (5), 433–433. https://doi.org/10.1002/actp.1984.010350518.

(10) Houga, C.; Giermanska, J.; Lecommandoux, S.; Borsali, R.; Taton, D.; Gnanou, Y.; Le Meins, J.-F. Micelles and Polymersomes Obtained by Self-Assembly of Dextran and Polystyrene Based Block Copolymers. *Biomacromolecules* **2009**, *10* (1), 32–40. https://doi.org/10.1021/bm800778n.

(11) Jiang, W.; Zhou, Y.; Yan, D. Hyperbranched Polymer Vesicles: From Self-Assembly, Characterization, Mechanisms, and Properties to Applications. *Chem. Soc. Rev.* **2015**, *44* (12), 3874–3889. https://doi.org/10.1039/C4CS00274A.

(12) Landman, J.; Ouhajji, S.; Prévost, S.; Narayanan, T.; Groenewold, J.; Philipse, A. P.; Kegel, W. K.; Petukhov, A. V. Inward Growth by Nucleation: Multiscale Self-Assembly of Ordered Membranes. *Science Advances* **2018**, *4* (6), eaat1817. https://doi.org/10.1126/sciadv.aat1817.

(13) Schulz, F.; Lokteva, I.; Parak, W. J.; Lehmkühler, F. Recent Notable Approaches to Study Self-Assembly of Nanoparticles with X-Ray Scattering and Electron Microscopy. *Particle & Particle Systems Characterization* **2021**, *38* (9), 2100087. https://doi.org/10.1002/ppsc.202100087.

(14) Rolley, N. Formulation Microfluidique de Nanocapsules Lipidiques Par Inversion de Phase En Composition : Études Mécanistiques et Phénoménologiques. These de doctorat, Angers, 2021. https://www.theses.fr/2021ANGE0035 (accessed 2023-04-07).

(15) Lebleu, C. Polymersomes Based on PEG-b-PTMC towards Cell-Mediated Delivery of Nanomedicines. phdthesis, Université de Bordeaux, 2019. https://tel.archives-ouvertes.fr/tel-03463393 (accessed 2022-04-20).

(16) Rolley, N.; Bonnin, M.; Lefebvre, G.; Verron, S.; Bargiel, S.; Robert, L.; Riou, J.; Simonsson, C.; Bizien, T.; Gimel, J.-C.; Benoit, J.-P.; Brotons, G.; Calvignac, B. Galenic Lab-on-a-Chip Concept for Lipid Nanocapsules Production. *Nanoscale* **2021**, *13* (27), 11899–11912. https://doi.org/10.1039/D1NR00879J.

(17) Valente, A. J. M.; Söderman, O. Do the Solvent Properties Affect the Propensity for Self-Association of α-Cyclodextrin? Insights from NMR Self-Diffusion. *Journal of Molecular Liquids* **2019**, *295*, 111869. https://doi.org/10.1016/j.molliq.2019.111869.
(18) Sugiura, S.; Nakajima, M.; Iwamoto, S.; Seki, M. Interfacial Tension Driven Monodispersed Droplet Formation from Microfabricated Channel Array. *Langmuir* **2001**, *17* (18), 5562–5566. https://doi.org/10.1021/la010342y.
(19) Dangla, R.; Kayi, S.; Baroud, C. Droplet Microfluidics Driven by Gradients of Confinement. *Proceedings of the National Academy of Sciences of the United States of America* **2013**, *110*. https://doi.org/10.1073/pnas.1209186110.
(20) Wei, C.; Yu, C.; Li, S.; Meng, J.; Li, T.; Cheng, J.; Pan, F.; Li, J. Easy-to-Operate Co-Flow Step Emulsification Device for Droplet Digital Polymerase Chain Reaction. *Anal. Chem.* **2022**, *94* (9), 3939–3947. https://doi.org/10.1021/acs.analchem.1c04983.
(21) Bonhomme, O. Étude de La Formation de Fibres En Microfluidique : Compétition Entre Mise En Forme et Gélification de Fluides Complexes Sous Écoulement. These de doctorat, Bordeaux 1, 2011. https://www.theses.fr/2011BOR14306 (accessed 2023-01-17).
(22) de Jesús-González, N. E.; Pérez de la Luz, A.; López-Lemus, J.; Alejandre, J. Effect of the Dielectric Constant on the Solubility of Acetone in Water. *J. Chem. Eng. Data* **2018**, *63* (5), 1170–1179. https://doi.org/10.1021/acs.jced.7b00573.
(23) Pedersen, J. S.; Gerstenberg, M. C. Scattering Form Factor of Block Copolymer Micelles. *Macromolecules* **1996**, *29* (4), 1363–1365. https://doi.org/10.1021/ma9512115.

General conclusion and perspectives

In this PhD project, we developed a microfluidic process allowing to obtain vesicles with low polydispersity and high reproducibility from the self-assembly of PEG-*b*-PTMC, for drug delivery application.

The optimization of microfluidic assisted self-assembly process was reported in Chapter II. The choice of aqueous solvent to be used was made in anticipation of *in vitro* / *vivo* assays. Phosphate buffer saline (PBS) and glucose solution, both at pH = 7.4 and 300 mOsm.L^{-1} were selected as mimicking biological conditions. Microfluidic process was developed in parallel with two organic solvents, DMSO and Acetone, both presenting low toxicity when present in small quantities. The removal of the organic solvent was done by evaporation for acetone and by dialysis via a solvent exchange between residual DMSO and a larger volume of PBS solution. Microfluidic settings, including organic/aqueous ratio, copolymer concentration and total flow rate, were studied to ensure the formation of monodisperse and reproductible suspension of vesicles. Copolymer concentration and total flow rate were identified as key parameters to vary vesicle diameter when DMSO/PBS were selected as organic/aqueous solvents. An increase of the hydrodynamic diameter was observed from 76 to 224 nm when the initial copolymer concentration was increased from 1 to 30 mg.mL^{-1}. Another increase of the size of vesicles was measured from 160 to 218 nm when the total flow rate was decreased from 1000 to 100 µL.min^{-1}. Nanoparticles were proven to be vesicles by multi-angle light scattering and cryo-TEM analysis. This ability to vary vesicle diameter without changing copolymer chemical composition and molar mass offers unique and powerful tool to study the influence of vesicle size in biodistribution evaluation.

Loading capacity of well-defined PEG-*b*-PTMC polymersomes was studied in Chapter III through the loading of three molecules, Ganciclovir and Doxorubicin HCl, which are rather hydrophilic, and should be loaded in the aqueous core of vesicle, and Coumarin 6, a strongly hydrophobic molecule, which should be loaded in vesicle membrane. Passive loading was intended on three molecules by adding them in the organic solvent of pre-established microfluidic assisted-self-assembly of PEG_{22}-*b*-$PTMC_{51}$. After purification, loaded vesicles were disturbed to release the loading molecules for quantification by UV-vis spectroscopy and fluorescent spectroscopy. By measuring the UV absorbance of Ganciclovir (λ_{abs} = 252 nm) and the fluorescent emission of Doxorubicin HCl and Coumarin 6 (respectively λ_{Ex} = 481 nm and λ_{Em} = 592 nm for Doxorubicin HCl; λ_{Ex} = 468 nm and λ_{Em} = 514 nm for Coumarin 6), we systematically measured low drug contents (< 0.1%). To explain this low loading capacity, we hypothesized leakiness coming from the low thickness of membrane vesicle. To overcome this drawback, we intended to develop a PEG_{46}-*b*-$PTMC_{119}$ copolymer with a higher molar mass and consequently with a higher membrane thickness. This copolymer self-assembles into vesicles with a thicker membrane of 21 nm, compared to the membrane of 11.5 nm obtained for the vesicles formed with PEG_{22}-*b*-$PTMC_{51}$. Passive loading of free drugs into vesicles with thicker membranes did not result in a significantly higher loading rate, as no drug loading content exceeded 0.5%. Active loading of Ganciclovir using both pH and ionic gradients were performed on self-assembled PEG_{22}-*b*-$PTMC_{51}$ vesicles, resulting in the systematic rearrangement of vesicle into wormlike micelles. This rearrangement might be allowed by the use of DMSO as a plasticizer. Loading content could not be measured in that case. Such low loading content has been reported to be attributable to a specific self-assembly mechanism.

In Chapter IV, we studied self-assembly mechanism of PEG_{22}-*b*-$PTMC_{51}$ to better explain this lower loading results. Literature reports two main self-assembly mechanism. The first one proposes that free copolymer chains start to self-assemble into spherical micelles, which evolve into worm-like micelles that flatten and close up to form vesicles. This mechanism involves the possibility to load free molecules present in the surrounding medium and consequently, reasonable levels of encapsulation of hydrophilic molecules should be expected. In the second mechanism, the micelles that were obtained in the first stage evolve into swollen micelles, which then restructure into vesicles. This mechanism is expected to prevent loading of high levels of hydrophilic molecules. We intended to prove that PEG_{22}-*b*-$PTMC_{51}$ was following the second mechanism during it self-assembly. We first studied intermediate morphologies obtained with both organic solvents (DMSO and acetone) with their direct observation under confocal microscopy through water addition. Both organic solvents show similar behavior: first, a liquid-liquid phase separation in which copolymer is concentrated in coacervate droplets appears. Droplets coalesce up to a certain water content and budding is then observed at the surface of the droplets. System seems to remain kinetically trapped at this stage for experiment involving DMSO as an organic solvent. When acetone was used as organic solvent, vesicles were formed and spontaneously detached from the coacervate surface. Study was carried on with *in operando* monitoring of X-Ray measurements in a microfluidic assisted self-assembly system. A co-flow set up was home made to allow X-Ray measurement during flow running. Both DMSO and Acetone were used as organic solvents and flow rate parameters were used to allow the observation of phenomena happening during or after interdiffusion of solvents. Fly scans were measured along the capillary width at 3 heights of the capillary and signals were analyzed. In the Acetone experiment, vesicular objects were detected from the initial measurement, suggesting that the co-flow setup or flow parameters were not optimized for observing the initial stages of self-assembly. However, further analysis along the capillary revealed a transition in morphology from vesicles to elongated micelles, which is difficult to explain. Conversely, the analysis of the DMSO experiment highlighted a problem of water climbing in the organic capillary, leading to premature self-assembly before reaching the observable area. Consequently, it is challenging to draw a definitive conclusion regarding the self-assembly mechanism.

Despite low loading content, vesicles ready to use for *in vitro* / *in vivo* experiments with a precise size control remain an interesting tool for the evaluation of the impact of nanoparticle size in biological conditions and literature reported examples of studies on nanoparticle size affecting biodistribution. For instance, Kaga *et al.* reported the impact of polymeric nanoparticle size on biodistribution. In this case, poly(glycidyl methacrylate)-*b*-poly(oligo(ethylene glycol) methyl ether methacrylate)-*b*-polystyrene (PGMA-*b*-POEGMA-*b*-PS) nanoparticles of different size are obtained by modifying polystyrene chain length.[1] This study present a higher accumulation of smaller particle into tumor than bigger particles. He *et al.* reports a study on carboxymethyl chitosan grafted NPs (CMCNP) and chitosan hydrochloride grafted NPs (CHNP). NPs were prepared through grafting polymerization of methyl methacrylate (MMA) onto chitosan derivatives, varying amount of MMA, CMC and CH used to obtain NPs of different size (150 to 500 nm).[2] Study reports that NPs of 150 nm tend to accumulate more efficiently in tumors than bigger NPs. In most articles that evaluate the influence of nanoparticle size on biodistribution properties, a bias exists by varying the type of copolymer or the molecular weight. Here, we propose chemically identical models of vesicles of different diameters, thus eliminating the impact of any parameter other than vesicle size on biodistribution.

While the impact of nanoparticle size on biodistribution could be a potential field of application for this project, the primary fields of interest are the impact of polymersome size on bioconjugation and drug release control. Both of these aspects were part of the larger "TEPEE" project in which this doctoral project is involved. Human cytomegalovirus (HCMV) causes serious illness and high mortality

in immunocompromised hosts and when Ganciclovir is administrated in free state, limited efficacy and toxic side effects occur. Therefore, there is a need for more efficient treatments to combat this virus and the GCV encapsulation inside polymersomes, which can induce local delivery of this drug near the infection site through a control of the drug release in space and time, could be a potential strategy (Figure 1). First attempts of the encapsulation of Ganciclovir in PEG-*b*-PTMC polymersomes have thus been done and detailed in this manuscript. Controlled drug release over time will be ensured by polymersome membrane rupture by light-induced osmotic shock. Photo-cleavable molecule will be encapsulated in polymersomes to induce hypotonic shock under light radiation. Matthieu Kamierzac PhD project is dedicated to the synthesis of photo-cleavable molecules under infrared to visible wavelength. Photo-cleavable molecule sensitive to more energetic wavelength have already been developed[3] but the use of such radiation in human body might induce side effects[4–6]. Here we aim at using harmless radiation by synthesizing Rhodamine and Squaraine derivatives sensitive to IR-Visible radiations. Controlled release of the drug according to its location in the human body will be provided by Tcell-polymersomes conjugation. Recently, a subpopulation of T-cells called γδ T-Cell have been proven to recognize CMV and thus could migrate near the infected area[7–9]. Using GlycoMetabolic Engineering, azide functional group will be expressed at the surface of γδ TCell[10–12]. On the other hand, dibenzocyclooctyne functionalized polymersomes will be produced to induce strain promoted alkyne-azide cycloaddition (SPAAC), also called Cu-free click reaction, in contact with functionalized cells.[13–15] Selma Cornillot-Clément PhD project will be dedicated to the optimization of GlycoMetabolic Engineering on γδ TCell, vesicle-Tcell conjugation and Tcell behavior evaluation *in vitro* and *in vivo*. To enable the tracking of vesicles *in vivo* and *in vitro*, the functionalization of PEG-b-PTMC with Cyanine 5.5, a fluorescent dye with an excitation peak at 683 nm and an emission peak at 703 nm, was performed. PEG-*b*-PTMC-Cy5.5 was obtained via the synthesis of PEG-*b*-PTMC-COOH. PEG-*b*-PTMC Copolymer was also functionalized with DBCO to enable click chemistry and DBCO-PEG-*b*-PTMC was synthesized via NH_2-PEG-*b*-PTMC intermediate. Both functionalized copolymers were synthetized by Pierre Lalanne. These functionalized copolymers were used in small amounts as supplementary building blocks of vesicles, with the unfunctionalized PEG-b-PTMC remaining the major building block, as shown in Figure 2.

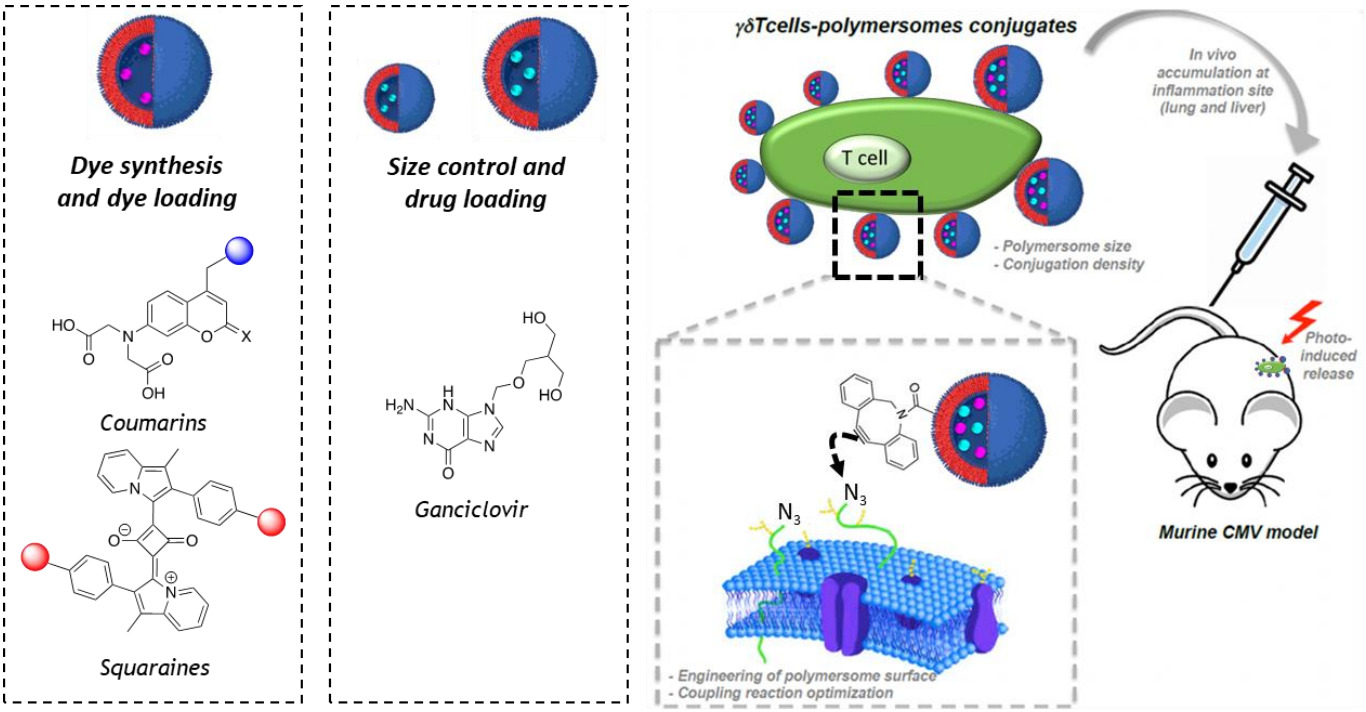

Figure 1: *Overview of the three axes of TEPEE project: Photo-sensitive dye synthesis and loading in polymersomes, size control and drug loading in polymersomes and γδT Cells-polymersomes conjugates towards the controlled drug release of Ganciclovir.*

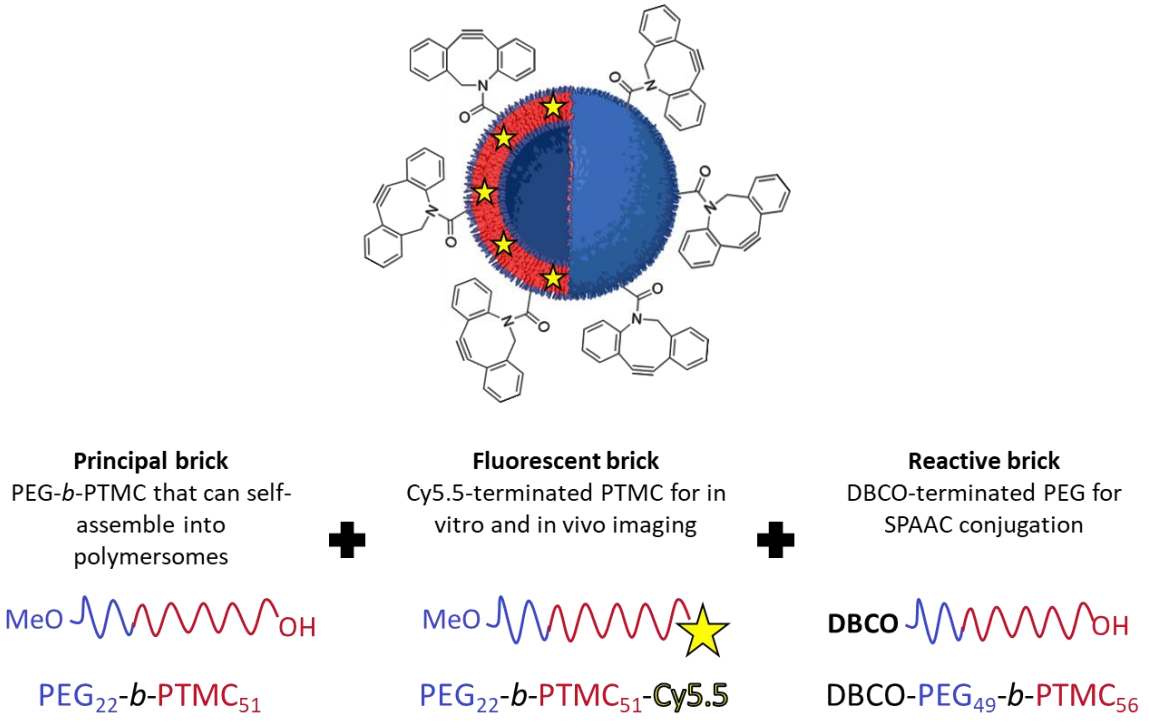

Figure 2*: Schematic representation of functionalized PEG-b-PTMC vesicle with Cyanine 5.5 fluorescent probe and DBCO functions for alkyne-azide cycloaddition and the associated functionalized* PEG_{22}*-b-*$PTMC_{51}$*-Cy5.5 and DBCO-*PEG_{49}*-b-*$PTMC_{56}$ *functionalized copolymers.*

Preliminary results on functionalized vesicle formulation

Microfluidic-assisted self-assembly of PEG_{22}-*b*-$PTMC_{51}$ has been optimized along this PhD project to obtain monodisperse and reproducible vesicles, ready to use for in *vitro / in vivo* assays, with the supplementary interest of being able to tune the size of formulated vesicles. Preliminary experiments were performed to ensure that the use of functionalized copolymer PEG_{22}-*b*-$PTMC_{51}$-Cy5.5 and DBCO-PEG_{22}-*b*-$PTMC_{56}$ was not disturbing copolymer self-assembly into vesicles.

Microfluidic experiments were run as optimized: ratio of DMSO/PBS was kept at 20/80% v/v, total flow rate kept at 1000 µL.min^{-1} and a solution of copolymer at 10 mg.mL^{-1} in DMSO was used. However, composition of copolymer solution was changed as follow:

- 99 %wt PEG_{22}-*b*-$PTMC_{51}$ + 1 %wt PEG_{22}-*b*-$PTMC_{51}$-Cy5.5
- 99 %wt PEG_{22}-*b*-$PTMC_{51}$ + 1 %wt DBCO-PEG_{49}-*b*-$PTMC_{56}$
- 95 %wt PEG_{22}-*b*-$PTMC_{51}$ + 5 %wt DBCO-PEG_{49}-*b*-$PTMC_{56}$

Samples collected at the output of microfluidic were purified by dialysis and characterized by DLS with an angle of 90° to measure hydrodynamic radius and polydispersity index (PDI), as previously done. Table 1 compares results obtained using functionalized chains to results obtained from pure PEG_{22}-*b*-$PTMC_{51}$ vesicles, produced in the same conditions. No drastic change was observed on vesicle size or polydispersity index. Consequently, the self-assembly of functionalized PEG-b-PTMC vesicles is supposed to be unchanged.

Table 1: *Hydrodynamic diameter D_H and polydispersity index (PDI) acquisitions obtained by DLS 90° after self-assembly of PEG_{22}-b-$PTMC_{51}$, PEG_{22}-b-$PTMC_{51}$-Cy5.5 and DBCO-PEG_{49}-b-$PTMC_{56}$ vesicles. Purification performed by dialysis with a membrane of 25 kDa, with 3 bath changes (of 2L each) in 24h. The indicated values are the average of three assays with the calculated standard deviation for pure PEG_{22}-b-$PTMC_{51}$ vesicles. Other values are obtained from a unique sample.*

Sample	D_H (nm)	PDI
PEG_{22}-*b*-$PTMC_{51}$ with no functionalization	161 ± 4	0.138 ± 0.015
+ 1 %wt Cy5.5 functionalized block copolymer	160	0.122
+ 1 %wt DBCO functionalized block copolymer	149	0.119
5 %wt DBCO functionalized block copolymer	161	0.133

However, a change in the correlation function was observed for vesicle functionalized with Cyanine 5.5, as shown in Figure 3. The reduction in amplitude of the correlation function can be attributed to the partial absorption of light beam from the DLS laser (λ= 633 nm) by the fluorescence dye Cyanine 5.5 (λabs = 630 – 680 nm). Importantly, this absorption did not affect the calculation of the hydrodynamic radius or the polydispersity index.

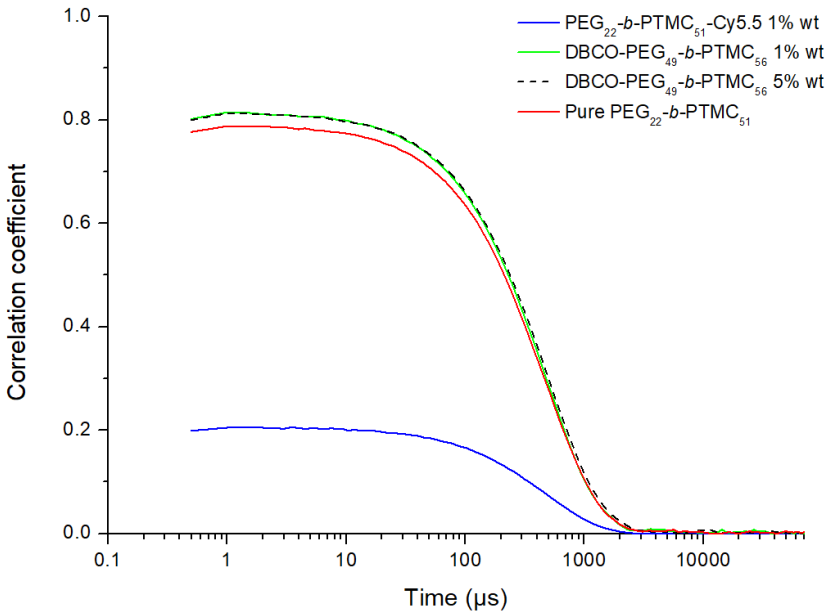

Figure 3: *Correlation function given by DLS 90° analysis of vesicles made of pure PEG_{22}-b-$PTMC_{51}$ (red line), with 1 %wt of PEG_{22}-b-$PTMC_{51}$-Cy5.5 (blue line), 1 %wt of DBCO-PEG_{49}-b-$PTMC_{56}$ (green line) or 5 %wt of DBCO-PEG_{49}-b-$PTMC_{56}$ (dotted line).*

TEM experiments were performed on samples containing 1 %wt of PEG_{22}-*b*-$PTMC_{51}$-Cy5.5 and 5 %wt of DBCO-PEG_{49}-*b*-$PTMC_{56}$ (Figure 4). As previously described by using Samarium Acetate as staining agent, TEM analyses performed on object formulated with pure PEG_{22}-*b*-$PTMC_{51}$ appears as full spheres (Ch2.1.3). Those full sphere has been proven to be vesicles by Cryo-TEM. As samples formulated with 1 %wt of PEG_{22}-*b*-$PTMC_{51}$-Cy5.5 and 5 %wt of DBCO-PEG_{49}-*b*-$PTMC_{56}$ showed the same characteristics in TEM (observation of spheres), we assumed that microfluidic-assisted self-assembly of PEG-b-PTMC into vesicles is maintained even with the addition of 1 %wt of PEG_{22}-*b*-$PTMC_{51}$-Cy5.5 or up to 5 %wt of DBCO-PEG_{49}-*b*-$PTMC_{56}$ (Figure 4).

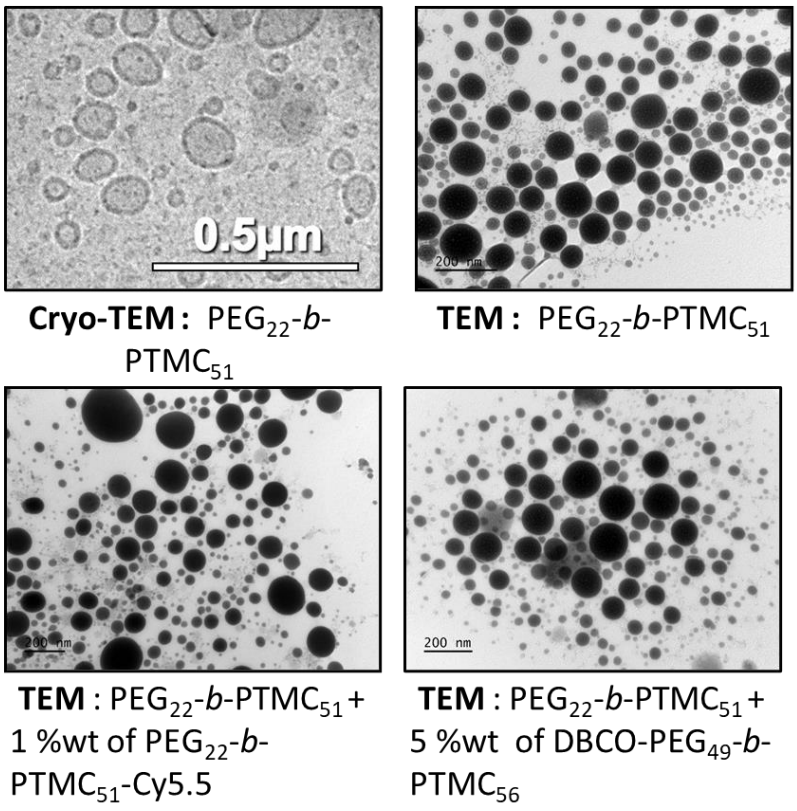

Figure 4: *Cryo-TEM representation of vesicles made of pure PEG_{22}-b-$PTMC_{51}$. TEM representations of vesicles made of pure PEG_{22}-b-$PTMC_{51}$, with 1 %wt of PEG_{22}-b-$PTMC_{51}$-Cy5.5 or 5 %wt of DBCO-PEG_{49}-b-$PTMC_{56}$.*

As functionalized PEG-*b*-PTMC-Cy5.5 can be added in PEG-*b*-PTMC self-assembly process without disturbing vesicle formation, we can easily produce fluorescent vesicles ready to use for *in vitro* / *in vivo* experiment. A collaboration with Dr Magali Gary-Bobo (Institut des Biomolécules Max Mousseron IBMM, Univ. Montpellier) is currently in progress to study impact of vesicle size biodistribution in Zebra fish larvae model.

Preliminary results on DBCO function availability on vesicle surface

Availability of DBCO functions at the surface of polymersomes will be determinant for polymersomes-cell conjugation. To demonstrate the availability of this function, vesicles were formulated with either 1%wt or 5%wt of DBCO-PEG_{49}-b-$PTMC_{56}$ and exposed to fluorescein azide to induce strain promoted alkyne-azide cycloaddition. Briefly, 100 µL of vesicle suspension diluted at 1 $mg.mL^{-1}$ were incubated for 2 h with 100 µL of fluorescein-azide solution at 2 µM. The suspension was then purified by dialysis against a large volume of PBS in order to remove the molecules of fluorescein-azide which would not have reacted with the vesicles. Dialysis bath changes were made until the fluorescence of the dialysis bath returned to nearly zero. The fluorescence emission of the free fluorescein-azide compound was measured in PBS at different concentrations, with an excitation wavelength of λ_{Ex} = 494 nm. A dependence of fluorescein-azide concentration on fluorescence emission intensity measured at λ_{Em} = 518 nm was observed; with the following linear relation:

$$Fluo_{518nm} = 30.3 \times 10^9 \times [Fluoresceine\ Azide] \qquad P.1$$

where $[Fluoresceine\ Azide]$ is the concentration of fluorescein-azide (in $mol.L^{-1}$) in PBS.

The fluorescence emission of vesicles suspension after purification were then measured in the same condition, as shown in Figure 5. According to the calibration curve *P.1*, the concentration of Fluoresceine Azide remained on the surface of vesicles can be calculated (Table 2).

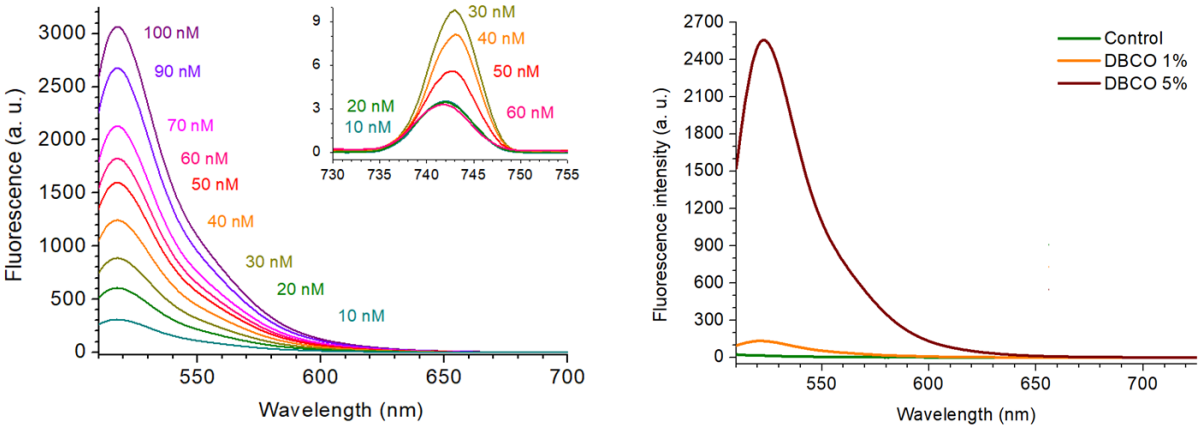

Figure 5: *Fluoresceine-azide emission measured by fluorescent spectroscopy when excited at 494 nm for different Fluoresceine-azide concentration (from 10 nM to 10 nM) in PBS solution (left). Fluorescence emission measured in the same conditions for vesicle suspension (right) with no functionalization (green line), with a presence of 1 %wt of DBCO-PEG$_{49}$-b-PTMC$_{56}$ (orange line) or 5 %wt of DBCO-PEG$_{49}$-b-PTMC$_{56}$. Maximum emission is measured at 518 nm.*

The concentration of copolymer in the suspension of PEG-*b*-PTMC vesicles, with and without DBCO-PEG$_{49}$-b-PTMC$_{56}$ (in quantity of 1 or 5 %wt), was estimated after dialysis by measuring the derived count rate (DCR) with DLS. The DCR values were dependent on the copolymer concentration, and the following calibration curves were obtained::

$$DCR_{PEG-b-PTMC} = 5821 \times [copolymer] - 263 \qquad P.2$$

$$R^2 = 0.9875$$

$$DCR_{1\%\,DBCO} = 3502 \times [copolymer] - 160 \qquad P.3$$

$$R^2 = 0.942$$

$$DCR_{5\%\,DBCO} = 3218 \times [copolymer] - 205 \qquad P.4$$

$$R^2 = 0.981$$

DCR is expressed in kcps and copolymer concentration in g.L^{-1}.

Table 2 shows the estimated number of fluorescein-azide per gram of copolymer. These results demonstrate that the use of DBCO-functionalized copolymer enabled successful conjugation of fluorescein-azide on vesicles. Furthermore, increasing the number of DBCO-functionalized copolymer chains led to a higher degree of fluorescein-azide conjugation. However, the lack of linearity in this phenomenon might be due to either DBCO functionalization yield or an uneven distribution of functionalized copolymer chain between inner and outer layer of the bilayer membrane of the polymersome.

Table 2: *Copolymer concentration obtained via estimation using DCR measurement with DLS 90°, fluorescein-azide concentration obtained using emission measurement (λ_{Ex} = 494 nm, λ_{Em} = 518 nm). Both measurement refers to pre-established calibration curves. Fluorescein-azide concentration normalized by copolymer concentration deducted from measurements.*

Sample	Copolymer concentration (g/L)	Fluorescein-azide concentration (nM)	Fluorescein-azide concentration normalized by copolymer concentration (nmol/g)
Control	0.18	0.28	1.56
1% DBCO	0.202	4	19.8
5% DBCO	0.248	78.8	318

Further characterization of DBCO-PEG_{49}-*b*-$PTMC_{56}$ and vesicles formulated with DBCO-PEG_{49}-*b*-$PTMC_{56}$ is required using techniques such as Cryo-TEM, and fluorescence spectroscopy. However, the successful formulation of monodisperse vesicles expressing sufficient fluorescence and ready for *in vitro/in vivo* use has been demonstrated, enabling the evaluation of their conjugation to Tcells expressing azide functions on their surface.

References

(1) Kaga, S.; Truong, N. P.; Esser, L.; Senyschyn, D.; Sanyal, A.; Sanyal, R.; Quinn, J. F.; Davis, T. P.; Kaminskas, L. M.; Whittaker, M. R. Influence of Size and Shape on the Biodistribution of Nanoparticles Prepared by Polymerization-Induced Self-Assembly. *Biomacromolecules* **2017**, *18* (12), 3963–3970. https://doi.org/10.1021/acs.biomac.7b00995.

(2) He, C.; Hu, Y.; Yin, L.; Tang, C.; Yin, C. Effects of Particle Size and Surface Charge on Cellular Uptake and Biodistribution of Polymeric Nanoparticles. *Biomaterials* **2010**, *31* (13), 3657–3666. https://doi.org/10.1016/j.biomaterials.2010.01.065.

(3) Peyret, A.; Ibarboure, E.; Tron, A.; Beauté, L.; Rust, R.; Sandre, O.; McClenaghan, N. D.; Lecommandoux, S. Polymersome Popping by Light-Induced Osmotic Shock under Temporal, Spatial, and Spectral Control. *Angew Chem Int Ed Engl* **2017**, *56* (6), 1566–1570. https://doi.org/10.1002/anie.201609231.

(4) Weinkauf, B.; Rukwied, R.; Quiding, H.; Dahllund, L.; Johansson, P.; Schmelz, M. Local Gene Expression Changes after UV-Irradiation of Human Skin. *PLOS ONE* **2012**, *7* (6), e39411. https://doi.org/10.1371/journal.pone.0039411.

(5) Baadsgaard, O. In Vivo Ultraviolet Irradiation of Human Skin Results in Profound Perturbation of the Immune System: Relevance to Ultraviolet-Induced Skin Cancer. *Archives of Dermatology* **1991**, *127* (1), 99–109. https://doi.org/10.1001/archderm.1991.01680010109019.

(6) Wang, Z.; Boudjelal, M.; Kang, S.; Voorhees, J. J.; Fisher, G. J. Ultraviolet Irradiation of Human Skin Causes Functional Vitamin A Deficiency, Preventable by All-Trans Retinoic Acid Pre-Treatment. *Nat Med* **1999**, *5* (4), 418–422. https://doi.org/10.1038/7417.

(7) Khairallah, C.; Déchanet-Merville, J.; Capone, M. Γδ T Cell-Mediated Immunity to Cytomegalovirus Infection. *Front Immunol* **2017**, *8*, 105. https://doi.org/10.3389/fimmu.2017.00105.

(8) Khairallah, C.; Netzer, S.; Villacreces, A.; Juzan, M.; Rousseau, B.; Dulanto, S.; Giese, A.; Costet, P.; Praloran, V.; Moreau, J.-F.; Dubus, P.; Vermijlen, D.; Déchanet-Merville, J.; Capone, M. Γδ T Cells Confer Protection against Murine Cytomegalovirus (MCMV). *PLoS Pathog* **2015**, *11* (3), e1004702. https://doi.org/10.1371/journal.ppat.1004702.

(9) Kaminski, H.; Marsères, G.; Cosentino, A.; Guerville, F.; Pitard, V.; Fournié, J.-J.; Merville, P.; Déchanet-Merville, J.; Couzi, L. Understanding Human Γδ T Cell Biology toward a Better Management of Cytomegalovirus Infection. *Immunol Rev* **2020**, *298* (1), 264–288. https://doi.org/10.1111/imr.12922.

(10) Pan, H.; Li, P.; Li, G.; Li, W.; Hu, B.; He, H.; Chen, Z.; Wang, F.; Liu, L.; Gong, Y.; Han, Y.; Luo, Y.; Zheng, M.; Ma, Y.; Cai, L.; Jin, Y. Glycometabolic Bioorthogonal Chemistry-Guided Viral Transduction for Robust Human T Cell Engineering. *Advanced Functional Materials* **2019**, *29* (22), 1807528. https://doi.org/10.1002/adfm.201807528.

(11) Cioce, A.; Bineva-Todd, G.; Agbay, A. J.; Choi, J.; Wood, T. M.; Debets, M. F.; Browne, W. M.; Douglas, H. L.; Roustan, C.; Tastan, O. Y.; Kjaer, S.; Bush, J. T.; Bertozzi, C. R.; Schumann, B. Optimization of Metabolic Oligosaccharide Engineering with Ac4GalNAlk and Ac4GlcNAlk by an Engineered Pyrophosphorylase. *ACS Chem. Biol.* **2021**, *16* (10), 1961–1967. https://doi.org/10.1021/acschembio.1c00034.

(12) Saxon, E.; Bertozzi, C. R. Cell Surface Engineering by a Modified Staudinger Reaction. *Science* **2000**, *287* (5460), 2007–2010. https://doi.org/10.1126/science.287.5460.2007.

(13) Idiago-López, J.; Moreno-Antolín, E.; Eceiza, M.; Aizpurua, J. M.; Grazú, V.; de la Fuente, J. M.; Fratila, R. M. From Bench to Cell: A Roadmap for Assessing the Bioorthogonal "Click" Reactivity of Magnetic Nanoparticles for Cell Surface Engineering. *Bioconjugate Chem.* **2022**, *33* (9), 1620–1633. https://doi.org/10.1021/acs.bioconjchem.2c00230.

(14) Kim, E.; Koo, H. Biomedical Applications of Copper-Free Click Chemistry: In Vitro , in Vivo , and Ex Vivo. *Chemical Science* **2019**, *10* (34), 7835–7851. https://doi.org/10.1039/C9SC03368H.

(15) Tomás, R. M. F.; Gibson, M. I. Optimization and Stability of Cell–Polymer Hybrids Obtained by "Clicking" Synthetic Polymers to Metabolically Labeled Cell Surface Glycans. *Biomacromolecules* **2019**, *20* (7), 2726–2736. https://doi.org/10.1021/acs.biomac.9b00478.

Résumé de thèse en français

Au cours des dernières décennies, le domaine de l'administration des médicaments a connu des progrès considérables dans l'amélioration de la précision et de l'efficacité thérapeutiques pour le traitement de diverses maladies, grâce à la volonté de surmonter les limites des thérapies médicamenteuses conventionnelles en minimisant leurs effets secondaires. Dans ce contexte, les nanoparticules se sont avérées d'excellents candidats pour améliorer l'efficacité thérapeutique de nombreux médicaments, grâce à leur capacité à modifier la pharmacocinétique et la possibilité de contrôler leur biodistribution. Une stratégie prometteuse est l'utilisation de polymersomes comme nano-carrier. Les polymersomes sont issus de l'auto-assemblage de copolymères à blocs amphiphiles en vésicules, de structures similaires à celle des liposomes. Celles-ci offrent un large éventail d'avantages par rapport aux systèmes d'administration de médicaments conventionnels, ce qui en fait un domaine de recherche intéressant avec un potentiel important pour améliorer les résultats thérapeutiques. La conception et l'ingénierie des polymères offrent une plate-forme polyvalente pour l'encapsulation et l'administration d'un large éventail d'agents thérapeutiques, notamment de petites molécules, des peptides, des protéines et des acides nucléiques. En adaptant les propriétés physicochimiques des composants polymériques, tels que la composition du copolymère, la longueur de la chaîne, l'hydrophobicité et le changement de surface, les chercheurs peuvent contrôler avec précision leur taille, leur stabilité, leur capacité de chargement de médicament et leur cinétique de libération. Ces vésicules polymères biocompatibles ont l'avantage unique de pouvoir encapsuler des actifs hydrophiles et hydrophobes dans leur noyau aqueux interne ou leur membrane, respectivement. Cette dualité les rend adaptés à une large gamme d'applications en tant que système d'administration de médicaments. Ces structures peuvent également être modifiées avec un ligand de ciblage, tel que des anticorps ou des peptides, fournissant alors un contrôle spatial sur l'administration de médicaments en ciblant des lignées cellulaires, des tissus ou des organes spécifiques. Par ailleurs, en incorporant des éléments sensibles aux stimuli tels que des polymères sensibles au pH ou sensibles à la température, ces vésicules peuvent être adaptées pour fournir un contrôle spatio-temporel précis sur la libération d'actifs, permettant ainsi une administration de médicament spécifique au site et réduisant de surcroît le risque de toxicité systémique.

Dans ce contexte, ce projet de thèse vise à développer des vésicules encapsulant un actif, prêtes à l'emploi pour des essais *in vitro/in vivo* et fabriquées avec un copolymère à bloc biocompatible et biodégradable : poly(éthylène glycol)-bloc-poly(triméthylène carbonate) ou PEG-*b*-PTMC. La composition du copolymère à blocs a été choisie en sélectionnant le bloc PEG hydrophile pour sa biocompatibilité (le PEG est éliminé principalement par excrétion rénale) et aussi pour son effet furtif. En effet, lorsque les nanoparticules sont enrobées de PEG, les chaînes PEG hydrophiles à la surface des particules créent une couche hydratée, ou "brosse", qui peut gêner stériquement l'adsorption des protéines, en particulier les opsonines responsables de l'activation des macrophages. Cette « PEGylation » entraîne alors une diminution du taux d'absorption des particules par les cellules phagocytaires et une augmentation du temps de circulation, ce qui est favorable pour les applications d'administration de médicaments. D'autre part, le choix du bloc hydrophobe PTMC est gouverné par sa biodégradabilité. Dans le corps, le PTMC subit une hydrolyse ou une dégradation enzymatique conduisant à la formation de triméthylène glycol qui est ensuite métabolisé pour former de l'acide glycolique. Les produits de dégradation du PTMC sont considérés comme non toxiques pour le corps, ce qui fait du PTMC un matériau adapté aux applications biomédicales.

L'objectif principal de ce projet de thèse était d'évaluer le comportement d'auto-assemblage de deux copolymères PEG-*b*-PTMC, à savoir PEG_{22}-*b*-$PTMC_{51}$ et PEG_{46}-*b*-$PTMC_{119}$, dont il a

été démontré qu'ils forment préférentiellement des vésicules. L'utilisation de la "PEGylation" permet d'échapper au processus d'opsonisation, mais la taille des nanoparticules reste un paramètre clé à contrôler et la taille peut influencer leur temps de circulation, leur absorption hépatique et rénale et leur accumulation dans les tissus. Parmi tous les procédés existant pour la formulation de vésicules, et en particulier de polymersomes, la microfluidique a été largement reconnue comme un système idéal pour produire des vésicules bien définies avec une reproductibilité élevée, en raison de sa capacité à fournir un accès facile à des paramètres de procédé qui peuvent être finement réglés pour contrôler avec précision la taille des vésicules et d'autres caractéristiques importantes. Dans le but de produire des vésicules à faible dispersité, nous avons utilisé l'auto-assemblage assisté par microfluidique pour produire et ajuster la taille des vésicules de PEG-*b*-PTMC.

Un autre objectif de ce projet de thèse est d'améliorer notre compréhension des mécanismes d'encapsulation des molécules à l'intérieur des polymersomes. Concernant l'encapsulation de l'actif, une des caractéristiques importantes à prendre en compte est la préférence de l'actif pour les milieux aqueux ou organiques, donnée par le coefficient de partage octanol/eau (log P). Cette valeur de log P pourrait être un premier paramètre à considérer pour prédire si le médicament ira dans le noyau hydrophile ou la membrane hydrophobe de la vésicule, ce qui sera évalué au cours de ce projet de doctorat. Une approche plus précise serait d'utiliser les paramètres de Hansen du polymère et des médicaments, que nous n'avons pas considérés, ici, dans une première approche.

Enfin, le troisième objectif de ce projet de thèse est de tirer parti de l'utilisation des procédés microfluidiques pour approfondir la compréhension du mécanisme d'auto-assemblage du PEG-*b*-PTMC en vésicules. Cela sera réalisé grâce à des mesures de diffusion dynamique de la lumière, de microscopie confocale et de mesures *in operando* utilisant des techniques de rayons X. Ainsi, cet objectif final nous permettra d'optimiser les conditions d'encapsulation des médicaments en améliorant notre compréhension de la transition des copolymères à blocs de l'état de nucléation à l'état de croissance, conduisant *in fine* à la formation de vésicules.

Ce manuscrit de thèse est organisé en cinq chapitres. Le premier chapitre sera consacré à un aperçu de la littérature sur les stratégies actuelles employées pour produire des vésicules et contrôler leur diamètre hydrodynamique. Un aperçu des stratégies d'encapsulation de médicaments ainsi que des exemples détaillés sur la façon de contrôler spatio-temporellement la libération de médicaments à partir de polymersomes sont compilés. Le chapitre II rassemble l'optimisation du processus d'auto-assemblage assisté par microfluidique des vésicules de PEG-*b*-PTMC . Les paramètres influençant l'auto-assemblage des copolymères à blocs tels que le choix de la puce microfluidique, la concentration en copolymère et le débit total seront discutés. Dans le chapitre III, trois molécules présentant une hydrophilie différente ont été choisies comme modèles de principe actif : le Ganciclovir un antiviral hydrophile utilisé contre les infections humaines à cytomégalovirus ; la Doxorubicine HCl, en tant que médicament chimiothérapeutique amphiphile ; et la Coumarine 6, une sonde fluorescente hydrophobe qui jouera le rôle de médicament hydrophobe. Des encapsulations passives et actives seront envisagées, comparant l'efficacité d'encapsulation de vésicules présentant différentes épaisseurs de membrane. Le chapitre IV présente les résultats obtenus à partir des observations en microscopie confocale de l'auto-assemblage des copolymères, ainsi que des mesures de rayons X effectuées sur le système de co-écoulement *in operando* pour l'auto-assemblage des copolymères, au Synchrotron Soleil. Enfin, différentes perspectives de ce projet de recherche doctorale seront présentées : La première étant l'utilisation de vésicules fluorescentes de PEG-*b*-PTMC comme modèle pour l'évaluation de la biodistribution des polymersomes. La seconde perspective d'utilisation des vésicules de PEG-*b*-PTMC est leur fonctionnalisation de surface pour créer des conjugués de cellules polymériques avec des cellules immunitaires, dans le but d'améliorer la délivrance locale de Ganciclovir en cas d'infection à cytomégalovirus.

Chapitre II : Auto-assemblage assisté par microfluidique de polymersomes : méthode avec contrôle de taille pour la production de polymersomes « prêts à l'emploi » pour des expériences in vitro/vivo

Dans le chapitre I, nous avons exploré plusieurs voies d'auto-assemblage du PEG_{22}-*b*-$PTMC_{51}$ en vésicules, également appelées polymersomes, de taille ajustable, dans des conditions leur permettant d'être prêts à l'emploi pour des expériences *in vivo/in vitro.*

Nous avons d'abord prouvé l'importance de choisir un tampon aqueux de type physiologique lors de l'auto-assemblage des vésicules. La sensibilité des polymersomes à la variation de pression osmotique a été démontrée par une diminution significative de leur taille lorsqu'un échange de solvant externe est effectué, dans le cas de l'échange de l'eau pure contre un milieu mimant les conditions physiologiques, passant de 65 nm dans l'eau à 35 nm dans les conditions physiologiques. Cette transformation due au choc hypertonique pourrait conduire à un effet de libération incontrôlé si des vésicules chargées d'actif sont placées dans des fluides biologiques présentant des disparités d'osmolarité.

Nous avons réussi à obtenir des polymersomes préparés dans un tampon proche des conditions physiologiques (pH = 7,4, 300 mOsm.L-1) qui garantiront l'intégrité des polymersomes lors de leur administration. Le choix des solvants organiques pour l'auto-assemblage des polymersomes a été évalué comme étant le plus biocompatible, par une sélection de solvants organiques présents sur la liste des solvants de classe 3 par Q3C-Tables et List Guidance for Industry de la FDA, ce qui signifie une faible toxicité lorsqu'ils sont présents en petites quantités.

La teneur en eau critique pour induire l'auto-assemblage (CWC) du PEG_{22}-*b*-$PTMC_{51}$ a été mesurée par diffusion de la lumière pour les deux solvants organiques (acétone et DMSO) et a été utilisée pour optimiser un rapport solvant organique/aqueux minimal afin d'assurer la formation de vésicules pendant tous les processus de formulation des expériences microfluidiques. La CWC dans le DMSO a été mesurée à environ 11 % vol de solvant aqueux, en fonction de la concentration du copolymère, et la CWC dans l'acétone a été mesurée à environ 20 % vol de solvant aqueux, en accord avec les valeurs théoriques des paramètres de solubilité Hildebrand.

Afin de développer une méthode microfluidique pour produire des polymersomes avec la plus grande fiabilité et reproductibilité, le rapport solvant aqueux/organique optimal a été évalué pour les deux paires de solvants : acétone/glucose et paire DMSO/PBS. On a profité de cette étude pour comparer deux puces microfluidiques avec un processus de mélange rapide (Micromixer et puce Herringbone). Les deux designs de puces microfluidiques ont montré un comportement similaire, avec une formation de vésicules ayant une faible valeur pour l'indice de polydispersité dans les conditions évaluées.

Nous avons modifié les paramètres de notre procédé microfluidique pour étudier leur influence sur la formation des polymersomes de PEG_{22}-*b*-$PTMC_{51}$: influence du choix du solvant organique, du rapport solvant aqueux/organique, de la concentration initiale en PEG_{22}-*b*-$PTMC_{51}$ et du débit total. Concernant le choix du solvant organique, aucun impact n'a été observé sur la formation des polymersomes ; le DMSO et l'acétone conduisent à la formation de vésicules avec une faible valeur pour le PDI. L'étude sur la variation du rapport organique/aqueux ne montre également aucun effet sur la formation de vésicules. Concernant l'influence de la concentration en copolymère, des expériences ont été réalisées avec du DMSO/PBS comme solvant aqueux/organique et une augmentation de la taille des nanoparticules obtenues a été observée en fonction de la concentration en copolymère, avec des diamètres allant de 76 à 224 nm avec une gamme de concentration initiale en copolymère de 1 à 30 $mg.mL^{-1}$(Figure 1). Concernant l'impact du débit total sur l'auto-assemblage du copolymère, une augmentation de la taille des vésicules est observée lorsque le débit total est diminué, de 160 nm pour le débit le plus élevé (1000 µL.min-1), à 242 nm pour la plus basse (50 µL.min-1) (Figure 2). L'indice de polydispersité qui reste inférieur à PDI = 0,15 pour toutes les conditions, met en évidence l'homogénéité de la population de nanoparticules, dont il a été prouvé qu'elle conservait une forme vésiculaire en utilisant la diffusion de la lumière multi-angle et les caractérisations Cryo-TEM (Figure 3 et 4).

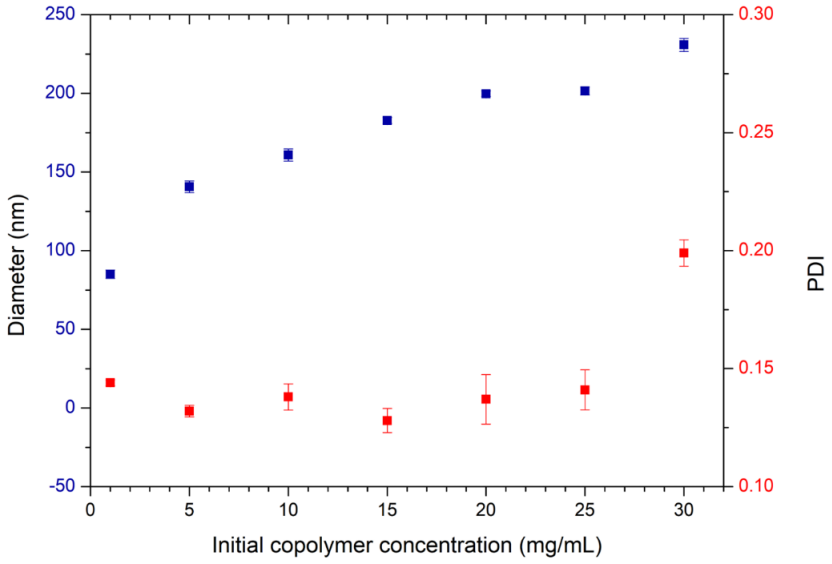

Figure 1 : Diamètre hydrodynamique et PDI mesurés par DLS 90° pour les nanoparticules de PEG22-b-PTMC51 purifiées, formulées en faisant varier la concentration initiale de copolymère dans le solvant DMSO, en fixant le ratio de solvant DMSO/PBS à 20/80 % vol. Chaque valeur correspond à la valeur de taille moyenne de 3 expériences et les barres d'erreur correspondent à l'écart type.

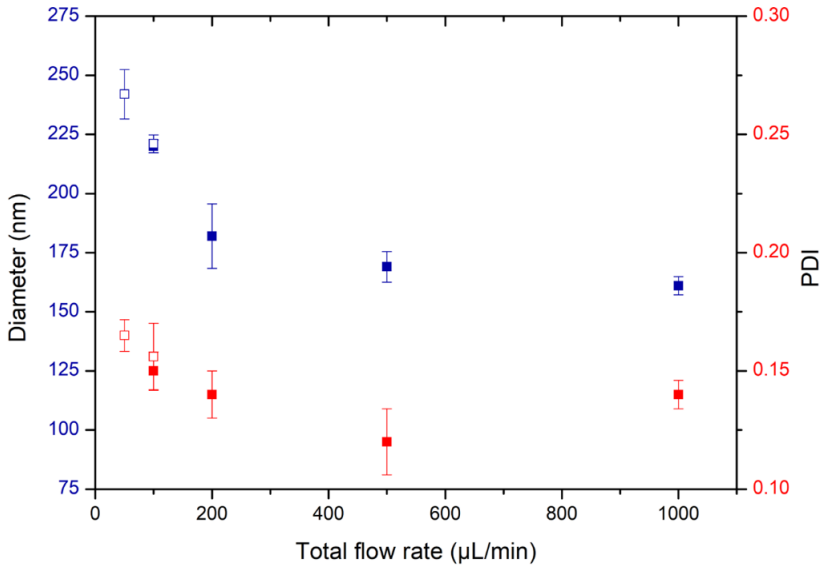

Figure 2 : *Diamètre hydrodynamique et PDI mesurés par DLS 90° pour des nanoparticules de PEG_{22}-b-$PTMC_{51}$ purifiées, formulées en faisant varier le débit total de solvant, fixant un débit de 100 à 1000 µL.min-1. Chaque valeur correspond à la valeur de taille moyenne de 3 expériences et les barres d'erreur correspondent à l'écart type. Les carrés pleins représentent les expériences réalisées avec les pompes Mitos et les vides avec le pousse-seringue Harvard.*

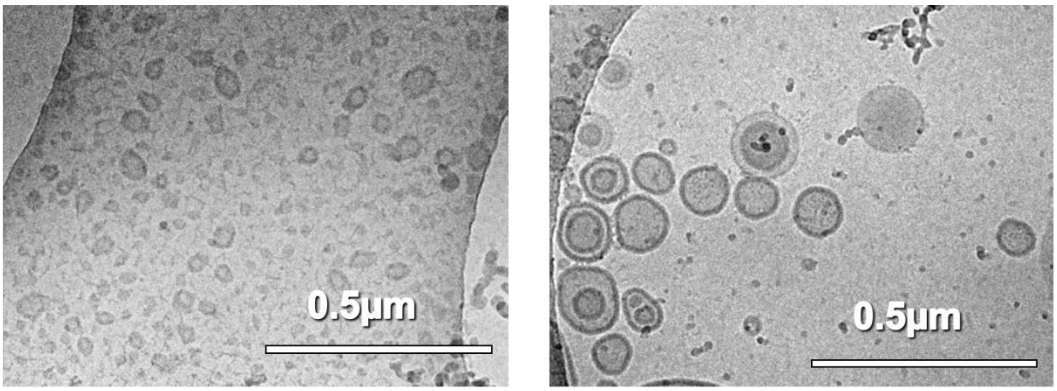

Figure 3 : *Images Cryo-TEM représentatives pour différentes conditions de formulation de polymersomes PEG_{22}-b-$PTMC_{51}$ lors de l'utilisation de DMSO/PBS comme solvant organique/aqueux avec deux concentrations initiales extrêmes de copolymère de 1 mg.mL^{-1} (gauche) et 30 mg. mL^{-1} (à droite). La barre d'échelle correspond à 0,5 µm.*

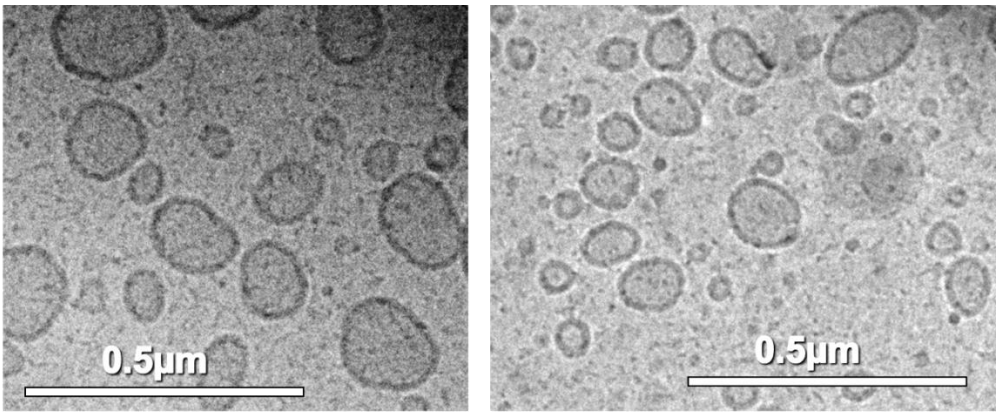

***Figure 4** : Images TEM représentatives pour différentes conditions de formulation de polymersomes PEG_{22}-b-$PTMC_{51}$ lors de l'utilisation de DMSO/PBS comme solvant organique/aqueux avec deux débits initiaux extrêmes de 100 µL.min^{-1} (gauche) et 1000 µL.min^{-1} (droite). La barre d'échelle correspond à 0,5 µm.*

Pour les vésicules formulées avec de l'acétone/glucose comme solvant organique/aqueux, aucun impact n'a été observé sur la taille des vésicules avec la variation de la concentration en copolymère ou du débit total. Cependant, notre étude a mis en évidence que dans le cas de ce couple de solvant organique/aqueux, le système microfluidique ne permettait que l'étape de nucléation, l'étape de croissance des nanoparticules se produisant lors de l'évaporation de l'acétone. Ainsi, le paramètre clé pour régler la taille des vésicules, lorsque l'on travaille avec de l'acétone/glucose à 60/40 %vol en auto-assemblage assisté microfluidique, est enfait le temps d'évaporation de l'acétone. Par exemple, une évaporation rapide (30 min) conduit à des polymersomes d'une taille de 140 nm alors qu'une évaporation lente (4h15) conduit à une taille de 280 nm.

En plus de fournir un processus hautement reproductible pour la formation de polymères en terme de taille et d'indice de polydispersité, l'auto-assemblage assisté par microfluidique donne accès à des paramètres facilement ajustables pour affiner leur diamètre. L'approche proposée pour la production de polymersomes reproductibles, monodisperses et prêts à l'emploi pour des essais *in vitro/in vivo* est une avancée majeure dans la production de nano-carrier, permettant ainsi une fabrication à grande échelle tout en respectant les contraintes pharmaceutiques.

Chapitre III : Encapsulation d'actifs dans les polymersomes de PEG-b-PTMC

Dans ce chapitre nous avons voulu profiter de la capacité des polymersomes à pouvoir charger des molécules hydrophobes et hydrophiles pour encapsuler le Ganciclovir et la Doxorubicine HCl, qui sont plutôt hydrophiles, et la Coumarine 6 qui est fortement hydrophobe.

Après avoir déterminé la teneur en eau critique pour la précipitation des actifs, dans le but d'éviter la précipitation anticipée du médicament avant l'auto-assemblage du polymère, nous avons tenté d'encapsuler passivement chaque actif en les ajoutant dans le processus préétabli d'auto-assemblage microfluidique de PEG_{22}-*b*-$PTMC_{51}$. Après purification, l'actif a été libéré de la vésicule en

utilisant soit un tensioactif pour déstabiliser la membrane de la vésicule, soit un solvant organique pour solubiliser à nouveau le copolymère. La spectroscopie UV-vis et la spectroscopie de fluorescence ont été utilisées pour quantifier le médicament libre grâce à l'utilisation d'une courbe d'étalonnage préétablie. Ainsi, en mesurant l'absorbance UV du Ganciclovir à 252 nm, l'émission fluorescente de la Doxorubicine HCl à 592 nm lorsqu'elle est excitée à 481 nm et l'émission fluorescente de la Coumarine 6 à 514 nm lorsqu'elle est excitée à 468 nm, nous avons réalisé que la charge passive des trois actifs entraînait systématiquement une faible teneur en actif, le tout inférieur à 0,1 %. Ces teneurs ne sont pas satisfaisantes car la littérature rapporte que le Ganciclovir a déjà été chargé jusqu'à une teneur de charge de 16,3 % dans les liposomes[1] et la Doxorubicine a été chargée jusqu'à 23 % dans les polymersomes[2].

Face à ce faible taux d'encapsulation, nous avons d'abord supposé que la membrane de la vésicule n'était pas assez épaisse pour retenir les actifs chargés. Nous avons donc décidé de remplacer l'habituel PEG_{22}-*b*-$PTMC_{51}$ (fPEG = 16%) par un copolymère deux fois plus long, à savoir le PEG_{46}-*b*-$PTMC_{119}$ (fPEG = 14%). Après avoir optimisé l'auto-assemblage assisté par microfluidique du PEG_{46}-*b*-$PTMC_{119}$ comme précédemment réalisé avec le PEG_{22}-*b*-$PTMC_{51}$, nous avons procédé à l'encapsulation passive de nos trois modèles. Nous envisagions alors une amélioration de l'encapsulation de l'actif hydrophobe, car la membrane était plus épaisse, mais le taux d'encapsulation reste inchangé. Cela peut être dû au fait que le processus d'auto-assemblage lui-même est inefficace pour l'encapsulation passive. Une autre hypothèse serait qu'un enchevêtrement plus dense de copolymère ne fournit pas un réservoir plus important pour l'actif hydrophobe. Si l'encapsulation d'actif hydrophile semble plus importante avec un copolymère plus long, elle reste insuffisante pour la délivrance de médicament, atteignant à peine 0,5%.

En comparant les méthodes de purification, l'échantillon purifié par Sephadex (colonne d'exclusion de taille) a montré un taux d'encapsulation inférieur à celui dialysé pour le médicament hydrophile. Nous supposons alors que les molécules adsorbées ont été éliminées plus efficacement par la colonne Sephadex par rapport à la dialyse.

Afin d'améliorer le taux d'encapsulation, une encapsulation active de Ganciclovir a été tentée, en utilisant soit un gradient de pH, avec un noyau interne à pH = 3 et un milieu externe à pH = 7,4, ou un gradient ionique, utilisant du sulfate d'ammonium. Après auto-assemblage microfluidique et échange de milieu externe pour créer le gradient, du Ganciclovir solubilisé dans du DMSO a été ajouté et laissé sous agitation pendant plusieurs heures. Le DMSO était censé jouer le rôle de plastifiant pour permettre au médicament de traverser la membrane des vésicules, mais il semble que 20 %vol de DMSO permette à la membrane PEG_{22}-*b*-$PTMC_{51}$ de se réorganiser en ce que les images Cryo-TEM montrent comme étant des micelles worm-like (Figure 5).

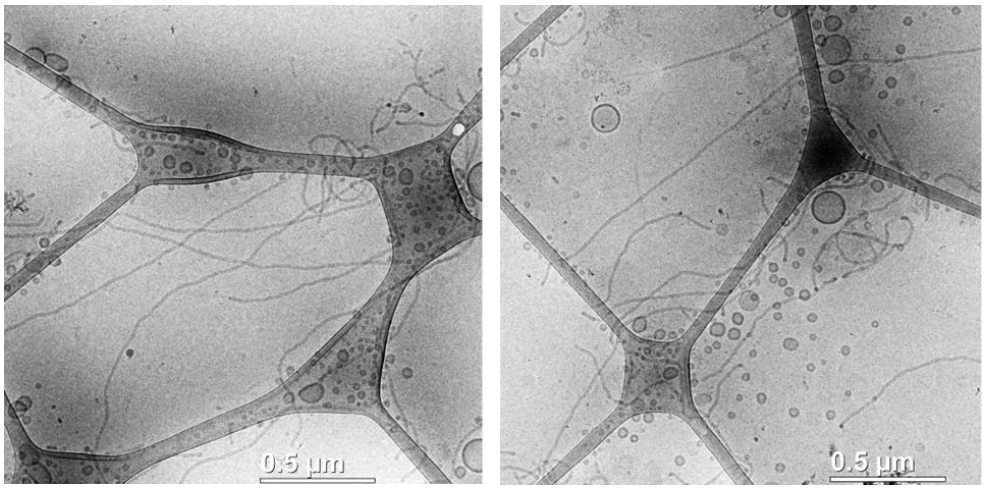

***Figure 5** : Images Cryo-TEM obtenues à partir de vésicule PEG_{22}-b-$PTMC_{51}$ après chargement actif par gradient ionique de Ganciclovir avec un temps d'agitation en présence de Ganciclovir de 38 h.*

Pour augmenter le taux d'encapsulation, plusieurs expériences sont encore envisageables. L'encapsulation passive simple utilisant l'auto-assemblage assisté par microfluidique ne semble pas être pertinente. Nous aimerions ajuster les paramètres microfluidiques tels que la composition du solvant organique et le contrôle de la température, pour permettre ainsi la précipitation du médicament et l'auto-assemblage du copolymère à la même quantité d'eau pour permettre le chargement des cristaux de noyaux d'actif, et non l'actif libre en solution.

L'absence d'encapsulation d'actifs pendant l'encapsulation passive pourrait également être due au mécanisme d'auto-assemblage lui-même. En effet, les vésicules résultent soit de la formation et de la fermeture de membranes, soit de la transformation de micelles gonflées. Si le dernier mécanisme est privilégié, il a été démontré que l'encapsulation était assez inefficace car les actifs traversent à peine la membrane des vésicules hydrophobes.
Le chapitre 4 sera donc consacré à l'élucidation du mécanisme d'auto-assemblage lors de la formulation microfluidique.

Chapitre IV : Elucidation du mécanisme d'auto-assemblage

Dans ce chapitre, nous avons essayé d'élucider le mécanisme d'auto-assemblage du PEG_{22}-*b*-$PTMC_{51}$ pour expliquer les résultats de faible taux d'encapsulation mis en évidence au chapitre III. La littérature rapporte deux principaux mécanismes d'auto-assemblage (Figure 6).
Le premier mécanisme implique que la première étape de l'auto-assemblage des chaînes libres est une structure micellaire. Elle évolue en micelles allongées qui s'aplatissent et se referment pour former des vésicules. Ce mécanisme implique l'encapsulation du milieu environnant, ainsi, des niveaux raisonnables d'encapsulation de molécules hydrophiles sont attendus. Le deuxième mécanisme propose que les micelles de la première étape évoluent en micelles gonflées qui se restructurent en vésicule. On s'attend à ce que ce mécanisme empêche l'encapsulation de niveaux élevés de molécules hydrophiles. Nous avions l'intention de prouver que PEG_{22}-*b*-$PTMC_{51}$ suivait le deuxième mécanisme lors de son auto-assemblage.

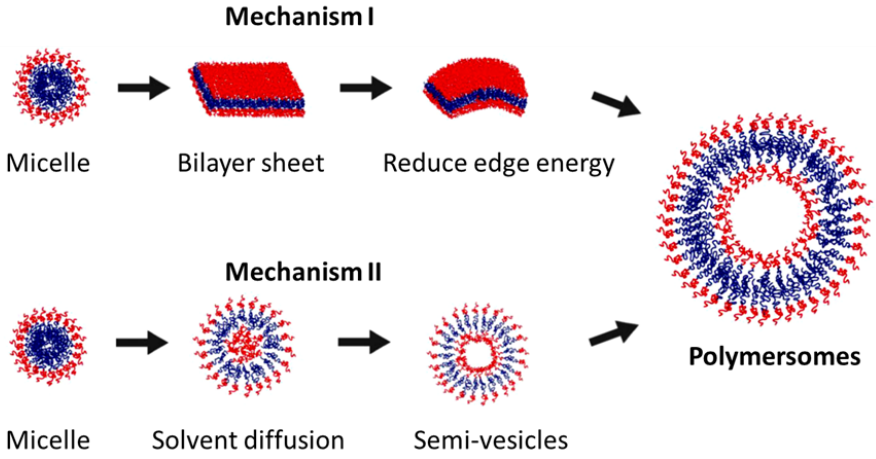

***Figure 6** : Représentation schématique des mécanismes d'auto-assemblage supposés pour la formation de vésicules. Iqbal et al.[3]*

Nous avons d'abord prouvé qu'il était possible de piéger cinétiquement des morphologies intermédiaires en stoppant l'augmentation de la teneur en eau. Nous avons utilisé la microscopie confocale pour observer ces morphologies intermédiaires avec les deux solvants organiques : DMSO et Acétone. Ces deux solvants organiques présentent un comportement similaire. Nous avons d'abord observé une séparation de phases liquide-liquide dans laquelle le copolymère forme des gouttelettes de coacervat avec le solvant organique. Ces gouttelettes fusionnent jusqu'à une teneur en eau qui empêche la poursuite de la coalescence. On observe alors un bourgeonnement à la surface de celles-ci. Le système impliquant le DMSO comme solvant organique semble rester cinétiquement piégé à ce stade, empêchant alors les vésicules de se détacher des gouttelettes (Figure7). D'autre part, l'expérience impliquant l'acétone donne lieu à des vésicules qui se détachent spontanément de la surface du coacervat.

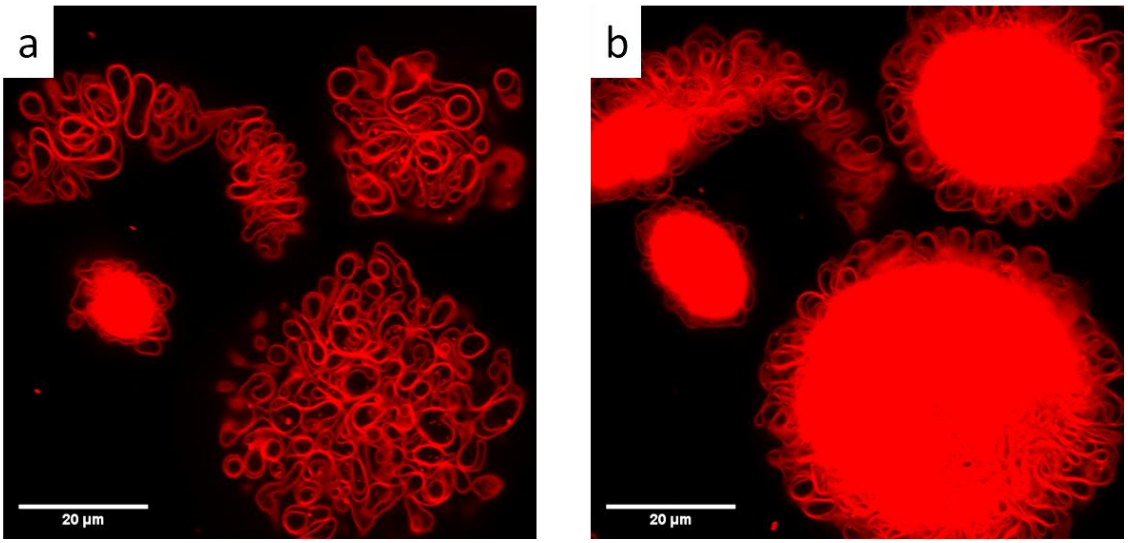

***Figure 7** : Observations en microscopie confocale dans le canal rouge de PEG_{22}-b-$PTMC_{51}$ et PEG_{22}-b-$PTMC_{51}$-Cy5.5 dans du DMSO après addition de 80%vol d'eau. b : surface de l'objet, a : centre de l'objet révélant des boucles membranaires compactées.*

Après avoir prouvé l'observabilité des vésicules de PEG_{22}-*b*-$PTMC_{51}$ par mesure rayons X sur une source de rayons X de laboratoire, une étude a été menée sur l'auto-assemblage assisté par microfluidique, formant des vésicules qui ne peuvent pas être observées par microscopie confocale en raison de leur taille (< 200 nm), avec suivi *in operando* de la diffusion des rayons X dans un système d'auto-assemblage assisté microfluidique. Une configuration de co-flux a été faite au laboratoire pour permettre la mesure des rayons X pendant le fonctionnement du flux. Plusieurs paramètres de débit ont été utilisés pour nous permettre d'observer les phénomènes se produisant pendant ou après l'interdiffusion des solvants, selon que l'auto-assemblage du copolymère soit plus rapide ou plus lent que l'interdiffusion du solvant.

Une expérience utilisant l'acétone comme solvant organique a montré la formation rapide d'objet vésiculaire, observable dès la première mesure. De plus, les signaux obtenus restent difficiles à expliquer en raison d'un mécanisme inhabituel qui impliquerait la formation de vésicules avant les micelles allongées. L'expérience doit être reproduite pour une meilleure compréhension. On présume que la configuration co-flux n'est pas le design approprié pour observer les toutes premières étapes de l'auto-assemblage. Un autre design de puce pourrait être alors envisagé ainsi que d'autres paramètres d'écoulement. Toutes les expériences utilisant du DMSO montrent des résultats identiques pour tous les débits utilisés, mettant ainsi en évidence un problème de remontée d'eau dans le capillaire interne, provoquant de ce fait la rencontre prématurée du copolymère et de l'eau avant la zone observable avec les rayons X.

En ce qui concerne les résultats détaillés dans ce chapitre, il reste difficile de confirmer un quelconque mécanisme d'auto-assemblage. La microscopie confocale n'est pas en faveur d'un mécanisme d'auto-assemblage impliquant le rapprochement de micelles allongées, ce qui pourrait expliquer le faible taux d'encapsulation de nos vésicules, mais cette hypothèse n'a pu être confirmée par des mesures SAXS.

Perspectives

Malgré un faible taux d'encapsulation, les vésicules prêtes à l'emploi pour des expériences *in vitro/in vivo* avec un contrôle précis de la taille restent un outil intéressant pour l'évaluation de l'impact de la taille des nanoparticules dans les conditions biologiques. La littérature rapporte des exemples d'études sur la taille des nanoparticules affectant la biodistribution. Par exemple, Kaga *et al.* ont rapporté l'impact de la taille de nanoparticules polymères sur la biodistribution.[4] Dans ce cas, des nanoparticules de poly(méthacrylate de glycidyle)-*b*-poly(oligo(éthylène glycol) méthacrylate d'éther méthylique)-*b*-polystyrène (PGMA-*b*-POEGMA-*b*-PS) de tailles différentes sont obtenues en modifiant la longueur de la chaîne de polystyrène. Cette étude présente une accumulation plus élevée de particules plus petites dans la tumeur que de particules plus grosses. He *et al.* relatent une étude sur les NPs greffées de carboxyméthyl chitosan (CMCNP) et les NPs greffées de chlorhydrate de chitosan (CHNP).[5] Les NPs ont été préparées par polymérisation de méthacrylate de méthyle (MMA) sur des dérivés de chitosane, une quantité variable de MMA, CMC et CH étant utilisée pour obtenir des NPs de différentes tailles (150 à 500 nm). Cette étude met en exergue que les NPs de 150 nm ont tendance à s'accumuler plus efficacement dans les tumeurs que les NPs plus grosses. Dans la plupart des articles qui évaluent l'influence de la taille des nanoparticules sur les propriétés de biodistribution, un biais existe car le type de copolymère ou le poids moléculaire est varié dans le but de faire varier la taille des objets. Ici, nous proposons des modèles chimiquement identiques de vésicules de diamètres différents, éliminant ainsi l'impact de tout paramètre autre que la taille des vésicules sur la biodistribution.

Alors que l'impact de la taille des nanoparticules sur la biodistribution pourrait être un champ d'application potentiel pour ce projet, les principaux domaines d'intérêts sont l'impact de la taille des polymères sur la bioconjugaison et le contrôle de la libération des médicaments. Ces deux aspects faisaient partie du projet plus large "TEPEE" dans lequel ce projet doctoral est impliqué. Le cytomégalovirus humain (HCMV) provoque une maladie grave et une mortalité élevée chez les hôtes immunodéprimés, et lorsque le Ganciclovir est administré à l'état libre, une efficacité limitée et des effets secondaires toxiques se produisent. Par conséquent, il existe un besoin de traitements plus efficaces pour combattre ce virus et l'encapsulation du GCV à l'intérieur des polymersomes, pourrait alors induire une délivrance locale de ce médicament près du site d'infection grâce à un contrôle de la libération du médicament dans l'espace et dans le temps, ce qui pourrait être une stratégie potentielle (Figure 8).

Des premières tentatives d'encapsulation du Ganciclovir dans des polymersomes PEG-*b*-PTMC ont ainsi été réalisées et détaillées dans ce manuscrit. La libération contrôlée du médicament dans le temps sera assurée par la rupture de la membrane polymérique par choc osmotique induit par la lumière. La molécule photo-clivable sera encapsulée dans des polymersomes pour induire un choc hypotonique sous rayonnement lumineux. Le projet de thèse de Matthieu Kamierzac est dédié à la synthèse de molécules photo-clivables sous rayonnement infrarouge à visible. Des molécules photo-clivables sensibles à des longueurs d'onde plus énergétiques ont déjà été développées[6] mais l'utilisation d'un tel rayonnement dans le corps humain pourrait induire des effets secondaires.[7–9] Ici,

nous visons à utiliser des rayonnements inoffensifs en synthétisant des dérivés de Rhodamine et de Squaraine sensibles aux rayonnements IR-Visible.

La libération contrôlée du médicament en fonction de sa localisation dans le corps humain sera assurée par la conjugaison Lymphocyte T - polymersomes. Récemment, il a été prouvé qu'une sous-population de lymphocytes T appelées lymphocytes T γδ reconnaissait le CMV et pouvait donc migrer près de la zone infectée[10–12]. En utilisant l'ingénierie GlycoMetabolic, le groupe fonctionnel azide sera exprimé à la surface des lymphocytes T γδ[13–15]. D'autre part, des polymersomes fonctionnalisés par le dibenzocyclooctyne seront produits pour induire une cycloaddition d'alcyne-azide promu par la contrainte (SPAAC), également appelée: réaction de clic sans Cuivre, au contact de cellules fonctionnalisées[16–18]. Le projet de thèse de Selma Cornillot-Clément sera dédié à l'optimisation de l'ingénierie GlycoMetabolic sur lymphocytes T γδ, la conjugaison Lymphocyte T - polymersomes et l'évaluation du comportement des lymphocytes *in vitro et in vivo.*

Pour permettre le suivi des vésicules *in vivo et in vitro*, la fonctionnalisation du PEG-*b*-PTMC par la Cyanine 5.5, un colorant fluorescent avec un pic d'excitation à 683 nm et un pic d'émission à 703 nm, a été réalisée. Le PEG-*b*-PTMC-Cy5.5 a été obtenu via la synthèse de PEG-*b*-PTMC-COOH. Le copolymère PEG-*b*-PTMC a également été fonctionnalisé avec du DBCO pour permettre la chimie du clic et le DBCO-PEG-*b*-PTMC a été synthétisé via l'intermédiaire NH2-PEG-*b*-PTMC. Les deux copolymères fonctionnalisés ont été synthétisés par Pierre Lalanne. Ces copolymères fonctionnalisés ont été utilisés en petites quantités comme blocs supplémentaires dans les vésicules ; le PEG-*b*-PTMC non fonctionnalisé restant le bloc de construction principal, comme le montre la Figure 9.

Les résultats préliminaires révèlent le succès de la formulation de vésicules monodisperses fluorescentes exprimant des fonctions DBCO à leur surface, et prêtes pour une utilisation *in vitro/in vivo*, permettant l'évaluation de leur conjugaison aux lymphocytes T exprimant des fonctions azide à leur surface.

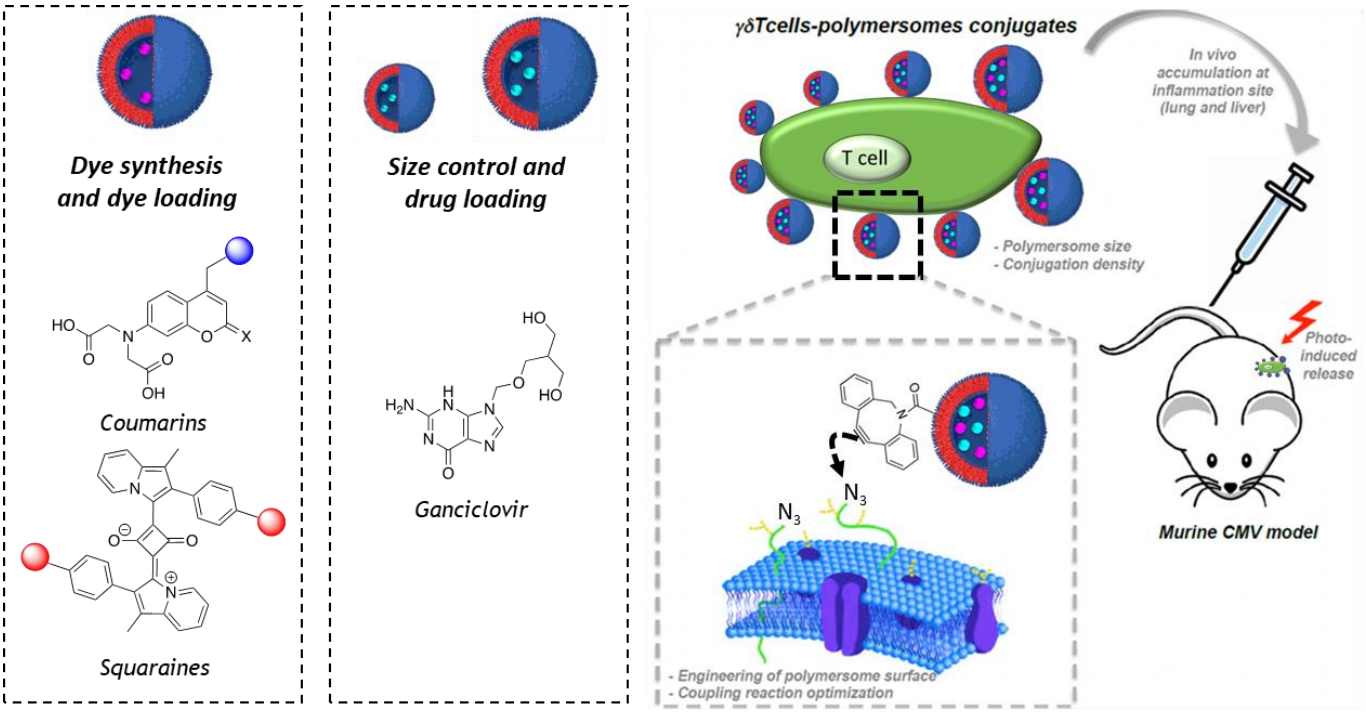

Figure 8 *: Vue d'ensemble des trois axes du projet TEPEE : synthèse et chargement de colorants photosensibles dans les polymersomes, contrôle de la taille et chargement du médicament dans les polymersomes et les conjugués cellules γδT-polymersomes vers la libération contrôlée du médicament du Ganciclovir.*

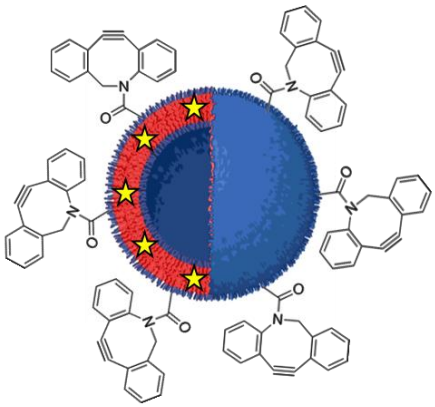

Principal brick
PEG-*b*-PTMC that can self-assemble into polymersomes

Fluorescent brick
Cy5.5-terminated PTMC for in vitro and in vivo imaging

Reactive brick
DBCO-terminated PEG for SPAAC conjugation

MeO–OH — PEG_{22}-*b*-$PTMC_{51}$

MeO–Cy5.5 — PEG_{22}-*b*-$PTMC_{51}$-Cy5.5

DBCO–OH — DBCO-PEG_{49}-*b*-$PTMC_{56}$

Figure 9 *: Représentation schématique de la vésicule de PEG-b-PTMC fonctionnalisée avec la sonde fluorescente Cyanine 5.5 et les fonctions DBCO pour la cycloaddition alcyne-azoture et les copolymères fonctionnalisés PEG_{22}-b-$PTMC_{51}$-Cy5.5 et DBCO-PEG_{49}-b-$PTMC_{56}$ fonctionnalisés associés.*

Références

(1) Asasutjarit, R.; Managit, C.; Phanaksri, T.; Treesuppharat, W.; Fuongfuchat, A. Formulation Development and in Vitro Evaluation of Transferrin-Conjugated Liposomes as a Carrier of Ganciclovir Targeting the Retina. *Int J Pharm* **2020**, *577*, 119084. https://doi.org/10.1016/j.ijpharm.2020.119084.

(2) Sanson, C.; Schatz, C.; Le Meins, J.-F.; Soum, A.; Thévenot, J.; Garanger, E.; Lecommandoux, S. A Simple Method to Achieve High Doxorubicin Loading in Biodegradable Polymersomes. *J Control Release* **2010**, *147* (3), 428–435. https://doi.org/10.1016/j.jconrel.2010.07.123.

(3) Iqbal, S.; Blenner, M.; Alexander-Bryant, A.; Larsen, J. Polymersomes for Therapeutic Delivery of Protein and Nucleic Acid Macromolecules: From Design to Therapeutic Applications. *Biomacromolecules* **2020**, *21* (4), 1327–1350. https://doi.org/10.1021/acs.biomac.9b01754.

(4) Kaga, S.; Truong, N. P.; Esser, L.; Senyschyn, D.; Sanyal, A.; Sanyal, R.; Quinn, J. F.; Davis, T. P.; Kaminskas, L. M.; Whittaker, M. R. Influence of Size and Shape on the Biodistribution of Nanoparticles Prepared by Polymerization-Induced Self-Assembly. *Biomacromolecules* **2017**, *18* (12), 3963–3970. https://doi.org/10.1021/acs.biomac.7b00995.

(5) He, C.; Hu, Y.; Yin, L.; Tang, C.; Yin, C. Effects of Particle Size and Surface Charge on Cellular Uptake and Biodistribution of Polymeric Nanoparticles. *Biomaterials* **2010**, *31* (13), 3657–3666. https://doi.org/10.1016/j.biomaterials.2010.01.065.

(6) Peyret, A.; Ibarboure, E.; Tron, A.; Beauté, L.; Rust, R.; Sandre, O.; McClenaghan, N. D.; Lecommandoux, S. Polymersome Popping by Light-Induced Osmotic Shock under Temporal, Spatial, and Spectral Control. *Angew Chem Int Ed Engl* **2017**, *56* (6), 1566–1570. https://doi.org/10.1002/anie.201609231.

(7) Weinkauf, B.; Rukwied, R.; Quiding, H.; Dahllund, L.; Johansson, P.; Schmelz, M. Local Gene Expression Changes after UV-Irradiation of Human Skin. *PLOS ONE* **2012**, *7* (6), e39411. https://doi.org/10.1371/journal.pone.0039411.

(8) Baadsgaard, O. In Vivo Ultraviolet Irradiation of Human Skin Results in Profound Perturbation of the Immune System: Relevance to Ultraviolet-Induced Skin Cancer. *Archives of Dermatology* **1991**, *127* (1), 99–109. https://doi.org/10.1001/archderm.1991.01680010109019.

(9) Wang, Z.; Boudjelal, M.; Kang, S.; Voorhees, J. J.; Fisher, G. J. Ultraviolet Irradiation of Human Skin Causes Functional Vitamin A Deficiency, Preventable by All-Trans Retinoic Acid Pre-Treatment. *Nat Med* **1999**, *5* (4), 418–422. https://doi.org/10.1038/7417.

(10) Khairallah, C.; Déchanet-Merville, J.; Capone, M. Γδ T Cell-Mediated Immunity to Cytomegalovirus Infection. *Front Immunol* **2017**, *8*, 105. https://doi.org/10.3389/fimmu.2017.00105.

(11) Kaminski, H.; Marsères, G.; Cosentino, A.; Guerville, F.; Pitard, V.; Fournié, J.-J.; Merville, P.; Déchanet-Merville, J.; Couzi, L. Understanding Human Γδ T Cell Biology toward a Better Management of Cytomegalovirus Infection. *Immunol Rev* **2020**, *298* (1), 264–288. https://doi.org/10.1111/imr.12922.

(12) Khairallah, C.; Netzer, S.; Villacreces, A.; Juzan, M.; Rousseau, B.; Dulanto, S.; Giese, A.; Costet, P.; Praloran, V.; Moreau, J.-F.; Dubus, P.; Vermijlen, D.; Déchanet-Merville, J.; Capone, M. Γδ T Cells Confer Protection against Murine Cytomegalovirus (MCMV). *PLoS Pathog* **2015**, *11* (3), e1004702. https://doi.org/10.1371/journal.ppat.1004702.

(13) Pan, H.; Li, P.; Li, G.; Li, W.; Hu, B.; He, H.; Chen, Z.; Wang, F.; Liu, L.; Gong, Y.; Han, Y.; Luo, Y.; Zheng, M.; Ma, Y.; Cai, L.; Jin, Y. Glycometabolic Bioorthogonal Chemistry-Guided Viral Transduction for Robust Human T Cell Engineering. *Advanced Functional Materials* **2019**, *29* (22), 1807528. https://doi.org/10.1002/adfm.201807528.

(14) Cioce, A.; Bineva-Todd, G.; Agbay, A. J.; Choi, J.; Wood, T. M.; Debets, M. F.; Browne, W. M.; Douglas, H. L.; Roustan, C.; Tastan, O. Y.; Kjaer, S.; Bush, J. T.; Bertozzi, C. R.; Schumann, B. Optimization of Metabolic Oligosaccharide Engineering with Ac4GalNAlk and Ac4GlcNAlk by an

Engineered Pyrophosphorylase. *ACS Chem. Biol.* **2021**, *16* (10), 1961–1967. https://doi.org/10.1021/acschembio.1c00034.

(15) Saxon, E.; Bertozzi, C. R. Cell Surface Engineering by a Modified Staudinger Reaction. *Science* **2000**, *287* (5460), 2007–2010. https://doi.org/10.1126/science.287.5460.2007.

(16) Idiago-López, J.; Moreno-Antolín, E.; Eceiza, M.; Aizpurua, J. M.; Grazú, V.; de la Fuente, J. M.; Fratila, R. M. From Bench to Cell: A Roadmap for Assessing the Bioorthogonal "Click" Reactivity of Magnetic Nanoparticles for Cell Surface Engineering. *Bioconjugate Chem.* **2022**, *33* (9), 1620–1633. https://doi.org/10.1021/acs.bioconjchem.2c00230.

(17) Kim, E.; Koo, H. Biomedical Applications of Copper-Free Click Chemistry: In Vitro , in Vivo , and Ex Vivo. *Chemical Science* **2019**, *10* (34), 7835–7851. https://doi.org/10.1039/C9SC03368H.

(18) Tomás, R. M. F.; Gibson, M. I. Optimization and Stability of Cell–Polymer Hybrids Obtained by "Clicking" Synthetic Polymers to Metabolically Labeled Cell Surface Glycans. *Biomacromolecules* **2019**, *20* (7), 2726–2736. https://doi.org/10.1021/acs.biomac.9b00478.

Abstract

This thesis is dedicated to the production of polymersomes for drug delivery applications, formulated by microfluidic-assisted self-assembly of amphiphilic PEG-b-PTMC copolymers. The microfluidic method was chosen in order to obtain polymersomes with a controlled size distribution and high reproducibility. Polymersomes are formulated in an aqueous solvent with controlled osmolarity, mimicking physiological conditions, allowing them to be directly usable during in vitro / in vivo experiments. The variation of the copolymer concentration as well as that of the total flow rate in the microfluidic chip highlighted the impact of these parameters on the diameter of the obtained polymersomes. It was therefore possible to obtain polymersomes of controlled size between 76 and 224 nm with low dispersity. Subsequently, the encapsulation of 3 model molecules, Ganciclovir, Doxorubicin HCL and Coumarin 6 was studied. The passive encapsulation of these 3 molecules showed low encapsulation efficiencies. The hypothesis according to which the membrane thickness of the polymersome was not thick enough to retain the molecules was studied by the use of a copolymer of higher molar mass. The encapsulation efficiency was not significantly improved in this case. Active encapsulation of Ganciclovir by ion gradient or pH gradient resulted in destabilization of the vesicles and was not further investigated. The self-assembly mechanism of the vesicle copolymer was then studied in order to better understand these low encapsulation rates. Self-assembly was first studied by observation under a confocal microscope revealing a very interesting phenomenon of coacervation of copolymers and budding from their surface. A microfluidic co-flow system allowing monitoring of structures formed under flow in a synchrotron environment was then developed with the aim of describing the formulation path of polymersomes by small-angle X-ray scattering (SAXS).

Cette thèse est consacrée à la production de polymersomes pour des applications de délivrance de principes actifs, formulés par auto-assemblage assisté par microfluidique de copolymères amphiphiles PEG-*b*-PTMC. Le procédé microfluidique a été choisi dans le but d'obtenir des polymersomes avec une distribution de taille contrôlée et une grande reproductibilité. Les polymersomes sont formulés dans un solvant aqueux à osmolarité contrôlée, mimant les conditions physiologiques, leur permettant d'être directement utilisables lors d'expériences *in vitro / in vivo.* La variation de la concentration en copolymère ainsi que celle du débit total en puce microfluidique ont permis de mettre en avant l'impact de ces paramètres sur la taille des polymersomes obtenus. Il a donc été possible d'obtenir des polymersomes de taille contrôlée entre 76 et 224 nm avec une faible dispersité. Par la suite, l'encapsulation de 3 molécules modèles, Ganciclovir, Doxorubicine HCL et Coumarine 6 a été étudiée. L'encapsulation passive de ces 3 molécules a montré de faibles efficacités d'encapsulation. L'hypothèse selon laquelle l'épaisseur de membrane du polymersome n'était pas assez importante pour retenir les molécules a été étudiée par l'utilisation d'un copolymère de masse molaire plus élevée. L'efficacité d'encapsulation n'a pas été significativement améliorée dans ce cas. L'encapsulation active du Ganciclovir par gradient ionique ou gradient de pH a engendré la déstabilisation des vésicules et n'a pas été approfondie. Le mécanisme d'auto-assemblage du copolymère en vésicule a ensuite été étudié dans le but de mieux comprendre ces faibles taux d'encapsulation. L'auto-assemblage a d'abord été étudié par une observation au microscope confocal révélant un phénomène très intéressant de coacervation des copolymères et de bourgeonnement à partir de leur surface. Un système de co-flow microfluidique permettant un suivi des structures formées sous écoulement dans un environnement synchrotron a ensuite été développé dans le but de décrire le chemin de formulation des polymersomes par diffusion des rayons X aux petits angles (SAXS).